Faculty of Aerospace Engineering

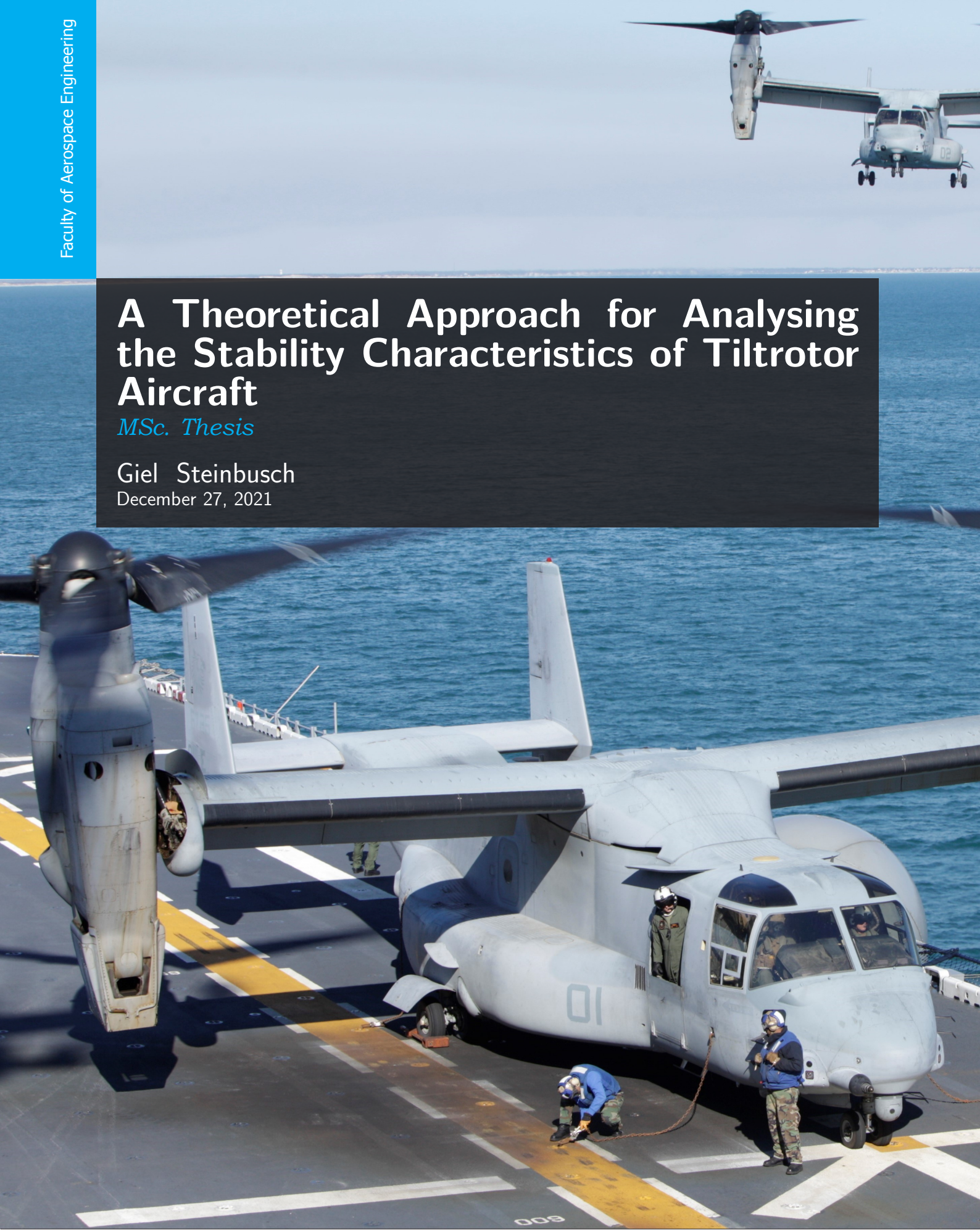

A Theoretical Approach for Analysing the Stability Characteristics of Tiltrotor Aircraft

MSc. Thesis

Giel Steinbusch

December 27, 2021

TU Delft Delft University of Technology

Challenge the future

A Theoretical Approach for Analysing the Stability Characteristics of Tiltrotor Aircraft

MSc. Thesis

by

Giel Steinbusch

In partial fulfilment of the requirements for the degree of

Master of Science
in Aerospace Engineering

at the Delft University of Technology,
to be defended publicly on January 11th, 2022 at 10:00

Student number:	4479289	
Thesis Supervisor	Dr. M.D. Pavel	TU Delft, chair
Thesis Committee	Dr. M.D. Pavel	TU Delft
	Dr. E. van Kampen	TU Delft
	Ir. P.C. Roling	TU Delft

An electronic version of this thesis is available at http://repository.tudelft.nl/.

Cover image (adapted): V-22 Osprey tiltrotor aircraft, February 2012 - Accessed December 2021
https://commons.wikimedia.org/wiki/File:US_Navy_120131-M-DK975-090_An_MV-22_Osprey_tiltrotor_aircraft_lands_aboard_the_amphibious_assault_ship_USS_Kearsarge_(LHD_3)_during_exercise_Bold_A.jpg

TU Delft

Preface

You are currently reading the final thesis report of my master Aerospace Engineering, which I conducted at Delft University of Technology. Throughout my studying career in aerospace engineering I have become intrigued by the helicopter in particular, and I find the technology behind it overwhelming but fascinating. Conducting my thesis research on the topic of tiltrotor aircraft, which have both helicopter and airplane characteristics, was a very challenging but enriching experience.

I would like to express my gratitude towards my thesis supervisor Marilena for providing me with the guidance and support that I needed throughout my thesis. Although you have a very busy schedule you always took your time to share your thoughts on my research progress with and help me steer into the right direction. Thank you for sharing your expertise on helicopters with me and enlighten me with more knowledge about these fascinating vehicles.

Furthermore, I would like to thank my roommates Bart, Bas, Guy and Tristan. We have made some amazing memories together during our student life in Delft. Although the past 2 years have not been up to normal standards due to current COVID-19 pandemic, I have enjoyed every second of it. Bart, being stuck at home and doing all our thesis work remotely has not been easy, but our lunches and coffee breaks together at home during which we would discuss our thesis troubles have helped me get through this final phase of my masters.

To my family, thank you bearing with me the past year while I worked on my thesis, but also for the other 23 years of my life. Thank you for giving me the opportunity to move to Delft and for encouraging me in times of little advancements. Your motivation and support means a lot to me.

Giel Steinbusch
Delft, December 2021

Contents

List of Figures

List of Tables

List of Abbreviations

ARL	articulated rotor, left
ARR	articulated rotor, right
BEM	blade element theory
c.g.	centre of gravity
c.m.	centre of mass
FCS	flight control system
FL	fuselage
HSL	horizontal stabilizer, left
HSR	horizontal stabilizer, right
JANRAD	joint army-navy rotorcraft analysis and design
LCTR	large civil tilt-rotor
LTR	large tilt-rotor
MOI	moment of inertia
RHILP	rotorcraft handling, interactions and loads prediction
VSTL	vertical stabilizer, bottom left
VSTR	vertical stabilizer, bottom right
VSTL	vertical stabilizer, top left
VSTR	vertical stabilizer, top right
VTOL	vertical take-off and landing
WAL	wing aileron, left
WAR	wing aileron, right
WFL	wing free, left
WFLL	wing flap, left
WFLR	wing flap, right
WFR	wing free, right

List of Symbols

General

a_0	coning angle (rad)
$a_{0,pre}$	Pre-coning angle (rad)
a_1	longitudinal disc tilt (rad)
a	acceleration (m/s^2)
A_{eq}	flat plate drag area (m^2)
$\mathbf{A}$	system matrix
b	span (m)
b_1	lateral disc tilt (rad)
BL	aircraft buttline (m)
$\mathbf{B}$	control matrix
c	chord (m)
C_D	Drag coefficient (-)
$C_{D,0\alpha}$	zero angle of attack fuselage drag coefficient (-)
C_H	in-plane longitudinal rotor force coefficient (-)
$c_{r,c}$	root chord (m)
$c_{t,c}$	tip chord (m)
C_L	Lift coefficient (-)
c_{L_α}	lift curve slope (-)
$C_{L,0\alpha}$	zero angle of attack fuselage lift coefficient (-)
c_{d_0}	zero-lift drag coefficient (-)
c_{d_1}	first order drag coefficient (-)
c_{d_0}	second order drag coefficient (-)
$C_{M,0\alpha}$	zero angle of attack fuselage moment coefficient (-)
C_O	in-plane longitudinal rotor moment coefficient (-)
C_P	in-plane lateral rotor moment coefficient (-)
C_Q	rotor torque coefficient (-)
C_S	In-plane lateral rotor force coefficient (-)
$C_{T,BEM}$	thrust coefficient calculated using the blade element momentum method (-)
$C_{T,GLAU}$	thrust coefficient calculated using the Glauert method (-)
D	drag (N)
$d_{x,c}$	distance from body cg to component cg along body x-axis (m)
$d_{y,c}$	distance from body cg to component cg along body y-axis (m)
$d_{z,c}$	distance from body cg to component cg along body z-axis (m)
e	oswald factor (rad)
$\mathbf{F}$	force vector (N)
$\mathcal{F}$	reference frame (-)
g	gravitational acceleration (m/s^2)
GW	gross weight (kg)
H	H-force, longitudinal in-plane rotor force (N)
I_{bl}	blade moment of inertia at the flapping hinge about the flapping axis (kg m^2)
$\mathbf{I}$	identity matrix
i	incidence angle (rad)
$\mathbf{u}$	input vector
I_x	moment of inertia about the x-axis (kg m^2)
I_y	moment of inertia about the y-axis (kg m^2)
I_z	moment of inertia about the z-axis (kg m^2)
J_{xz}	product of inertia about the x- and z-axis (kg m^2)
K_β	centre-spring rotor stiffness (Nm/rad)
$KI1$	inertia coefficient for I_x (-)
$KI2$	inertia coefficient for I_y (-)
$KI3$	inertia coefficient for I_z (-)
$KI4$	inertia coefficient for J_xz (-)
L	lift (N)
M	Rolling moment about the x-axis (Nm)
l_n	nacelle length (m)
L_p	roll damping derivative (1/s)
L_v	dihedral stability derivative (rad/s/m)
m	mass (kg)

MAC	mean aerodynamic chord position vector (m)
M_{bl}	blade hub moment (Nm)
M	Pitching moment about the y-axis (Nm)
M	moment vector (N)
M_q	pitch damping derivative (1/s)
M_u	speed stability derivative (rad/s/m)
M_w	incidence static stability derivative (rad/s/m)
N	number of rotors (-)
N	Yawing moment about the z-axis (Nm)
N_v	yaw damping derivative (1/s)
N_v	weathercock stability derivative (rad/s/m)
q	pitch rate, angular velocity component about the body y-axis (rad/s)
$\overline{q}$	non-dimensionalized pitch rate, angular velocity component about the body y-axis (-)
R	radius of rotor blade (m)
p	roll rate, angular velocity component about the body x-axis (rad/s)
$\overline{p}$	non-dimensionalized roll rate, angular velocity component about the body x-axis (-)
SL	aircraft stationline (m)
t	time (s)
T	thrust (N)
$\mathbf{T_{x2y}}$	transformation matrix from reference frame x to y (-)
u	velocity component along body x-axis (m/s)
V	airspeed (kts, m/s)
V	velocity vector (N)
v_i	induced velocity (ms)
V_{lat}	velocity component along the y-axis of the control plane reference frame (m/s)
V_{lon}	velocity component along the x-axis of the control plane reference frame (m/s)
v	velocity component along body y-axis (m/s)
W	weight (N)
WL	aircraft waterline (m)
w	velocity component along body z-axis (m/s)
$\mathbf{x}$	state vector
$\mathbf{x_0}$	initial state vector
X_{COL}	collective stick deflection (in)
XFL	flap setting (-)
X	force component along x-axis (N)
X_{LAT}	lateral cyclic stick deflection (in)
X_{LON}	longitudinal cyclic stick deflection (in)
X_{PED}	pedal deflection (in)
X_u	drag damping derivative (1/s)
r	yaw rate, angular velocity component about the body z-axis (rad/s)
$\overline{r}$	non-dimensionalized yaw rate, angular velocity component about the body z-axis (-)
Y	force component along y-axis (N)
Y_v	Direct side force damping derivative (1/s)
Z	force component along z-axis (N)
Z_w	heave damping derivative (1/s)
α	angle of attack (rad)
α_{0L}	zero-lift angle of attack (rad)
α_d	downwash angle of attack (rad)
β_m	mast angle (rad)
γ	flight path angle (rad)
Γ	dihedral angle (rad)
$\hat{\gamma}$	lock number (-)
δ	side slip angle (rad)
δ_a	aileron deflection (rad)
δ_e	elevator deflection (rad)
δ_f	flap deflection (rad)
δ_r	rudder deflection (rad)
ζ	damping ratio (-)
η	nacelle angle (rad)
$\dot{\eta}$	rate of nacelle angle change (rad/s)
$\overline{\dot{\eta}}$	non-dimensionalized rate of nacelle angle change (-)
θ	pitch angle, Euler angle defining the orientation of the aircraft relative to the Earth (°, rad)
θ_0	collective pitch (rad)
θ_{00}	Zero collective stick displacement collective (rad)
θ_{bl0}	blade twist angle at the blade root (rad)
θ_{0d}	differential collective pitch angle (rad)
θ_{075}	Collective pitch lower limit at 0.75 blade radius (rad)
$\theta_{0,LL}$	lower limit of the collective pitch at the blade root (deg)
$\theta_{0,mod}$	global collective pitch modifier (deg)

$\theta_{0,R}$	blade pitch at the root (deg)
θ_{bl1}	blade twist angle gradient (rad)
θ_{1s}	longitudinal cyclic angle (rad)
θ_{1sd}	differential longitudinal cyclic angle (rad)
λ_i	induced velocity ratio (-)
λ_c	inflow ratio (-)
λ	eigenvalue (1/s)
Λ	sweep angle (rad)
$\hat{\mu}$	advance ratio (-)
ρ	air densitiy (kg/m^3)
ϕ	roll angle, Euler angle defining the orientation of the aircraft relative to the Earth (°, rad)
σ	rotor solidity (-)
$\Psi_{x\to y}$	Gearing from x to y (-)
ψ	yaw angle, Euler angle defining the orientation of the aircraft relative to the Earth (°, rad)
Ω	rotor speed (rad/s, RPM)
ω	frequency (rad/s)

Subscripts

bl	blade
b	body
c	component
CP	control plane
DP	disc plane
dr	Dutch roll
f	fuselage
h	heave subsidence
h	hub
hs	horizontal stabilizer
NPP	nacelle pivot point
P	pylon
ph	phugoid
p	pitch subsidence
r	roll mode
sp	short period
s	spiral mode
hs	vertical stabilizer
$waCP$	wind axis control plane
$waDP$	wind axis disc plane
w	wing

Part I

Scientific Article

A Theoretical Approach for Analysing the Stability Characteristics of Tiltrotor Aircraft

G.G.J. Steinbusch

Delft University of Technology, Faculty of Aerospace Engineering

ABSTRACT

A tiltrotor is an aircraft that is able to combine the vertical take-off and landing capabilities of a conventional helicopter with the high-speed cruise and long-range characteristics of an airplane. This is made possible by the tiltable rotors which are mounted on the wingtips of a fixed-wing aircraft. Three flight modes can be distinguished in which the rotors are either oriented vertically (helicopter mode), horizontally (airplane mode) or somewhere in between (conversion mode). The aim of this research is to get a better understanding of the dynamic stability characteristics of this type of aircraft. For this purpose a six-degrees-of-freedom model has been developed using the Bell XV-15 as a reference aircraft. This non-linear model has been trimmed and linearized using a numerical differentiation technique. This paper describes the model and its main features, together with a trim analysis and an analysis of the control and stability derivatives following from the linearization. Using the linear model the stability characteristics are assessed at different combinations of airspeed and nacelle angle. It is found that the phugoid and Dutch roll modes are unstable in hover. The dihedral effect L_v destabilizes the tiltrotor Dutch roll. The spiral mode is unstable at low speeds in helicopter mode. This is mainly caused by the lack of yaw damping, which is provided by a tail rotor for conventional helicopters. Increasing the airspeed has generally a stabilizing effect to the modes. The damping of the Dutch roll and phugoid increases with decreasing nacelle angle, which can be attributed to the increase in yaw damping N_r and drag damping X_u respectively. The frequency of the spiral mode and roll mode increases and decreases respectively with decreasing nacelle angle.

Keywords: Tiltrotor, Flight dynamics, Dynamic Stability, Stability Characteristics

List of Symbols

c.g.	Centre of gravity
$\boldsymbol{A}$	System matrix
$\boldsymbol{B}$	Control matrix
$\boldsymbol{u}$	Input vector
$\boldsymbol{x_0}$	Initial state vector
$\boldsymbol{x}$	State vector
C_D	Drag coefficient (-)
C_L	Lift coefficient (-)
c_{D_0}	Zero-lift drag coefficient (-)
c_{L_α}	Lift curve slope (-)
C_T	Thrust coefficient (-)
d_{r2m}	Normal distance from the rotor disc to the MAC (m)
g	Gravitational acceleration (m/s^2)
p, q, r	Angular velocities (rad/s)
R	Radius of rotor blade (m)
SL	Aircraft stationline (m)
t	Time (s)
u, v, w	Translational velocities (m/s)
v_i	Induced velocity (ms)
w_r	Downwash due to the rotor system (m/s)
WL	Aircraft waterline (m)
X_{COL}	Collective stick deflection (in)
X_{LAT}	Lateral cyclic stick deflection (in)
X_{LON}	Longitudinal cyclic stick deflection (in)
X_{PED}	Pedal deflection (in)
α_{0L}	Zero-lift angle of attack (rad)
α	Angle of attack (rad)
δ_a	Aileron deflection (rad)
δ_e	Elevator deflection (rad)
δ_r	Rudder deflection (rad)
η	Nacelle angle (rad)
λ_i	Induced velocity ratio (-)
λ	Eigenvalue (1/s)
ϕ, θ, ψ	Euler angles defining the orientation of the aircraft relative to the Earth (°, rad)
ρ	Air densitiy (kg/m^3)
θ_0	Blade collective pitch (rad)
θ_{0d}	Differential collective pitch angle (rad)
θ_{1sd}	Differential longitudinal cyclic angle (rad)
θ_{1s}	Longitudinal cyclic angle (rad)

1. Introduction

A tilt-rotor aircraft, also referred to as simply tiltrotor, is an aircraft that is able to perform vertical take-off and landing manoeuvres like a conventional helicopter, as well as

achieving cruise speeds and long ranges that are common for a fixed-wing aircraft. This is achievable due to its rotor tilting capabilities. The rotors, also called proprotors, are mounted on the wingtips of a fixed-wing aircraft and can be tilted around 90 degrees during flight to perform both horizontal and vertical manoeuvres. The travel time to and from airports could be reduced significantly as the tiltrotor is much more flexible in take-off and landing locations because it does not require an entire landing strip [1]. This feature could make air transport much more time efficient.

For a tiltrotor three different modes can be distinguished during flight. The vehicle is said to be in helicopter mode (H-mode) when the nacelles have an angle of 90 degrees with respect to the fixed wing. In this mode the proprotors are positioned vertically generating a lift force like a conventional helicopter allowing the aircraft to perform vertical manoeuvres such as take-off, landing and hover. If the nacelles are oriented parallel to the wing, the tiltrotor is said to be in airplane mode (A-mode). In this mode, the proprotors function as airplane propellers generating thrust and the tiltrotor is able to reach high speeds. The lift in this mode is provided by the wings. If the nacelles are not oriented perpendicular or parallel with respect to the wing the tiltrotor is said to be in conversion mode (C-mode).

Although there have been several projects and developments in tiltrotor technology, the only tiltrotor that has made it to the market yet is the Bell Boeing V-22 Osprey which has solely military applications. The development of the V-22 has primarily relied on the data and experiences of the Bell XV-15. The XV-15 is a experimental tiltrotor which was the first in its sort to successfully reach a cruise velocity which could never be achieved with a conventional helicopter [2]. Many different researches have build forward on the data and experiences of the XV-15. The Generic Tilt-Rotor Simulator (GTRS) model has been developed to support tiltrotor aircraft design, pilot training and flight testing [3, 4, 5]. This real time model is mainly based on 1/5 scale wind-tunnel test data, in combination with basic physical equations and correction factors. Many different look-up tables are provided including among others the effects on the aerodynamic coefficients of the angle of attack, nacelle angle, sideslip, Mach number and flap defection. Because of its high accuracy and availability of data the GTRS model is often used for tiltrotor modelling. Tischler developed a tiltrotor flight dynamics model using frequency domain identification technology [6, 7]. Johnson investigated the dynamics of tilting proprotor aircraft in cruise flight [8]. The linear state space modelling a tiltrotor was investigated by Klein using JANRAD (Joint Army-Navy Rotorcraft Analysis and Design)[9]. This model is however unable to investigate the conversion mode. A simple open-source flight dynamics model using basic aerodynamic equations was developed by Kleinhesselink [10]. At the University of Liverpool a flight dynamics model of the XV-15 has been developed using FLIGHTLAB: the FXV-15 [11]. FLIGHTLAB is a multi-body modelling environment, providing a modular approach to the creation of flight dynamics models. The FXV-15 served as the baseline model for several civil tiltrotor variants. The EUROTILT tiltrotor configuration was developed and used for the 'Rotorcraft Handling, Interactions and Loads Prediction' (RHILP) project which is one the first projects to develop handling qualities criteria for a civil tiltrotor [12]. The longitudinal stability, control and handling qualities of the Large Tilt-Rotor (LTR) model, also developed in FLIGHTLAB, are assessed by Walker and Perfect [13]. Berger et al. investigated the trim data, linearized control and stability derivatives and eigenvalues of a lift offset coaxial rotorcraft and a tiltrotor configuration. The generic models of both aircraft were developed using HeliUM, a comprehensive rotorcraft simulation code [14].

Currently, more research is conducted into the civil applications of the tiltrotor. The development of several tiltrotor projects is still ongoing, amongst others the Agusta Westland AW609 project. This tiltrotor has been under development for over 15 year but has not made it to the market yet at the time of writing this article. In 2015 the AW609 suffered a fatal crash when a high-speed dive during a test flight became unstable. The AW609 showed unstable behavior about the roll and yaw axis which could be described as a diverging Dutch roll mode [15]. The overview above shows that there is already quite some literature about tiltrotor aircraft, but most literature is focused on flight dynamics modeling or handling quality evaluation. The stability of the tiltrotor is however much less investigated and there is primarily a lack of knowledge how the dynamic behavior is influenced by different flight parameters. The AW609 accident shows that the stability of the tiltrotor is still not sufficiently predictable. The aim of this research is to get a better understanding on the stability characteristics of tiltrotor aircraft. It will be analysed how the stability and control derivatives behave as a function of airspeed and nacelle angle and which components contribute to each derivative. Furthermore, data from different models are compared and their similarities and differences in results are explained by comparing their model properties. The linear models are then used to investigate the dynamic modes of the tiltrotor and how the modes are affected by the stability derivatives.

Firstly, the non-linear flight dynamics model used for this analysis is described. Thereafter, the model is linearized at its trim conditions and the most important stability and

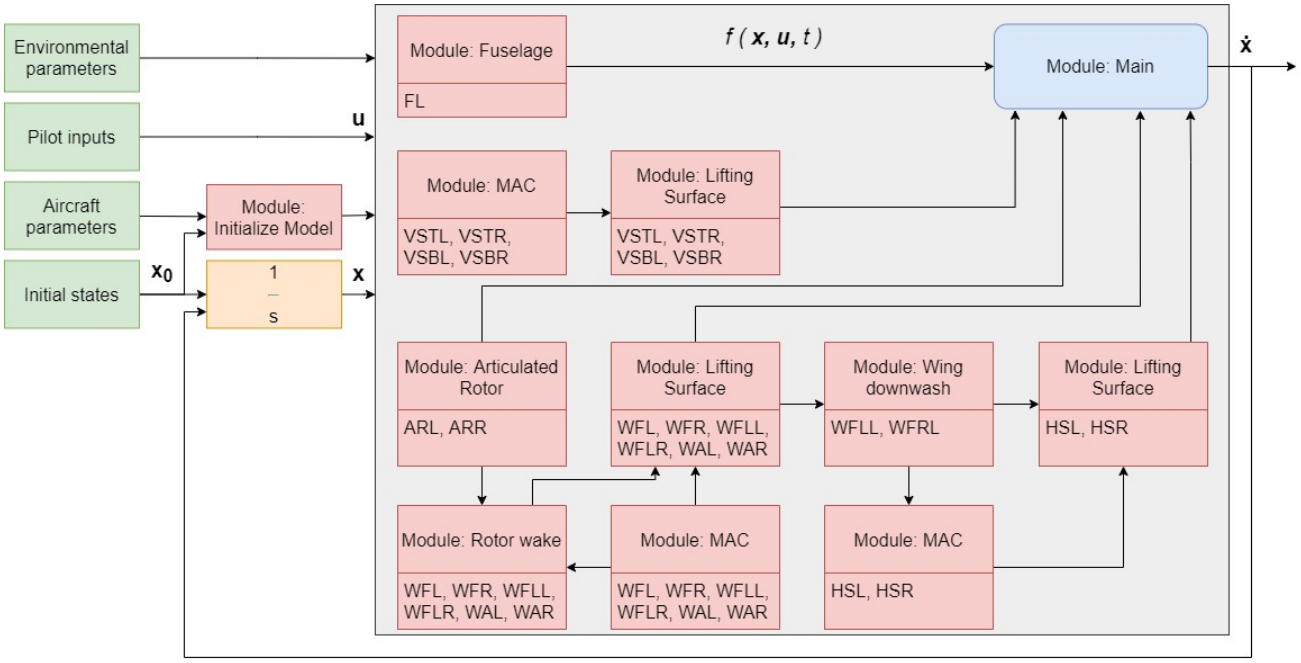

Fig. 1. Block diagram of the 6-DoF flight dynamics model

control derivatives are discussed. This is followed by a discussion on the dynamic modes of the aircraft, after which the conclusions of the research are drawn.

2. Nonlinear model

In this chapter the non-linear six-degrees-of-freedom tiltrotor flight dynamics model, from now on referred to as 6-DoF model, will be described. A detailed description of the model is written by Sokolowski [16]. For the analysis the XV-15 tiltrotor aircraft is used as the reference aircraft. A detailed description of this aircraft together with all its important parameters can be found in reference [4].

2.1 General Model Description

In general, the flight dynamics model describing the motion of an aircraft takes the following non-linear form:

$$\dot{\boldsymbol{x}} = f(\boldsymbol{x}, \boldsymbol{u}, t) \tag{1}$$

where $\boldsymbol{x}$ denotes the state vector, $\boldsymbol{u}$ denotes the input vector and t is the response time. The block diagram in Figure 1 depicts the structure of the 6-DoF model. The required inputs for the model are shown in the green blocks. Firstly, some environmental parameters are required. The aerodynamic forces are dependent on the air density ρ and gravitational forces are dependent on the gravitational acceleration g. Secondly, the inputs of the pilot are required. These inputs contain the collective stick deflection X_{COL}, the longitudinal and lateral cyclic stick deflections X_{LON} and X_{LAT} and the pedals deflection X_{PED}. The input vector $\boldsymbol{u}$ therefore looks as follows:

$$\boldsymbol{u} = [X_{COL}, X_{LON}, X_{LAT}, X_{PED}] \tag{2}$$

Thirdly, some general aircraft parameters are required as inputs. These parameters contain among others aircraft geometry parameters and derivatives describing the effect of the control surfaces deflections on the aerodynamic coefficients. Lastly, the initial states of the aircraft serve as input to the model. These states contain the translational velocities, rotational velocities and aircraft attitude. The state vector $\boldsymbol{x}$ has the following form:

$$\boldsymbol{x} = [u, v, w, p, q, r, \phi, \theta, \psi] \tag{3}$$

The model is build using a multi-body modeling approach to construct the aircraft configuration using its subcomponents (rotors, wing-parts, horizontal and vertical stabilizers, fuselage etc.). In total, the XV-15 has been subdivided into 15 different components which are shown in Figure 2. All components have been numbered and given an acronym. The forces and moments created by all com-

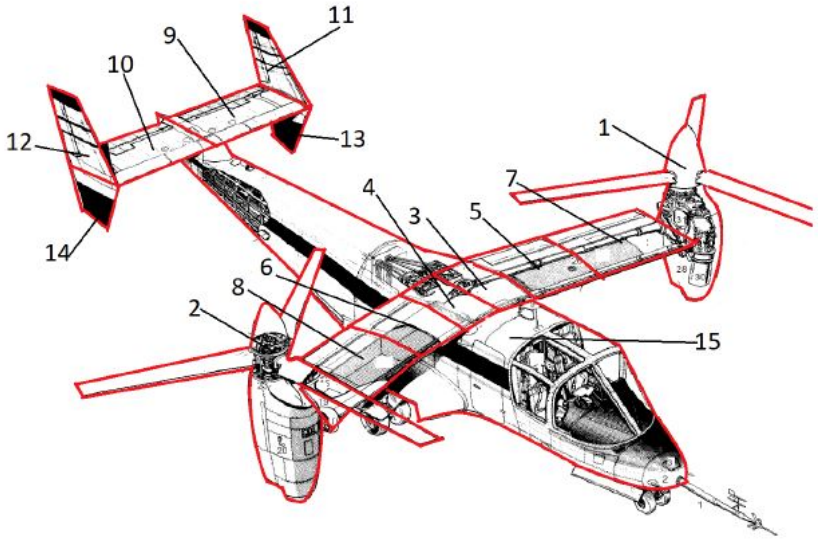

Nr.	Component	Acronym
1	Articulated Rotor Left	ARL
2	Articulated Rotor Right	ARR
3	Wing Free, Left	WFL
4	Wing Free, Right	WFR
5	Wing Flap, Left	WFLL
6	Wing Flap, Right	WFLR
7	Wing Aileron, Left	WAL
8	Wing Aileron, Right	WAR
9	Horizontal Stabilizer, Left	HSL
10	Horizontal Stabilizer, Right	HSR
11	Vertical Stabilizer, Top Left	VSTL
12	Vertical Stabilizer, Top Right	VSTR
13	Vertical Stabilizer, Bottom Left	VSBL
14	Vertical Stabilizer, Bottom Right	VSBR
15	Fuselage	FL

Fig. 2. Overview of the XV-15 and its subcomponents

ponents are computed using different modules. Some modules require the outcome of other modules. The order in which the modules should be used is also shown in Figure 1. In the bottom of each module the acronyms of the components for which the module applies are given. The different modules are discussed in the next section.

2.2 Modules

In this subsection the different modules of the model are discussed.

2.2.1 Module: Initialize Model

When modelling the flight dynamics of a tiltrotor aircraft, one should keep in mind that the rotation of the nacelles causes a significant shift in aircraft c.g. along the longitudinal axis. This also affects the moments of inertia (MOI) of the aircraft. Linear equations describing these MOI as a function of mast angle β_m have been integrated in the model. The mast angle is 0 degrees in H-mode and 90 degrees in A-mode. For example, I_x is computed using

$$I_x = I_{x|_{\beta_m=0}} - KI1\beta_m \tag{4}$$

where $KI1$ is a constant and $I_{x|_{\beta_m=0}}$ is the MOI in helicopter mode. Similarly, expressions describing the c.g. stationline (SL) and waterline (WL) have been integrated. If the nacelle angle is kept constant while running the model this module only needs to be ran once at the beginning of the simulation.

2.2.2 Module: Articulated Rotor

The rotor system is modelled by an articulated hub with a flapping hinge and spring, but no lead-lag hinge nor hinge offset. Furthermore, the lateral cyclic θ_{1c} is omitted so the swashplate inputs consist of the collective θ_0 and the longitudinal cyclic θ_{1s}. The rotor-induced velocity v_i is assumed to be constant across the rotor disc. The induced velocity ratio λ_i is found by computing the thrust coefficient C_T using both the beam element method en the Glauert method and comparing the results. Both C_T and λ_i are found when the following condition holds

$$C_{T,GLAU}(\lambda_i) - C_{T,BEM}(\lambda_i) = 0 \tag{5}$$

Using this value for λ_i all forces and moments induced by the rotors can be computed.

2.2.3 Module: MAC

This module is used to compute the position of the mean aerodynamic chord (MAC) of the lifting surfaces with respect to the aircraft centre of gravity. It is assumed that all forces created by the lifting surface act on this point. Firstly, the MAC along the surface is computed. This is a function of surface dimensions and sweep. Secondly, by taking into account the incidence angle and dihedral angle the position of the MAC along the surface is combined with the position of the lifting surface root with respect to the c.g..

2.2.4 Module: Rotor Wake

The goal of the 'Rotor Wake' module is to check whether there is interaction between the wake of the rotor system and the wings of the tiltrotor. If so, it is computed how this interaction affects the airflow around the wings. The interference of the rotor wake on the wing is calculated based on fixed wake theory and the projection relationship between the rotor disc and wing [17]. This more clearly visualized in Figure 3. If the MAC of the wing component is located within the projection of the wake on the wing component it is assumed that the whole component is affected by the wake. If this is the case, the downwash due to the rotor is computed using

$$w_r = v_i(1 + \frac{\eta_w}{\sqrt{1+\eta_w^2}}), \quad \eta_w = \frac{d_{r2m}}{R} \tag{6}$$

with d_{r2m} the normal distance from the rotor disc to the MAC.

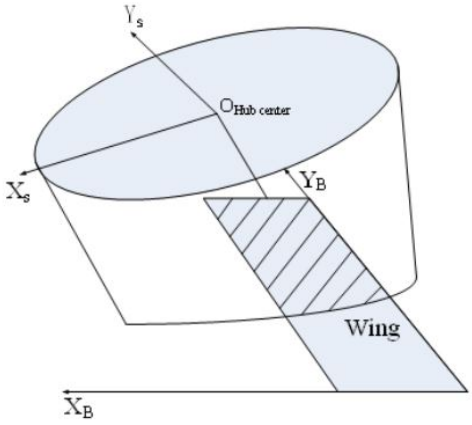

Fig. 3. Schematic view of the interference of the rotor wake with the wing [17]

2.2.5 Module: Wing Downwash

In this module the downwash on the horizontal stabilizers caused by the wake of the wing is computed. This module is only used for the wing parts containing the flaps, so its concerns components WFLR and WFLL. The downwash angle is obtained from the GTRS model data[4], and is implemented as a function of wing angle of attack, flap deflection and nacelle angle. The downwash angle that is found by interpolating the GTRS data can then subtracted from the effective horizontal stabilizer angle of attack.

2.2.6 Module: Lifting Surface

The forces and moments created by the lifting surfaces are computed in this module. These forces and moments are a function of the dynamic pressure, surface area and aerodynamic coefficients. The lift and drag coefficients are computed using a combination of linear aerodynamics and the flat plate area theory. According to the linear aerodynamics theory, the coefficients can be computed using

$$C_{L,l} = C_{L_\alpha}(\alpha - \alpha_{0L}) + \Delta C_L \tag{7}$$

$$C_{D,l} = C_{D0} + \frac{C_{L,f}^2}{\pi ARe} + \Delta C_D \tag{8}$$

According to the flat plate area theory, the coefficients are computed using

$$C_{L,f} = 2\sin(\alpha)\cos(\alpha)C_{L,max} + \Delta C_L \tag{9}$$

$$C_{D,f} = \sin(\alpha - \alpha_{0L})^2 C_{D,max} + \Delta C_D \tag{10}$$

The former method gives inaccurate results at low airspeeds (H-mode) due to the large angle of attack of the wings as a result of the rotor wake downwash. The latter method is less accurate at high airspeeds (A-mode). Therefore, C_L and C_D are computed using a combination of both methods as a function of nacelle angle

$$n = \eta/90 \tag{11}$$

$$C_L = nC_{L,l} + (1-n)C_{L,f} \tag{12}$$

$$C_D = nC_{D,l} + (1-n)C_{D,f} \tag{13}$$

The ΔC_L and ΔC_D are computed based on the deflections of the secondary control surfaces.

2.2.7 Module: Fuselage

In this module the aerodynamic forces created by the fuselage are computed. The longitudinal aerodynamic coefficients are computed using GTRS model data [4]. The GTRS model data provides tables for the lift, drag and pitching moment coefficient of the fuselage of the XV-15, and these are implemented as a function of angle of attack. The lateral forces and moments created by the fuselage have not been implemented.

2.2.8 Module: Main

All the forces and moments created by the components serve as input to the main module. In this module all force vectors converted to the body frame of reference are added up to compute the resultant force vector acting on the aircraft. The same is done for the resultant moment vector, however the moments due to the forces also have to be

considered. These resultant forces and moments are then inserted into the Euler equations of motion together with the aircraft states to compute the dynamics acting on the vehicle.

2.3 Trim Results

This section discusses the trim results of the 6-DoF model. An aircraft is said to be in a trim state when the resultant of the applied forces and moments equals zero [14]. The aircraft has been trimmed in steady, horizontal, symmetrical flight conditions. The trim results of the 6-DoF model are validated against the GTRS model curves [5]. Both models use the XV-15 as reference aircraft so their trim curves should be very similar. The trim results of the body pitch angle θ_b, collective stick deflection X_{COL} and longitudinal cyclic stick deflection X_{LON} are shown as a function of airspeed in Figure 4. Various nacelle angle configurations are compared.

The body pitch angle is approximately zero in hover and decreases with airspeed. This is because the rotors need to be tilted forward to provide more horizontal thrust to reach higher speeds. When the nacelles are tilted more forward higher speeds can be reached at higher values of θ_b. The curves of the two models in H-mode look very similar. In conversion mode three different nacelle angle configurations are compared. For all three curves the 6-DoF has a relatively higher trim body pitch angle. In airplane mode the curves look again very alike. Both models find a maximum trim speed in A-mode of 280 kts.

The collective stick can have a deflection between 0-10 inch. The curves are shown as a percentage of the maximum deflection instead of as a function of the deflection in inch. This has been done because the collective rotor governor of the XV-15 has not been implemented in the 6-DoF model. Instead, the rotor governor collective control is superimposed on the collective stick control. This allows the collective stick to have deflections larger than 10 inch in order to reach the high collective pitch angles which are required to reach trim at speeds up to 280 kts. Because the maximum deflection of the 6-DoF model is thus significantly higher than the maximum deflection of the GTRS model, which does include the rotor governor, the curves are shown as a percentage of their deflection bounds. These differences in collective pitch control method however still cause quite some discrepancies between the two models. The percentage stick deflection of the GTRS model is significantly higher in H-mode and C-mode. Nevertheless, The shapes of the curves look quite similar which gives some validation for the results. In A-mode the curves look very similar and there is quite some overlap.

The longitudinal cyclic can have a deflection between -4.8 and 4.8 inch. These curves are also shown as a percentage of the total deflection. This means that a 50% deflection corresponds to a 0 inch deflection. The shapes of the curves look quite similar and there is some overlap. Only the 90 degrees nacelle angle curves have different shapes. The GTRS curve increases faster with airspeeds while the 6-DoF curve appears to stabilize at a value. Overall the trim curves show quite some similarities so the model can be assumed valid.

3. Linear Model

The linear model is analyzed in this section. The linearization is briefly described followed by a description of the most important stability and control derivatives.

3.1 Linearization

Once trimmed, the 6-DoF model can be linearized at various airspeeds and nacelle angles coinciding with the conditions at which trimming was possible. A numerical linearization algorithm is applied, estimating the the derivatives using a finite central difference scheme [18]. The estimation of the derivatives is iterated until the truncation and round-off errors are minimized. The leads to the following linear form of the equation of motion

$$\dot{\boldsymbol{x}} = \boldsymbol{A}\boldsymbol{x} + \boldsymbol{B}\boldsymbol{u} \tag{14}$$

$$\boldsymbol{x} = [u, v, w, p, q, r, \phi, \theta, \psi] \tag{15}$$

$$\boldsymbol{u} = [\theta_0, \theta_{0d}, \theta_{1s}, \theta_{1sd}, \delta_e, \delta_a, \delta_r] \tag{16}$$

Instead of the pilot control, $\boldsymbol{u}$ now contains the the symmetrical and differential collective pitch (θ_0, θ_{0d}), symmetrical and differential longitudinal cyclic pitch (θ_{1s}, θ_{1sd}), and elevator (δ_e), aileron (δ_a) and rudder (δ_r) deflections. For the control analysis of the 6-DoF model it is more interesting to look at these controls rather than at the pilot inputs. The aircraft response due to pilot inputs can quite easily be altered by changing the gearing of the control system. This has already been done for the collective pitch angle to be able to reach 280 kts in airplane mode. The aircraft responses to pilot inputs are therefore also harder to validate. For this reason, the input vector of the linear 6-DoF model has been altered.

3.2 Stability Derivatives

In total there are 36 stability derivatives in the linearized 6-DoF equations of motion set. A number of the most important ones are discussed below, and the 6-DoF model derivatives are compared and validated with the 3-DoF

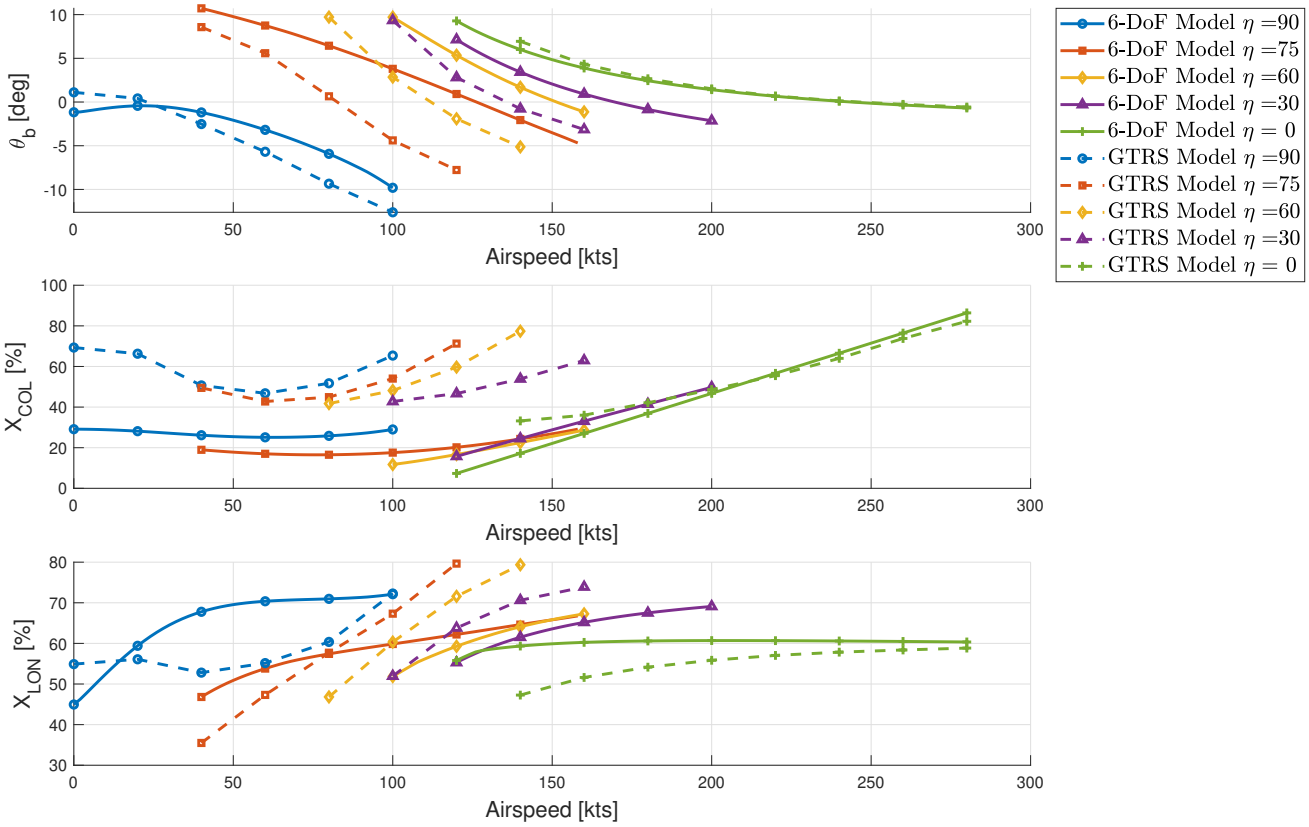

Fig. 4. Trim body pitch angle (θ_b), collective stick deflection (X_{COL}) and longitudinal cyclic stick deflection (X_{LON}) as a function of airspeed.

preliminary tiltrotor model [19], the FLIGHTLAB model (FXV-15) [11] and the GTRS model derivatives [5]. All derivatives have been converted to the units shown in Table 1. The forces and moment derivatives have been normalized by dividing them with the aircraft mass and MOI respectively. Furthermore, they are defined in the body orthogonal axes system [11].

Tab. 1. The S.I. units of the stability derivatives

Force/translational velocity	e.g. X_u	1/s
Force/angular velocity	e.g. X_q	m/s/rad
Moment/translational velocity	e.g. M_u	rad/s/m
Moment/angular velocity	e.g. M_q	1/s

3.2.1 Longitudinal Stability Derivatives

The drag damping derivative X_u usually shows a linear relationship with speed and should be negative at any condition to have stability [11]. Compared to a conventional helicopter X_u should be larger for tiltrotors because of the additional rotor and wings which create additional drag.

Figure 5 shows that the 6-DoF and 3-DoF model derivatives are approximately constant with speed in H-mode while for the other two models a decrease is observable. The rotor system which dominates the derivative at this mode has a roughly constant contribution with airspeed for the 3-DoF and 6-DoF model. From subfigure (d) it becomes clear that when the thrust vector is tilted towards the horizontal axis the contribution of the rotor system increases and X_u increases in magnitude.

The heave damping derivative Z_w should also be negative at all times to ensure stability. At low airspeeds, the heave-damping derivative is generally larger for rotary aircraft than for fixed-wing aircraft [11]. At low airspeeds the derivative is mainly determined by the rotors, but with increasing airspeed the wings and horizontal stabilizers start creating lift and also affect the derivative. Generally the derivative decreases with airspeed as shown in Figure 6(a-c). The rotor contribution decreases with decreasing nacelle angle but simultaneously the wing contribution increases due to the increase in angle of attack. This explains why Z_w remains roughly constant with nacelle angle

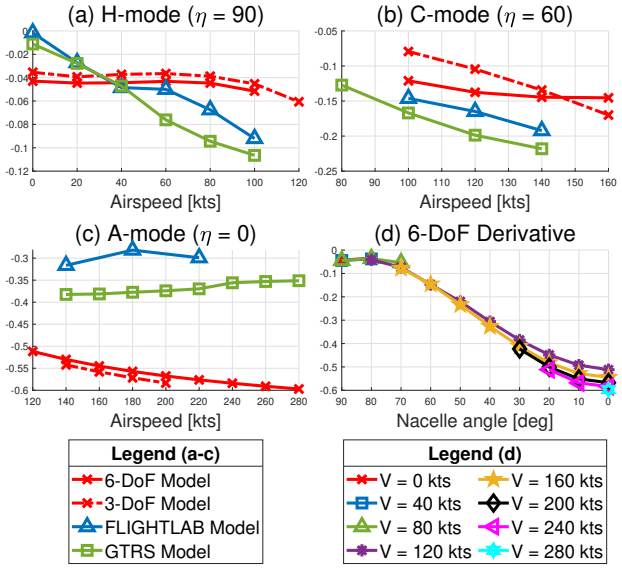

Fig. 5. Stability derivative X_u

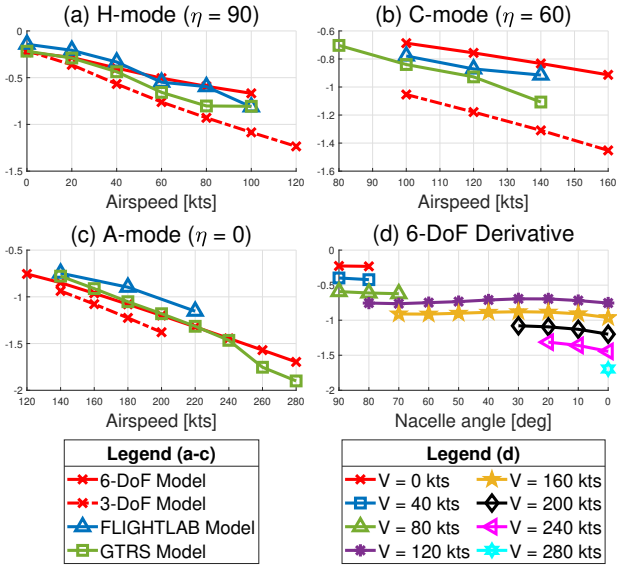

Fig. 6. Stability derivative Z_w

as shown in subfigure (d).

The speed stability derivative M_u has a mayor effect on the longitudinal stability and handling qualities of an aircraft [14]. For a conventional airplane M_u is practically zero at subsonic speeds because all aerodynamic moments cancel eachother out. For a conventional helicopter however M_u is important along the entire flight envelope [11]. Clear differences can be observed between the models in H-mode in Figure 7(a). The negative contribution of the horizontal stabilizers causes the 3-DoF and 6-DoF derivative to become negative after a certain airspeed which does not happen for the FXV-15 and the GTRS model. For the same reason, the 3-DoF model derivative in C-mode is still significantly lower than for the other models. The 6-DoF model looks more comparable to the GTRS and FLIGHTLAB model results and remains positive. In A-mode all four models have a positive M_u. The rotors have a positive contribution to M_u which increases with decreasing nacelle angle because the thrust is increasingly sensitive to perturbation in u. This is visible in subfigure (d).

The incidence static derivative, also called the longitudinal static stability derivative M_w is shown in Figure 8. Together with M_u this derivative largely affects the longitudinal stability of an aircraft [11]. A negative M_w is desired for static stability. The fuselage, wings and rotor system are generally destabilizing while the horizontal stabilizers are stabilizing. The 3-DoF model assumes that the aerodynamic centre and the centre of gravity of the fuselage coincide which means that the fuselage is not stabilizing nor destabilizing which explains the steeper slope. The GTRS model has an outlier in the data at 40 kts H-mode [5]. In A-mode the 6-DoF model derivative looks similar to the GTRS model derivative, while the 3-DoF and FLIGHTLAB model derivatives are a factor 2-3 larger. The trim angle of attack increases with nacelle angle, meaning that the horizontal stabilizers create more lift and contribute more to a stable M_w. This results in the slightly negative slope at high nacelle angles in subfigure (d). When the nacelle almost reach A-mode, the contribution of the rotors change from negative to positive. This causes the increase in slope at low values of η.

The pitch damping derivative M_q plays a very important role in the longitudinal short-term handling characteristics [14]. A positive perturbation in q should always results in a restoring pitching down moment, meaning that M_q should be negative. The derivative is shown in Figure 9. In hover the pitch damping derivative is almost entirely determined by the rotor system, which is stabilizing. When the airspeed increases the horizontal stabilizers also create a stabilizing contribution to M_q, leading to a linear decrease in value. The FXV-15 derivative decreases in magnitude when the proprotors are tilted towards airplane mode, because the destabilizing effects of the in-plane rotor forces increase [11]. From subfigure (d) it can be concluded that the 6-DoF M_q increases in magnitude with nacelle angle for the 6-DoF model. The destabilizing effect of the rotor indeed increases when rotating towards airplane mode, but so does the trim angle of attack. This means that the horizontal stabilizers create more lift and as a result the stabilizing contribution to M_q increases as well. This stabilizing

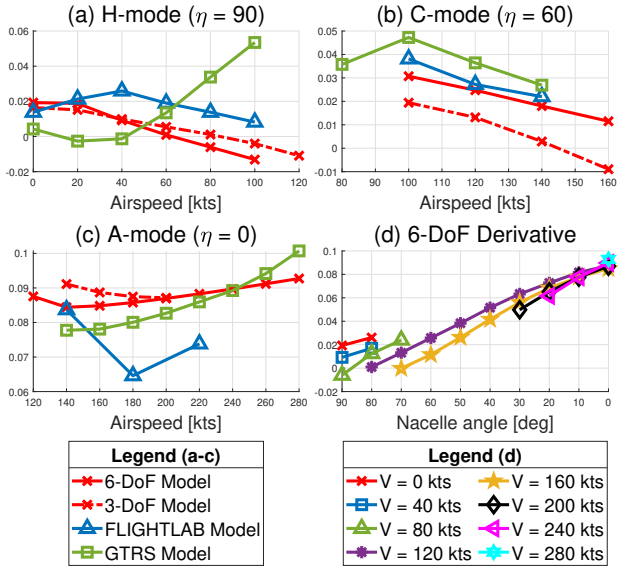

Fig. 7. Stability derivative M_u

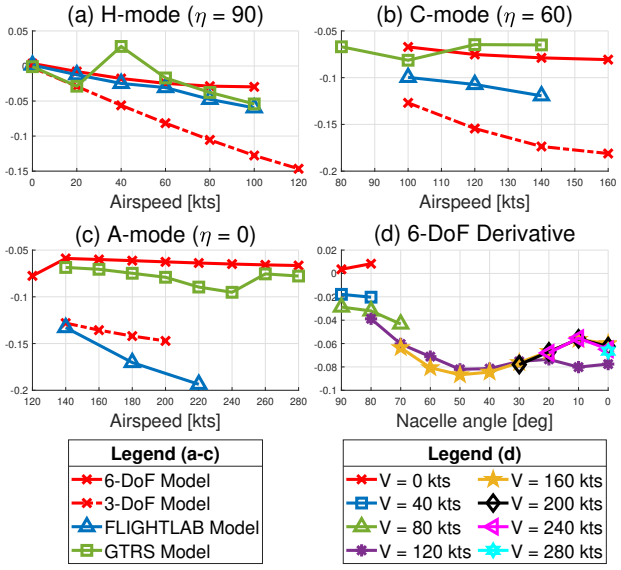

Fig. 8. Stability derivative M_w

effect by the horizontal stabilizers is bigger than the destabilizing effect of the rotor causing the negative slope. One possible explanation for this difference in trend compared to the FXV-15 could be the different rotor hub model. The FXV-15 is modelled with a gimballed rotor hub which has usually larger in-plane forces than an articulated rotor hub [11].

3.2.2 Lateral/directional Stability Derivatives

One of the two most important sideslip derivatives is L_v, called the dihedral stability derivative. It is desirable for stability that L_v is negative. The rotor system is the largest contributor to this derivative, while the vertical stabilizers also have a significant contribution. Both contributions are stabilizing. The rotor contribution remains fairly constant with airspeed, while the contribution of the vertical stabilizers increases. For the GTRS and FLIGHTLAB model curves a clear linear decrease with airspeed is found. For these models the contribution of the vertical stabilizers might be larger. In C-mode and A-mode the vertical stabilizers are dominant, causing a decrease with airspeed. The contribution of the vertical stabilizers increases with nacelle angle, while the rotor contribution decreases with a similar magnitude. This explains why the derivative is roughly constant with nacelle angle as seen in subfigure (d).

The other important sideslip derivative is N_v, the weathercock stability derivative. N_v is critically important for both static and dynamic stability [11]. In contrary to L_v, N_v is preferred to be positive. From Figure 11 it can be concluded that N_v increases linearly with speed. The results of the 6-DoF model in helicopter mode show that the weathercock stability derivative is dependent on the rotor system and the vertical stabilizers which are both stabilizing. The yawing moment created by the fuselage has not been modelled in the 6-DoF model so its contribution to N_v is missing. The positive increasing contribution of the vertical stabilizers with airspeed is dominant for N_v. While the contribution of the rotors becomes increasingly negative when the nacelles are rotated towards airplane mode, the positive moment created by the vertical stabilizers increases as well. The latter increases slightly more which causes an increase of N_v with decreasing nacelle angle.

The roll-damping derivative L_p plays an important roll in the short-term handling qualities about the x-axis. A positive perturbation in p should result in a restoring negative rolling moment L, meaning that L_p should be negative. The roll-damping derivatives have been plotted in Figure 12. Although this derivative is insensitive to speed for a conventional helicopter, the speed highly affects the tiltrotor roll damping derivative in all flight modes [20]. This is because of the lateral offset of the two rotors and the contribution of wings. The stabilizing contribution of the wings increases with airspeed. The rotors are stabilizing as well. With decreasing nacelle angle L_p decreases in magnitude because the rotors become less aligned with the airflow resulting from a rolling motion.

The yaw-damping derivative N_r should also be negative for stability. For a conventional helicopter the tail rotor is the main contributor to the yaw damping, especially at low ve-

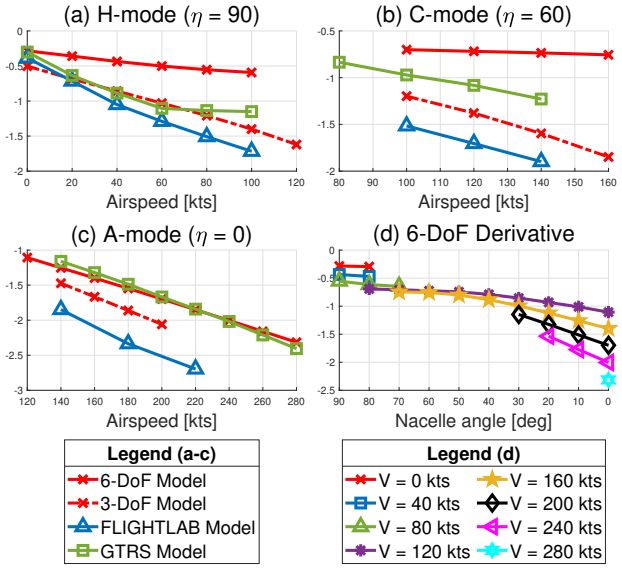

Fig. 9. Stability derivative M_q

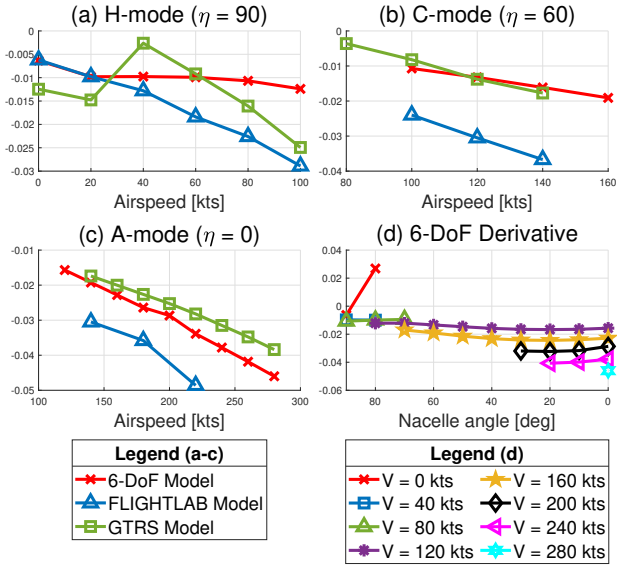

Fig. 10. Stability derivative L_v

locities. Since the tiltrotor has no tail rotor the magnitude of the yaw damping is relatively small at low airspeeds [14]. The stabilizing contribution of the vertical stabilizers increases when the airspeed increases resulting in a linear decrease of N_r with speed. when the nacelles are tilted forward the stabilizing effect of the proprotors to the yaw damping increases as the thrust force becomes aligned with the airflow resulting from a yawing motion. This increase in yaw damping with decreasing nacelle angle is clearly visible in subfigure (d).

3.3 Control Derivatives

The linearized set of equations consists of 42 different control derivatives. In this section the most important ones will be discussed. The 6-DoF derivatives are compared with the FLIGHTLAB derivatives. All derivatives have been converted to the units shown in Table 2. The longitudinal and lateral/directional control derivatives are discussed respectively.

Tab. 2. The S.I. units of the control derivatives

Force/control angle	e.g. X_{θ_0}	m/s^2/rad
Moment/control angle	e.g. M_{θ_0}	1/s

3.3.1 Longitudinal Control Derivatives

In Figure 14 the longitudinal control derivatives are shown. The top two rows show the derivatives with respect to the collective pitch θ_0. By increasing θ_0 the total average blade pitch increases. This means that the blades create more lift and thus the total rotor thrust force is increased. In helicopter mode the thrust vector points in negative Z-direction. The thrust force increases when θ_0 increases, so Z_{θ_0} is negative in H-mode. When the nacelles are in A-mode, the thrust is more aligned with the X-axis. This explains the smaller value of Z_{θ_0} and bigger value of X_{θ_0} in this configuration. The derivatives of the two models show a very similar trend. On the right figures the same derivatives of the 6-DoF model are shown as a function of nacelle angle with the airspeed V kept constant. The decrease of Z_{θ_0} and increase of X_{θ_0} is also clearly visible in these figures.

Symmetric longitudinal cyclic control is used in helicopter mode to move the aircraft horizontally. Simultaneously increasing the longitudinal cyclic angle on both rotors causes the tip-path plane to tilt forward resulting in an increase in forward speed [21]. This means that the resultant force along the X-axis increases which explains why $X_{\theta_{1s}}$ is positive. The derivative appears to be almost independent of airspeed. At a nacelle incidence of 60 degrees we suddenly see a negative value for this derivative. An increase in θ_{1s} still causes the thrust vector to tilt forward but simultaneously the total thrust force drops which explains the negative derivative. In airplane mode the derivatives with respect to θ_{1s} become meaningless because the longitudinal cyclic angle is fixed in this configuration [4]. By tilting the tip-path plane forward in helicopter mode the Z-component of the the rotor which is negative decreases in magnitude. This causes the resultant Z-force to increases

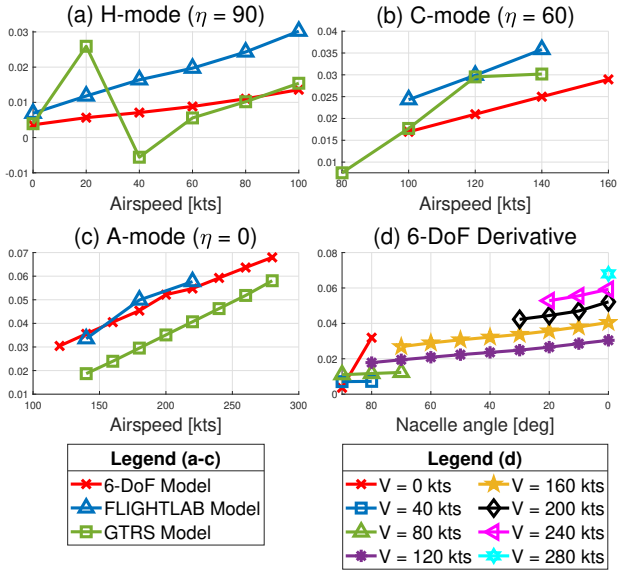

Fig. 11. Stability derivative N_v

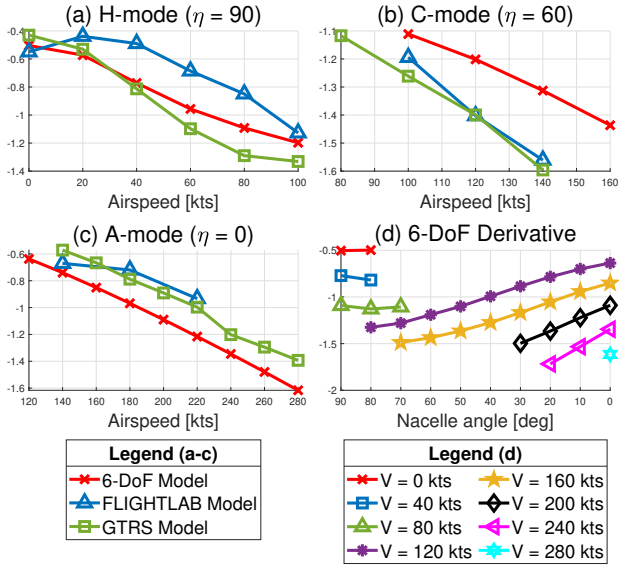

Fig. 12. Stability derivative L_p

which means that $Z_{\theta_{1s}}$ is positive. A clear increase with airspeed is shown for $Z_{\theta_{1s}}$, while the derivative slightly decreases with nacelle angle.

In airplane mode the elevators are used to control the pitching of the aircraft. Downward deflection of the elevators is defined as positive. The following relationship for Z_{δ_e} can be derived from the 6-DoF model:

$$\frac{dZ}{d\delta_e} = -\frac{1}{2}\rho V_{hs}^2 S_{hs} \frac{dC_{L,hs}}{d\delta_e} \cos\alpha_{hs} \tag{17}$$

The derivative grows proportionally with V^2. The same goes for the M_{δ_e} derivative which heavily depends on $\frac{dZ}{d\delta_e}$. This is clearly visible in the bottom two graphs. The nacelle angle has no influence on the elevator derivatives at all.

3.3.2 Lateral/directional Control Derivatives

The most important lateral/directional control derivatives are shown in Figure 15. The top two rows show the derivatives with respect to the differential collective pitch θ_{0d}. Differential collective pitch is used in H-mode to control the rolling motion. An increase and decrease of the collective pitch on the right and left rotor respectively is defined as a positive differential collective control input. If the right rotor collective is higher than the left rotor collective the right rotor creates more lift. This leads to a negative rolling moment L which is why $L_{\theta_{0d}}$ is negative. When the nacelles rotate towards A-mode the derivative significantly decreases in magnitude. The FLIGHTLAB derivative is approximately three times larger than the 6-DoF model derivative. This difference is also most likely due to the higher in-plane forces of the gimballed rotor hub which also create a significant rolling moment. The two plots on the second row show the yawing moment due to differential collective derivative $N_{\theta_{0d}}$. This derivative has a similar order of magnitude as $L_{\theta_{0d}}$ but is small in H-mode and large in A-mode. This makes sense because in airplane mode the thrust vector is more aligned with the yawing airflow.

Differential longitudinal cyclic θ_{1sd} is used at low airspeeds to control yaw. An increase and decrease of the longitudinal cyclic on the right and left rotor respectively is defined as a positive differential longitudinal cyclic input. The $L_{\theta_{1sd}}$ curve shows some similarities between the models. In helicopter and conversion mode the derivative is positive and increases with airspeed. When the right rotor increases its longitudinal cyclic its thrust vector is tilted forward while the left rotor thrust vector is tilted aft. An increase in longitudinal cyclic however decreases the total force created by the rotor. Therefore the left rotor creates a larger thrust force than the right rotor which results in a positive rolling moment. Since the main purpose of differential longitudinal cyclic is to control the yawing motion of the aircraft $N_{\theta_{1sd}}$ is its primary derivative. A positive θ_{1sd} input results in a negative N in H-mode. When the nacelles are tilted forward the thrust vectors are also tilted forward resulting in a positive X-component. Since the thrust magnitude of a rotor decreases when θ_{1s} increases the left rotor produces more forward thrust force resulting

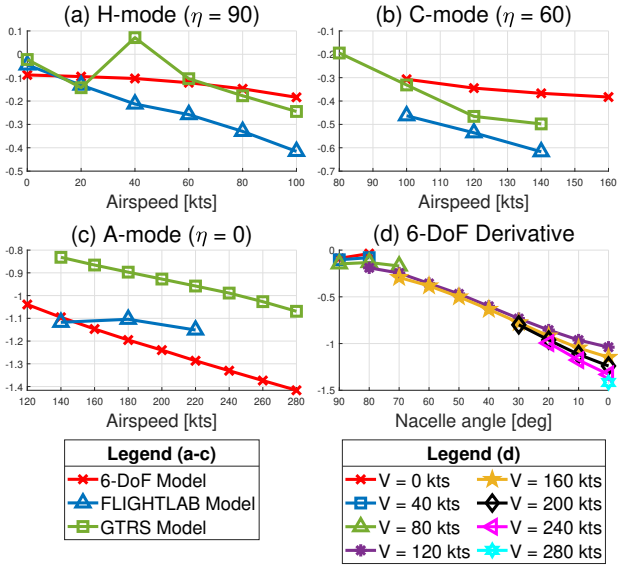

Fig. 13. Stability derivative N_r

in a negative $N_{\theta_{1sd}}$. The derivatives in A-mode are not of interest since the θ_{1s} is fixed in this mode.

In A-mode the ailerons are used to control roll. A positive aileron deflection means that the right aileron is deflected downward and the left aileron upward. The result of this deflection is that the right wing will produce more lift than the left wing, resulting in a negative rolling moment L. The derivative can analytically (before normalization) be defined as

$$L_{\delta_a} = \frac{\delta L}{\delta_a} = \frac{1}{2}\rho V_w^2 S_w \frac{\delta C_{L,w}}{\delta_a} b_w \tag{18}$$

This equation shows that L_{δ_a} decreases proportionally with V^2 which is clearly visible in the figure. The rudders on the vertical stabilizers are used to control yaw in this mode. A positive rudder deflection creates a lateral force in positive Y-direction. This creates are negative yawing moment so therefore N_{δ_r} is negative. This derivative can very similarly as L_{δ_a} be approximated (before normalization) using

$$N_{\delta_r} = \frac{\delta N}{\delta_r} = \frac{1}{2}\rho V_{vs}^2 S_{vs} \frac{\delta C_{L,vs}}{\delta_r} d_{x,vs} \tag{19}$$

The FLIGHTLAB curves are a bit steeper than the 6-DoF model curves which could indicate that a different $\frac{\delta C_L}{\delta_r}$ and $\frac{\delta C_L}{\delta_a}$ are used. Furthermore, the drag of the ailerons and rudders have not been modelled which could also a difference in the results. From the graphs on the right side it can be concluded that the nacelle angle does not affect the derivatives with respect to the control surfaces.

4. Dynamic Modes

In this section the eigenvalues of the linear 6-DoF model will be analysed. The eigenvalues can be determined using

$$\boldsymbol{A} - \lambda \boldsymbol{I} = \boldsymbol{0} \tag{20}$$

The eigenvalues of the system describe the behavior of the tiltrotor by means of five different dynamic modes. The eigenvalues describing these modes have been plotted as a function of airspeed in Figure 16, Figure 17 and Figure 18. These figures illustrate the dynamic modes in H-mode ($\eta = 90$deg), C-mode ($\eta = 60$deg) and A-mode ($\eta = 0$deg) respectively. For validation purposes the FLIGHTLAB eigenvalues have been included in the figures as well. Furthermore, the variations of the eigenvalues of the 6-DoF model modes with nacelle angle are shown in Figure 19. For this analysis the airspeed is kept constant at 120 kts. The five different modes are discussed below.

4.1 Short period

The short period is a relatively highly damped longitudinal oscillatory dynamic mode which consists of a coupled pitching and heaving motion. At low airspeeds in helicopter mode the short period is uncoupled into a pitch and a heave subsidence. Their eigenvalues are located on the real axis. The two subsidences can usually be approximated using:

$$\lambda_h = Z_w \tag{21}$$
$$\lambda_p = M_q \tag{22}$$

This means that the subsidence eigenvalues can be assumed approximately equal to their damping derivatives. Derivatives Z_w and M_q equal -0.226 and -0.284 respectively in hover. This shows that the heave damping derivative very accurately represents the heave subsidence (-0.227). The pitch subsidence (-0.703) has a lot more damping than the pitch damping derivative would suggest. The relatively low value of M_q results in translational velocities building up during pitching motion, resulting in a strong coupling between pitch and surge [11]. When the airspeed increases the subsidences couple together and form the short period. The short period can accurately be predicted using the following characteristic equation [20]:

$$\lambda_{sp}^2 - (Z_w + M_q)\lambda_{sp} + Z_w M_q - M_w u_0 = 0 \tag{23}$$

This shows that the mode is dependent on derivatives Z_w,

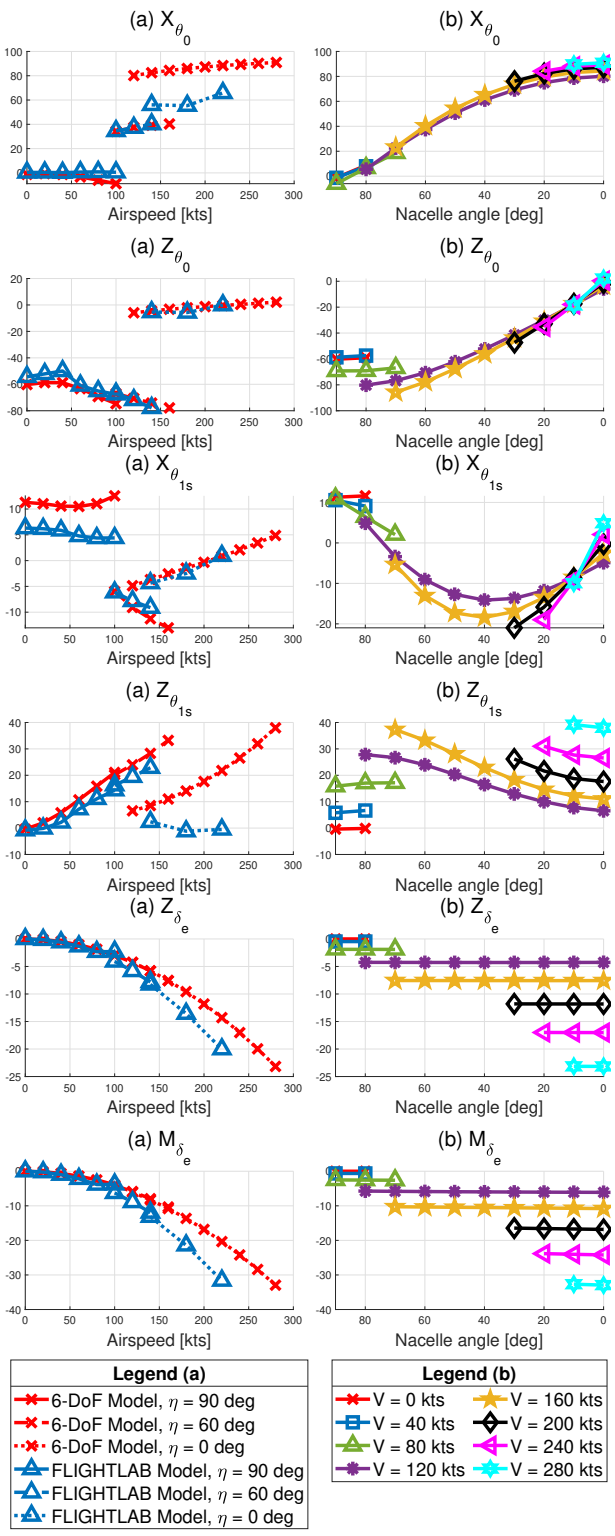

Fig. 14. Longitudinal Control Derivatives

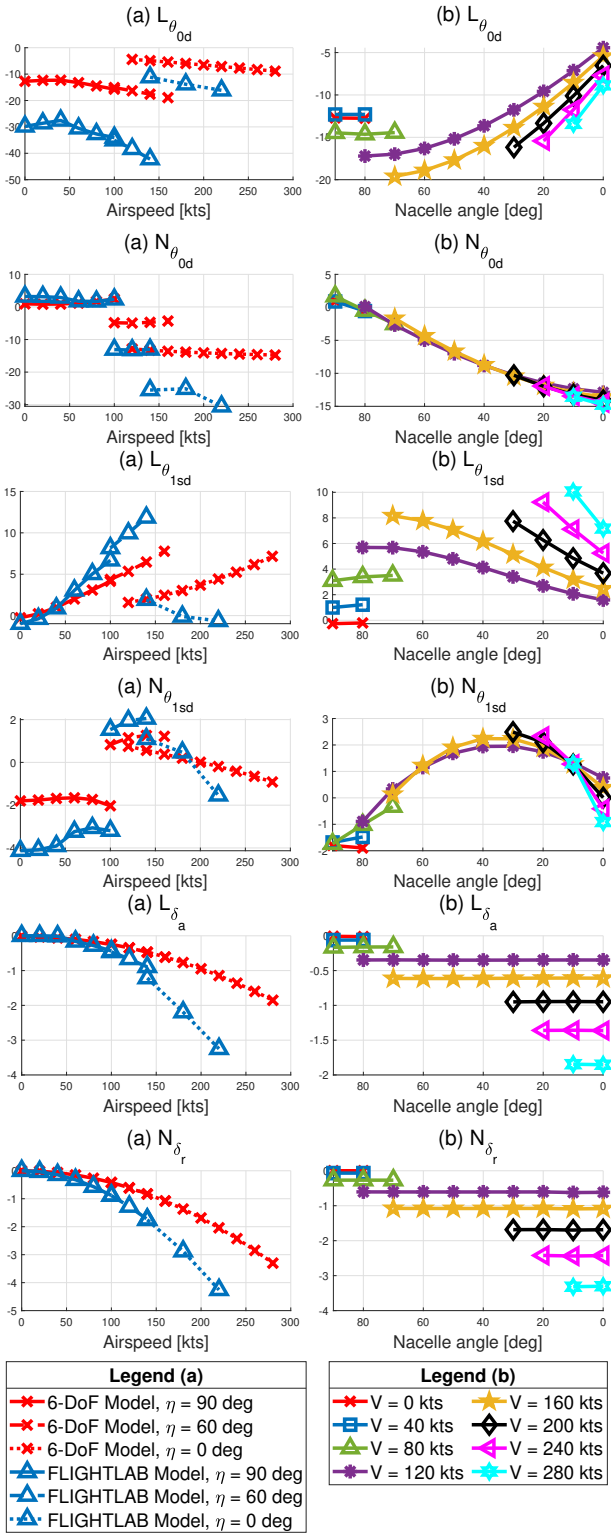

Fig. 15. Lateral/directional Control Derivatives

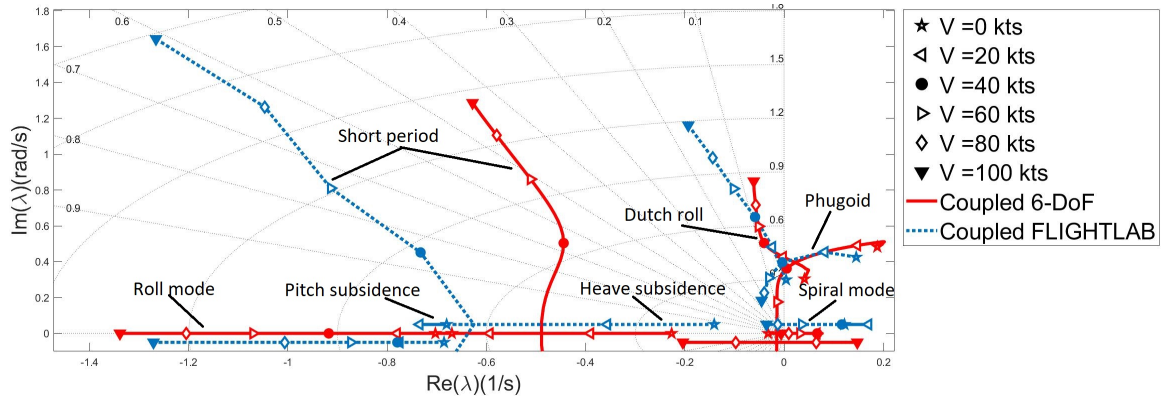

(a) Full picture

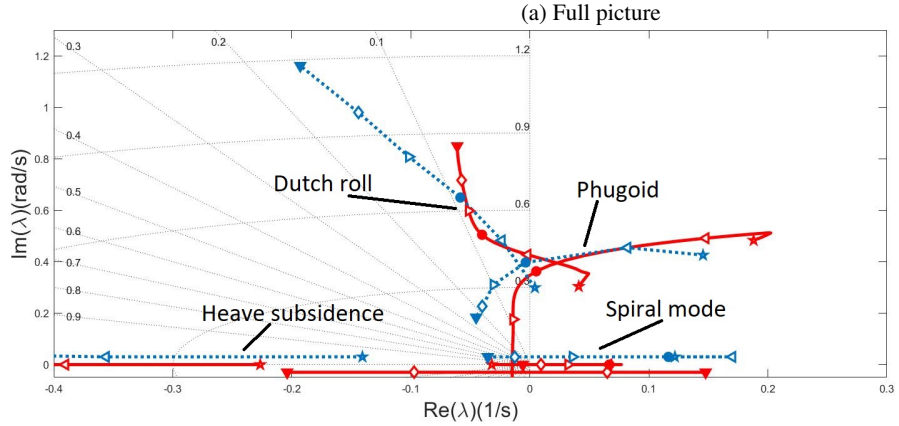

(b) Low frequency modes

Fig. 16. XV-15 6-DoF model coupled eigenmodes in helicopter mode (η = 90deg) compared with the FLIGHTLAB eigenmodes

M_q and M_w. Furthermore, the frequency increases with airspeed since the horizontal trim velocity component u_0 is included in the term. This is also clearly visible in the eigenmodes figures. The variation of the damping with airspeed is somewhat different for the flight modes. In helicopter mode (Figure 16) and conversion mode (Figure 17) the damping decreases slightly with airspeed, while in airplane mode (Figure 18) the damping increases with airspeed

The short period of the FLIGHTLAB shows in general a similar trend. In H-mode the frequency increases with airspeed while the damping decreases. However, the FLIGHTLAB mode presents a stronger increase in frequency and is more heavily damped. The damping and frequency of the short period are both heavily dependent on M_q. From Figure 9 it became clear that the pitch damping derivative is significantly higher for the FLIGHTLAB model than for the 6-DoF model. This was mainly attributed to the destabilizing rotor contribution for the latter model which is stabilizing for the former. This is also true in C-mode. In A-mode the 6-DoF model short period is more heavily damped than the FLIGHTLAB model mode while the latter has a higher frequency. Both observations can be explained by looking at differences in static stability derivative M_w in airplane mode (Figure 8(c)). The 6-DoF model derivative is a factor 2-3 smaller. A smaller value of M_w increases the damping of the short period while it decreases the frequency.

The variation of the short period eigenvalues with nacelle angle is shown in Figure 19a. The figure shows that at high nacelle angles the short period frequency increases when the rotors are tilting towards airplane mode. This is caused by the decrease of the incidence static stability derivative M_w with nacelle angle up to 40 degrees after which it remains somewhat constant. This is also the point at which the frequency in Figure 19a stops increasing rapidly. The damping ratio of the short period is less affected by the rotations of the rotors. Along the η range the damping is constantly between 0.3 and 0.4 at an airspeed of 120 kts.

4.2 Phugoid

The phugoid is a longitudinal oscillatory mode with a variation of airspeed, pitch angle and altitude over time. The mode has a large period because of which the angle of attack remains almost constant over time. There is a very slow interchange between kinetic and potential energy during the mode, while the aircraft attempts to restore the steady horizontal equilibrium state. From Figure 16b it can be concluded that the phugoid is unstable in hover. When the airspeed increases the phugoid becomes stable and the damping increases. For the 6-DoF model the damping increases so fast that at approximately 70 kts the phugoid becomes non-oscillatory. This non-oscillatory behavior of the phugoid is not something that is found in literature. To analyse what causes this behavior, a closer look has to be taken at the derivatives affecting the phugoid. The phugoid of the tiltrotor is best approximated using [11]

$$\lambda_{ph}^2 - (X_u - X_w \frac{M_u}{M_w})\lambda_{ph} - \frac{g}{u_0}(Z_u - Z_w \frac{M_u}{M_w}) = 0 \qquad (24)$$

The eigenvalues of the phugoid are located on the real axis when the damping is equal to 1. According to this equation the damping is mainly dependent on X_u, X_w, M_u and M_w. Comparing the 6-DoF model M_u derivative in H-mode with other models in Figure 7 leads to the observation that the 6-DoF model and 3-DoF model derivatives are negative at high airspeeds while the other models' derivatives are positive. This means that the second term in Equation 24 of the damping increases the damping instead of decreasing it. This results in damping ratios reaching 1 and thus a non-oscillatory phugoid. In C-mode and A-mode the M_u derivative of the 6-DoF model is positive and thus the phugoid is oscillatory.

Because the FLIGHTLAB model has a positive M_u in helicopter mode its phugoid is also oscillatory at higher airspeed. Both models' curves in helicopter mode show quite some overlap up until 60 kts. In A-mode and C-mode there is less overlap, mainly due to the quite significant differences in X_u and M_u. However, both models have an unstable phugoid in hover and the tendency of the eigenvalues with airspeed is quite similar. The damping increases with airspeed while the frequency remains somewhat constant.

The variation of the phugoid eigenvalues with nacelle angle is shown in Figure 19b. The airspeed is kept at 120 kts while the nacelles are tilted from 80 to 0 degrees. The fact that the phugoid is oscillatory at at nacelle angles between 80 and 0 degrees shows that the mode is only non-oscillatory at nacelle angles very close to hover. As the nacelle are rotating away from helicopter mode the M_u derivative increases as shown in Figure 7(d). At the same time the drag damping X_u becomes larger and X_w increases. The combination of these three results in an increase in damping with decreasing nacelle angle. At the same time the frequency of the phugoid increases slightly.

4.3 Roll mode

The rolling mode is usually a pure roll subsidence, which is stable, highly damped and non-oscillatory. The roll subsidence eigenvalues are located on the real axis, meaning that the mode is critically damped. When airspeed increases the roll mode eigenvalue moves to the left which indicates that the frequency of the mode increases. The roll motion can be written in the first-order differential form of a rate response type :

$$\dot{p} = L_p p \qquad (25)$$

Which simply leads to the following approximation for the roll mode eigenvalue:

$$\lambda_r = L_p \qquad (26)$$

This approximation is quite accurate, but the exact values of λ_r are roughly 15% larger than L_p. The relatively lower value of L_p shows that there is some coupling with the sway motion, meaning that there are translational velocities building up along the y-axis during the rolling motions. In conversion mode and airplane mode the roll mode frequency similarly increases with airspeed. In general the FLIGHTLAB curves show a similar trend with airspeed.

From Figure 19a it can be concluded that the roll mode eigenvalue moves moves to the right on the real axis when the nacelle angle decreases. This means that the frequency of the mode decreases. In Figure 12(d) it is illustrated that L_p decreases in magnitude with decreasing nacelle angle. This is mainly due to decreasing roll damping of the rotors. The coupling of the roll mode with yaw increases with decreasing nacelle angle because of the orientation of the rotors.

4.4 Spiral mode

The spiral mode is the second non-oscillatory lateral/directional mode. The mode is usually developed very slowly and involves a combination of roll, yaw and sideslip. The spiral mode for conventional helicopters at low speeds is usually primarily a yawing motion, meaning $\lambda_s = N_r$. Since N_r is a damping derivative the spiral is a stable mode and equilibrium is restored by the helicopter itself [11]. The dihedral effect is destabilizing the spiral mode [22], and this effect is much more prominent for tiltrotors than for conventional helicopters. In Figure 16b

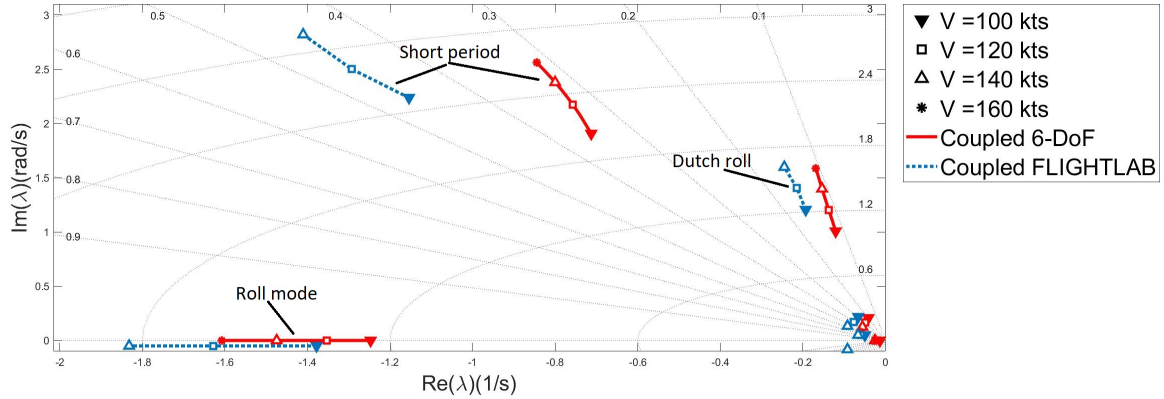

(a) Full picture

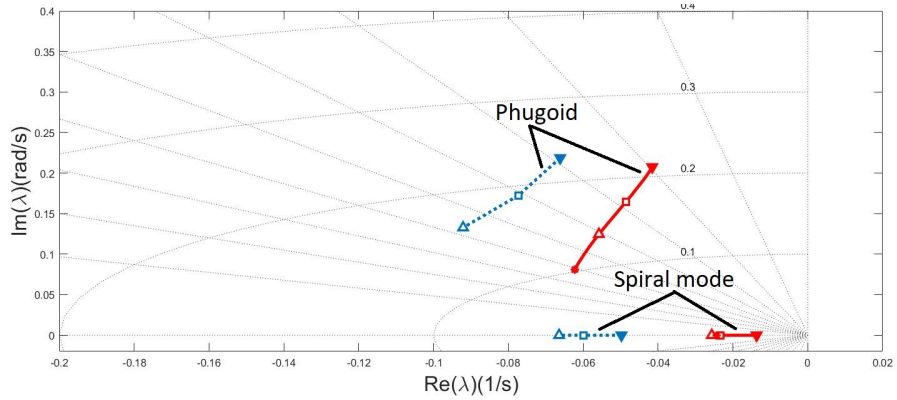

(b) Low frequency modes

Fig. 17. XV-15 6-DoF model coupled eigenmodes in conversion mode (η = 60deg) compared with the FLIGHTLAB eigenmodes

we see a negative real eigenvalue for the spiral mode in hover, meaning that the mode is stable. Padfield gives the following approximation equation for the spiral mode [11]

$$\lambda_s = \frac{g}{L_p}\frac{(L_v N_r - N_v L_r)}{(u_0 N_v + \sigma_s L_v)} \tag{27}$$

with

$$\sigma_s = \frac{g - N_p u_0}{L_p} \tag{28}$$

In hover this equation can be simplified to

$$\lambda_s = N_r - \frac{N_v}{L_v} L_r \tag{29}$$

The first term in this approximation is the yaw damping derivative, which is negative and thus stabilizing. The yaw damping derivative for tiltrotors in H-mode is significantly lower than for helicopters due to the absence of a tail rotor. The second term consist of the dihedral effect L_v and weathercock stability derivative N_v which are negative and positive respectively. Besides the two sideslip derivatives the yaw-roll coupling derivative L_r is included in the equation which is positive in H-mode. This means that the second term of the approximation equation is destabilizing. In hover, the stabilizing N_r term is bigger than the destabilizing second term, although they are not far off (-0.0883 and 0.0618 respectively). When the airspeed increases to moderate airspeeds N_r does not significantly increase, while the other derivatives affecting the spiral do. This causes the 6-DoF model spiral mode to become unstable. The peak of instability is reached at approximately 30 kts, where the real positive eigenvalue is at its largest. Thereafter the eigenvalue moves towards the stable axis again which mainly happens because N_r starts increasing in magnitude.

In C-mode the spiral is stable and barely affected by the airspeed. Derivative N_r is higher than in H-mode and L_r which was destabilizing in H-mode is now stabilizing. In

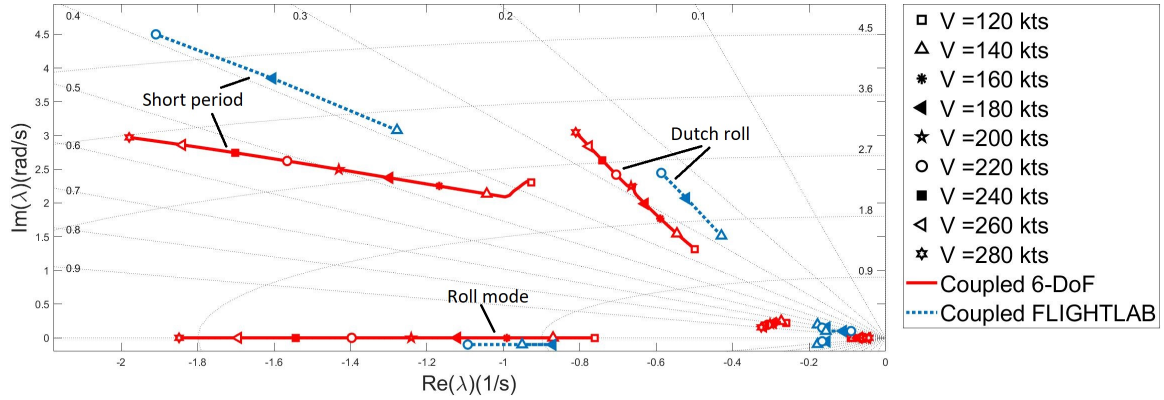

(a) Full picture

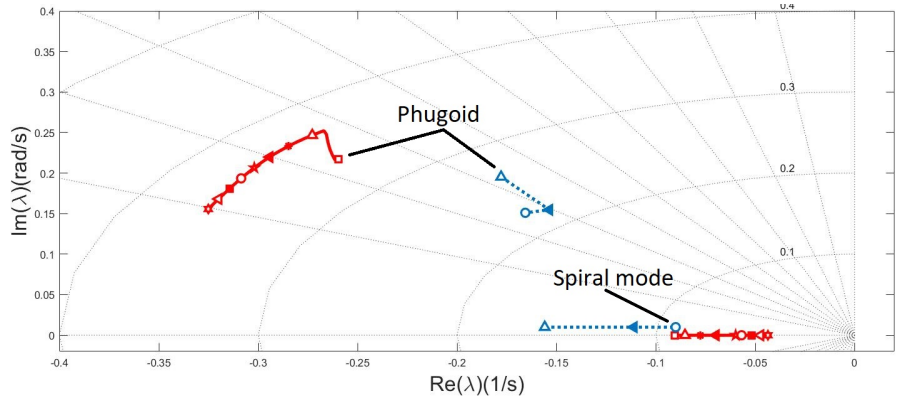

(b) Low frequency modes

Fig. 18. XV-15 6-DoF model coupled eigenmodes in airplane mode (η = 0deg) compared with the FLIGHTLAB eigenmodes

A-mode (Figure 18b) the spiral mode is also stable but the frequency decreases with airspeed. The roll damping derivative L_p increases in magnitude with airspeed which contributes to the decrease in magnitude of λ_s.

The FLIGHTLAB spiral mode shows similar trends with airspeed in C-mode and A-mode. In H-mode the mode is already unstable in hover, in contrary to the 6-DoF model mode. Its stabilizing yaw damping N_r is hover is smaller (Figure 13). The mode destabilizes even more with airspeeds up to 20 kts, after which the eigenvalue moves towards the stable side of the axis. Both models' spiral modes are stable at airspeeds higher than approximately 80 kts.

In Figure 19b the spiral eigenvalues as a function of nacelle angle are shown. It can be concluded from the figure that the spiral mode becomes more stable when the nacelles are rotated towards airplane mode. The positive roll-yaw coupling derivative L_r is destabilizing at high nacelle angles. The derivative decreases and becomes negative when the nacelles are rotated towards 0 degrees. This contributes to the stabilization of the spiral mode. Simultaneously the roll damping derivative L_p decreases in size which also contributes to the spiral becoming more stable.

4.5 Dutch roll

The Dutch Roll mode is an oscillatory lateral/directional mode which consists of a combination of yawing, rolling and sidesliping motion. The Dutch Roll has quite a short period and is usually lightly damped. The Dutch Roll is often considered an undesirable mode since it interferes with the pilot's ability to hold a trim. Besides this, the mode is quite unpleasant for passengers [23]. In Figure 16 the Dutch Roll eigenvalues in helicopter mode as a function of airspeed are shown. In hover the mode is unstable which is also sometimes the case for conventional helicopters [11]. When the airspeed increases the Dutch Roll becomes a very lightly damped stable mode. The frequency increases with airspeed, while the damping remains roughly constant. The eigenvalues in conversion mode and airplane mode show a similar trend. The instability of the Dutch

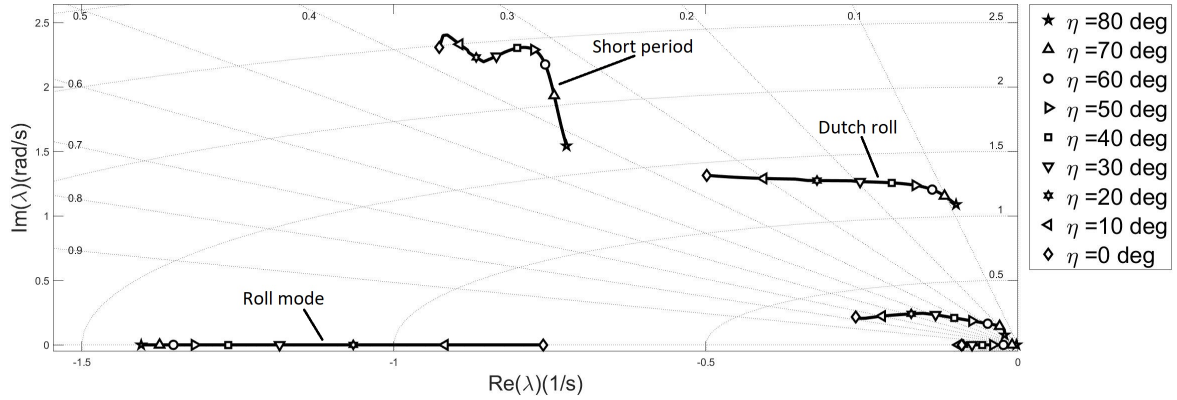

(a) Full picture

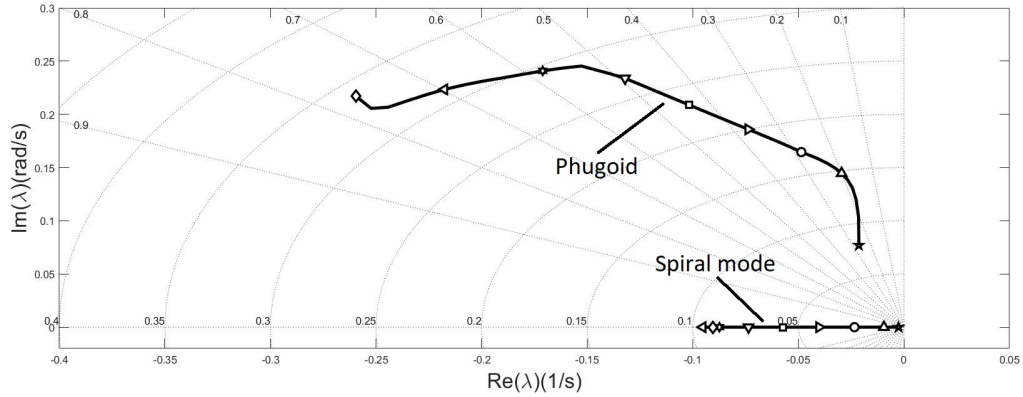

(b) Low frequency modes

Fig. 19. XV-15 6-DoF model coupled eigenmodes as a function of nacelle angel (V = 120 kts)

roll in hover is captured by the following approximation equation:

$$\lambda_d^2 - (N_r + Y_v - \frac{g}{L_p^2} L_v)\lambda_p + \frac{g}{L_p} L_v = 0 \qquad (30)$$

The dihedral derivative L_v is negative as seen in Figure 10. That means that the third term for the damping is destabilizing. Since the stabilizing damping derivatives N_r and Y_v are low in hover this results in an unstable Dutch roll. The damping derivatives increase with airspeed causing the mode to stabilize. The FLIGHTLAB curves look very similar to the 6-DoF model curves.

Figure 19a shows the dutch roll eigenvalues as a function of nacelle angle. From the figure it can be concluded that the frequency of the mode slowly increases with decreasing nacelle angle. The frequency of the Dutch roll is mainly determined by N_v and u_0. Since the forward speed is kept constant the effect of u_0 can be neglected. From Figure 11 it can be concluded that N_v slightly increases with decreasing nacelle which explains the slight increase in frequency. The increase of the damping slowly builds up with decreasing nacelle. This mainly happens due to the increase in yaw damping N_r. Furthermore, the roll-yaw coupling derivative N_p first increases in magnitude up to ≈ 30 degrees which withholds the damping from increasing faster. Thereafter the derivative decreases again, which explains why the damping suddenly increases faster with nacelle angle.

5. Conclusions

The aim of this research was to get a better understanding of the stability characteristics of tiltrotor rotor. For this purpose, a six-degrees-of-freedom nonlinear flight dynamics has been developed and linearized. The stability and control derivatives following from this linearization have been analysed, together with the eigenvalues describing the dynamic modes of the aircraft. From the research described in this paper the following main conclusions can be drawn:

- The six-degrees-of-freedom nonlinear flight dynamics model described in this paper has been proven to be valid for stability and control related research purposes.

- The stability derivatives of the 6-DoF model have proven to be comparable to the derivatives found by other models. The damping derivatives (e.g. X_u, L_p) are all negative and increase in magnitude with airspeed. The rotors have a large effect on the heave and roll derivatives (e.g. Z_w, L_p) in helicopter mode and on the surge and yaw derivatives (e.g. X_u, N_r) in airplane mode.

- The control derivatives of the 6-DoF model show a lot of similarities with the FLIGHTLAB model data and the control inputs lead to the desired responses. The assumption that elevators, ailerons and rudders create no drag results in some discrepancies between the curves of the models. The effectiveness of the control surfaces of the models seems to be dissimilar while they should be equal.

- In hover, the heave and pitch subsidences are both non-oscillatory but stable. As airspeed increases, the heave and pitch subsidence couple together and form the short period. The frequency of the short period increases with airspeed while the damping slightly decreases at high nacelle angle configurations. At low nacelle angle configurations the damping increases with airspeed. When the airspeed is kept constant and the nacelle angle decreases the frequency slowly increases while the damping remains roughly constant. In hover the phugoid is oscillatory but unstable. The mode stabilizes when the airspeed increases and becomes at some point non-oscillatory. This can be attributed to the negative value of M_u which amplifies the phugoid damping. In C-mode and A-mode the phugoid is oscillatory and stable. At constant airspeed and decreasing nacelle angle the phugoid damping increases. At the same time the frequency of the mode increases slightly. The roll mode is mostly a pure roll subsidence which is stable, highly damped and non-oscillatory. Its frequency increases with airspeed but decreases with decreasing nacelle angle. The coupling with yaw increases with decreasing nacelle angle. The spiral mode is mostly unstable in helicopter mode. In hover the mode is stable, but as airspeed increases the mode destabilizes. The instability increases with airspeed up to $\pm$ 30 kts, after which it decreases again. At airspeeds higher than $\pm$ 80kts in H-mode the spiral is again stable. The spiral mode also becomes more stable with decreasing nacelle angle. In hover the Dutch roll is also unstable, but becomes stable after airspeed increases. The dutch roll frequency increases with airspeed while the damping remains constant. Decreasing the nacelle angle however clearly increases the damping of the mode. The 6-DoF model eigenmodes results showed a lot of similarities with the FXV-15. Both models have an unstable phugoid and Dutch roll in hover. The spiral modes are often unstable in helicopter mode and have similar trends with airspeed. The FXV-15 spiral is however already unstable in hover, due to its lower value of N_r. The FXV-15 short period in H-mode and C-mode is relatively more damped due to its higher pitch damping M_q. The biggest difference in modes between the two models is the phugoid in helicopter mode. The 6-DoF model phugoid is non-oscillatory at high airspeeds because of the negative M_u at those flight conditions. In the same flight conditions the FLIGHTLAB M_u is positive and thus the phugoid remains oscillatory.

BIBLIOGRAPHY

[1] L. A. Young, W. W. Chung, A. Paris, D. Salvano, R. Young, H. Gao, K. Wright, D. Miller, and V. Cheng, "A study of civil tiltrotor aircraft in nextgen airspace," in *10th AIAA Aviation Technology, Integration, and Operations (ATIO) Conference*, (Forth Worth, Texas), pp. 1–18, American Institute of Aeronautics and Astronautics, 2010.

[2] M. D. Maisel, D. J. Giulianetti, and D. C. Dugan, *The Histort of The XV-15 Tilt Rotor Research Aircraft: From Concept to Flight*. National Aeronautics and Space Administration, 2000.

[3] P. B. Harendra, M. Joglekar, T. M. Gaffey, and R. L. Marr, "V/stol tilt rotor study-volume 5: A mathematical model for real time flight simulation of the bell model 301 tilt rotor research aircraft," tech. rep., NASA CR-114614, 1973.

[4] S. W. Ferguson, "A mathematical model for real time flight simulation of a generic tilt-rotor aircraft," tech. rep., NASA CR-166536, 1988.

[5] S. W. Ferguson, "Development and validation of a simulation for a generic tilt-rotor aircraft," tech. rep., NASA CR-166537, 1989.

[6] M. B. Tischler, "Identification and verification of frequency domain models for xv-15 tilt-rotor aircraft dynamics," tech. rep., NASA-TM-86009, 1984.

[7] M. B. Tischler and R. K. Remple, *Aircraft and Rotorcraft System Identification: Engineering Methods with Flight Test Examples*. Reston: AIAA, 2nd edn ed., 2012.

[8] W. Johnson, "Dynamics of tilting proprotor aircraft in cruise flight," tech. rep., Ames Research Center and U.S. Army Air Mobility R&D Laboratory, Moffett Field, Carlif., 1974.

[9] G. D. Klein, "Linear modelling of tiltrotor aircraft (in helicopter and airplane modes) for stability analysis and preliminary design," Master's thesis, Naval Post Graduate School, Monterey, CA, 1996.

[10] K. M. Kleinhesselink, "Stability and control modeling of tiltrotor aircraft," Master's thesis, University of Maryland, Department of Aerospace Engineering, 2007.

[11] G. D. Padfield, *Helicopter Flight Dynamics, Including a Treatment of Tiltrotor Aircraft*. Wiley, third ed., 2018.

[12] G. D. Padfield and M. M. Meyer, "First steps in the development of handling qualities criteria for a civil tiltrotor," *Journal of the American Helicopter Society*, vol. 50, no. 1, p. 33–46, 2005.

[13] D. Walker and P. Perfect, "Longitudinal stability and control of large tilt-rotor aircraft," tech. rep., Engineering Department, Liverpool University, 2007.

[14] T. Berger, O. Juhasz, M. J. S. Lopez, M. B. Tischler, and J. F. Horn, "Modeling and control of lift offset coaxial and tiltrotor rotorcraft," *CEAS Aeronautical Journal*, vol. vol. 11, no. no. 1, pp. pp. 191–215, 2020.

[15] D. Perry, "Aw609 control laws initiated 'dutch roll': investigators," *Flight Global*, 2016.

[16] P. Sokolowski, "Msc. thesis: Flight dynamics modelling of a tiltrotor aircraft," Master's thesis, Delft University of Technology, 2021.

[17] Y. Yuan, D. Thomson, and D. Anderson, "Manoeuvrability investigation for tiltrotor aircraft with an integrated simulation engine," *47th European Rotorcraft Forum*, 2021.

[18] B. L. Stevens, F. L. Lewis, and E. Johnson, *Aircraft control and simulation: Dynamics, controls design, and autonomous systems*. John Wiley & Sons, third ed., 2016.

[19] P. Sokolowski, "Literature study: Flight dynamics modelling of a tiltrotor aircraft," Master's thesis, Delft University of Technology, 2020.

[20] K. Lu, C. Liu, C. Li, and R. Chen, "Flight dynamics modeling and dynamic stability analysis of tilt-rotor aircraft," *International Journal of Aerospace Engineering*, vol. vol. 2019, pp. 1–15, 2019.

[21] T. van Holten, J. A. Melkert, B. Marrant, and M. Pavel, "Helicopter performance, stability and control lecture notes," 2002.

[22] R. Prouty, *Helicopter Performance, Stability and Control*. PWS Publishers, 1986.

[23] M. Pavel, "Rotorcraft mechanics course ae4314, lecture slides," March 2020.

Part II

Technical Report

1

Introduction

A tilt-rotor aircraft, also referred to as simply tiltrotor, is an aircraft that is able to perform vertical take-off and landing manoeuvres like a conventional helicopter, as well as achieving cruise speeds and long ranges that are common for a fixed-wing aircraft. This is achievable due to its rotor tilting capabilities. The rotors, also called proprotors, are mounted on the wingtips of a fixed-wing aircraft and can be tilted around 90 degrees during flight to perform both horizontal and vertical manoeuvres. The travel time to and from airports could be reduced significantly as the tiltrotor is much more flexible in take-off and landing locations because it does not require an entire landing strip [9]. This feature could make air transport much more time efficient.

Although there have been several projects and developments in tiltrotor technology, the only tiltrotor that has made it to the market yet is the Bell Boeing V-22 Osprey. This aircraft, which is used by the US Marine Corps, US Air Force Special Operations Command and the US Navy has solely military applications. The development of the V-22 has primarily relied on the data and experiences of its predecessor, the Bell XV-15. This experimental tiltrotor, funded by NASA, was the first in its sort to successfully reach a cruise velocity which could never be achieved with a conventional helicopter [1]. Currently, more research is conducted into the civil applications of the tiltrotor. The developments of several tiltrotor projects are still ongoing, amongst which the Agusta Westland AW609 project. This civil tiltrotor has been under development for over 15 year but has not made it to the market yet at the time of writing this thesis report.

In 2015 the AW609 suffered a fatal crash when a high-speed dive during a test flight became unstable. The pilots commenced the dive with a 180-degree turn, targeting 293 knots for the manoeuvre. The aircraft started oscillating about the roll axis after exiting the turn. Shortly after the first roll oscillation, the aircraft experienced additional oscillations about the yaw axis. Initially, the crew did not react to these oscillations, as they believed they were self-damping and thus not dangerous. When the pilot felt that the oscillations increased in magnitude, he tried to counter them using roll-tracking, but this resulted in a pronounced yaw, which he tried to counter using the rudder pedals. Although the pilot followed the standard procedure for controlling the aircraft, the yaw oscillation was amplified even more, causing the proprotor to interfere with the right wing, causing an in-flight break-up and fire, eventually resulting in a fatal crash. Investigations into the crash pointed out that the AW609's flight control system (FCS) control laws were a cause for the crash, together with a project simulator that was unable to predict this instability in any way. [10].

The fatal AW609 crash shows that it is crucial to be able to accurately predict the flight dynamics of an aircraft at any situation in order to prevent fatalities. The AW609 showed unstable behavior which could be described as a diverging Dutch roll mode [11]. There is already quite some literature about tiltrotor aircraft, but most literature is focused on flight dynamics modeling or handling quality evaluation. The stability of the tiltrotor is however much less investigated. The aim of this research is to get a better understanding on the stability characteristics of tiltrotor aircraft. A six-degrees-of-freedom tiltrotor flight dynamics model has been developed which will be trimmed and linearized. It will be analysed how the stability and control derivatives behave as a function of airspeed and nacelle angle and which components contribute to each derivative. Furthermore, data from different models are compared and their similarities and differences in results are explained by comparing their model properties. Coupled and uncoupled linear models are then

used to investigate the dynamic modes of the tiltrotor and how the modes are affected by the stability derivatives.

The report is structured as follows. This introductory chapter is concluded with the research objective and the research questions. Chapter 2 gives some background information about tiltrotor aircraft in general and the XV-15 in particular, which is used as the reference aircraft throughout this research. Furthermore, some previously developed tiltrotor models are discussed and their strong and weak points are elaborated upon. The chapter is concluded with a brief description of stability in general. chapter 3 describes the main non-linear model which is used throughout this research and provides a computation scheme encapsulating the mathematics behind the modelling. The chapter is concluded with a trim analysis and validation of the trim results. In chapter 4 the linearization process of the model is described and the stability and control derivatives following from the linearization are analysed in detail. The dynamic modes following from the linear model are investigated in chapter 5. This thesis is concluded in chapter 6 after which recommendations for future work are given.

1.1. Research Objective

Although there already exists quite some literature on tiltrotors, most literature is limited to the flight dynamics modelling of the aircraft or is focused on addressing the handling qualities characteristics. The dynamic stability characteristics of the tiltrotor are less investigated, and a thorough analysis of the variation of the characteristics with airspeed and nacelle angle is missing in literature. In order to get a better understanding of how the tiltrotor behaves when it is moving through its conversion corridor a detailed analysis of its dynamic characteristics is provided in this research. The main objective of this research can be formulated as follows

> *"To investigate the stability characteristics of tiltrotor aircraft theoretically by using the technique of linearized stability derivatives on a six-degrees-of-freedom tiltrotor flight dynamics model"*

1.2. Research Questions

In order to reach this objective and to structure the research, several research questions are posed at the start of this research. The main research question can be formulated as follows

> "Which tiltrotor stability characteristics can be identified by analyzing a linearized six-degrees-of-freedom tiltrotor flight dynamics model?"

The main research question is split up into several subquestions for which it is intended to find an answer to during the research. These questions can then be broken down into lower layer subquestions.

- Which features characterize a tiltrotor aircraft?
  - Which general features distinguishes the tiltrotor from a conventional helicopter or fixed-wing aircraft?
  - What are the differences between the control strategies of a tiltrotor and a conventional helicopter or fixed-wing aircraft?
- How can the dynamic behavior of the tiltrotor most accurately be predicted by modelling its principles into a flight dynamics model?
  - What are the largest weak points of the current six-degrees-of-freedom model and how can they be improved?
- Which conclusions can be drawn about the stability characteristics of the tiltrotor from the linearized stability and control derivatives?
  - Which derivatives are supposed to be negative and which are supposed to be positive in order to have a stable tiltrotor?
  - How do the derivatives compare to the derivatives for conventional helicopters or fixed-wing aircraft?

  - How do the derivatives compare to the derivatives found by other tiltrotor models?

- Which conclusions can be drawn about the stability characteristics of the tiltrotor from the eigenvalues of the dynamic modes?
  - Under which circumstances are the dynamic modes stable and under which circumstances unstable?
  - How are the dynamic modes influenced by the airspeed and nacelle angle?
  - How do the eigenvalues from the uncoupled linear systems compare to the eigenvalues from the coupled linear system?
  - How do the found eigenvalues compare to the eigenvalues found by other tiltrotor models?

2
Background

This chapter serves as an introduction to tiltrotor aircraft and to tiltrotor research in general. The features that characterize tiltrotor aircraft are elaborated upon and the current state-of-the-art in tiltrotor modelling is discussed. The tiltrotor is introduced in section 2.1 and the history in tiltrotor development is elaborated upon. The reference aircraft that will be used during this research is the Bell XV-15. This tiltrotor aircraft will be introduced in section 2.2. The flight dynamics modelling of tiltrotor is no unknown territory; several tiltrotor models exist and are described in literature. The most prominent ones are described in section 2.3. Lastly, the chapter is concluded with a general introduction to aircraft stability.

2.1. Tiltrotor Aircraft

This section serves as an introduction to tiltrotor aircraft in general. Firstly, the general characteristics of the aircraft are discussed with its advantages and potential benefits to air traffic. Thereafter, the history of the tiltrotor is elaborated upon together with its recent developments. Lastly, the different flight modes that can be distinguished for tiltrotor aircraft are discussed.

2.1.1. Introduction to Tiltrotor Aircraft

A tilt-rotor aircraft, also referred to as tiltrotor aircraft or simply tiltrotor, is a hybrid aircraft that attempts to combine the vertical take-off and landing (VTOL) and hover capabilities of a helicopter with the speed and range characteristics of an fixed-wing airplane. The tiltrotor uses multiple rotors, also called proprotors, to generate lift during vertical manoeuvres and to provide thrust during high-speed horizontal manoeuvres. The rotors have the ability to be tilted in order to increase or decrease flight speed. By far the most popular and promising tiltrotor configuration is one with two proprotors, both located at the wing tips of a fixed-wing aircraft. The XV-15, one of the most well-known tiltrotor aircraft is shown in 2.1. In this figure the proprotors, mounted on nacelles, are rotated 90 degrees with respect to the fixed wing, meaning that the aircraft is in helicopter mode. This angle between the fixed wing and the rotor nacelle, from now on referred to as the nacelle angle (η), can vary between around 0 and 90 degrees.

The biggest advantage of the tiltrotor compared to other aircraft that are functional at the moment is its combination of the VTOL capabilities of helicopters with the speed and range of an airplane. This makes the tiltrotor a runway independent aircraft, which has the potential of increasing the airspace capacity due to its flexibility in take-off and landing locations. This could make air transport more time efficient since the travel time to and from the airports would be reduced significantly, resulting in an increased throughput through the entire system [9]. Besides this advantage, the flight ceiling of the tiltrotor is around 25,000 feet, which is more than twice as high as for conventional helicopters allowing the aircraft to circumvent bad weather.

2.1.2. History

Although the first tilt-rotor was developed decades later, the idea of a vehicle that combines the VTOL characteristics of a helicopter with the speed and range of an airplane already existed in the 1920s. One of these ideas came from Henry Berliner, who came up with a design that resembled a fixed wing biplane

Figure 2.1: The XV-15 Tiltrotor aircraft in helicopter mode [1]

aircraft with 2 two propellers mounted on vertical shafts near the tip of the wings. The shafts would be slightly tilted forward during forward flight which, although they could not be tilted 90 degrees, had a similar rotor arrangement as the current tiltrotor aircraft [1].

Several others tried to come up with a good reliable design to combine vertical lift and forward flight in the decades following, but none of them were able to succeed. The reasons for this were among others performance, structural dynamics or control deficiencies or a lack of financial support. In 1947 the development of the Transcendental 1-G was initiated which was able to conduct its first successful test flight in 1954. This model is generally recognized as the first tilt rotor aircraft which was able to explore the conversion between vertical lift and airplane mode [1].

A year later the prototype crashed during a test flight after which the Transcendental Model 2 was created. This project was funded by the US Air Force, but they decided to withdrawn the funding and instead start investing in the Bell Model 200 which was later designated the XV-3. This model had stability issues and limited hover and cruise performance; the maximum cruise speed of 115 knots was not enough to show that the vehicle had adequate airplane mode performance. On the positive side, the XV-3 project has proven us that the conversion from vertical lift to horizontal flight and back can be performed in a stable, controllable, reliable manner. This ensured that the interest in the development of tiltrotor technology did not disappear [1].

In 1972 the development of the XV-15 was initiated with funding from NASA, the US Army and the US navy. This new project resulted from improved technologies, new test techniques and a thorough research into the issues of the XV-3. The XV-15 was the first tilt rotor aircraft which was able to demonstrate high-speed performance during airplane mode and reach flight speeds which could never be achieved with a conventional helicopter [1].

Based on the results of the XV-15 testing the V-22 Osprey program was initiated. The V-22 was the follow on operational aircraft developed jointly by Bell-Boeing for the US Marine Corps, US Air Force Special Operations Command, and the US Navy. This was in 2003, and four year later the V-22 fully entered service for the US Marines. Nowadays, more than a decade later, the V-22 is still the only operational tiltrotor that exists.

The year 2003 was also the first year that the first prototype off the Bell-Agusta BA609 flew. The BA609 is similar in size to the XV-15 and was designed to meet the civil airworthiness regulatory standards[2]. The BA609, nowadays called the AgustaWestland AW609, has had quite some difficulties during its development and testing, including a fatal accident during testing in Italy in 2015 [10]. At the time of writing this thesis

report in 2021, the aircraft is still not operational.

2.1.3. Flight Modes

For a tiltrotor three different modes can be distinguished during flight. The vehicle is said to be in helicopter mode (H-mode) when the nacelles have an angle of 90 degrees with respect to the fixed wing. In this mode the proprotors are positioned vertically generating a lift force like a conventional helicopter. During the helicopter mode the forward speed is relatively low or even equal to zero, meaning that this mode can be used for vertical manoeuvres including take-off, landing and hover.

If the nacelles are oriented parallel to the wing, the tiltrotor is said to be in airplane mode (A-mode). In this mode, the proprotors function as airplane propellers generating thrust and allowing the tiltrotor to reach high horizontal velocities comparable to conventional airplanes.

A tiltrotor converts from helicopter mode to airplane mode and vice-versa by rotating its nacelles with respect to the fixed wing. If the nacelles are not oriented perpendicular or parallel with respect to the wing, the aircraft is said to be in conversion mode (C-mode). Back in the days when the first tiltrotors were developed, this mode was merely used as a transitional mode between the two previously described modes, but nowadays the potential benefits of operating in this so-called conversion mode are being further investigated [12].

2.2. The XV-15 Tiltrotor Research Aircraft

Throughout this research, the analysis is mainly conducted on the XV-15 Tilt Rotor Research Aircraft which employs the tilt rotor concept and displays generic tiltrotor characteristics. An image of the XV-15 is shown in Figure 2.1. The XV-15 has two three-bladed rotors mounted on a stiff in-plane gimballed hub. This aircraft has been chosen for the analysis simply because it is the only tilt rotor aircraft for which enough data is publicly available to conduct the analysis. The flight envelope of the XV-15 can be expressed in a so called conversion corridor. This conversion corridor is elaborated upon in subsection 2.2.1. There after, the control strategy and the control inceptors of the aircraft are discussed in subsection 2.2.2 and subsection 2.2.3 respectively.

2.2.1. Conversion Corridor

Because of the ability of the XV-15 to convert between three different flight modes, the aircraft also has an extensive operating range. At low velocities the tiltrotor is usually in helicopter mode, but as velocity increases the nacelles can be tilted towards airplane mode. At different nacelle angles there also exist different airspeed boundaries at which it is safe to operate. The safe regions to operate in are defined as the conversion corridor. The conversion corridor of the XV-15 is shown in Figure 2.2. In the conversion corridor, also called the transition corridor, it is safe to convert between helicopter, conversion and airplane mode. A conversion is called successful when the change in lift created by the wing and the rotor compensate for each other, keeping the total lift and the altitude constant [2]. The normal nacelle tilt rate is around 7.5 deg/s for the XV-15. If the tilt rate is too small while accelerating the right boundary of the corridor could be reached, which could lead to exceeding the control and power limits of the vehicle or reaching unsteady rotor loads. On the other side, if the nacelles are tilted too fast, the left boundaries would be reached and there is the possibility that combined lift of the rotor and wing is insufficient to balance the weight of the aircraft [2]. The Leonardo AW609 features a corridor protection function to reduce the workload while manoeuvring in the conversion corridor [13]. This automatic conversion protection functions stops the conversion if a boundary of the corridor is reached. It first corrects the speed of the vehicle and then tilts without any further command the nacelles to the desired nacelle angle. A similar system is incorporated in the Bell-Boeing V22 Osprey [2].

2.2.2. Control Strategy

The tiltrotor is essentially a hybrid between a helicopter and an airplane. Therefore, it also uses the control strategies of both aircraft types. In helicopter mode the aircraft uses conventional helicopter control strategies. The control functions of the XV-15 in helicopter mode are shown in Figure 2.3a. Collective control is used to alter the pitch angle of all rotor blades which is mainly used to move the vehicle vertically. Cyclic control is used to alter the tip path plane tilt of the rotors, allowing the vehicle to move horizontally. A big difference with the conventional helicopter is that the tail rotor has become redundant as the tiltrotor

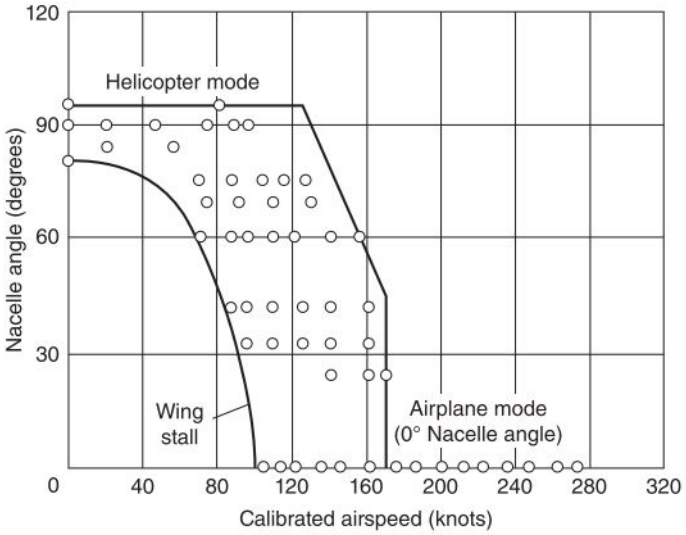

Figure 2.2: XV-15 conversion corridor [2]

has two counter-rotating rotors, eliminating the induced torques of each other. However, this also means that the directional stability has to be controlled in a different manner. This is done by using differential longitudinal cyclic control: if the pilot wishes to yaw to left, the right proprotor is tilted forward and the left rotor is tiled aft, creating a moment around the vertical axis. Moreover, in addition to the classic helicopter control strategies, the tiltrotor has an unique method to perform rolling manoeuvres. A roll can be initiated using differential collective pitch on the rotors. If the pilot wishes to roll to the right, he/she increases the collective angle on the left proprotor while decreasing the one on the right, creating a thrust imbalance, which together with the large moment arm induces a roll [12]. The control mechanisms for the different tiltrotors are quite similar but still there exist some differences: the AW609 for example does not use lateral cyclic pitch for lateral translation in helicopter mode[14].

When the XV-15 is in airplane mode it makes use of conventional airplane flight control surfaces. Ailerons (or flaperons) are located at the trailing edges of the wings to control the rolling motions about the longitudinal axis of the vehicle. Rudders are used to control the aircraft about its vertical axis, or in other words to control its yawing motions. This is however the case for the XV-15 [12], the AW609 does not have a rudder and uses differential collective blade pitch to control yaw [14]. Elevators are located on the horizontal stabilizers at the tail to control the pitching movements of the aircraft. The control mechanisms in airplane mode are shown in Figure 2.3b.

In conversion mode the control strategies of both the helicopter and airplane mode are combined. When the nacelles are rotating forward from a vertical to a horizontal orientation the control required by the proprotors decreases as the dynamic pressure increases and the airplane control strategy becomes more important. When the nacelles are almost completely rotated into airplane mode the effect of the proprotors on the lift has been phased out leaving only the thrust effects active. Naturally the opposite thing happens when the tiltrotor converts back to helicopter mode; the control required by the rotors increases while the dynamic pressure decreases. The effects of the airplane control surfaces do not completely phase out when horizontal speed decreases, but their influences are only minor.

2.2.3. Pilot inceptors

Since the tiltrotor combines both helicopter and airplane control strategies the question during the design arose: what is the most convenient way for the pilot to control this aircraft? Some designers argued that helicopter control inceptors should be used, because the most tricky manoeuvres including vertical take-off and landing happen in helicopter mode. This would have meant that a cyclic stick, a collective stick and pedals would be used. Other designers argued that airplane inceptors should be used because the tiltrotor

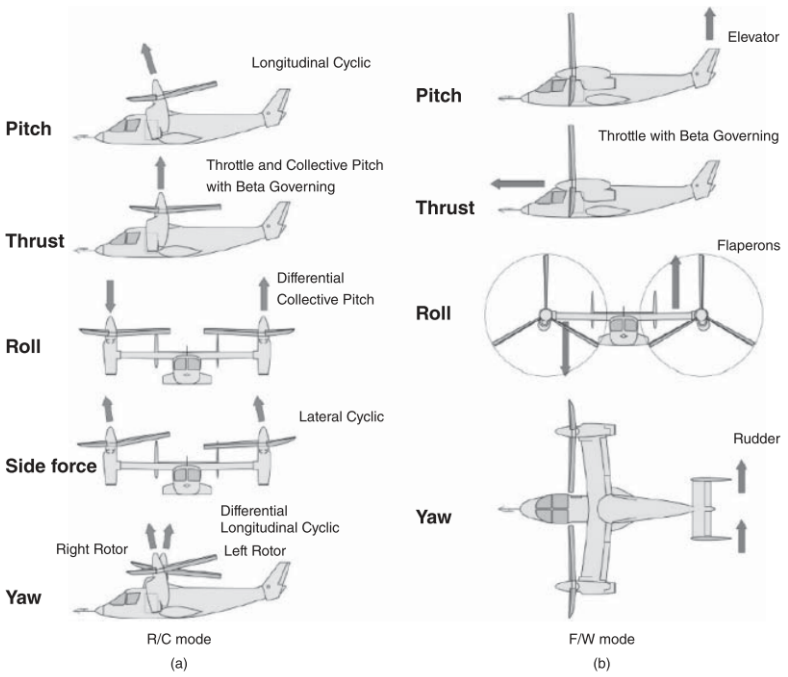

Figure 2.3: XV-15 control functions in both helicopter (a) and airplane mode (b) [2]

spends most of its time in airplane mode. This would have resulted in a yoke or stick, a throttle and pedals. It was decided that a center cyclic stick would be used for pitch and roll control and pedals for yaw control. A discussion arose when deciding between a collective stick of a throttle to alter the thrust of the aircraft. The collective stick is used in a helicopter to control the vertical motion by changing the collective pitch of the blades. If the pilot would pull the collective stick the helicopter would go up and by pushing the stick the helicopter would go down. The throttle of an airplane is used to control the horizontal velocity. By pushing the throttle the airplane would increase its velocity and by pulling the velocity would decrease. Picking one of these two inceptors raised an issue. If a collective control stick would be used, a counter-intuitive action would be required to increase the velocity of the tiltrotor in airplane mode: instead of the habitual action of pushing the throttle the pilot has to pull the collective stick. A similar problem would arise in helicopter mode when using a throttle instead of a collective stick. The arm extension which is normally used to descent in a helicopter would now cause the vehicle to go up. Eventually it was decided that a collective-like power lever would be used to control the thrust of the tiltrotor. In helicopter mode pulling the lever would increase the thrust and thus the aircraft would go up. When converting to airplane mode, the controls convert as well, so pushing the lever in airplane mode would cause the velocity to increase. This way both modes have intuitive controls [2].

2.3. Tiltrotor Models

Before being able to conduct a stability analysis, a flight dynamics model needs to be derived. Multiple tiltrotor models have been derived in the past, some with very high accuracy, some with a lot of simplifications. The choices and assumptions made during the modelling process affect the results and the accuracy of model. In this section, the most prominent tiltrotor models are described. Firstly, a preliminary three degrees of freedom model is described. This model has also been linearized and is used for the analysis of the longitudinal stability characteristics. Thereafter, multiple models found in literature are described, some of which will also be used later this research to validate the results.

2.3.1. 3-DoF Model

In this section the preliminary 3 degrees of freedom model, from now on referred to as 3-DoF model, will be briefly described. This model has been developed in previous research conducted at the Delft University of Technology by Sokolowski [15]. The model is capable of predicting symmetrical motions, so the three degrees of freedom are the surge and heave translations and the pitching rotation. During the development of the model, the following general assumptions were made [15]:

- The symmetric motions can be decoupled from the asymmetric motions.
- All subsystems of the tiltrotor are assumed to be rigid
- The mass of tiltrotor is constant as well as the longitudinal position of the centre of mass (c.m.).
- Gravity is constant, and therefore the c.m. coincides with the centre of gravity (c.g.).
- The geometry and mass distribution of the tiltrotor are symmetrical in the surge-heave plane.
- The simulation environment is defined by a flat, non-rotating Earth.
- The contributions of the vertical stabilizers to the longitudinal dynamics are negligible.

The 3-DoF model is developed in 3 different phases. The product of the last phase, meaning phase 3, is used for the analysis. In this phase, the external moments and forces contain the contributions from the rotor system, the wing, the fuselage and horizontal tail. The modelling of the rotor system is relatively complex and required the following simplifying assumptions [15]:

- The rotor is modelled as an articulated hub with a flapping hinge and spring. No lead-lag hinge nor a hinge offset is modelled.
- The blade aspect ratio is high, air is incompressible.
- The rotor angular velocity Ω is constant along the entire flight envelope.
- Rotor-induced velocity is uniform across the rotor disk.
- The blade cross-section is constant along its length.
- Blade is treated as a slender rod in terms of mass moment of inertia.
- The Lift coefficient of the blade increases linearly with angle of attack.
- The aerodynamic centre of the blade is located at quarter-chord.
- The feathering axis of the blade coincides with with the aerodynamic centre.

Furthermore, for the fuselage the following assumptions are made:

- The fuselage only produces drag, no lift nor a pitching moment is created.
- The aerodynamic centre of the fuselage coincides with the body c.g.
- The fuselage drag is aligned with the body velocity vector.
- The fuselage drag does not depend on the angle of attack.

For the wing and horizontal tail it is assumed that the forces and moments act at their aerodynamic centres, which are located at quarter chord. For the horizontal tail it is assumed that the change in lift coefficient is linearly proportional with the elevator deflection.

The above mentioned assumptions capture the most important simplifications made during the development of the preliminary model. The comparison of the trim curves with other literature has proven that the model is somewhat valid and can be used for preliminary estimations [15]. The mathematical equations behind the model are encapsulate by the computation scheme shown below. For an elaborate description of the model and derivation of the equations the reader is referred to the report by Sokolowski.

Table 2.1: 3-DoF preliminary model computation scheme

Input parameters	
Environmental parameters	$\rho \quad g$
Aircraft parameters	$m \quad I_y \quad A_{eq} \quad N_R$
Rotor parameters	$m_b \quad \Omega \quad R \quad c_b \quad I_b \quad K_\beta \quad \theta_{tw} \quad N_b \quad C_{l_\alpha,b} \quad C_{d_0,b} \quad C_{d_1,b} \quad C_{d_2,b}$
Wing parameters	$C_{l_\alpha,w} \quad \alpha_{0L,w} \quad C_{D0,w} \quad c_{m_{ac},w} \quad S_w \quad AR_w \quad e_w \quad i_w \quad d_{x,w} \quad d_{z,w}$
Horizontal stabilizer parameters	$C_{l_\alpha,hs} \quad \alpha_{0L,hs} \quad C_{D0,hs} \quad c_{m_{ac},hs} \quad S_{hs}s \quad AR_{hs} \quad e_{hs} \quad i_{hs} \quad \frac{dCl_{hs}}{dElev} \quad \frac{dElev}{d\theta_{0s}} \quad d_{x,hs} \quad d_{z,hs}$
Nacelle parameters	$l_n \quad d_{x,n} \quad d_{z,n}$
Control variables	$X_{COL} \quad X_{LON} \quad \eta$
State variables	$u \quad w \quad q \quad \theta_f$
Calculations	
	$V = \sqrt{u^2 + w^2}$
	$\alpha_f = \arctan(\frac{w}{u})$
	$\theta_{1s} = 0.0367 X_{LON} \cos(\eta)$
Wing calculations	$u_w = V\cos(\alpha_f) - q d_{x,w}$
	$w_w = V\sin(\alpha_f) - q d_{z,w}$
	$V_w = \sqrt{u_w^2 + w_w^2}$
	$\gamma_w = \arctan\frac{w_w}{u_w}$
	$\alpha_w = \gamma_w + i_w$
	$C_{L,w} = C_{l_\alpha,w}(\alpha_w - \alpha_{0L,w})$
	$C_{D,w} = C_{D0,w} + \frac{C_{L,w}^2}{\pi AR_w e_w}$
	$L_w = \frac{1}{2}\rho V_w^2 S_w C_{L_w}$
	$D_w = \frac{1}{2}\rho V_w^2 S_w C_{D_w}$
	$X_w = L_w\sin(\gamma_w) - D_w\cos(\gamma_w)$
	$Z_w = -L_w\cos(\gamma_w) - D_w\sin(\gamma_w)$
	$M_w = \frac{1}{2}\rho V_w^2 S_w C_{m_{ac},w}$
Horizontal stabilizer calculations	$u_{hs} = V\cos(\alpha_f) - q d_{x,hs}$
	$w_{hs} = V\sin(\alpha_f) + q d_{z,hs}$
	$V_{hs} = \sqrt{u_{hs}^2 + w_{hs}^2}$
	$\gamma_{hs} = \arctan\frac{w_{hs}}{u_{hs}}$
	$\alpha_{hs} = \gamma_{hs} + i_{hs}$
	$C_{L,hs} = C_{l_\alpha,hs}(\alpha_{hs} - \alpha_{0L,hs}) + \frac{dCl_{hs}}{dElev}\frac{dElev}{d\theta_{1s}}\theta_{1s}$

continues on next page

	$C_{D,hs} = C_{D0,hs} + \frac{C_{L,hs}^2}{\pi AR_{hs} e_{hs}}$ $L_{hs} = \frac{1}{2}\rho V_{hs}^2 S_{hs} C_{L_{hs}}$ $D_{hs} = \frac{1}{2}\rho V_{hs}^2 S_{hs} C_{D_{hs}}$ $X_{hs} = L_{hs}\sin(\gamma_{hs}) - D_{hs}\cos(\gamma_{hs})$ $Z_{hs} = -L_{hs}\cos(\gamma_{hs}) - D_{hs}\sin(\gamma_{hs})$ $M_{hs} = \frac{1}{2}\rho V_{hs}^2 S_{hs} C_{m_{ac,hs}}$
Control phasing	$\theta_{0,LL} = -0.0401(1 + 6.5324\eta)$ $\theta_{0_{mod}} = \theta_{0,LL} - 0.1113$ $\theta_{00} = \theta_{tw} + \theta_{mod}$ $\theta_0 = 1.6X_{col}\frac{\pi}{180} + \theta_{00}$
Control plane	$\alpha_{DP} = \theta_{1s} - \alpha_f - \eta$ $\mu_{CP} = \frac{V}{\Omega R}\cos(\alpha_{CP})$ $\lambda_{CP} = \frac{V}{\Omega R}\sin(\alpha_{CP})$ $d_{x,dp} = l_n\sin(\theta_c) + d_{z,n}\sin(\theta_c - \eta) + d_{x,n}\cos(\theta_c - \eta)$ $d_{z,cp} = l_n\cos(\theta_c) - d_{x,n}\sin(\theta_c - \eta) + d_{z,n}\cos(\theta_c - \eta)$ $\gamma = \frac{\rho C_{l_{\alpha,b}} c_b R^4}{I_b}$ $\hat{q} = \frac{q}{\Omega}$ $\sigma = \frac{N_b c_b}{\pi R}$ $d_{x,hub} = l_n\sin(\eta) + d_{x,n}$ $d_{z,hub} = -l_n\cos(\eta) - d_{z,n}$ $\lambda_{qt} = \frac{q d_{z,cp}}{\Omega R}$ $\lambda_{qp} = \frac{q d_{x,cp}}{\Omega R}$
	Choose λ_i until $F(\lambda_i) = 0$
	$a_1 = f(\mu_{CP}, \lambda_{qt}, \lambda_{qp}, I_b, \theta_0, \lambda_{CP}, \lambda_i, \gamma, \Omega, q, K_\beta)$ (see Appendix A Equation A.2) $C_{T\,BEM} = \frac{NI_b\gamma}{4R^5\rho\pi}((\lambda_{qt}^2 - 2\mu_{CP}\lambda_{qt} + \mu_{CP}^2 + \frac{2}{3})\theta_0$ $-\frac{a_1\lambda_{qt}}{2} + \frac{a_1\mu_{CP}}{2} + \lambda_{qt} - \lambda_{CP} - \lambda_i)$ $C_{T\,GLAU} =$ $2\lambda_i\sqrt{(\frac{V}{\Omega R}cos(\alpha_{CP} - \alpha_1))^2 + (\frac{V}{\Omega R}\sin(\alpha_{CP} - \alpha_1) + \lambda_i)^2}$ $F(\lambda_i) = C_{T\,BEM} - C_{T;\,GLAU}$

continues on next page

	$a_0 = f(\mu_{CP}, \lambda_{qt}, \lambda_{qp}, I_b, \theta_0, \lambda_{CP}, \lambda_i, \gamma, \Omega, K_\beta)$ (see Appendix A Equation A.1)
	$b_1 = f(\mu_{CP}, \lambda_{qt}, \lambda_{qp}, I_b, \theta_0, \lambda_{CP}, \lambda_i, \gamma, \Omega, q, K_\beta)$ (see Appendix A Equation A.3)
	$T = N_R C_{T\ BEM} \rho \Omega^2 \pi R^4$
	$H = f(I_b, N_b, \gamma, \mu_{CP}, \theta_0, a_0, a_1, b_1, \lambda_i, \hat{q}, \lambda_{qp}, \lambda_{qt}, q, \Omega, \lambda_{CP}, R, c_R, \rho, C_{l_\alpha}, C_{d_{0,b}}, C_{d_{1,b}}, C_{d_{2,b}})$ (see Appendix A Equation A.4)
	$M_{K\beta} = \frac{N_R N_b K_\beta a_1}{2}$
	$D_f = \frac{1}{2}\rho V^2 A_{eq}$
	$\theta_{DP} = \theta_c - a_1 - \eta$
State equations	$\dot{u} = -g\sin(\theta_f) - \frac{D_f}{m}\cos(\alpha_f) + \frac{T}{m}\sin(\theta_{DP}) - \frac{H}{m}\cos(\theta_{DP}) - qw + \frac{X_w}{m} + \frac{X_{hs}}{m}$
	$\dot{w} = g\cos(\theta_f) - \frac{D_f}{m}\sin(\alpha_f) - \frac{T}{m}\cos(\theta_{DP}) - \frac{H}{m}\sin(\theta_{DP}) + qu + \frac{Z_w}{m} + \frac{Z_{hs}}{m}$
	$\dot{q} = \frac{T}{I_y}(\sin(\theta_{DP})d_{z,hub} - \cos(\theta_{DP})d_{x,hub}) - \frac{H}{I_y}(\cos(\theta_{DP})d_{z,hub} + \sin(\theta_{DP})d_{x,hub}) + \frac{M_{K\beta}}{I_y} + \frac{M_w}{I_y} + \frac{M_{hs}}{I_y} + \frac{Z_w d_{x,w} - X_w d_{z,w}}{I_y} + \frac{Z_h d_{x,hs} - X_{hs} d_{z,hs}}{I_y}$
	$\dot{\theta}_f = q$

2.3.2. GTRS Model

Ferguson [8] documented the Generic Tilt-Rotor Simulation (GTRS) model, a real time model that can be used in support of aircraft design, pilot training and flight testing. The model is mainly based on 1/5 model scale wind-tunnel test data, in combination with basic physical equations and correction factors. The model consists of more than 20 different modules that account for different subsystems within the aircraft, such as the fuselage, the wings, the rotors, the landing gear, the SCAS, the engines and the horizontal and vertical stabilizers.

The model has been validated with XV-15 flight test data [6]. Due to its high level of detail and accuracy the model is often used as the baseline of current tiltrotor research and development activities. It contains many lookup tables including among others the effects of angle of attack, nacelle angle, sideslip, Mach number and flap defection on the aerodynamic coefficients and they contain the correction factors to the dynamic response of the aircraft. The GTRS data is also often used to validate the stability characteristics of a tiltrotor model. Ferguson included many tables containing the the stability and control derivatives of the XV-15 under different flight conditions, nacelle angles and velocities.

The mathematical was originally developed by Bell Helicopter Textrom (BHT), also under a contract of NASA, for the Bell Model 301 Tilt Rotor Research Aircraft. This real-time model, documented by Harendra et al. [16], was developed to support tiltrotor design, pilot training and flight testing. The model was developed with as much precision as possible, representing the kinematic, dynamic and aerodynamic characteristics of the Model 301. The model development was constrained by two important factors. Firstly the fast loop computational time had to be less than 50 milliseconds in order to maintain real time simulation. For this reason, the rotor representation was limited to steady, linearized aerodynamics with uniform inflow. Compressibility effects and rotor stall were only used to define a maximum rotor thrust coefficient limit, and

further not considered not in the model. This has the consequence that the rotor model is accurate enough for most handling qualities studies, but not sufficiently adequate to evaluate certain flight conditions where stall and compressibility effects are significantly present. Secondly, the rigorousness of the model is limited due to the lack of available validation data. For example, the rotor interference at the wing and tail were not properly tested at the time of the development of the model.

Ferguson used this model as the foundation for the GTRS model, but made quite a lot of changes to both the model and the report structure. Ferguson had a lot more data at his disposal coming from XV-15 flight tests, and he used this data to revise and improve the equations of the BHT model. He used the XV-15 flight test data together with multiple other program data to validate the results, and the deficiencies that were found were corrected for. In order to keep the GTRS model real-time, Ferguson was not able to solve the stall and compressibility deficiencies that were part of the BHT model. The rotor wake-airframe aerodynamic interactions are however significantly improved in the GTRS model, using XV-15 test data.

2.3.3. FLIGHTLAB Model

At the University of Liverpool, a multi-body modelling environment called FLIGHTLAB has been developed, which provides a modular approach for creating flight dynamics models. This tool enables the user to create a complete vehicle model from a library of predefined components. FLIGHTLAB was originally developed for rotorcraft, using blade element theory (BEM) models, but has been further developed to also support fixed-wing aircraft. Based on the BHT model [16], a FLIGHTLAB model of the XV-15 has been developed, the FXV-15. The development of the multi-body dynamics model has been extensively described by Padfield [2]. The main components of the FXV-15 have been divided into subcomponents, which in turn have been further split into even smaller components. At the lowest sub-branche, the components have been modelled and using multiple body dynamics (MBD) FLIGHTLAB assembles all components into one system. The hub and rotor system are modelled as a rigid gimbal combined with torsional spring-damping components allowing motion in pitch and roll directions. FLIGHTLAB neglects the coning and the first harmonic flapping motion due to the blade flexibility and only models lower frequency flapping due to the motions of the gimbal. The Peters-He three-state inflow model is used for the FXV-15, which is derived from the general Peters-He finite-state model. Twist, chord, inertia, sweep and droop are included in the blade modelling.

The rotor wake on the wing and empennage are derived from wind tunnel tests. The rotor wake on the horizontal stabilizers causes an upwash during low-speed helicopter flight, and a downwash during high-speed flight in airplane mode, according to Padfield. This rotor wake has a significant influence on the stability of the tiltrotor, and may cause a pitching moment or sideslip. The wake also affects the directional stability due to interactions with the vertical stabilizer.

The FXV-15 is validated performing trim, stability and response analyses and comparing the results with the among other the GTRS model [8] and the SID model [17]. The stability results are discussed in more detail later in this report, but proved to be quite accurate. For this reason, the FXV-15 is taken as the baseline configuration in the 'Rotorcraft Handling, Interactions and Loads Prediction' (RHILP) project [18]. The RHILP project is one the first projects to develop handling qualities criteria for a civil tiltrotor. The tiltrotor design concept that was used besides the FXV-15 during this project is the EUROTILT configuration, developed by Eurocopter. Because of the promising results of the FXV-15, a FLIGHTLAB model of this tiltrotor has been created as well, used to study tiltrotor handling qualities.

Walker and Perfect [19] analysed the longitudinal stability and control of a Large Tilt-Rotor (LTR). The research contains the modelling of a large tiltrotor and consequently using this model to improve the handling qualities of the aircraft. The model has been developed using FLIGHTLAB as well. Consequently the model is tested using HELIFLIGHT, which is a real-time piloted simulation facility, located at the university of Liverpool. The focus of this research is mainly limited to conversion mode, and only the longitudinal modes of the aircraft are assessed. It was found that the handling qualities of the large tiltrotor are characterized by poor predictability, which is mainly due to the pitch drop back phenomenon. Instability occurs in low-speed helicopter mode.

2.3.4. JANRAD Model

Klein [20] investigated the linear state space modeling of a tiltrotor by modifying an existent MATLAB model which is used for conventional helicopter stability analysis. This software model, called JANRAD (Joint Army-Navy Rotorcraft Analysis and Design) takes in the physical and aerodynamic characteristics of a rotorcraft as inputs and generates performance, stability and control data based on these inputs. The tiltrotor in helicopter mode has similar characteristics as a conventional helicopter, so for analysis in helicopter mode the JANRAD model already had most of its important parameters included. The only parameter that needed to be added was a flapping spring constant. The flapping of the rotor blades in a gimballed rotor system is constrained by centrifugal force, and in most designs also by a flapping spring. This spring produces additional significant moments when the blades flap. In airplane mode a lot more parameters needed to be added. The wing, fuselage and tail parameters which were included were not sufficient to accurately model a tiltrotor so these needed to be modified. Completely new routines needed to be written to analyse the stability characteristics of the tiltrotor in airplane mode because the dynamics differ so much from conventional rotorcraft. Separate trimming and linearization routines were written for the helicopter and airplane modes because their dynamics are very different. To simplify the modelling process, several assumptions were made. The body of the tiltrotor is assumed to be rigid, and the effects of the rotor wake on the fuselage were neglected. In order to verify the model, four analysis methods were used:

1. Stability and control derivatives comparison
2. Eigenvalue comparison of the linear system A matrix.
3. Frequency response comparison.
4. Time response comparison to various inputs.

The model is validated using XV-15 data and by comparing the results with two other models; Ferguson's GTRS [8] and an airframe state space model of the V-22. Although this model is a lot simpler than many higher order models such as the GTRS, the results proved to be fairly accurate. The conversion mode is however not addressed in this project.

2.3.5. HeliUM Model

Berger et al. [3] investigated the trim data, linearized control and stability derivatives and eigenvalues of two types of aircraft: a lift offset coaxial rotorcraft and a tiltrotor. The generic models of both rotorcraft were developed using HeliUM, which is a comprehensive rotorcraft simulation code that uses a finite-element approach to model flexible rotor blades with nonlinear coupled torsion, lag and flap dynamics to capture the aerodynamic, inertial and structural loads along each blade segment. The two aircraft configurations are build within the model using a multi-body-like approach, combining all aircraft independent subsystems. The coaxial model has been validated against the Sikorsky X2 GenHel model, while the tiltrotor has been validated against XV-15 flight data, the GTRS model and a CAMRAD II model of the Large Civil Tiltrotor (LCTR), which will be described later in this section. As the main topic of this research is the stability characteristics of a tiltrotor a further description of the coaxial rotorcraft model is left out of this review.

The generic tiltrotor configuration developed in this research is a combination of the XV-15, V22 Osprey and the NASA Large Civil Tilt-Rotor 2 (LCTR2)[21]. A render of the configuration is shown in Figure 2.4. The configuration has a stiff in-plane hingeless rotor system with 4 rotor blades. The airfoil is similar to the LCTR2, while the baseline properties for twist and chord are taken from the XV-15 but slightly tuned to be more consistent with trends of current more advanced tiltrotors, which use a stiffer but lighter rotor system. The wings do not have any forward sweep, but have inboard flaps and outboard ailerons just like the XV-15. The inflow model which is used for this configuration leaves the wake of each rotor isolated, impinging on the wing which results in an additional down force. Instead of a horizontal tail plane combined with two vertical tails which we know for the XV-15, this configuration uses a V-tail, which properties come from lookup tables of representative airfoils. The flaperons on the tail can deflect symmetrically creating a pitching moment or asymmetrically inducing a yawing moment, combining the tasks of the elevators and the rudders respectively. The nacelle angle ranges from 0 degrees in airplane mode to 95 degrees in helicopter mode.

After completion of the trim, the models were linearized in order to assess their stability characteristics. The tiltrotor linearized model contains nine rigid-body states, together with four second-order rotor states per

Figure 2.4: The generic tiltrotor model developed in HeliUM [3]

blade, three inflow states per rotor and two second-order nacelle rotational dynamic states per nacelle. In addition to these in total fifty-one states the model has ten inputs; symmetric longitudinal and lateral cyclic and collective, differential longitudinal cyclic and collective, deflection of the aileron, elevator and rudder and the torque of both nacelles. The reduced form of this linearized model together with its states and inputs is shown below:

$$\dot{x} = Ax + Bu \tag{2.1}$$

$$x = [u, v, w, p, q, r, \phi, \theta, \psi] \tag{2.2}$$

$$u = [\theta'_{1s}, \theta'_{1c}, \theta'_0, \Delta\theta_{1s}, \Delta\theta_0, \delta_a, \delta_e, \delta_r, Q_{nac_1}, Q_{nac_2}] \tag{2.3}$$

The two nacelle inputs were transformed to symmetric (δ_{nac}) and differential ($\Delta\delta_{nac}$) angles before further analysis was done. The further analysis contains the analysis of the trends of the stability and control derivatives with airspeed for six different nacelle angles: 0, 30, 60, 75, 90 and 95 degrees. Furthermore, the blade natural frequencies and deflections are analysed and the eigenvalues and modes are investigated.

2.3.6. Other Models

One of the first successful flight dynamics models for tiltrotors has been developed by Tischler [17]. Tischler has developed a flight dynamics model using frequency domain identification technology. The XV-15 bare-airframe dynamics have been evaluated and documented, and the results of the simulation model have been compared with actual flight test data. In total four different flight conditions have been compared, from hover to cruise. This model, however, has been verified by comparison of trim data, and the stability analysis has been left as a recommendation for later research.

Many years later Tischler wrote a book on aircraft and rotorcraft system identification [22]. In this book, Tischler explains the procedures of system identification, and presents example results of handling qualities and flight control analyses of different types of rotorcraft and fixed-wing aircraft. One of these example rotorcraft is the XV-15. Tischler also treats amongst others state space model identification, and produces state space matrices which are then validated with GTRS model data.

Johnson [23] investigated the dynamics of tilting proprotor aircraft in cruise flight. For this purpose, a nine degrees of freedom theoretical model is developed for dynamic analysis of a proprotor mounted on a cantilever wing operating at high velocity. The nine degrees of freedom contain the longitudinal and lateral cyclic flap, the longitudinal and lateral cyclic lag, the collective flap and lag and the wing vertical bending, chordwise bending and torsion. The cyclic and collective pitch controls serve as input to the model, together with three-dimensional gust perturbations. Johnson also investigates the contribution of the proprotor to the stability derivatives of the aircraft by deriving analytical expressions. In contrary to other literature about tiltrotor stability derivatives, Johnson uses more classical airplane derivatives instead of helicopter derivatives, which entail the forces and moments due to angle of attack and sideslip, e.g. C_{l_β} and C_{z_α}.

Kleinhesselink [12] attempted to create an open-source model of a tiltrotor, using basic equations of motion. This model is focused on the control and stability characteristics of the XV-15 tiltrotor and uses simple

linear analysis. The features of the model are based on the minimum required model complexity for piloted simulation for handling qualities, as defined by Heffley and Mnich [24]. The most important features of this model entail the all rigid-body degrees of freedom, the first-order flapping dynamics of the rotor and the first order main rotor induced velocity approximations. The rotor was modelled as an articulated rotor, meaning that there is no lead-lag degree of freedom. Furthermore, the model includes blade twist, hinge offset and a flapping spring. The model has 6 degrees of freedom, meaning that there are forces and moments along 3 axis, which are used in conjunction with the nonlinear rigid body Euler equations of motion. In this model no correction or scaling factors are used to obtain a better comparison with actual flight data. The analysis included a trim- and time history solution, whereafter the model was linearized. All steps of the analysis included validation using the GTRS. During the linearization process the stability and control derivatives were determined for several nacelle angle and airspeed combinations. The A and B matrices, which contain the stability and control derivatives respectively were constructed. Using the A matrix, the eigenvalues could be determined which are then compared with the GTRS data roots during hover in helicopter mode and 200 kts in airplane mode.

Lu et al. [4] developed a nonlinear flight dynamics model for tiltrotor aircraft and investigated its dynamic stability characteristics. The analysis conducted in the research is performed using XV-15 data. Lu et al. modelled several tiltrotor subsystems separately and combines them to form the full model. The most challenging subsystem to model is the rotor. The XV-15 has two 3-bladed gimballed rotors. The motion of the gimballed hub relative to the rotor shaft has two degrees of freedom; the longitudinal tilt angles and lateral tilt angles. This is something that we also see for articulated blades, making them in some sense similar. Therefore, Lu et al. decided to model the gimballed hub system as an articulated system, just like Kleinhesselink [12]. Furthermore, the wing is modelled using functions dependent on angle of attack, nacelle angle and flap setting. The effect of the rotor wake on the wing is also included. The empennage is modelled similar to the wings, also including the downwash due to the wing and the rotors. The full flight dynamics model includes 47 states, of which 26 are rotor inflow states, 12 are flapping motion states and 9 are rigid-body aircraft states. Validation is firstly executed through comparison of the trim results with the GTRS. Secondly, the model is linearized resulting in a reduced model with only the 9 aircraft states and 4 control inputs:

$$\dot{x} = Ax + Bu \tag{2.4}$$

$$x = [u, v, w, p, q, r, \phi, \theta, \phi] \tag{2.5}$$

$$u = [\delta_{coll}, \delta_{long}, \delta_{lat}, \delta_{ped}] \tag{2.6}$$

By comparison of the eigenvalues of the **A** matrix from Equation 2.4 with results from flight tests and the GTRS, the model is further validated. With the eigenvalues conclusions can be drawn about the dynamic modes of the tiltrotor. The Dutch roll and phugoid are unstable in helicopter mode. In airplane mode, all eigenmodes are stable.

Lu et al. also analyse the tiltrotor speed stability. This speed stability stability defines the relationship between the forward speed and the longitudinal stick. Positive speed stability is required for cyclic control, as defined by ADS-33E-PRF handling quality requirements [25]. This means that pushing the cyclic stick forward should result in an increase in flight speed. Four different nacelle angle cases were analysed, and their migration of the longitudinal stick with respect to speed is shown in Figure 2.5. It can be observed that the requirement is not met for an increase in velocity between 20 and 40 knots in helicopter mode, as this requires pulling the cyclic stick. This occurs mainly due to the aerodynamic interference of rotor wake and horizontal stabilizer. The dotted line in the figure shows a conversion path from helicopter mode to airplane mode. It can be seen that the speed stability is positive when the aircraft is converting from helicopter mode to conversion mode with a nacelle angle of 60 degrees. However, when converting from this condition, through 140 knots with a 30 degrees nacelle angle, to 160 knots in airplane mode, the longitudinal cyclic migrates aft. This results in negative speed stability. This feature can be explained by the increase of the efficiency of the elevator with increasing flight speed. This feature is also mentioned by Kleinhesselink [12].

NASA [21] [26] developed the 'Large Civil Tilt-Rotor' concept. The project started with the Large Civil Tilt-Rotor (LCTR), but has evolved into an even newer concept: the LCTR2. The LCTR2 is intended to

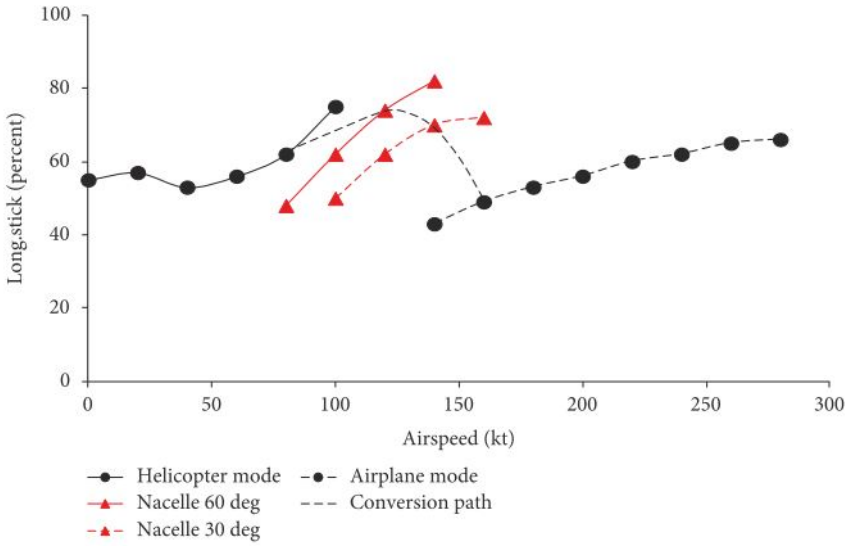

Figure 2.5: Migration of longitudinal stick w.r.t. airspeed [4]

replace regional medium range airliners, with a passenger capacity of 90, a cruise speed of 300 knots and a range of over 1000 nautical miles. A high-fidelity flight dynamics model model has been developed which also incorporates flexible wing dynamics. This model is validated against XV-15 test data and against the GTRS model. This research is however mainly focused on the flight dynamics modelling, control system architecture and the handling qualities of a tiltrotor, and less on the dynamic stability characteristics of the aircraft.

2.4. Aircraft Stability

The stability of an aircraft can be viewed as the problem of finding an equilibrium state and maintaining this equilibrium while coping with all types of perturbations from all different directions. A body is said to be in equilibrium when the net forces and net moments acting on the body all equal zero. This means that there are no accelerations acting on the body and all states are kept constant. The aspects of aircraft stability can be divided into static stability and dynamic stability. Respectively, both will be addressed in the upcoming two subsections.

2.4.1. Static stability

An aircraft response to a perturbation in one of the states is defined statically stable when the initial tendency to that perturbation is toward the equilibrium state. However, if the aircraft increases the orientation following the disturbance, the aircraft is said be statically unstable. If the aircraft changes attitude following a disturbance and retains in this new orientation without further changes in attitude, the aircraft is said to be statically neutral.

In Figure 2.6 the different static stability cases are depicted for an aircraft that is disturbed about the pitching axis. Subfigure (a) shows the aircraft in equilibrium state in steady horizontal flight. In subfigure (b) a disturbance occured causing the angle of attack of the aircraft to increase. After the disturbance, the angle of attack keeps on increasing instead of returning to the original state, meaning the airplane is statically unstable. In subfigure (c) a similar disturbance occured causing the angle of attack to increase. The aircraft maintains this new attitude and a new equilibrium state is found. This is an example of statically neutral aircraft.

2.4.2. Dynamic stability

The dynamic stability of an aircraft describes how an aircraft behaves over time following a disturbance. When an aircraft is statically stable, there are three different types of oscillatory motions it may undergo

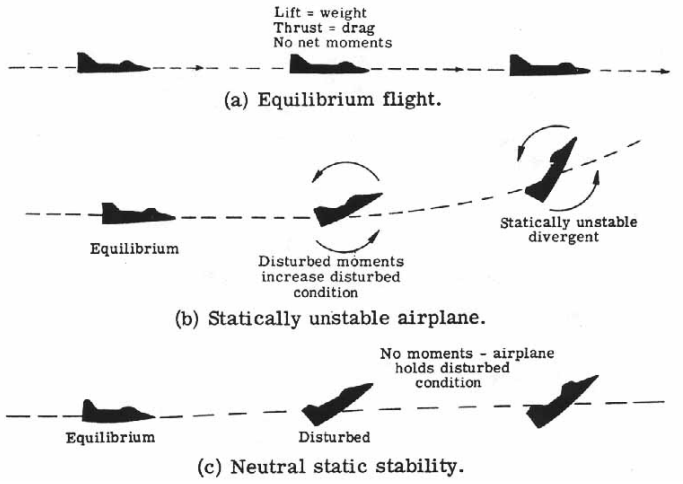

Figure 2.6: Static stability

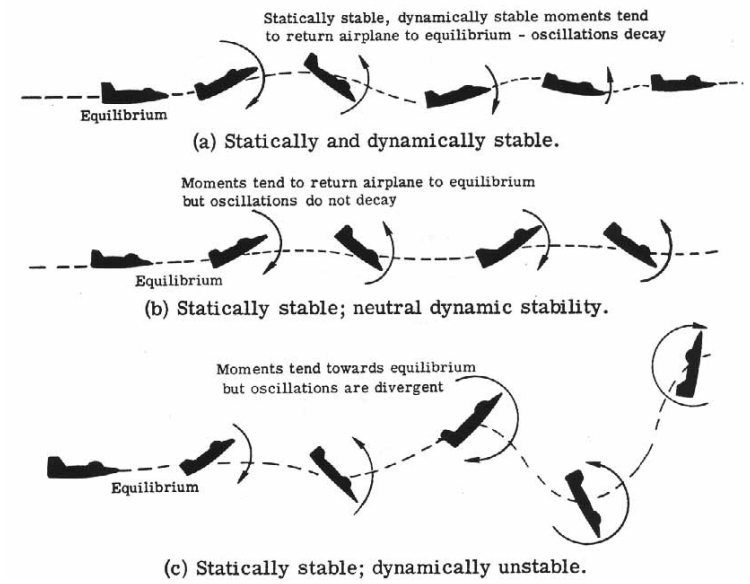

Figure 2.7: Dynamic stability

after a perturbation. If the magnitude of the oscillations decreases over time and the aircraft returns to its original equilibrium the vehicle is said to be dynamically stable. However, if the magnitude of the oscillations increases over time the equilibrium position will never be reached again without interference by the pilot the aircraft is dynamically unstable. If the oscillations are neither damped nor increasing, a dynamically neutral state is reached by the aircraft.

In Figure 2.7 the three different types of dynamic stability are depicted using the same disturbance example as in the previous subsection about static stability. In subfigure (a), the aircraft is dynamically stable since the pitching oscillations decrease and the same equilibrium state is reached over time. In subfigure (b) the magnitude of the oscillations is constant over time meaning that the aircraft is dynamically neutral. In subfigure (c) the vehicle is dynamically unstable; the oscillations increase over time, eventually reaching angles of attack which are very dangerous to fly under.

The dynamic responses experienced by an aircraft can be further divided into five different types. These five types are also known as the dynamic modes of the aircraft, and play a very important role in stability analysis. There are 2 longitudinal and 3 lateral/directional dynamic modes. All five will be briefly discussed hereafter.

Phugoid

The first longitudinal dynamic mode is called the phugoid. The phugoid is an oscillatory mode with a variation of airspeed, pitch angle and altitude over time. This basically means that the motion consists of a coupling between a pitch and surge subsidence, which is why the phugoid is sometimes referred to as the 'pitch-surge' mode. The mode has a large period because of which the angle of attack remains almost constant over time. There is a very slow interchange between kinetic and potential energy during the mode, while the aircraft attempts to restore the steady horizontal equilibrium state. For conventional helicopters, the phugoid is often unstable, primarily at low airspeeds [27]. For airplanes, the mode is most often stable and easily controlled by a pilot [28]. The difference between the two lies in the stability derivative M_u. Helicopters often have a positive M_u value, which destabilizes the mode. For airplanes, the M_u is often approximately zero for subsonic speeds. The moments from all aerodynamic surfaces are proportional to dynamic pressure and tend to cancel eachother out [2]. A tiltrotor in hover has a lot of helicopter stability characteristics. Because the aerodynamic surfaces do not contribute to the stability when the airspeed is zero, the phugoid of the tiltrotor is also unstable in hover. As airspeed increases the tiltrotor starts to behave more like an airplane and the phugoid stabilizes [3].

Short Period

The second longitudinal mode is called the short period, and as the name already suggest, is an oscillatory mode with a relatively short period. The short period is a rapid pitching motion with a variation in pitching rate and angle of attack, but with almost constant velocity. In hover and low airspeeds the VTOL short period is decoupled into non-oscillatory heave and pitch subsidences. This happens because the pitch-heave coupling derivative M_w is very small [2]. For airplanes this decoupling does not occur because they only operate at relatively high airspeeds. For both helicopters and airplanes the short period is usually a heavily damped stable mode. For airplanes, the damping of the short period is mainly provided by the horizontal tailplane. [28]. A tiltrotor also experiences the decoupling of the heave and pitch subsidences at low airspeeds. At high airspeeds the tiltrotor short-period is highly damped and oscillatory [3].

Roll Subsidence Mode

The roll subsidence mode is a lateral dynamic mode, and is simply the damping of the rolling motion. A damping moment should be created by the aircraft in order to damp an induced roll rate, preventing roll rates from building up. For both helicopters and airplanes the mode is stable, and the damping increases with airspeed. The same holds for the tiltrotor.

Spiral Mode

The spiral mode is a non-oscillatory lateral/directional mode which combines roll, yaw and sideslip. The mode usually happens so slow that it can not be sensed by the pilots, but only perceived visually. The spiral mode for conventional helicopters at low speeds is usually primarily a yawing motion only dependent on N_r. Since N_r is a damping derivative the spiral is a stable mode and equilibrium is restored by the helicopter itself [2]. The dihedral effect is destabilizing the spiral mode [29], and this effect is much more prominent for fixed-wing aircraft than for conventional helicopters. Therefore, airplanes and tiltrotor often experience an unstable spiral mode. However, the mode usually happens so slow that this is not considered a big problem.

Dutch Roll

The Dutch Roll mode is an oscillatory lateral/directional mode which consists of a combination of yawing, rolling and sidesliping motion. For VTOL aircraft in hover the Dutch roll mainly consists of a coupling between roll and sway, and the mode is often referred to as the 'lateral phugoid' because of its similar character as the longitudinal phugoid [3]. The Dutch Roll has quite a short period and is usually lightly damped. The mode is often considered an undesirable mode since it interferes with the pilot's ability to hold a trim. Besides this, the mode is quite unpleasant for passengers [27]. The Dutch roll is strongly influenced by the yaw damping and the dihedral effect, of which the former is stabilizing and the latter destabilizing. A conventional helicopter often has high yaw damping due to its tail rotor and the dihedral effect is small because of the absence of wings. Therefore, the Dutch roll is most often stable for helicopters [2].

For an airplane, the Dutch roll mode is the more or less the lateral/directional equivalent of the short period. The moments of inertia in pitch and yaw or an airplane are of similar magnitude and therefore is the frequency of the two modes of similar order. However, the fin which damps the Dutch roll is less effective in damping than the tail plane which damps the short period. Therefore, the Dutch roll is more lightly damped. Nevertheless, the mode is most often stable for airplanes [28]. For a tiltrotor, the Dutch roll damping is provided by the vertical stabilizers. This creates a lightly-damped but stable mode at moderate to high airspeeds. At low airspeeds, the aerodynamic efficiency of the vertical stabilizers is low and not enough yaw damping is created. The destabilizing dihedral effect is more dominant in hover and at low airspeeds which causes an unstable Dutch roll [2].

3

Non-linear Model

In this chapter the non-linear six-degrees-of-freedom tiltrotor flight dynamics model, from now on referred to as 6-DoF model, will be described. The basis of this model has been developed by Sokolowski and is modelled in MATLAB [30]. The model serves as the main model for the stability analysis conducted in the research described in this report. This chapter contains a general description of the model and a schematic overview of the equations describing the dynamics. If the reader is interested in a more thorough explanation about the underlying equations, he/she is referred to the report by Sokolowski. Multiple changes have been made to the 6-DoF model in order to increase the accuracy of the stability analysis results. These changes will also be elaborated upon in this chapter.

In the first section of this chapter a global description of the 6-DoF is given. The second section elaborates upon the assumptions made during the modelling process. The third section describes the different modules of which the 6-DoF model consists and gives a schematic representation of the underlying equations.

3.1. Model Description

In general, the flight dynamics model describing the motion of an aircraft takes the following non-linear form:

$$\dot{\mathbf{x}} = f(\mathbf{x}, \mathbf{u}, t) \tag{3.1}$$

where $\mathbf{x}$ denotes the state vector, $\mathbf{u}$ denotes the input vector and t is the response time. The block diagram in Figure 3.1 depicts the top-level structure of the 6-DoF model. The required inputs for the model are shown in the green blocks. Firstly, some environmental parameters are required. The aerodynamic forces are dependent on the air density ρ and gravitational forces are dependent on the gravitational acceleration g. Secondly, the inputs of the pilot are required. These inputs contain the collective stick deflection X_{COL}, the longitudinal and lateral cyclic stick deflections X_{LON} and X_{LAT} and the pedals deflection X_{PED}. The input vector u therefore looks as follows:

$$\mathbf{u} = [X_{COL}, X_{LON}, X_{LAT}, X_{PED}] \tag{3.2}$$

The tilt toggle, with which the pilot can control the nacelle angle, has not been integrated into the model yet. Thirdly, some general aircraft parameters are required as inputs. These parameters contain among others aircraft geometry parameters and derivatives describing the effect of the control surfaces deflections on the aerodynamic coefficients. Lastly, the initial states on the aircraft serve as input to the model. These states contain the translational velocities, rotational velocities and aircraft attitude. The state vector x has the following form:

$$\mathbf{u} = [u, v, w, p, q, r, \phi, \theta, \psi] \tag{3.3}$$

The 6-DoF model describes the motion of the tiltrotor body centre of gravity. The motion of the body is defined in the body reference frame ($\mathcal{F}_b$), which is a non-inertial rotating frame. The different components of the tiltrotor create separate forces and moments which all influence the general motion of the aircraft.

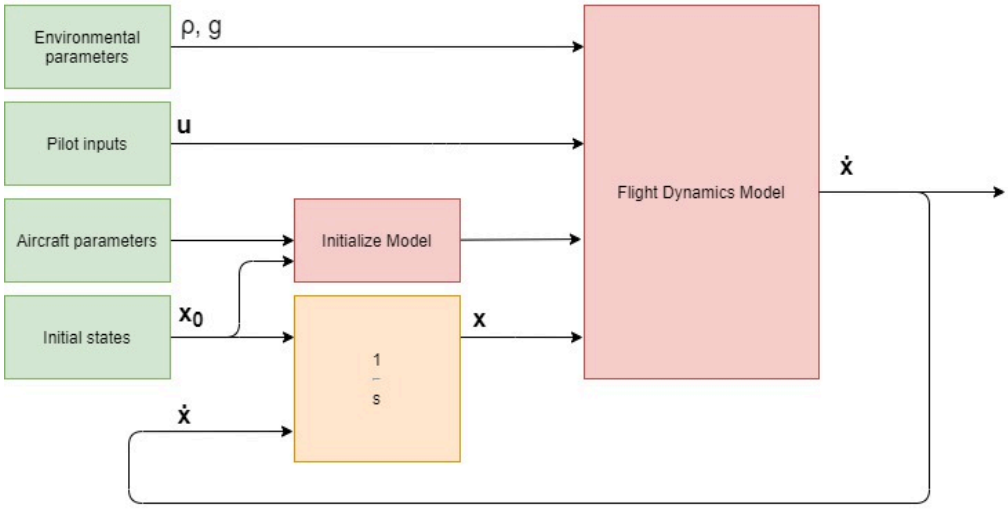

Figure 3.1: Top-level block diagram of the 6-DoF flight dynamics model

These forces and moments are often more easily defined in a reference frame aligned with the component itself instead of directly in ($\mathcal{F}_b$). Therefore the XV-15 has been split up in different components and for all components the forces and moments are calculated separately in their preferred reference frame. These forces and moments are then converted to the body reference frame using transformation matrices after which they can be summed up to compute the total resultant forces and moments acting on the aircraft. The 6-DoF model makes a distinction between 15 different components, which are all numbered in Table 3.1. The numbers in the table coincide with the numbers in Figure 3.2, which gives a clear overview which exact components are dealt with.

In order to compute the forces and moments created by the different components several modules have been constructed. A lot of components are very similar so not every component requires its own separate module. For example, each wing is separated in three different components. The only thing that distinguishes these components are the secondary control surfaces attached to them and their distance to the body centre of gravity. Therefore the calculations of the forces and moments are very similar. In Figure 3.3 a detailed block diagram of the 6-DoF flight dynamics model is given containing all the modules and the order in which all modules should be executed. Some components require the outputs of other components so therefore the order of calculation of all components is very important. At the top of each block the required module is given and at the bottom the components are given for which the module should be ran. In the end the sum of forces and moments of all components are gathered in the main module in which the equations of motion are derived. The output of this main module defines the behavior of the body centre of gravity. All modules will be elaborated upon in more detail later this chapter.

3.2. General Assumptions

In order to bound the scope of the model and to simplify the modelling process several general assumptions have been made. The assumptions which are component specific are discussed in the descriptions of the modules, which are elaborated upon in the next section. The most important general assumptions are listed below

- All subsystems of the tiltrotor are assumed to be rigid.
- The mass of tiltrotor is constant, although the longitudinal position of the centre of mass may vary.
- The geometry and mass distribution of the tiltrotor are symmetrical in the surge-heave plane.
- The simulation environment is defined by a flat, non-rotating Earth.
- Gravity is constant, and therefore the centre of mass coincides with the centre of gravity.
- The engine dynamics can be integrated into the model by changing the rotor gearing.

Table 3.1: The components considered in the 6-DoF model

Nr.	Component	Acronym
1	Articulated Rotor Left	ARL
2	Articulated Rotor Right	ARR
3	Wing Free, Left	WFL
4	Wing Free, Right	WFR
5	Wing Flap, Left	WFLL
6	Wing Flap, Right	WFLR
7	Wing Aileron, Left	WAL
8	Wing Aileron, Right	WAR
9	Horizontal Stabilizer, Left	HSL
10	Horizontal Stabilizer, Right	HSR
11	Vertical Stabilizer, Top Left	VSTL
12	Vertical Stabilizer, Top Right	VSTR
13	Vertical Stabilizer, Bottom Left	VSBL
14	Vertical Stabilizer, Bottom Right	VSBR
15	Fuselage	FL

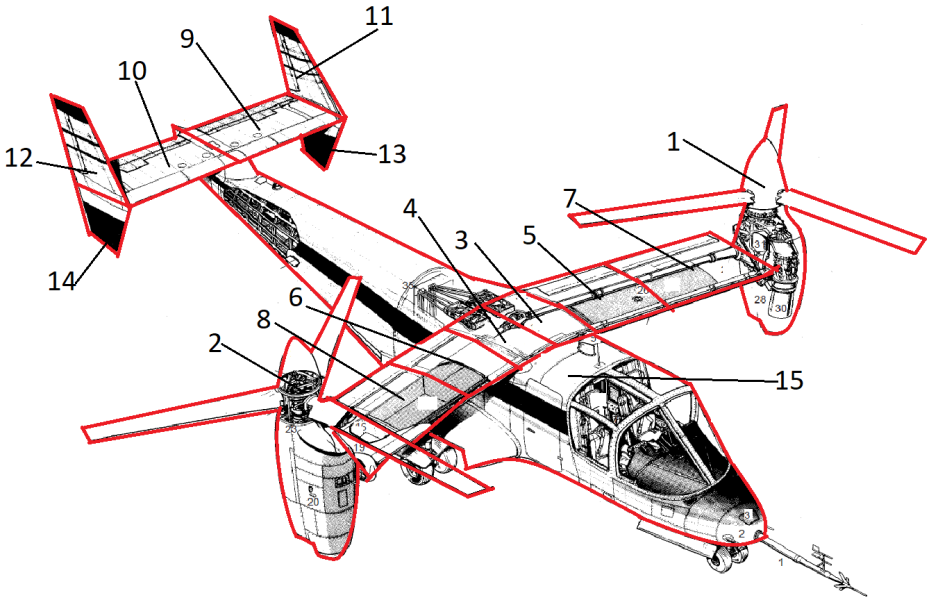

Figure 3.2: Schematic figure of the XV-15 with all separate components numbered [1]

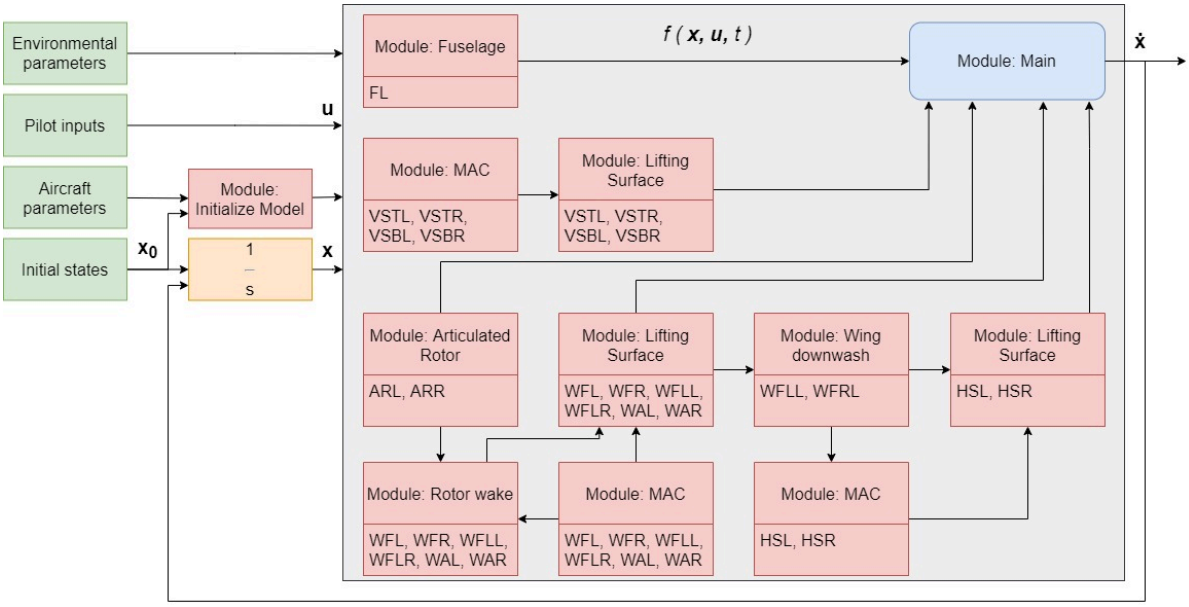

Figure 3.3: Detailed block diagram of the 6-DoF flight dynamics model

3.3. Modules

In this section all different modules of the flight dynamics model are elaborated upon. The inputs for each module are given as well as the aircraft components to which the modules apply. The specifics of each component are highlighted as well as the important outputs. Furthermore, if a variable in the right column of the module is **bold**, then we are dealing with a vector. This vector, with an x- y- and z-component, is defined in the reference frame indicated in the left column. For a more detailed description of the reference frames the reader is referred to the report by Sokolowski.

3.3.1. Module: Initialize Model

When modelling the flight dynamics of a tiltrotor aircraft, one should keep in mind that the rotation of the nacelles causes a significant shift in aircraft c.g. along the longitudinal axis. Often for simplicity's sake this nacelle shift effect on the c.g. is neglected and the helicopter c.g. is assumed for the entire conversion corridor [12]. The same goes for the moments of inertia, for which the H-mode MOI's are often used. This was also the case for the initial 6-DoF model. For the stability analysis the stability and control derivatives quite heavily depend on the moments of inertia and therefore it was chosen to integrate this effect of nacelle angle. Linear equations describing the moments of inertia as a function of mast angle β_m have been integrated in the model. The mast angle is 0 degrees in H-mode and 90 degrees in A-mode. Similarly, expressions describing the c.g. stationline (SL) and waterline (WL) have been integrated. These expressions are also a function of the mast angle. The moments of inertia changes with nacelle angle are shown in Figure 3.5. The SL and WL have been plotted as a function of nacelle angle in Figure 3.4.

The expressions mentioned above are integrated in the Initialize Model module, and the SL, WL and moments of inertia are used in other modules. Using the SL and WL the distances between the body c.g. and the components can be computed. As long as the nacelle angle is kept constant this module only has to be used once at the start of the simulation.

Furthermore, it is important to mention that the 6-DoF model uses a different definition of the nacelle than used throughout the rest of this report. In theory the nacelle angle equals 90 degrees in H-mode and 0 degrees in A-mode. In this model the nacelle angle has shifted 90 degrees; this means in helicopter mode the nacelle angle equals 0 degrees and in airplane mode -90 degrees. The mast angle however still equals 0 degrees in H-mode and 90 degrees in A-mode, which explains the relation $\beta_m = -\eta$ in the scheme below.

Input parameters	
Aircraft parameters	$W_P \quad GW \quad SL_{NPP} \quad WL_{NPP} \quad SL_P \quad WL_P \quad SL_{CG}\vert_{\beta_m=0} \quad WL_{CG}\vert_{\beta_m=0}$ $I_x\vert_{\beta_m=0} \quad I_y\vert_{\beta_m=0} \quad I_z\vert_{\beta_m=0} \quad J_{xz}\vert_{\beta_m=0} \quad KI1 \quad KI2 \quad KI3 \quad KI4$
Components parameters	$SL_c \quad WL_c \quad BL_c$
Aircraft states	η
Calculations	
$\mathcal{F}_b$	$\beta_m = -\eta$ $DX = \frac{W_P}{GW}(SL_{NPP} - SL_P)$ $DZ = \frac{W_P}{GW}(WL_{NPP} - WL_P)$ $DX_{CG} = DZ(\sin\beta_m) + DX(1 - \cos\beta_m)$ $DZ_{CG} = DZ(1 - \cos\beta_m) - DX(\sin\beta_m)$ $SL_{CG} = SL_{CG}\vert_{\beta_m=0} + DX_{CG}$ $WL_{CG} = WL_{CG}\vert_{\beta_m=0} + DZ_{CG}$ $I_x = I_x\vert_{\beta_m=0} - KI1\beta_m$ $I_y = I_y\vert_{\beta_m=0} - KI2\beta_m$ $I_z = I_z\vert_{\beta_m=0} + KI3\beta_m$ $J_{xz} = J_{xz}\vert_{\beta_m=0} - KI4\beta_m$ for every component 'c': $d_{x,c} = SL_c - SL_{CG}$ $d_{y,c} = BL_c$ $d_{z,c} = WL_c - WL_{CG}$

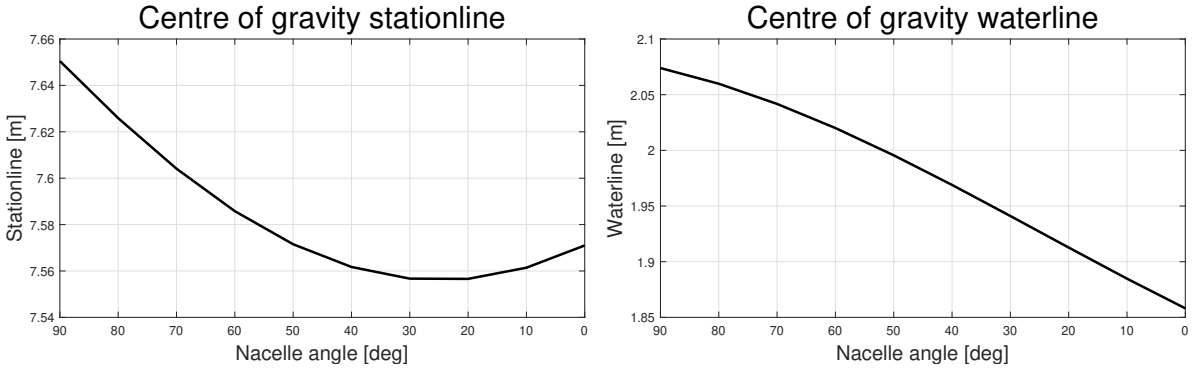

Figure 3.4: The shift of the centre of gravity as a function of nacelle angle

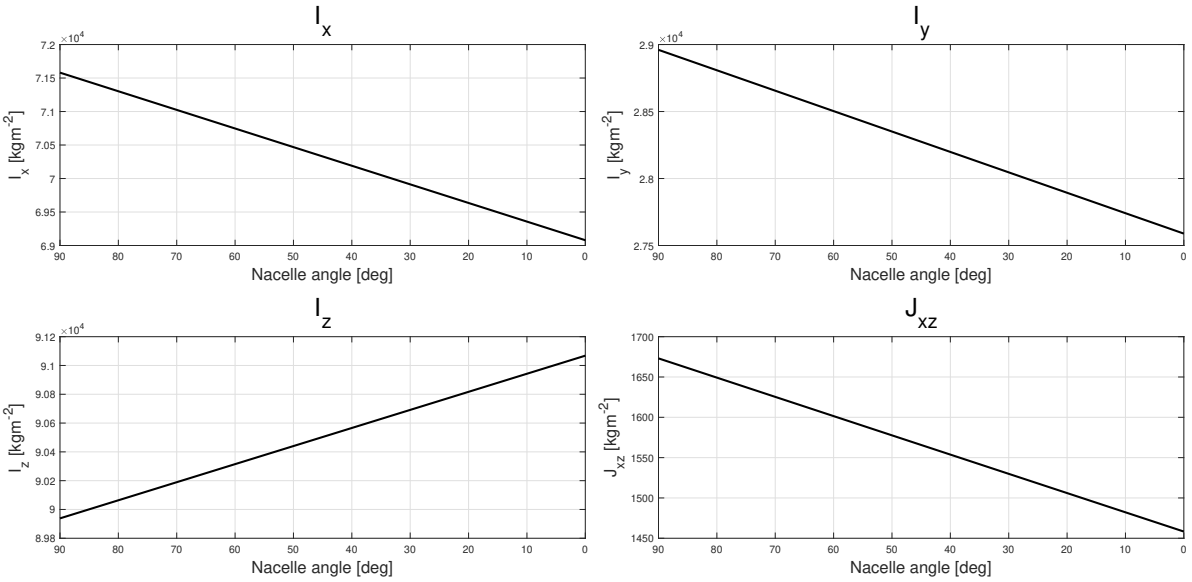

Figure 3.5: The moments of inertia as a function of nacelle angle

3.3.2. Module: Articulated Rotor

The articulated rotor module is, as the name already suggests, used to compute the forces and moments induced by the articulated rotor system. The XV-15 has two rotors, ARL and ARR, so the module should be ran for each rotor separately. The distinction between the two rotors is made by the inputs d_{sgn} and Ω_{sgn} which are both negative for ARL but positive for ARR. A few important assumptions have been during the modelling process:

- The rotor is modelled as an articulated hub with a flapping hinge and spring instead of a gimballed hub. No lead-lag hinge nor a hinge offset is modelled.
- The blade aspect ratio is high, air is incompressible.
- The rotor angular velocity Ω is constant when the nacelle angle is kept constant.
- Rotor-induced velocity is uniform across the rotor disk.
- The blade cross-section is constant along its length.
- Blade is treated as a slender rod in terms of mass moment of inertia.
- The Lift coefficient of the blade increases linearly with angle of attack.
- The aerodynamic centre of the blade is located at quarter-chord.
- The feathering axis of the blade coincides with with the aerodynamic centre.
- The aerodynamic forces created by the rotor nacelles are neglected.
- The inertial angular rates are equal to the aerodynamic angular rates.

The most inputs required for the module are rotor parameters. Furthermore, the distances from the body c.g. to the nacelle root are required. These distances are defined along the axes of the body reference frame. The force and moment vectors of the rotors are defined in the wind axis control plane $\mathcal{F}_{waCP}$. These vectors and then converted to the control plane reference frame $\mathcal{F}_{CP}$, after which they are converted to $\mathcal{F}_b$.

The force and moment vectors in $\mathcal{F}_b$ are used in module 'Main' to compute the resultant forces acting on the aircraft. Furthermore, distances from the body c.g. to the nacelle root and the induced velocity v_i are required in the module 'Rotor Wake'.

The rotor flapping angles and force/moment coefficients expressions have been derived in MAPLE by Sokolowski [30]. These angles and coefficients depend on many different variables, which lead to very extensive expressions. In order to keep the accuracy of the model as high as possible these expressions have not been simplified before they were implemented in MATLAB. In Appendix B the extensive expressions for

the flapping equations, the rotor forces and the rotor torque can be found. Besides the long expressions, for each variable a simplified short(er) version of the expression is included. These simplified versions have been included to make the equations more understandable and to be able to compare them with the equations that are known for a conventional helicopter. In order to simplify the expressions, the following assumptions have been made:

- The rate of change of the nacelle angle is negligible: $\dot{\eta} = 0$
- The sideslip angle is small, and can be set equal to zero: $\beta = 0$
- The longitudinal cyclic angle is small, and can be set equl to zero: $\theta_{1s} = 0$
- The hub accelerations are negligible: $a_{x,h} = a_{y,h} = a_{z,h} = 0$
- The higher order terms of the angular rates are negligible: $p^n = q^n = r^n = 0$ for n > 1
- The angular accelerations equal zero: $\dot{p} = \dot{q} = \dot{r} = 0$
- $\overline{\Omega}_{RZR} = \Omega_{sgn}$

Furthermore, the rotor solidity σ has been substituted into the expressions, with

$$\sigma = \frac{Nc}{R\pi} \tag{3.4}$$

The assumptions lead to a massive reduction in the amount of terms in the expressions. Although they have been simplified a lot, the accuracy of the equations does not decrease a lot since the fundamental terms have remained. This is although only true if the model is used for analysis in symmetrical flight. If the simplified tiltrotor equations are compared to the flapping and force equations of a conventional helicopter [31], they show a lot of similarities. The tiltrotor expressions are however more dependent on the yaw rate r, which is often neglected for helicopters. Besides that, the strong twisting of the tiltrotor blades significantly influences the flapping angles and rotor forces.

Input parameters	
Rotor parameters	$N \quad R \quad c_{bl} \quad \theta_{bl0g} \quad \theta_{bl0} \quad \theta_{bl1} \quad \Omega \quad I_{bl} \quad M_{bl} \quad K_\beta \quad C_{l_\alpha bl}$ $c_{d_0} \quad c_{d_1} \quad c_{d_2}$
Nacelle parameters	$d_{x,n} \quad d_{y,n} \quad d_{z,n} \quad l_n$
Environmental parameters	ρ
Control variables	$X_{COL} \quad X_{LON} \quad X_{LAT} \quad X_{PED}$
State variables	$u \quad v \quad w \quad p \quad q \quad r \quad \phi \quad \theta \quad \psi \quad \eta$
If:	
Left rotor	$d_{sgn} = -1 \quad \Omega_{sgn} = -1$
Right rotor	$d_{sgn} = 1 \quad \Omega_{sgn} = 1$
Transformation matrices	
$\mathcal{F}_b \rightarrow \mathcal{F}_{CP}$	$\mathbf{T}_{b2CP} = \begin{bmatrix} \cos\eta - \theta_{1s} & 0 & -\sin\eta - \theta_{1s} \\ 0 & 1 & 0 \\ \sin\eta - \theta_{1s} & 0 & \cos\eta - \theta_{1s} \end{bmatrix}$
$\mathcal{F}_{CP} \rightarrow \mathcal{F}_b$	$\mathbf{T}_{CP2b} = \mathbf{T}_{b2cp}^{-1}$

continues on next page

$\mathcal{F}_{CP} \rightarrow \mathcal{F}_{waCP}$	$\mathbf{T}_{CP2waCP} = \begin{bmatrix} \cos\delta & -\sin\delta & 0 \\ \sin\delta & \cos\delta & 0 \\ 0 & 0 & 1 \end{bmatrix}$
$\mathcal{F}_{waCP} \rightarrow \mathcal{F}_{CP}$	$\mathbf{T}_{waCP2CP} = \mathbf{T}_{CP2waCP}^{-1}$
$\mathcal{F}_{waCP} \rightarrow \mathcal{F}_{waDP}$	$\mathbf{T}_{CP2waDP} = \begin{bmatrix} \cos a_1 & 0 & \sin a_1 \\ \sin a_1 \sin b_1 & \cos b_1 & -\cos a_1 \sin b_1 \\ -\sin a_1 \cos a_1 & \sin b_1 & \cos a_1 \cos b_1 \end{bmatrix}$
$\mathcal{F}_{waDP} \rightarrow \mathcal{F}_{waCP}$	$\mathbf{T}_{waDP2waCP} = \mathbf{T}_{waCP2waDP}^{-1}$
Calculations	
$\mathcal{F}_b$	$\theta_{0,LL} = \theta_{0,R} + \theta_{0,mod}$ $\theta_0 = (\Psi_{col\rightarrow 0} X_{COL} + d_{sgn} \Psi_{lat\rightarrow 0} X_{LAT} + \theta_{0,LL}) \frac{pi}{180}$
	$\Psi_{lon\rightarrow 1s} = 2.1 \cos\eta$ $\Psi_{ped\rightarrow 1s} = cos\eta(\frac{1.2}{e^{0.1944u-8}+1} + 0.4)$ $\theta_{1s} = (\Psi_{lon\rightarrow 1s} X_{LON} + d_{sgn} \Psi_{ped\rightarrow 1s} X_{PED}) \frac{pi}{180}$
	$\overline{p} = \frac{p}{\Omega}$ $\overline{q} = \frac{q}{\Omega}$ $\overline{r} = \frac{r}{\Omega}$ $\dot{\overline{\eta}} = \frac{\dot{\eta}}{\Omega}$
$\mathcal{F}_{waCP}$	$\overline{\Omega}_{RZR} = \overline{p}\cos\eta \sin\theta_{1s} - \overline{r}\cos\eta cos\theta_{1s} - \overline{p}\sin\eta\cos\theta_{1s}$ $-\overline{r}\sin\eta\cos\theta_{1s} + \Omega_{sgn}$
	$V_{lon} = \cos\eta\cos\theta_{1s} u + \cos\eta\sin\theta_{1s} w - \cos\theta_{1s}\sin\eta w$ $-\cos\theta_{1s}\dot{\eta} l_n + \sin\eta\sin\theta_{1s} u - \cos\theta_{1s} l_n q$ $-\cos\eta\cos\theta_{1s} d_{z,n} q + \cos\eta\sin\theta_{1s} d_{x,n} q$ $-\sin\eta\sin\theta_{1s} d_{z,n} q - \cos\eta\cos\theta_{1s} d_{sgn} d_{y,n} r$ $+\cos\eta\sin\theta_{1s} d_{sgn} d_{y,n} p - \cos\theta_{1s}\sin\eta d_{sgn} d_{y,n} p$ $-\sin\eta\sin\theta_{1s} d_{sgn} d_{y,n} r - \cos\theta_{1s}\sin\eta d_{x,n} q$ $V_{lat} = v + d_{z,n} p - d_{x,n} r + \cos\eta l_n p - \sin\eta l_n r$ $V_{ver} = \cos\eta\cos\theta_{1s} w - \cos\eta\sin\theta_{1s} u + \cos\theta_{1s}\sin\eta u$ $+\sin\eta\sin\theta_{1s} w + \sin\theta_{1s}\dot{\eta} l_n + \sin\theta_{1s} l_n q$ $+\cos\eta\cos\theta_{1s} d_{x,n} q + \cos\eta\sin\theta_{1s} d_{z,n} q -$ $+\sin\eta\sin\theta_{1s} d_{x,n} q + \cos\eta\cos\theta_{1s} d_{sgn} d_{y,n} p$

continues on next page

	$+\cos\eta\sin\theta_{1s}d_{sgn}d_{y,n}r - \cos\theta_{1s}\sin\eta d_{sgn}d_{y,n}r$ $+\sin\eta\sin\theta_{1s}d_{sgn}d_{y,n}p - \cos\theta_{1s}\sin\eta d_{z,n}q$ $\delta = \arctan\frac{V_{lat}}{V_{lon}}$ $\hat{\mu}_c = \frac{V_{lon}}{\Omega R}$ $\hat{\lambda}_c = \frac{V_{ver}}{\Omega R}$ $\gamma_{bl} = \frac{\rho C_{l_\alpha} c R^4}{I_{bl}}$ $a_{x,h} = \cos\eta\dot{u} - \sin\eta\dot{w} - \dot{\eta}l_n - l_n\dot{q} - \cos\eta d_{z,n}\dot{q} - \sin\eta d_{x,n}\dot{q}$ $+\cos\eta\Omega^2 d_{x,n}\overline{q}^2 + \cos\eta\Omega^2 d_{x,n}\overline{r}^2 - \Omega^2\sin\eta d_{z,n}\overline{p}^2$ $-\Omega^2\sin\eta d_{z,n}\overline{q}^2 - \cos\eta d_{sgn}d_{y,n}\dot{r} - \sin\eta d_{sgn}d_{y,n}\dot{p}$ $-\cos\eta\Omega^2\sin\eta l_n\overline{p}^2 + \cos\eta\Omega^2\sin\eta l_n\overline{r}^2 - \cos\eta\Omega^2 d_{z,n}\overline{pr}$ $-\cos\eta^2\Omega^2 l_n\overline{pr} + \Omega^2\sin\eta d_{x,n}\overline{pr}$ $+\Omega^2\sin\eta^2 l_n\overline{pr} + \cos\eta\Omega^2 d_{sgn}d_{y,n}\overline{pq} - \Omega^2\sin\eta d_{sgn}d_{y,n}\overline{qr}$ $a_{y,h} = \dot{v} + d_{z,n}\dot{p} - d_{x,n}\dot{r} + \cos\eta l_n\dot{p} - \sin\eta l_n\dot{r} - \Omega^2 d_{sgn}d_{y,n}\overline{p}^2$ $-\Omega^2 d_{sgn}d_{y,n}\overline{r}^2 - \Omega^2 d_{x,n}\overline{pq} - \Omega^2 d_{z,n}\overline{qr}$ $-2\cos\eta\Omega^2\dot{\overline{\eta}}l_n\overline{r} - \cos\eta\Omega^2 l_n\overline{qr} - 2\Omega^2\sin\eta\dot{\overline{\eta}}l_n\overline{p}$ $-\Omega^2\sin\eta l_n\overline{pq}$ $a_{z,h} = \Omega^2 l_n\dot{\overline{\eta}}^2 + 2\Omega^2 l_n\overline{q\eta} + \cos\eta\dot{w}$ $+\sin\eta\dot{u} + \cos\eta d_{x,n}\dot{q} - \sin\eta d_{z,n}\dot{q} + \Omega^2 l_n\overline{q}^2 + \cos\eta\Omega^2 d_{z,n}\overline{p}^2$ $+\cos\eta\Omega^2 d_{z,n}\overline{q}^2 + \cos\eta^2\Omega^2 l_n\overline{p}^2 + \Omega^2\sin\eta d_{x,n}\overline{q}^2$ $+\Omega^2\sin\eta d_{x,n}\overline{r}^2 + \cos\eta d_{sgn}d_{y,n}\dot{p} + \Omega^2\sin\eta^2 l_n\overline{r}^2$ $-\cos\eta\Omega^2 d_{x,n}\overline{pr} - \Omega^2\sin\eta d_{z,n}\overline{pr}$ $-2\cos\eta\Omega^2\sin\eta l_n\overline{pr} + \cos\eta\Omega^2 d_{sgn}d_{y,n}\overline{qr}$ $+\Omega^2\sin\eta d_{sgn}d_{y,n}\overline{pq} - \sin\eta d_{sgn}d_{y,n}\dot{r}$
$\mathcal{F}_{waCP}$	Loop through λ_i until $F(\lambda_i) = 0$ $a_0 = f(\hat{\mu}_c, \hat{\lambda}_c, \overline{p}, \overline{q}, \overline{r}, \overline{\Omega}_{RZR}, \theta_{1s}, \eta, \delta, a_{x,h}, a_{y,h}, a_{z,h}, \Omega, I_{bl}, K_\beta, \gamma_{bl}, \theta_{bl0},$ $\theta_{bl1}, \Omega_{sgn}, R, \lambda_i, a_1, M_{bl}) + a_{0,pre}$ (see section B.1) $a_1 = f(\dot{p}, \dot{q}, \dot{r}, \hat{\mu}_c, \hat{\lambda}_c, \overline{p}, \overline{q}, \overline{r}, \dot{\overline{\eta}}, \overline{\Omega}_{RZR}, \theta_{1s}, \eta, \delta, a_{x,h}, a_{y,h}, I_{bl},$ $\gamma_{bl}, \theta_{bl0}, \theta_{bl1}, \Omega_{sgn}, R, \lambda_i, a_0, M_{bl})$ (see section B.2) $b_1 = f(\dot{p}, \dot{q}, \dot{r}, \hat{\mu}_c, \hat{\lambda}_c, \overline{p}, \overline{q}, \overline{r}, \dot{\overline{\eta}}, \overline{\Omega}_{RZR}, \theta_{1s}, \eta, \delta, a_{x,h}, a_{y,h}, I_{bl},$ $K_\beta, \gamma_{bl}, \theta_{bl0}, \theta_{bl1}, \Omega_{sgn}, R, a_0, a_1, M_{bl})$ (see section B.3) $C_{T\ BEM} = f(\rho, \hat{\mu}_c, \hat{\lambda}_c, \overline{p}, \overline{q}, \overline{r}, \overline{\Omega}_{RZR}, \theta_{1s}, \eta, \delta, I_{bl}, \gamma_{bl}, \theta_{bl0}, \theta_{bl1},$

continues on next page

	$\Omega_{sgn}, R, a_1, \lambda_i)$ (see section B.4) $C_H = f(\rho, \hat{\mu}_c, \hat{\lambda}_c, \overline{p}, \overline{q}, \overline{r}, \overline{\Omega}_{RZR}, \dot{\overline{\eta}}, \eta, \delta, \theta_{1s}, I_{bl}, \gamma_{bl}, \theta_{bl0}, \theta_{bl1}, \Omega_{sgn}, R, N,$ $C_{l_\alpha bl}, c_{d_0}, c_{d_1}, c_{d_2}, a_0, a_1, b_1, \lambda_i)$ (see section B.5) $C_S = f(\rho, \hat{\mu}_c, \hat{\lambda}_c, \overline{p}, \overline{q}, \overline{r}, \overline{\Omega}_{RZR}, \dot{\overline{\eta}}, \eta, \delta, \theta_{1s}, I_{bl}, \gamma_{bl}, \theta_{bl0}, \theta_{bl1}, \Omega_{sgn}, R, N,$ $C_{l_\alpha bl}, c_{d_1}, c_{d_2}, a_0, a_1, b_1, \lambda_i)$ (see section B.6)
$\mathcal{F}_{waDP}$	$\begin{bmatrix} -C_{H,waDP} \\ -C_{S,waDP} \\ -C_{T\ BEM,waDP} \end{bmatrix} = \mathbf{T}_{waCP2waDP} \begin{bmatrix} -C_H \\ -C_S \\ -C_{T\ BEM} \end{bmatrix}$ $C_{T\ GLAU} = 2\,\lambda_i \sqrt{{a_1}^2\,\hat{\lambda}_c^2 - 2\,a_1\,\lambda_i\,\hat{\mu}_c + {\lambda_i}^2 - 2\,\lambda_i\,\hat{\lambda}_c + \hat{\lambda}_c^2 + \hat{\mu}_c^2}$ $F(\lambda_i) = C_{T\ BEM,waDP} - C_{T\ GLAU}$
$\mathcal{F}_{waCP}$	$C_T = C_{T,BEM}$ $C_O = \frac{N b_1 K_\beta}{2\rho\pi\Omega^2 R^5}$ $C_P = \frac{-N a_1 K_\beta}{2\rho\pi\Omega^2 R^5}$ $C_Q = f(\rho, \hat{\mu}_c, \hat{\lambda}_c, \overline{p}, \overline{q}, \overline{r}, \overline{\Omega}_{RZR}, \eta, \delta, \theta_{1s}, I_{bl}, \gamma_{bl}, \theta_{bl0}, \theta_{bl1}, \Omega_{sgn}, R, N,$ $C_{l_\alpha bl}, c_{d_0}, c_{d_1}, c_{d_2}, a_0, a_1, b_1, \lambda_i)$ (see section B.7) $\mathbf{F} = \begin{bmatrix} -C_H \\ -C_S \\ -C_T \end{bmatrix} \rho\pi\Omega^2 R^5$ $\mathbf{M} = \begin{bmatrix} -C_O \\ -C_P \\ -C_Q \end{bmatrix} \rho\pi\Omega^2 R^6$
$\mathcal{F}_b$	$\mathbf{F} = \mathbf{T}_{CP2b}\mathbf{T}_{waCP2CP}\mathbf{F}$ $\mathbf{M} = \mathbf{T}_{CP2b}\mathbf{T}_{waCP2CP}\mathbf{M}$

3.3.3. Module: MAC (Mean Aerodynamic Chord)

The module 'MAC' is used to to calculate the mean aerodynamic chord of the lifting surfaces of the aircraft. This module applies to the wings and horizontal and vertical stabilizers, and is used for components 3 to 14. The MAC of different components are required for multiple different modules. The MAC of the wing components are required to compute the rotor wake interference with the wings themselves. Furthermore the MAC is used to compute the aerodynamic forces and moments created by the lifting surfaces. The distinction between the left and right lifting surfaces is made by the input d_{sgn}. The inputs required for

this module are mainly geometric parameters of the lifting body surface, which is indicated in the module as 'component' and with the subscript 'c'. The distance vectors $[d_{x,c}, d_{y,c}, d_{z,c}]^T$ are the distances from the body c.g. to the root of the lifting surface.

The module essentially consists of two different parts. In the first part the MAC along the surface of the component is computed. This MAC, which is defined as $\mathbf{MAC}_{surface}$, is a position vector with respect to the root of the lifting surface defined in the reference frame of the component itself ($\mathcal{F}_c$). This vector is then converted to the body frame of reference. The distance vector from the body c.g. to the root of the lifting surface, defined as $\mathbf{MAC}_{root}$, is then added to $\mathbf{MAC}_{surface}$. This results in the final position vector $\mathbf{MAC}_c$, which defines the position of the point on the lifting surface at which the aerodynamic forces act with respect to the body centre of gravity.

Input parameters	
Component parameters	$d_{x,c} \quad d_{y,c} \quad d_{z,c} \quad b_c \quad c_{r,c} \quad c_{t,c} \quad \Gamma_c \quad i_c \quad \Lambda_c$
If:	
Left component	$d_{sgn} = -1$
Right component	$d_{sgn} = 1$
Transformation matrices	
$\mathcal{F}_b \rightarrow \mathcal{F}_c$	$\mathbf{T}_{b2c} = \begin{bmatrix} \cos i_c & -\sin i_c \sin \Gamma_c & \sin i_c \cos \Gamma_c \\ 0 & \cos \Gamma_c & \sin \Gamma_c \\ -\sin i_c & -\cos i_c \sin \Gamma_c & \cos i_c \cos \Gamma_c \end{bmatrix}$
$\mathcal{F}_c \rightarrow \mathcal{F}_b$	$\mathbf{T}_{w2b} = \mathbf{T}_{b2c}^{-1}$
Calculations	
$\mathcal{F}_c$	$\lambda_c = \frac{c_t}{c_r}$
	$\text{MAC}_{span} = \frac{b_c(1+2\lambda_c)}{6(1+\lambda_c)}$
	$\mathbf{MAC}_{surface} = \begin{bmatrix} -\text{MAC}_{span} \tan \Lambda_c \\ \text{MAC}_{span} \\ 0 \end{bmatrix}$
$\mathcal{F}_b$	$\mathbf{MAC}_{root} = \begin{bmatrix} d_{x,c} \\ d_{y,c} \\ d_{z,c} \end{bmatrix} \begin{bmatrix} 0 & d_{sgn} & 0 \end{bmatrix}$
	$\mathbf{MAC}_{surface} = \mathbf{T}_{c2b} \mathbf{MAC}_{surface}$
	$\mathbf{MAC}_c = \begin{bmatrix} \text{MAC}_x \\ \text{MAC}_y \\ \text{MAC}_z \end{bmatrix} = \text{MAC}_{root} + \text{MAC}_{surface}$

3.3.4. Module: Rotor Wake

The goal of the 'Rotor Wake' module is to check whether there is interaction between the wake of the rotor system and the wings of the tiltrotor. If so, it is computed how this interaction affects the airflow around the wings. This module should be applied to all wing components, so number 3 to 8 of Table 3.1. The interference between the rotor wake and the wing is calculated based on fixed wake theory and the projection relationship between the rotor disc and wing [5]. How the projection works is visualized in Figure 3.6.

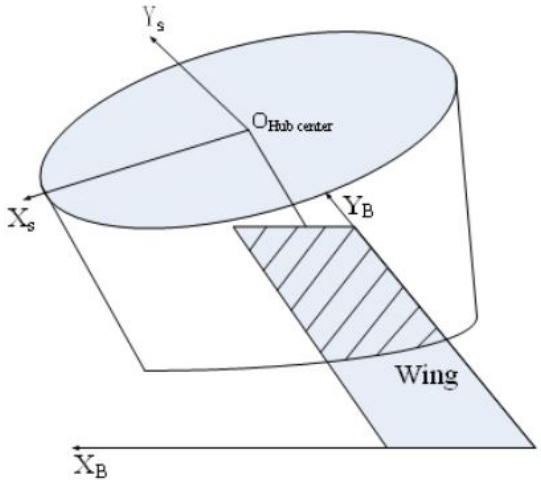

Figure 3.6: Schematic diagram visualizing the interference of the rotor wake with the wing [5]

The position and the orientation of the two rotors is determined in the 'Articulated Rotor' module. The position of the MAC of the wing components is determined in the 'MAC' module. The distance vector between the hub and the wing component MAC can be computed using both their positions with respect to the body c.g. and is then converted to the control plane reference frame $\mathcal{F}_{CP}$. To determine whether the wing component is located in the rotor wake two conditions have to be met. The first condition checks whether of the MAC of the component is located behind the hub. If not, the component can never be located in the wake. The second condition checks whether the MAC of the wing component is located within projection of the rotor disc on the wing. If both conditions are met the effect of the rotor wake on the velocity states can be computed. A few gross assumptions are made for this rotor wake effect computation. To fully take account of the rotor wake effects a complex vortex wake, distorted by itself and the aircraft motion should be modelled. For flight dynamics purposes this simplified representation of the rotor wake, based on actuator disc theory, is assumed sufficient [2]. Some of the assumptions made are listed below:

- The component is either as a whole or not at all affected by the rotor wake. This is completely dependent on the position of the MAC.
- The rotor has an infinite number of blades, able to uniformly accelerate the air through the rotor disc (rotor actuator disc theory).
- Only the the normal component of the rotor inflow is considered, i.e. the rotor-induced downwash.
- The wake is assumed to be steady, inviscid and incompressible.

The module requires a few rotor parameters which come from the 'Articulated Rotor' module and the MAC positions of the wing components computed in the 'MAC' module. If the component is located in the wake the velocity states u, w and z are recomputed for that specific component. These new states should then be used for the component in the 'Lifting Surface' module, which is discussed hereafter.

Input parameters	
Rotor parameters	R v_i $\mathbf{T}_{b2CP}$ $\mathbf{T}_{CP2b}$

continues on next page

Nacelle parameters	$d_{x,n} \quad d_{y,n} \quad d_{z,n}$
Component parameters	$\mathbf{MAC}_c$
Aircraft states	$u \quad v \quad w$
Calculations	
$\mathcal{F}_{CP}$	$\begin{bmatrix} d_{x,h2MAC} \\ d_{y,h2MAC} \\ d_{z,h2MAC} \end{bmatrix} = \mathbf{T}_{b2CP}(\begin{bmatrix} \text{MAC}_x \\ \text{MAC}_y \\ \text{MAC}_Z \end{bmatrix} - \begin{bmatrix} d_{x,n} \\ d_{y,n} \\ d_{z,n} \end{bmatrix})$ Check if the component is in the wake of the rotor: Condition 1: $d_{z,h2MAC} > 0$ Condition 2: $\sqrt{d_{x,h2MAC}^2 + d_{y,h2MAC}^2} < R$
$\mathcal{F}_b$	If both conditions are met: $\eta_w = \frac{d_{z,h2MAC}}{R}$ $w_w = v_i(1 + \frac{\eta_w}{\sqrt{1+\eta_w^2}})$ $\begin{bmatrix} u_{wake} \\ v_{wake} \\ w_{wake} \end{bmatrix} = \mathbf{T}_{waCP2b} \begin{bmatrix} 0 \\ 0 \\ w_w \end{bmatrix}$ $\begin{bmatrix} u \\ v \\ w \end{bmatrix} = \begin{bmatrix} u \\ v \\ w \end{bmatrix} - \begin{bmatrix} u_{wake} \\ v_{wake} \\ w_{wake} \end{bmatrix}$ If not : $\begin{bmatrix} u \\ v \\ w \end{bmatrix} = \begin{bmatrix} u \\ v \\ w \end{bmatrix}$

3.3.5. Module: Wing Downwash

In this module the downwash on the horizontal stabilizers caused by the wake of the wing is computed. This module is only used for the wing parts containing the flaps, so its concerns components WFLR and WFLL. The downwash angle is obtained from GTRS model tables[8], and is implemented as a function of wing angle of attack, flap deflection and nacelle angle. The downwash angle that is found by interpolating the GTRS data can then be subtracted from the effective horizontal stabilizer angle of attack. This is done in the 'Lifting Surface module'. The flap can be deflected under 4 different angles. XFL is defined as the flap setting. The flap deflection angles that come with the different flap settings are shown in Table 3.6 [12]. In helicopter and conversion mode usually XFL 3 is used, in airplane mode XFL 1. These settings are also used for the trim analysis at the end of this chapter.

Table 3.6: Different flap settings

XFL	Flap angle (deg)
1	0
2	20
3	40
4	75

Table 3.8: An overview of the lifting surface components and their control surfaces

Nr.	**Component**	**Control Surface**	$\frac{\delta CL}{\delta X}$	$\frac{\delta CD}{\delta X}$
3,4	WFL, WFR	-	-	-
5,6	WFLL, WFLR	flap	$\frac{\delta CL}{\delta \delta_f}$	$\frac{\delta CD}{\delta \delta_f}$
7,8	WAL, WAR	aileron	$\frac{\delta CL}{\delta \delta_a}$	-
9,10	HSL, HSR	elevator	$\frac{\delta CL}{\delta \delta_e}$	-
11,12	VSTL, VSTR	rudder	$\frac{\delta CL}{\delta \delta_r}$	-
13,14	VSBL, VSBR	-	-	-

Input parameters	
Wing parameters	$MAC_x \quad MAC_y \quad MAC_z \quad XFL \quad i_c \quad \Gamma_c$
Aircraft states	$u \quad v \quad w \quad p \quad q \quad r \quad \eta$
Transformation matrices	
$\mathcal{F}_b \rightarrow \mathcal{F}_c$	$\mathbf{T}_{b2c} = \begin{bmatrix} \cos i_c & -\sin i_c \sin \Gamma_c & \sin i_c \cos \Gamma_c \\ 0 & \cos \Gamma_c & \sin \Gamma_c \\ -\sin i_c & -\cos i_c \sin \Gamma_c & \cos i_c \cos \Gamma_c \end{bmatrix}$
$\mathcal{F}_c \rightarrow \mathcal{F}_b$	$\mathbf{T}_{w2b} = \mathbf{T}_{b2c}^{-1}$
Calculations	
$\mathcal{F}_b$	$\mathbf{V}_c = \begin{bmatrix} u \\ v \\ w \end{bmatrix} + \begin{bmatrix} p \\ q \\ r \end{bmatrix} x \begin{bmatrix} \text{MAC}_c \\ \text{MAC}_c \\ \text{MAC}_c \end{bmatrix}$
$\mathcal{F}_c$	$\mathbf{V}_c = \begin{bmatrix} u_c \\ v_c \\ w_c \end{bmatrix} = \mathbf{T}_{b2c}\mathbf{V}_c$
	$\alpha_c = \arctan \frac{w_c}{u_c} + i_c$
	$\alpha_d = \text{interpolate}(\alpha_c, [-90, 90], \eta, [90, 60, 30, 15, 0], \text{table}(XFL))$

3.3.6. Module: Lifting Surface

The purpose is this module is to compute the aerodynamic forces and moments induced by the lifting surfaces. This means that this module should be applied to the wing and horizontal and vertical stabilizers, which are components 3 to 14 in Table 3.1. These are the exact same components to which module 'MAC' should be applied, but both modules are separated because the 'Rotor Wake' module has to be applied to the wings in between. The module primarily requires some geometric parameters of the lifting surface component, which is indicated by the subscript 'c' for component. Two parameters have a different definition among the components, $\frac{dC_L}{dX}$ and $\frac{dC_D}{dX}$. These parameters define the change in lift and drag coefficients respectively due to a control surface deflection. The type of control surface varies per component. Which type of control surface each component contains can be found in Table 3.8. In the table it is also indicated if the control surface influences the aerodynamic coefficients in the 6-DoF model. The flaps, ailerons, elevators and rudder deflections all influence the lift coefficient, but contributions to the drag coefficient of the latter three are neglected.

The lift and drag coefficients are computed using a combination of linear aerodynamics and the flat plate area theory. The former method gives inaccurate results at low airspeeds (H-mode) due to the large angle of attack of the wings as a result of the rotor wake interference. The latter method is less accurate at high airspeeds (A-mode). Therefore, C_L and C_D are computed using a combination of both methods. The dependency on the two methods has been implemented as a function of nacelle angle. In helicopter mode the flat plate area method is used. When the nacelles are rotated towards airplane mode this method is phased out while the linear aerodynamics method is phased in. In airplane mode the coefficients are computed using solely the linear aerodynamics method.

Input parameters	
Aircraft states	$u \quad v \quad w \quad p \quad q \quad r$
Component parameters	$\mathbf{MAC}_c \quad b_c \quad c_{r,c} \quad c_{t,c} \quad \Gamma_c \quad i_c \quad \Lambda_c \quad C_{L_\alpha,c} \quad C_{D0,c}$ $C_{m_{ac},c} \quad \alpha_{0L,c} \quad e_c \quad \frac{dC_L}{dX} \quad \frac{dC_D}{dX}$
Environmental parameters	ρ
If:	
Left component	$d_{sgn} = -1$
Right component	$d_{sgn} = 1$
Transformation matrices	
$\mathcal{F}_b \rightarrow \mathcal{F}_c$	$\mathbf{T}_{b2c} = \begin{bmatrix} \cos i_c & -\sin i_c \sin \Gamma_c & \sin i_c \cos \Gamma_c \\ 0 & \cos \Gamma_c & \sin \Gamma_c \\ -\sin i_c & -\cos i_c \sin \Gamma_c & \cos i_c \cos \Gamma_c \end{bmatrix}$
$\mathcal{F}_c \rightarrow \mathcal{F}_b$	$\mathbf{T}_{w2b} = \mathbf{T}_{b2c}^{-1}$
Calculations	
$\mathcal{F}_b$	$\mathbf{V}_c = \begin{bmatrix} u \\ v \\ w \end{bmatrix} + \begin{bmatrix} p \\ q \\ r \end{bmatrix} x \begin{bmatrix} \text{MAC}_x \\ \text{MAC}_y \\ \text{MAC}_z \end{bmatrix}$

continues on next page

$\mathcal{F}_c$	$\mathbf{V}_c = \begin{bmatrix} u_c \\ v_c \\ w_c \end{bmatrix} = \mathbf{T}_{b2c}\mathbf{V}_c$ $V_{tot} = \sqrt{u_c^2 + v_c^2 + w_c^2}$ $\alpha = \arctan\frac{w_c}{u_c} + i_c - \alpha_d$ $\beta = \arctan\frac{v_c}{u_c}$ $C_{L,l} = C_{L_\alpha}(\alpha - \alpha_{0L}\cos\beta) + \frac{dC_L}{dX}X$ $\lambda = \frac{c_t}{c_r}$ $AR = \frac{b}{c_r(1+\lambda)}$ $C_{D,l} = C_{D0} + \frac{C_L^2}{\pi ARe} + \frac{dC_D}{dX}X$ $C_{L,f} = 2\sin(\alpha)\cos(\alpha)C_{L,max} + \frac{dC_L}{dX}X$ $C_{D,f} = \sin(\alpha - \alpha_{0L})^2 C_{D,max} + \frac{dC_D}{dX}X$ $n = (\frac{-2\eta}{\pi})$ $C_L = nC_{L,l} + (1-n)C_{L,f}$ $C_D = nC_{D,l} + (1-n)C_{D,f}$ $S = \frac{1}{4}b(c_t + c_r)$ $L = \frac{1}{2}\rho V^2 S C_L$ $D = \frac{1}{2}\rho V^2 S C_D$ $F_x = L\sin\alpha - D\cos\alpha$ $F_z = -L\cos\alpha - D\sin\alpha$ $M_y = \frac{1}{2}\rho V^2 S C_{m_{ac}}$ $\mathbf{F} = \begin{bmatrix} F_x \\ 0 \\ F_z \end{bmatrix}$ $\mathbf{M} = \begin{bmatrix} 0 \\ M_y \\ 0 \end{bmatrix}$
$\mathcal{F}_b$	$\mathbf{F} = \mathbf{T}_{c2b}\mathbf{F}$ $\mathbf{M} = \mathbf{T}_{c2b}\mathbf{M}$

3.3.7. Module: Fuselage

In the 'Fuselage' module the aerodynamic forces created by the fuselage are computed. Obviously this module only applies to the fuselage component. The initial fuselage module used the assumption that the fuselage only produces drag. The lift and moments created by the fuselage were assumed to equal zero. The drag was computed using

$$D_f = \frac{1}{2}\rho V_{lon}^2 A_{eq} \tag{3.5}$$

which then lead to the following force and moment vector

$$\mathbf{F} = \begin{bmatrix} -D_f \cos\alpha \\ 0 \\ -D_f \sin\alpha \end{bmatrix} \qquad \mathbf{M} = \begin{bmatrix} 0 \\ 0 \\ 0 \end{bmatrix} \tag{3.6}$$

According to multiple sources in literature the fuselage however quite significantly affects among others the pitching motion of the aircraft [2, 3, 6]. This would also result in a significant contribution to the pitching moment derivatives during the stability analysis. Therefore it was decided to use a look-up table for the aerodynamic coefficients of the fuselage. The GTRS model data provides tables for the lift, drag and pitching moment coefficient of the fuselage of the XV-15[8], and these are implemented as a function of angle of attack. The table can be found in section C.2. Interpolation is used to compute the coefficients. The 0 angle of attack force coefficients are added to the coefficient found by the interpolation. The resulting scheme is shown below. The force and moment vector calculated in this module serve as inputs to the 'Main' module.

Input parameters	
Fuselage parameters	$C_{L,0\alpha}$ $C_{D,0\alpha}$ $C_{M,0\alpha}$
Environmental parameters	ρ
Aircraft states	u w
Calculations	
$\mathcal{F}_b$	$V_{lon} = \sqrt{u^2 + w^2}$ $\alpha = \arctan\frac{w}{u}$ $q = \frac{1}{2}\rho V_{lon}^2$ $C_L = C_{L,0\alpha} + \text{interpolate}(\alpha, [-28, 28], \text{table}(C_L))$ $C_D = C_{D,0\alpha} + \text{interpolate}(\alpha, [-28, 28], \text{table}(C_D))$ $C_M = C_{M,0\alpha} + \text{interpolate}(\alpha, [-28, 28], \text{table}(C_M))$ $L = qC_L$ $D = qC_D$ $M = qC_M$ $F_x = L\sin\alpha - D\cos\alpha$ $F_z = -L\cos\alpha - D\sin\alpha$ $\mathbf{F} = \begin{bmatrix} F_x \\ 0 \\ F_z \end{bmatrix}$ $\mathbf{M} = \begin{bmatrix} 0 \\ M \\ 0 \end{bmatrix}$

3.3.8. Module: Main

All the forces and moments created by the different components serve as input to the final module: the main module. In this module all force vectors converted to the body frame of reference are added up to compute the resultant force vector acting on the aircraft. The same is done for the resultant moment vector, however the moments due to the forces also have to be considered. These resultant forces and moments are then inserted into the equations of motion together with the aircraft states to compute the accelerations acting on the vehicle.

Input parameters	
Aircraft parameters	$m \quad I_x \quad I_y \quad I_z \quad J_{xz}$
Components parameters	$\mathbf{F_c} \quad \mathbf{M_c} \quad d_{x,c} \quad d_{y,c} \quad d_{z,c}$
Environmental parameters	g
Aircraft states	$u \quad v \quad w \quad p \quad q \quad r \quad \phi \quad \theta \quad \psi$
Calculations	
$\mathcal{F}_b$	$\begin{bmatrix} X \\ Y \\ Z \end{bmatrix} = \begin{bmatrix} -mg\sin(\theta) \\ mg\cos\theta\sin\phi \\ mg\cos\theta\cos\phi \end{bmatrix} + \sum_{c=1}^{15} \mathbf{F_c}$
	$\begin{bmatrix} L \\ M \\ N \end{bmatrix} = \sum_{c=1}^{15} (\mathbf{M_c} + \mathbf{F_c} \; x \begin{bmatrix} d_{x,c} \\ d_{y,c} \\ d_{z,c} \end{bmatrix})$
	$\dot{u} = \frac{X}{m} - qw + rv$ $\dot{v} = \frac{Y}{m} - rv + pw$ $\dot{w} = \frac{Z}{m} - pv + qu$ $\dot{r} = \frac{I_x}{I_z - J_{xz}^2}(N - (I_y - I_x)pq + J_{xz}(\frac{L-(I_z-I_y)qr+J_{xz}pq}{I_x} - rq))$ $\dot{q} = \frac{1}{I_y}(M - (I_x - I_z)rp - J_{xz}(p^2 - r^2))$ $\dot{p} = \frac{1}{I_z}(L - (I_z - I_y)qr + J_{xz}(\dot{r} + pq))$

3.4. Trim results

Trim curves are often used to verify and validate a model. An aircraft is said to be in trim when the resultant of the applied forces and moments equals zero [3]. In the trim condition the pilot controls are fixed and are the unknowns in the trim computation. A trim state is found by solving the differential equations which describe the motion of the body. These differential equations are defined in the 'Main' module described in subsection 3.3.8.

In this section the 6-DoF model trim curves are validated against the GTRS model curves documented by Ferguson [6]. Both models use the XV-15 as reference aircraft so their trim curves should be very similar. The aircraft has been trimmed in steady, horizontal flight conditions for various nacelle angles and airspeeds.

The trim curves of the body pitch angle θ_b, the collective stick defection X_{COL} and the longitudinal stick deflection X_{LON} are shown in Figure 3.7. For each parameter five different flight configurations have been plotted, ranging from 90 to 0 degrees nacelle angle. The curves are shown as a function of airspeed.

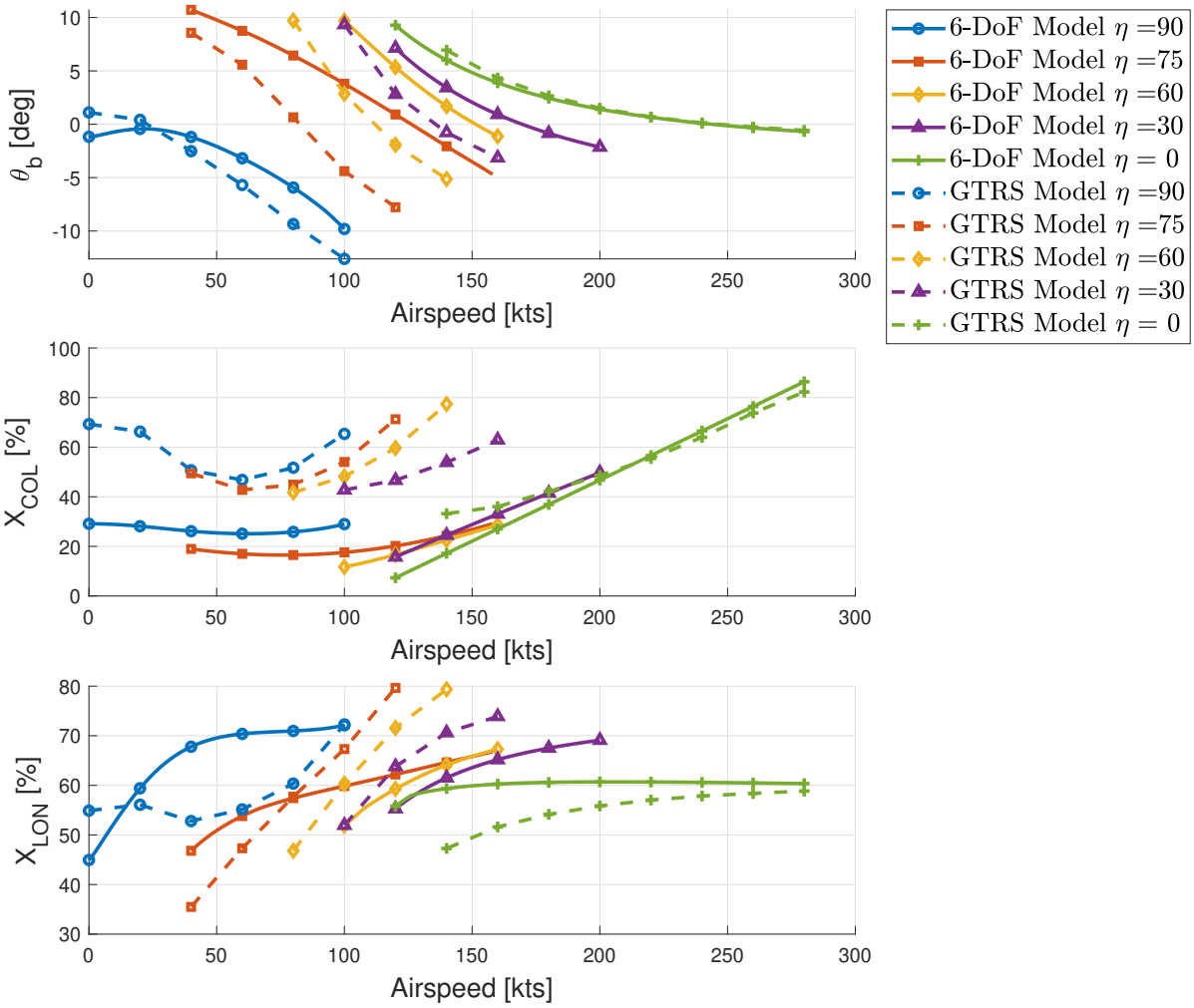

Figure 3.7: Body pitch angle (θ_b), collective stick deflection X_{COL} and longitudinal cyclic stick X_{LON} trim curves compared with GTRS model data [6].

The H-mode θ_b trim curves look very similar. In hover the body pitch angle is very close to zero, but the angle decreases when airspeed increases. The maximum trim speed is 100 kts for both models. In conversion mode three different nacelle angle configurations are compared; a 75, 60 and 30 degrees configuration. For all three configurations the 6-DoF model has a relatively higher trim body pitch angle. Furthermore, the trim airspeed ranges of both models in C-mode are of almost equal lengths, but the 6-DoF model is able to find trim solutions at higher airspeeds. In airplane mode the curves look again very alike. Both models find a maximum trim speed of 280 kts.

The XV-15 collective stick can have a deflection of 0 to 10 inch. The trim collective stick curves are shown as a percentage of the maximum deflection instead of as a function of the deflection in inch. This has been done because the gearing between the collective stick and the collective pitch angle required a different approach for the 6-DoF model. The XV-15 contains a rotor governor, which also has control over the collective pitch angle. While the pilot control over the collective pitch angle using the collective stick is phased out when the nacelles are rotated towards airplane mode, the rotor governor has control over the collective pitch in all flight modes. The collective rotor governor is superimposed on on the collective stick input. This rotor governor is implemented in the GTRS model, but not in the 6-DoF model. This means

that, without changing the collective stick to collective pitch phasing, the 6-DoF model has no control over the collective pitch angle in airplane mode. This also has as a result that the 6-DoF is not able reach the high collective pitch angles which the XV-15 is able to achieve. In order to compensate for the absence of the rotor governor, the boundaries of the collective stick have been altered. The governor collective pitch bound is translated and superimposed on the collective stick bound. This altered bound allows collective stick deflections higher than 10 inch. The new lower and upper bound of the collective stick (which are usually 0 and 10) are computed using

$$X_{COL,UL} = 10(1 + \frac{\eta}{0.5\pi}) + \frac{\theta_{0,UL,R}}{\Psi_{col\rightarrow 0}}$$
$$X_{COL,LL} = \frac{\theta_{0,LL,R}}{\Psi_{col\rightarrow 0}}$$

The collective stick upper limit $X_{COL,UL}$ is now dependent on the phasing of the collective stick gearing with nacelle angle and the rotor governor collective pitch upper bound $\theta_{0,UL,R}$. For the XV-15 this means that the collective stick can be deflected 30.94in in H-mode and 20.94in in A-mode. Since the rotor governor can also give a negative collective pitch input the collective stick now also has a negative lower bound, which equals in this case -3.125. The 6-DoF model $X_{COL}[\%]$ is then calculated using

$$X_{COL}[\%] = \frac{X_{COL} + X_{COL,LL}}{X_{COL,UL} + |X_{COL,LL}|} * 100 \tag{3.7}$$

The GTRS model $X_{COL}[\%]$ is computed using

$$X_{COL}[\%] = \frac{X_{COL}}{10} * 100 \tag{3.8}$$

with the original 0 to 10 inch bounds. Although both stick deflections have been converted to a percentage of their boundaries, it is not a perfect method to validate the 6-DoF collective stick trim results. In Figure 3.7 we see that there are quite some discrepancies between the two models due to the different calculation methods. The percentage stick deflection of the GTRS model is significantly higher in H-mode and C-mode. Nevertheless, The shapes of the curves look quite similar which gives some validation for the results. In A-mode the curves look very similar and there is quite some overlap.

The longitudinal cyclic stick trim results have also been plotted as a percentage of their deflection range. The cyclic stick can have a deflection between -4.8 and 4.8 inch. This means that $X_{lon}[\%]$ can be computed using

$$X_{LON}[\%] = \frac{X_{LON}}{10} * 100 \tag{3.9}$$

This equation holds for both models, so the percentages should show similarities. In the bottom plot of Figure 3.7 it is shown that the shapes of the curves look quite similar and there is some overlap. Only the 90 degrees nacelle angle curves look very different. The GTRS curve grows exponentially with airspeeds while the 6-DoF curve converges to a value around 70 %. Furthermore, the GTRS conversion and airplane mode curves are a lot steeper than those of the 6-DoF model.

The cyclic stick can also have a lateral deflection between -4.8 and 4.8 inch. The trim curves of the lateral cyclic stick have not been included in this report. Since the aircraft is trimmed in steady, horizontal flight conditions the lateral cyclic stick is fixed at 0 inch deflection. The GTRS model data also shows no lateral stick deflection in similar trim conditions. Since the plot would only contain straight horizontal lines at a 50% deflection the plots have not been included.

The trim collective pitch angle (θ_0), cyclic pitch angle (θ_{1s}) and elevator deflection (δ_e) curves are compared with the GTRS data in in Figure 3.8. All three control variables are a function of the pilot inputs. In horizontal, symmetrical trim (which means X_{PED} and X_{LAT} equal zero) the following relations for the control variables with the pilot inputs hold:

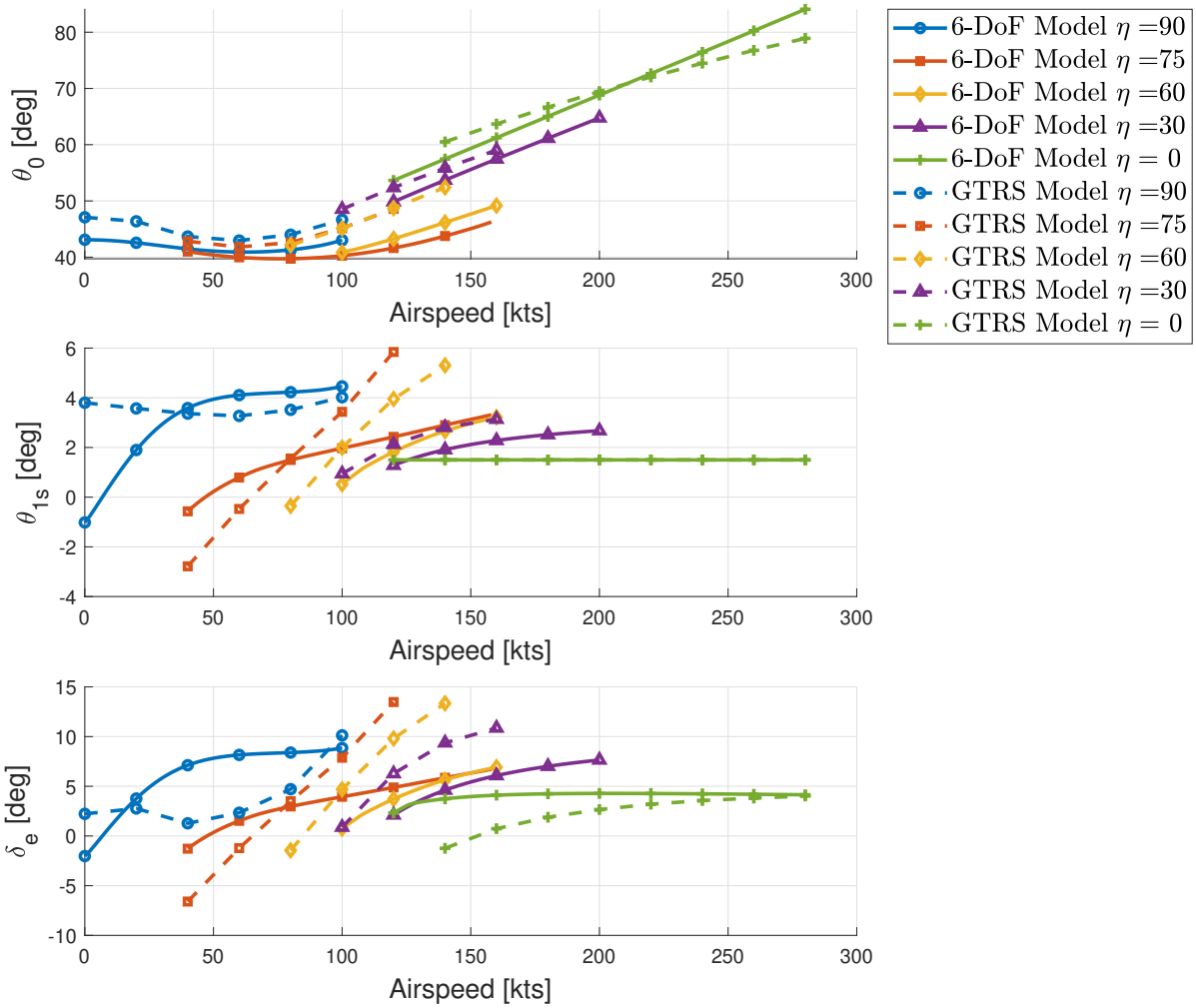

Figure 3.8: Collective pitch angle (θ_0), longitudinal cyclic angle (θ_{1s}) and elevator deflection angle (δ_e) trim curves compared with GTRS model data [6].

$$\theta_0 = 1.6X_{COL} + \theta_{0,LL} \tag{3.10}$$
$$\theta_{1s} = 2.1\cos\eta X_{LON} + 1.5(1 - \cos\eta) \tag{3.11}$$
$$\delta_e = 4.17X_{LON} \tag{3.12}$$

The collective pitch angle curves look very similar. In helicopter mode the trim collective angle first decreases and then increases with airspeed. At low nacelle angle configurations the angle increases linearly with airspeed. Since θ_0 is controlled using the collective stick, the shapes of the trim curves of both variables look very similar. The trim plots of the longitudinal cyclic angle θ_{1s} and elevator deflection angle δ_e look very alike. The differences between the models are also identical to what was found for the longitudinal cyclic curves. The GTRS model has generally steeper curves. The θ_{1s} trim curves in airplane mode perfectly coincide. This is because the longitudinal cyclic angle is fixed at 1.5 degrees in this configuration.

In Figure 3.9 the trim curves of the flapping angles are shown. The first plot shows the coning angle a_0, while the second and third plot show the longitudinal and lateral cone tilt angles a_1 and b_1 respectively. In order to validate the results by comparing them with the GTRS model some modifications to the validation data had to be made. The disk tilt angles of the GTRS model are derived in the mast axis system [8], while the 6-DoF model derives the angles with respect to the control plane. To transform the flapping angles from the mast axis reference frame to the control plane reference frame the cyclic pitch angles have to be added. Because the 6-DoF model assumes that there is no lateral cyclic input, the lateral tilt angles b_1 of

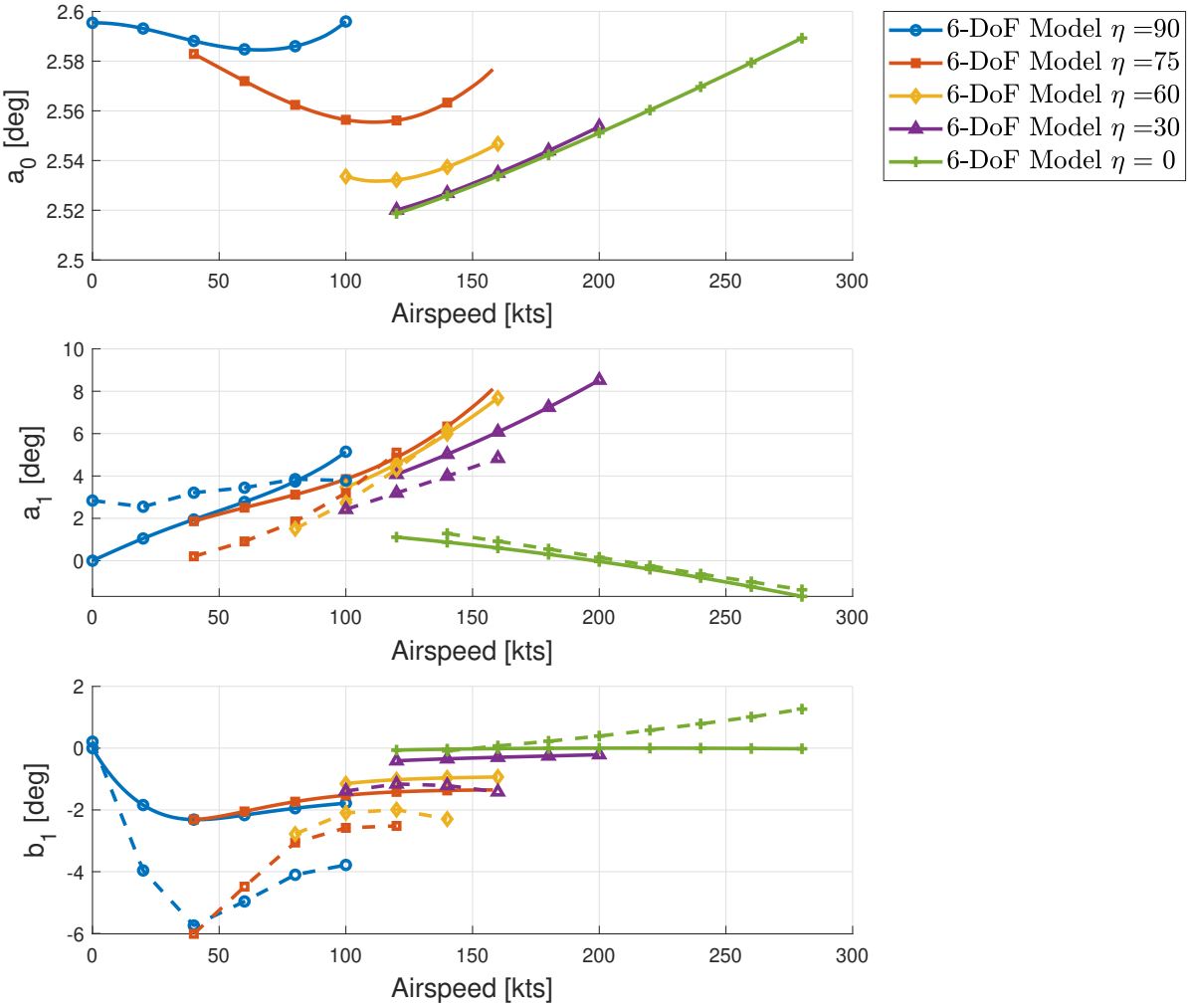

Figure 3.9: Flapping angle trim curves compared with GTRS model data [6].

the models are equivalent. The GTRS longitudinal coning angle a_1 has to be offset by the longitudinal cyclic θ_{1s} in order to match the 6-DoF model angle. Unfortunately, no comparable coning angle a_0 data was found for the GTRS model, so the first plot only shows the 6-DoF model data. Angle a_0 has a value between 2.5 and 2.6 degrees in all flight conditions. The pre-coning angle $a_{o,pre}$, which has a fixed value of 2.5 degrees, mainly determines the value of a_0. The a_1 curves look quite comparable. In helicopter and conversion mode the longitudinal tilt angle increases with airspeed, while in airplane mode the angle decreases. The 6-DoF model angle is slightly higher than the GTRS model angle in conversion mode. In airplane mode there is a good overlap. The bottom figure shows the lateral tilt angle b_1. In hover, b_1 is approximately zero for both models. When airspeed increases b_1 decreases up to 40 kts after which it increases again. The trends of both curves in helicopter mode look comparable, although b_1 of the GTRS model is about 3 times larger in magnitude. The difference in magnitude is also quite clearly present in conversion mode. In airplane mode the lateral tilt angle is almost zero for the 6-DoF model while the GTRS model angle increases with airspeed.

4

Linear Model

Stability is concerned with the behavior of an aircraft following a disturbance from an equilibrium state. Although the response of an aircraft to pilot inputs or atmospheric disturbances is a nonlinear problem, many stability characteristics can be determined from an analysis of the linearized model. In this chapter the linear version of the nonlinear model elaborated upon in chapter 3 is described. Firstly, the methodology behind the linearization is described in section 4.1. Thereafter, the derivatives following from the linearization are analysed. Firstly, the stability derivatives are analysed in section 4.2. Thereafter, the control derivatives are investigated in section 4.3.

4.1. Linearized Equations of Motion

In this section the methodology behind the linearization of the nonlinear equations of motion is described. The linearization always happens at an equilibrium state. The trim results described in section 3.4 are used for this purpose. The nonlinear equations of motion can described in the following form:

$$\dot{\mathbf{x}} = f(\mathbf{x}, \mathbf{u}, t) \tag{4.1}$$

The equations of motions are written in expanded form in subsection 3.3.8. Just as a small recap, $\mathbf{x}$ is the state vector and $\mathbf{u}$ is the control vector. The state vector of the 6-DoF model contains nine different states:

$$\mathbf{x} = [u, v, w, p, q, r, \phi, \theta, \phi] \tag{4.2}$$

The nacelle angle could also be considered an aircraft state, but since this angle is kept constant throughout this analysis it is left out of the state vector. The input vector consists out of four different pilot inputs:

$$\mathbf{u} = [X_{COL}, X_{LON}, X_{LAT}, X_{PED}] \tag{4.3}$$

With these four pilot inputs the aircraft can be controlled by altering the symmetrical and differential collective pitch (θ_0, θ_{0d}), symmetrical and differential longitudinal cyclic pitch (θ_{1s}, θ_{1sd}), and elevator (δ_e), aileron (δ_a) and rudder (δ_r) deflections. For the control analysis of the 6-DoF model it is more interesting to look at these controls than at the pilot inputs. The aircraft response due to pilot inputs can quite easily be altered by changing the gearing of the control system. This has already been done for the collective pitch angle to be able to reach 280 kts in airplane mode. The aircraft responses to pilot inputs are therefore also harder to validate. For this reason, the input vector of the 6-DoF model has been altered to the following form:

$$\mathbf{u} = [\theta_0, \theta_{0d}, \theta_{1s}, \theta_{1sd}, \delta_e, \delta_a, \delta_r] \tag{4.4}$$

Now, returning to Equation 4.2. At the equilibrium state, all moments are forces are in equilibrium or in other words: the aircraft does not accelerate linearly or rotationally. This means that the following condition holds:

$$\dot{\mathbf{x}} = 0 \tag{4.5}$$

It can be assumed, using small perturbation theory, that during disturbed motion the behavior of the aircraft can be described as a perturbation from the trim condition

$$\mathbf{x} = \mathbf{x_0} + \delta\mathbf{x} \tag{4.6}$$

In this equation $\mathbf{x_0}$ is the trim condition. Linearization relies on the assumption that all forces and moments can be written as a Fourier series approximation of the nonlinear equations of motion and truncating the series at the first derivative. This results in a steady state term and linear derivatives. All forces and moments can then be described in the form shown below:

$$X = X_0 + \frac{\partial X}{\partial u}\partial u + \frac{\partial X}{\partial v}\partial v + \frac{\partial X}{\partial w}\partial w + ... + \frac{\partial X}{\partial \theta_0}\partial\theta_0 \tag{4.7}$$

All six forces and moments can be expanded in the same manner. The derivatives are generally written in the following form:

$$\frac{\partial X}{\partial u} = X_u \tag{4.8}$$

The obtained linear equations of motion of the perturbed motion around a trim condition can then be written as:

$$\dot{\mathbf{x}} = \mathbf{A}\mathbf{x} + \mathbf{B}\mathbf{u}(t) \tag{4.9}$$

In this equation $\mathbf{A}$ is the system matrix containing all force and moment derivatives with respect to the aircraft states:

$$\mathbf{A} = (\frac{\partial \mathbf{F}}{\partial \mathbf{x}})_{x=x_0} \tag{4.10}$$

Similarly, $\mathbf{B}$ is the control matrix containing all force and moment derivatives with respect to the control inputs:

$$\mathbf{B} = (\frac{\partial \mathbf{F}}{\partial \mathbf{u}})_{x=x_0} \tag{4.11}$$

The derivatives in matrix $\mathbf{A}$ are called stability derivatives, and those in matrix $\mathbf{B}$ are called control derivatives. The full expanded linear system is shown below.

$$\begin{bmatrix} \dot{u} \\ \dot{w} \\ \dot{q} \\ \dot{\theta} \\ \dot{v} \\ \dot{p} \\ \dot{\phi} \\ \dot{r} \end{bmatrix} = \begin{bmatrix} X_u & X_w - q_0 & X_q - w_0 & -g\cos\theta_0 & X_v + r_0 & X_p & 0 & X_r + v_0 \\ Z_u + q_0 & Z_w & Z_q + u_0 & -g\cos\phi_0\sin\theta_0 & Z_v - p_0 & Z_p - v_0 & -g\sin\phi_0\cos\theta_0 & Z_r \\ M_u & M_w & M_q & 0 & M_v & \begin{matrix} M_p - 2p_0 I_{xz} I_y \\ -r_0(I_x - I_z)I_y \end{matrix} & 0 & \begin{matrix} M_r - 2r_0 I_{xz} I_y \\ -2p_0(I_x - I_z)I_y \end{matrix} \\ 0 & 0 & \cos\theta_0 & 0 & 0 & 0 & -\Omega_0\cos\theta_0 & -\sin\theta_0 \\ Y_u - r_0 & Y_w + p_0 & Y_q & -g\sin\phi_0\sin\theta_0 & Y_v & Y_p + w_0 & g\cos\phi_0\cos\theta_0 & Y_r - u_0 \\ L'_u & L'_w & L'_q + k_1 p_0 - k_2 r_0 & 0 & L'_v & L'_p + k_1 q_0 & 0 & L'_r - k_2 q_0 \\ 0 & 0 & \sin\phi_0\tan\theta_0 & \Omega_0\sec\theta_0 & 0 & 1 & 0 & \cos\phi_0\tan\theta_0 \\ N'_u & N'_w & N'_q - k_1 r_0 - k_3 p_0 & 0 & N'_v & N'_p - k_3 q_0 & 0 & N'_r - k_1 q_0 \end{bmatrix} \begin{bmatrix} u \\ w \\ q \\ \theta \\ v \\ p \\ \phi \\ r \end{bmatrix} \tag{4.12}$$

$$+ \begin{bmatrix} X_{\theta_0} & X_{\theta_{0d}} & X_{\theta_{1s}} & X_{\theta_{1sd}} & X_{\delta_e} & X_{\delta_a} & X_{\delta_r} \\ Z_{\theta_0} & Z_{\theta_{0d}} & Z_{\theta_{1s}} & Z_{\theta_{1sd}} & Z_{\delta_e} & Z_{\delta_a} & Z_{\delta_r} \\ M_{\theta_0} & M_{\theta_{0d}} & M_{\theta_{1s}} & M_{\theta_{1sd}} & M_{\delta_e} & M_{\delta_a} & M_{\delta_r} \\ 0 & 0 & 0 & 0 & 0 & 0 & 0 \\ Y_{\theta_0} & Y_{\theta_{0d}} & Y_{\theta_{1s}} & Y_{\theta_{1sd}} & Y_{\delta_e} & Y_{\delta_a} & Y_{\delta_r} \\ L'_{\theta_0} & L'_{\theta_{0d}} & L'_{\theta_{1s}} & L'_{\theta_{1sd}} & L'_{\delta_e} & L'_{\delta_a} & L'_{\delta_r} \\ 0 & 0 & 0 & 0 & 0 & 0 & 0 \\ N'_{\theta_0} & N'_{\theta_{0d}} & N'_{\theta_{1s}} & N'_{\theta_{1sd}} & N'_{\delta_e} & N'_{\delta_a} & N'_{\delta_r} \end{bmatrix} \begin{bmatrix} \theta_0 \\ \theta_{0d} \\ \theta_{1s} \\ \theta_{1sd} \\ \delta_e \\ \delta_a \\ \delta_r \end{bmatrix} \tag{4.13}$$

(4.14)

Besides the linearized aerodynamic forces and moments, the kinematic, perturbation inertial and gravitational effects of the equations of motion are also incorporated in the linear system. The inertial effects in the A matrix are denoted by

$$[\phi_0, \theta_0, u_0, v_0, w_0, p_0, q_0, r_0] \tag{4.15}$$

Furthermore, the derivatives in Equation 4.12 are written in semi-normalized form. This means that the force derivatives are divided by the mass of the system and the moment derivatives by the appropriate moment of inertia.

$$X_u \equiv \frac{X_u}{m}, \quad M_u \equiv \frac{M_u}{I_y} \tag{4.16}$$

The rolling and yawing moment equation are often coupled. Because of this reason, primed derivatives are usually introduced [2, 12]. An example of a primed derivative is shown below:

$$L'_p = \frac{I_{zz}}{I_{xx}I_{zz} - I_{xz}^2} L_p + \frac{I_{xz}}{I_{xx}I_{zz} - I_{xz}^2} N_p \tag{4.17}$$

The stability and control derivatives can be determined in different ways. Firstly, analytic differentiation of the force and moment equations can be used to determine the exact values of the derivatives. One advantage of this method is that the derived equations for the derivatives shows exactly what parameters affect the derivative and to what extent. This method is however very time-consuming and might not be the most effective and error-prone method when a rigorous model has to be analysed.

By far the most popular method used is the numerical perturbation method method [3, 4, 12, 20, 26]. The aircraft states at trim are known as well as the initial values of the forces and moments which are zero. Now, perturbing one of the states will disturb the equilibrium of the aircraft. By investigating the effect of the disturbance on the forces and moments, their variations can be quantified. These variations are the numerical values for the stability derivatives. Similarly, the control inputs can be varied one by one to determine the values of the control derivatives.

A third method involves a model matching process, in which a linear model is adapted such that the responses fit the responses of the nonlinear system [17, 22]. This method can also be used to match flight data, and is a type of system identification. The accuracy of this method depends on the degree of nonlinearity, the noise of the flight data and the correlation between the states and the responses. The system identification approach seeks to find the best overall fit with the nonlinear response, and varies all derivatives simultaneously until this best fit is found.

It was decided that the stability and control derivatives of the 6-DoF model can best be determined using the numerical perturbation method. The derivatives are estimated using a finite central difference. If the motion of the aircraft is denoted by $f(\mathbf{x})$ with $\mathbf{x_0}$ the trim state and δ the perturbation size, the following generic finite central difference scheme can be used [7]:

$$Df^{(\delta)} = \frac{f(x_0 + \delta) - f(x_0 - \delta)}{2\delta} \tag{4.18}$$

As mentioned, this is only an estimation of the derivative. Complete accuracy would only be achieved if the number of significant numbers would be infinite and the perturbation would be infinitesimal. The level of inaccuracy of this method depends on two error sources. Firstly, we have the truncation error. The nonlinear functions are represented by Taylor-expansions where the higher order terms are neglected. Therefore, the accuracy of this method is dependent on the dominance of the constant, linear and quadratic terms of terms of the expansion with respect to the higher-order terms [7]. The error arises by truncating the higher order terms, or in other words truncating the Taylor expansion. In order to minimize the truncation error, the perturbation size should be as small as possible. Secondly, there is the problem of round-off errors. Computers have limited precision, meaning that they will never yield the exact result. Decreasing the perturbation to an arbitrary small value leads to the quantities $f(x_0 + \delta)$ and $f(x_0 - \delta)$ becoming almost equal. At this point, the finite central difference scheme starts losing accuracy again due to round-off errors.

Therefore, a trade-off between truncation and round-off errors has to be considered in order to achieve the most accurate linearization results. There exists an operational region in which the the error of the linearization is minimized. This region is shown in Figure 4.1. It can be seen that if the perturbation size is too small, the round-off error is relatively big. On the other side, if the perturbation size is too big, the truncation error plays the biggest role.

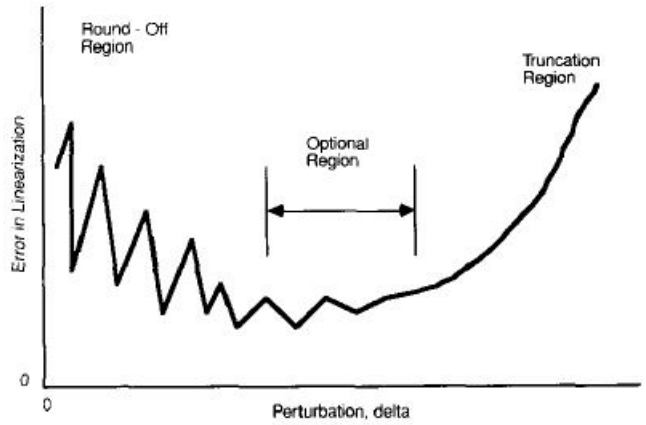

Figure 4.1: Conceptional relation between perturbation size and linearization error [7]

To determine which perturbation size gives the smallest error, an iterative process is introduced. This process is visualized in the flow chart in Figure 4.2. By picking an arbitrary large number as initial perturbation, the linearization error is most probably in the truncation region. The derivative can be computed using this perturbation size, after which the perturbation size is reduced and the derivative is recalculated. The two derivatives are compared, and as long as the difference between the two is above some threshold, the perturbation size keeps on reducing. At some point the derivative has converged to some value, indicating that the optional region is reached and the error is minimized. This process is repeated for all derivatives, resulting in the linear state space system.

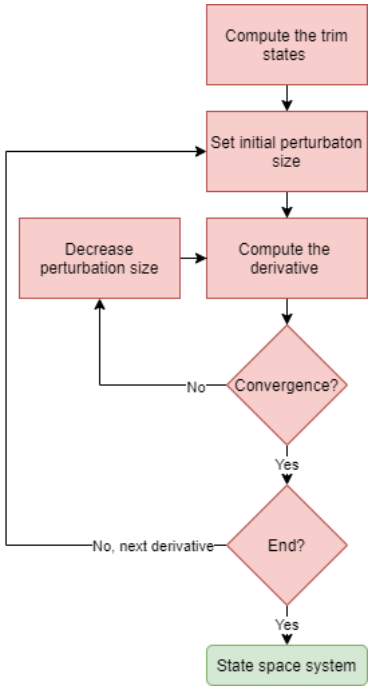

Figure 4.2: Linearization process

4.2. The Stability Derivatives

In this section the stability derivatives of the 6-DoF linear tiltrotor model are discussed. From these derivatives a lot can already be told about the stability of the aircraft. All derivatives are defined in the body

orthogonal axes system, which is shown in Figure 4.3. The origin of this reference system coincides with the body centre of gravity. The X-axis is aligned with the the centerline of the fuselage and points towards the nose. the velocity component along this axis is denoted by u. The Y-axis points towards the starboard of the aircraft and the lateral velocity component v is aligned with this axis. The Z-axis points down perpendicular to the centerline. The velocity component along this axis is denoted by w. The angular velocities in this reference frame follow the right-hand rule.

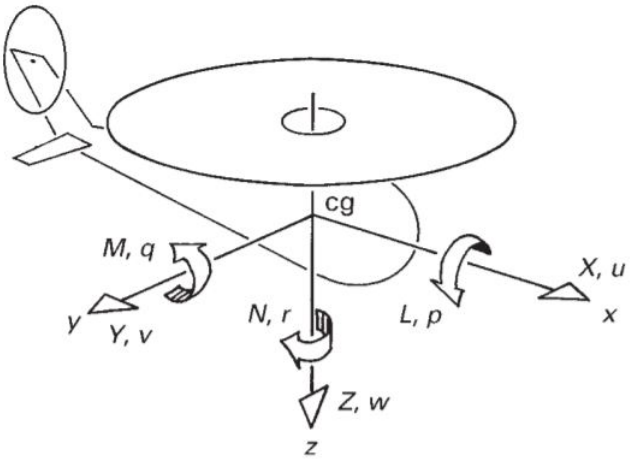

Figure 4.3: The orthogonal body axes system [2]

The derivatives are analysed at different combinations of airspeed and nacelle angle. The variations of the derivatives are analysed as a function of airspeed in all three flight modes. Furthermore, the influence of the nacelle angle variation on the derivatives is investigated. The 6-DoF model derivatives are also compared with data obtained from other models. This serves as validation for the results, but the differences between the models can also say a lot about the effects of the different assumptions made during the modelling process. All derivatives have been converted to the same units, which are shown in Table 4.1. Furthermore, no longitudinal-lateral coupling derivatives are described, only direct derivatives. The reason for this is that the coupling derivatives are usually negligibly small. Firstly the longitudinal stability derivatives are discussed. Thereafter, the lateral/directional stability derivatives are elaborated upon.

Table 4.1: The S.I. units of the stability derivatives

Force/translational velocity	e.g. X_u	1/s
Force/angular velocity	e.g. X_q	m/s/rad
Moment/translational velocity	e.g. M_u	rad/s/m
Moment/angular velocity	e.g. M_q	1/s

4.2.1. Longitudinal Stability Derivatives

In this subsection the longitudinal stability derivatives are described. These are the derivatives which describe the symmetric motions along the X- and Z-axis of the body frame of reference. The longitudinal derivatives of the 6-DoF model are compared with three different other models: the preliminary 3-DoF model, the GTRS model and the FLIGHTLAB model (FXV-15).

Stability Derivative X_u

The X_u derivative practically reflects the drag of the aircraft, according to Padfield [2]. The derivative usually shows a linear relationship with speed and should be negative at any condition in order to have stability. This means that X_u decreases with increasing airspeed which is also usually the case for a fixed-wing aircraft and a conventional helicopter. The tiltrotor drag damping derivative should actually decrease faster with

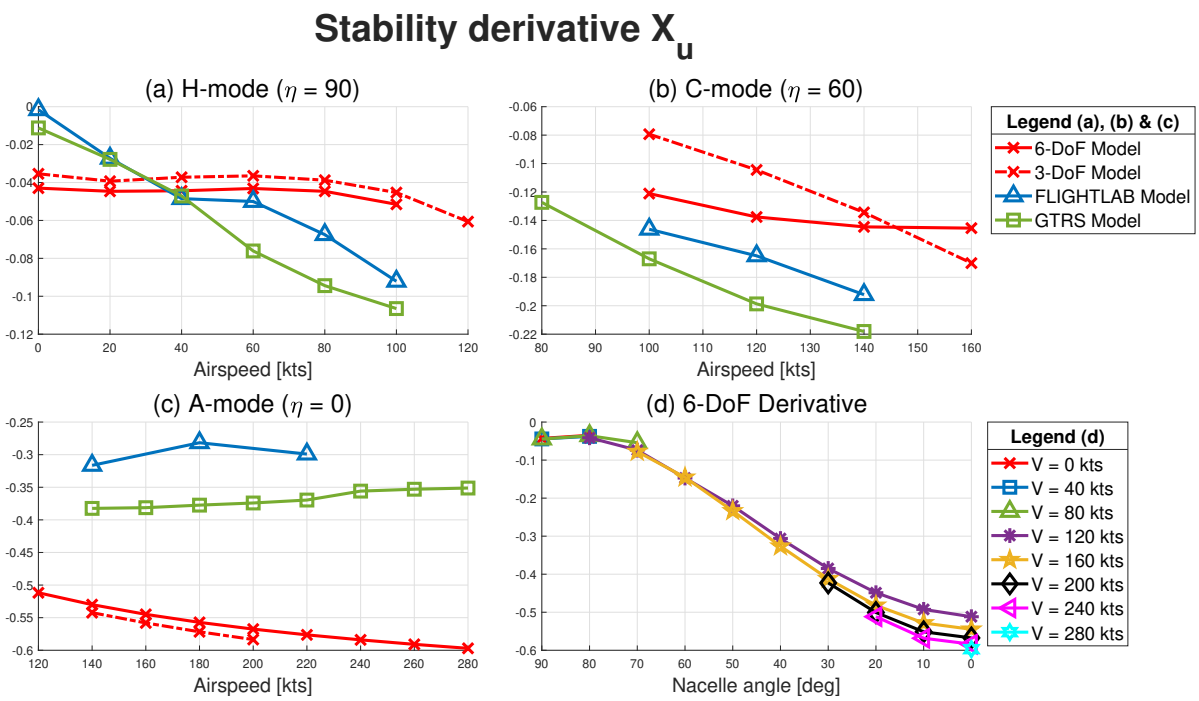

Figure 4.4: Stability derivative X_u in helicopter mode, conversion mode and airplane mode, and as a function of nacelle angle η

increasing speed compared to a conventional helicopter, because of its additional rotor and wings which significantly increases its drag. For a conventional helicopter the phugoid is usually unstable in hover, but the mode stabilizes with increasing airspeed. The tiltrotor phugoid shows similar behavior, but because of its higher drag damping the mode stabilizes at a lower airspeed [4].

In Figure 4.4 X_u is plotted for several models in several different configurations. From the four subfigures it can be concluded that the requirement that X_u should be negative is satisfied for all models in all configurations. The curves of the derivatives in helicopter mode are expected to show similarities with curves we know from conventional helicopters, which show a linear descent [2]. This linear decrease with airspeed is indeed the case for both the FLIGHTLAB and GTRS model. The X_u derivative of both the 3-DoF and 6-DoF model do not show this behavior and appear to be almost unaffected by the airspeed. Padfield mentions that the X_u reflects the drag of the whole aircraft, but while the drag does increase with airspeed, the rotor forces are the dominant contributor to X_u in this mode for both models. This contribution which is mainly due to the longitudinal in-plane forces of the rotors does not increase with airspeed and this the main reason why the X_u derivative also remains fairly constant.

The linear slope that was expected in helicopter mode is more visible in conversion mode. The derivative decreases in value with increasing airspeed, and shows a similar trend for all four models. The X-component of the fuselage drag, the thrust and H-force decrease in value when the horizontal velocity component u is increased, all contributing to the negative value of X_u. The biggest contributor to this derivative is still the rotor system, with a contribution of around 85% for the 6-DoF model.

In airplane mode the magnitude of X_u is larger than we saw in conversion and helicopter mode. This is because the thrust vector is now aligned with the body X-axis making the contribution of the rotors to X_u even more dominant in this mode. The derivatives of the 3-DoF model and 6-DoF model decrease slightly with airspeed, which makes sense as the drag still increases with airspeed. The FLIGHTLAB and GTRS model derivatives are more or less constant with speed.

In subplot (d) the variation of the derivative is plotted as a function of nacelle angle, using the 6-DoF model. As the nacelles are tilted from helicopter mode towards airplane mode the magnitude of the derivative increases. This happens because the thrust vector is tilted as well, increasing its force component along the x-axis and thus also its contribution to X_u.

Stability Derivative X_w

Derivative X_w is shown in Figure 4.5. Subplot (a) shows the derivative in helicopter mode. In hover, X_w is approximately zero, but as airspeed increases the derivative slowly decreases. This is the case for all models. As airspeed increases, the wing becomes the main contributor to the decreasing value of the derivative for the 3-DoF model with a contribution of around 70%. The angle of attack of the tiltrotor in helicopter mode is negative and decreases with increasing airspeed. This also means that the angle of attack of the wing becomes increasingly negative, which eventually leads to a negative C_L and thus a negative lift force. A positive perturbation in w decreases the total airspeed as w is negative, and thus the magnitude of the negative lift force decreases which decreases the X-direction force created by the wing. For the 6-DoF model the same principle applies, however the contribution of the wing to the derivative is significantly smaller, around 45 %. The rotor system which makes X_w more positive has a larger contribution for the 6-DoF model than for the 3-DoF model which explains the difference between the two plots.

While X_w is negative at high airspeeds in helicopter mode, positive derivative values are found in conversion mode. This is mainly because the horizontal X-component of the thrust force increases when the nacelles are tilted towards airplane mode. A positive perturbation in w causes an increase in thrust force, which largely contributes to the positive value of X_w. With increasing airspeed the derivative decreases for the 3-DoF model, FLIGHTLAB model and GTRS model which was also observed in helicopter mode and can be explained using similar logic. For the 6-DoF model a more constant value with airspeed is found. The trim angle of attack in a 60 degrees nacelle angle configuration decreases from approximately 10 to -1 degrees when the airspeed is increased from 100 to 160 kts. Because the angle of attack approaches zero the aerodynamic forces created by the wing decrease and thus also its contribution to X_w. For this reason X_w is mainly determined by the rotor forces, which contribution remains roughly constant with airspeed.

In airplane mode the decreasing trend with airspeed is present for all 4 models. All curves start at a positive X_w. The 3-DoF model decreases with airspeed and approaches zero, while the 6-DoF, FLIGHTLAB and GTRS models become negative at some point. At positive angles of attack the rotor thrust, the wing and the horizontal stabilizer have a positive contribution to X_w for both the 3-DoF and 6-DoF model. The 3-DoF model trim angle of attack decreases from 6.3 to 1.3 along the airspeed range of 140 to 200 kts. The 6-DoF and GTRS model can be trimmed at higher airspeeds and reach 280 kts. At airspeeds higher than 240 kts both models have a negative trim angle of attack. This change in sign of angle of attack is the reason why X_w changes sign as well for these two models and not for the 3-DoF model. The X-component of the lift force is directed along the negative x-axis when the angle of attack becomes negative. This could cause the derivative to change sign at high airspeeds.

In sub-figure (d) the variation of X_w with nacelle angle is shown. When the nacelles are tilted from helicopter mode towards airplane mode the derivative increases up to approximately 40 degrees where a peak appears to be reached. The increase in value can be explained by looking at the thrust vector which rotates towards the positive X-axis, and thus increasingly affects the resultant force in that direction. When the nacelles are tilted further towards airplane mode, the effect of a perturbation in w on the thrust force decreases because their vectors are approaching orthogonality. This also explains why X_w decreases again at some point.

Stability Derivative X_q

In helicopter mode the X_q derivative increases exponentially with speed as shown by Figure 4.6 (a). The increase in value is mainly due to the increasing magnitude of the inertial trim velocity w_0, which is subtracted from the derivative (see Equation 4.12). According to Ferguson [6], the only contributor to this derivative in hover is the rotor system. This is also in accordance with the memorandum by Pavel [32], who derived the following equation for X_q of a helicopter:

$$x_q = -C_T \frac{\delta a_1}{\delta \overline{q}} - \alpha_D \frac{\delta C_T}{\delta \overline{q}} - \frac{\delta C_{H_D}}{\delta \overline{q}} \tag{4.19}$$

This shows that the derivative in helicopter mode is dependent on the longitudinal coning angle a_1, the thrust force T and the longitudinal in-plane H-force. As airspeed increases, $-w_0$ increases which mainly causes the increase in the curves.

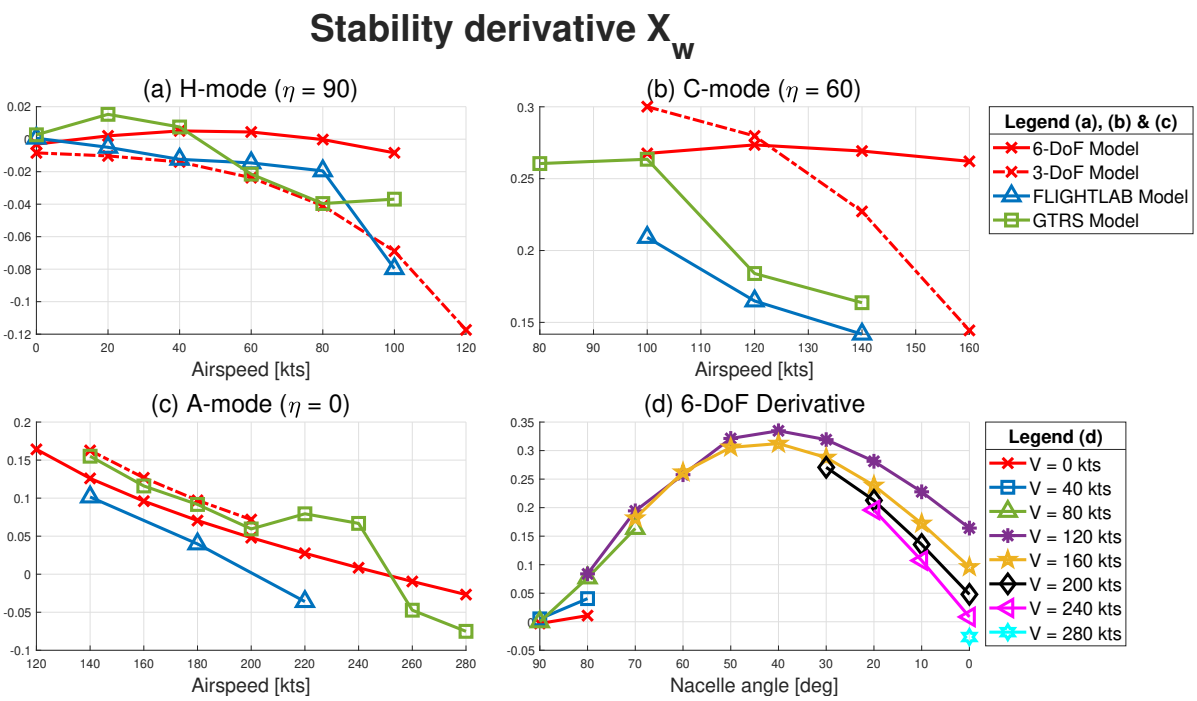

Figure 4.5: Stability derivative X_w in helicopter mode, conversion mode and airplane mode, and as a function of nacelle angle η

Subplot (b) shows that in conversion mode the derivative starts at a negative value and then increases somewhat linearly with velocity and becomes positive. The change in sign of angle of attack with increasing airspeed also causes the w_0 to change sign, which then causes the X_q derivative to change sign as well.

In airplane mode the X_q derivative plot is just as in the helicopter and conversion mode mainly dominated by w_0. The trim velocity component is equal to $V\sin(\theta_f)$. In the analysis of the X_w derivative it was mentioned that the angle of attack of the 3-DoF model is positive along the entire velocity range in A-mode, but the GTRS model and 6-DoF model angle of attack decreases below zero with increasing velocity. This also explains why the X_q derivative of the 3-DoF model remains negative while the derivative of the other two models changes sign when a certain flight speed is reached.

When the airspeed is kept constant and the nacelles are tilted towards airplane mode the angle of attack decreases and becomes negative at some point. This also means that the w_0 increases with decreasing η. Because the w_0 is subtracted from the derivative subplot (d) shows a decrease with nacelle angle.

Stability Derivative Z_u

The Z_u derivative shows the same trend with increasing airspeed in helicopter mode for all four models (Figure 4.7). In hover, a perturbation in u barely affects the resultant Z-force, but as velocity increases the derivative decreases fast up to around 40 knots after which it starts increasing again. This effect mainly occurs due to the wing. At low speeds the wing generates a positive lift force, meaning a negative resultant Z-force contributing to a negative Z_u. As airspeed keeps on increasing, the angle of attack of the wing decreases and eventually becomes negative, which eventually results in a negative lift force. This negative lift force has a positive contribution to Z_u, causing the derivative to increase in value.

In conversion mode the curves of the models differ quite a lot. The 3-DoF and 6-DoF model curves look very comparable but are positive while the FLIGHTLAB and GTRS model curves are negative. The derivative is for ± 90 % determined by the wing and rotor system, which have an nearly equal share. A positive perturbation in u causes an increases in lift by the wings and thus a negative change in Z-force, while for the same perturbation the rotor system creates a positive change in Z-force. For the 3-DoF and 6-DoF models the rotor system slightly dominates the derivative, which leads to its positive value. For the GTRS

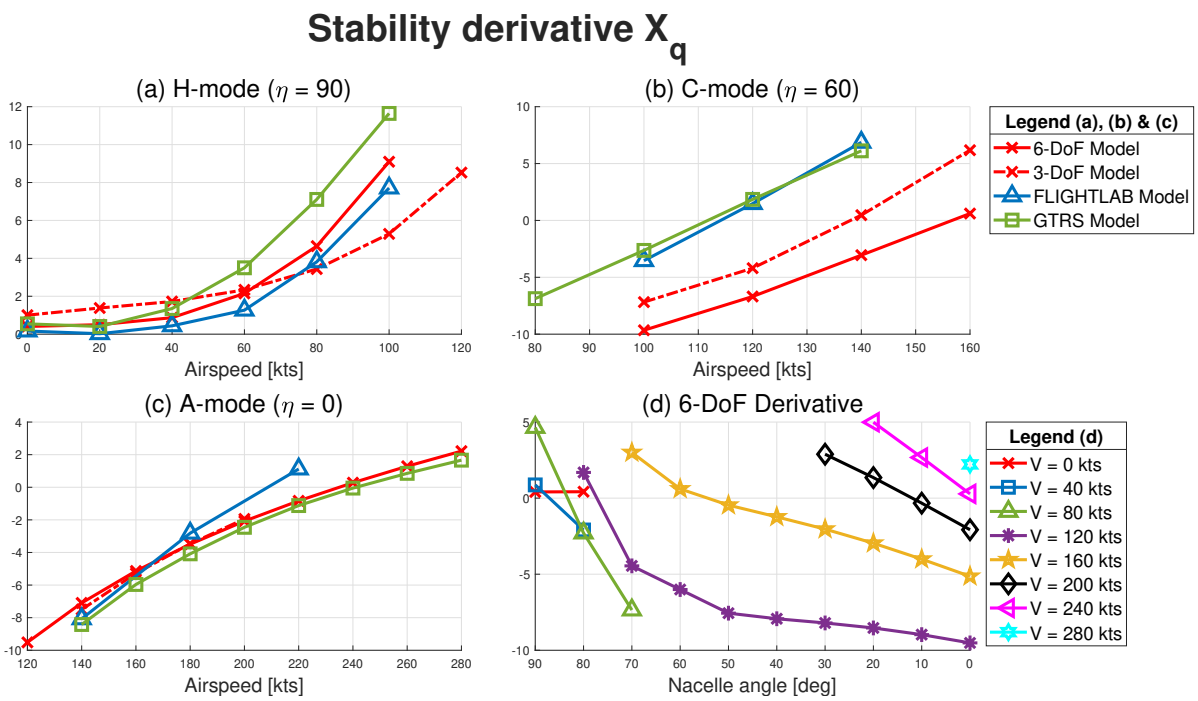

Figure 4.6: Stability derivative X_q in helicopter mode, conversion mode and airplane mode, and as a function of nacelle angle η

and FLIGHTLAB models this is the other way around; the wing is the dominant factor hence its negative value. For all four models the derivative slightly increases with airspeed. This happens because the angle of attack of the aircraft decreases with speed, resulting in a smaller lift force and thus a decreased influence of the wing on the derivative.

In airplane mode the Z_u derivative is negative for all four models. The 3-DoF and 6-DoF models and FLIGHTLAB model barely show any variation in Z_u with speed, while the GTRS model shows a small decrease. The derivative is mainly determined by the contribution of the wings which provide the lift in A-mode. An increase in airspeed usually also increases the lift force, but as the angle of attack decreases with increasing airspeed the lift force remains fairly constant. The data of the GTRS model however does show a small increase in lift with increasing airspeed, leading to the marginal decrease of Z_u [6].

Subplot (d) shows that the Z_u derivative increases with decreasing nacelle angle up to an angle of 40 degrees after which it starts decreasing again. When the nacelles are rotating from H-mode towards A-mode the influence of u on the rotor forces increases which causes the Z_u to increase at high nacelle angles. Simultaneously, the magnitude of the Z-component of the rotor forces decreases which decreases the dominance of the rotor system on the derivative, eventually causing the derivative to decreases in value again at low nacelle angles.

Stability Derivative Z_w

The heave-damping derivative Z_w should be negative in order to have stability. At low airspeeds, the heave-damping derivative is generally larger for rotary aircraft than for fixed-wing aircraft [2]. A helicopter is more sensitive to gust loads below approximately 50 knots. As speed increases, the heave response of the rotary aircraft flattens of while for the fixed-wing aircraft it increases linearly, as shown in Figure 4.8. This is because of the increasing contribution of the wings on the derivative as speed increases. As the tiltrotor also has fixed wings, the Z_w curve is more similar to the fixed-wing aircraft. This is also clearly visible in Figure 4.9. Subfigures (a), (b) and (c) show that a linear decrease of Z_w with airspeed is present for the four models in all flight modes. Furthermore, the derivative is negative along the flight envelope so there the aircraft is stable along the heave axis. At low airspeeds the derivative is mainly determined by the rotors, but with increasing airspeed the wings and horizontal stabilizers start creating lift and also affect the derivative. All subsystems contribute to the negative value of the derivative.

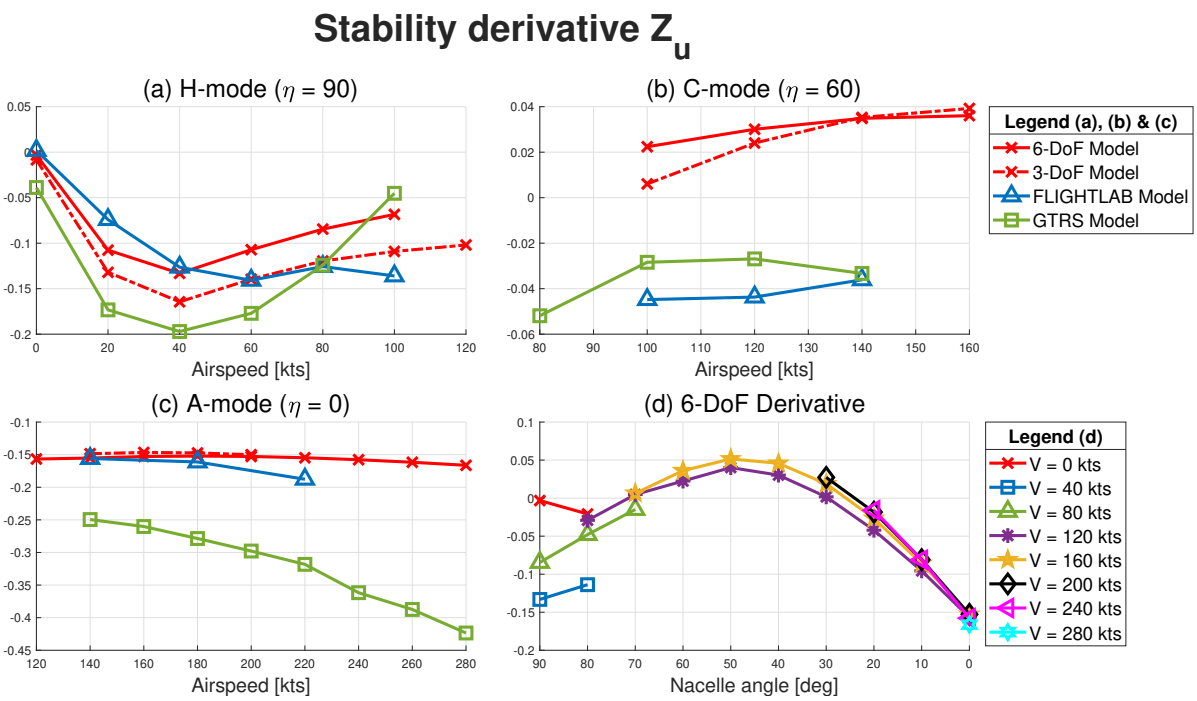

Figure 4.7: Stability derivative Z_u in helicopter mode, conversion mode and airplane mode, and as a function of nacelle angle η

In subfigure (d) the variation of the 6-DoF model derivative with nacelle angle is shown. The derivative is approximately constant with eta. Tilting the nacelle angle decreases the Z-component of the rotor force and thus its contribution to Z_w derivative. Simultaneously, the trim angle of attack of the aircraft increases resulting in more lift created by the wings. This increases the contribution of the wings to Z_w. The decrease and increase of the rotor and wing contributions respectively happens at a similar rate, which explains why Z_w remains approximately constant with nacelle angle.

Stability Derivative Z_q

In Figure 4.10 the Z_q derivative is depicted. The results of the models look very similar in all three flight modes. This is not that surprising, while the horizontal trim velocity u_0 is also included in the graph, which is added to derivative itself. This horizontal velocity component is almost identical for the three models and has a much larger magnitude that the derivative Z_q solely, thus is the dominant factor in the plot. The small differences between the models are due to the differences in trim angle of attack which means that u_0 is also different for the models. The nacelle angle barely affects Z_q as seen in subfigure (d). The angle of attack of the tiltrotor increases when the nacelles are tilted towards A-mode which decreases u_0 slightly. This results in a slightly negative slope which is barely observable in the figure.

Stability Derivative M_u

The speed stability derivative M_u has a mayor effect on the longitudinal stability and handling qualities of an aircraft [3]. For a conventional airplane M_u is practically zero at subsonic speeds, because all moments induced by the aerodynamic surfaces are proportional with dynamic pressure, so they cancel each other out during perturbations. For a conventional helicopter however M_u is important along the entire flight envelope. The moments induced by the main rotor due to changes in speed are roughly constant, but the aerodynamic loads acting on the fuselage and empennage vary strongly with increasing airspeed. Primarily the horizontal stabilizer produces a strong pitching moment around the centre of mass, affecting the speed stability derivative. According to Padfield [2] a positive M_u is beneficial for good handling qualities, but it can degrade the dynamic stability of the helicopter. If a positive perturbation in u causes a positive pitching up moment, the drag of the aircraft increases, which in turn decreases forward speed again. For a conventional helicopter M_u is usually positive, so a positive speed stability derivative can also be expected for a tiltrotor in helicopter

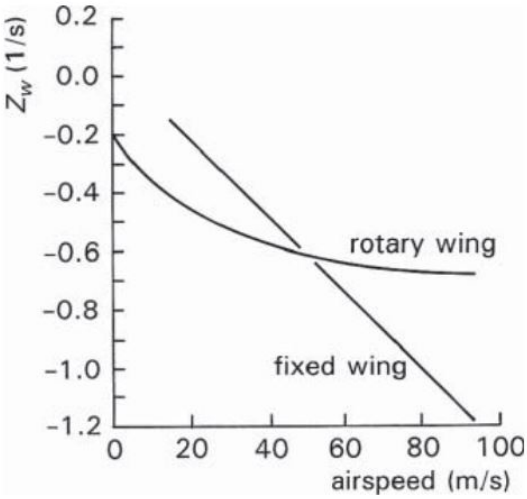

Figure 4.8: Variation of the heave-damping derivative Z_w for both rotary- and fixed-wing aircraft [2]

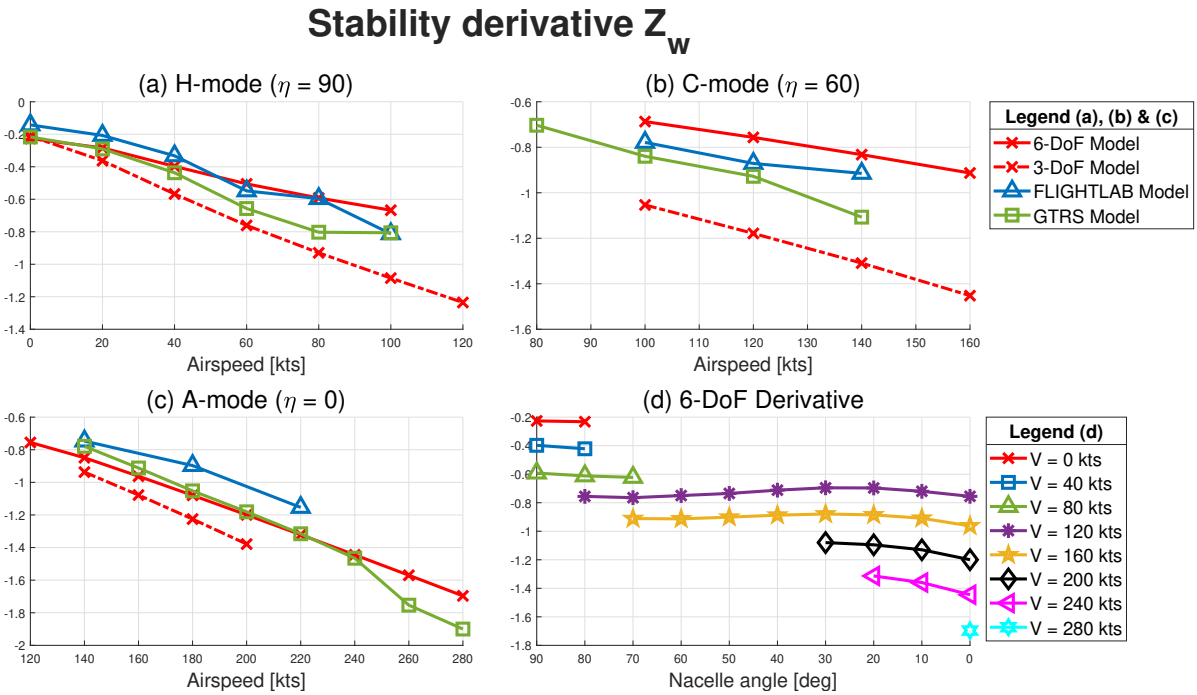

Figure 4.9: Stability derivative Z_w in helicopter mode, conversion mode and airplane mode, and as a function of nacelle angle η

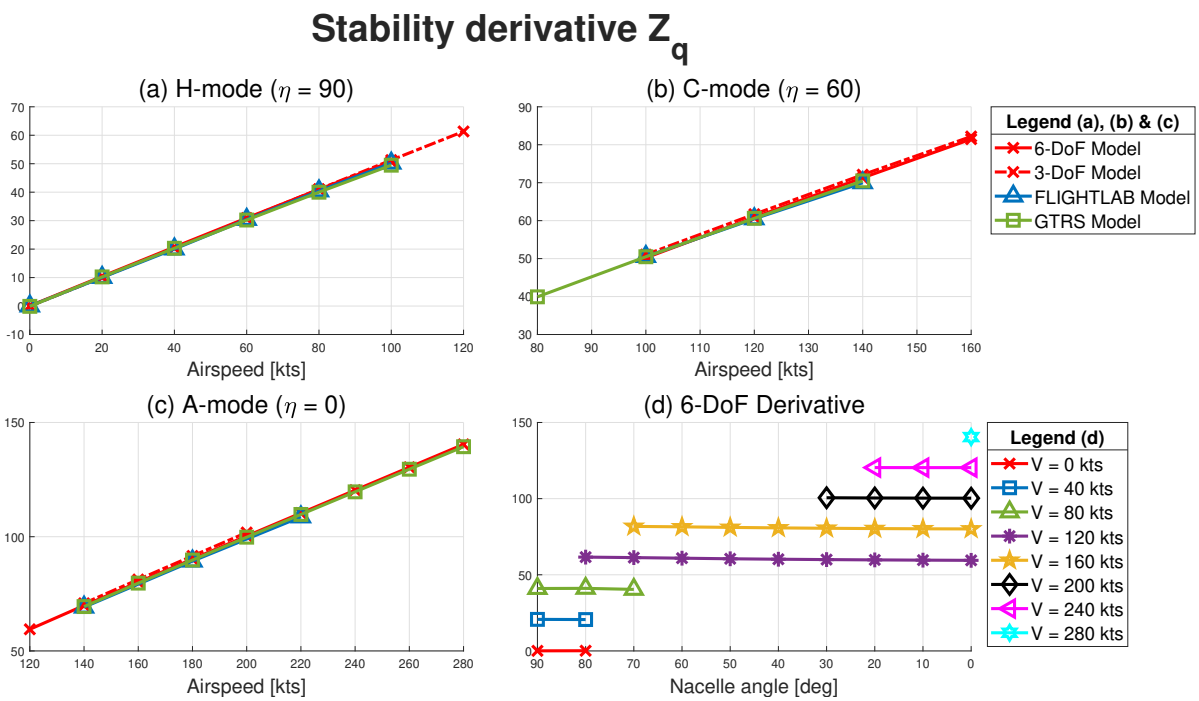

Figure 4.10: Stability derivative Z_q in helicopter mode, conversion mode and airplane mode, and as a function of nacelle angle η

mode. As airspeed increases and the nacelles are tilted towards airplane mode M_u should approach zero according to Berger et al. [3]. At high airspeeds the tiltrotor is expected to behave like a conventional fixed-wing aircraft, so the moments induced by the lifting surfaces should all be proportional to dynamic pressure and should cancel eachother out.

Looking at the curves for the speed stability derivative M_u in helicopter mode in Figure 4.11 (a), quite some significant differences between the models can be observed. The FLIGHTLAB model derivative is positive and increases with airspeed up to 40 knots after which it decreases again. The 6-DoF and 3-DoF models are positive at low airspeeds but start decreasing linearly after 20 kts. After approximately 60 and 90 knots the derivative becomes negative for the 6-DoF and 3-DoF model respectively. This is caused by the pitching moment induced by the horizontal stabilizers. At low airspeeds the effect of the horizontal stabilizer is relatively small and the derivative mainly depends on the rotor forces, but as airspeed increases an increasingly negative pitching moment is induced which eventually causes M_u to become negative. This horizontal stabilizer dominance is clearly not present in the GTRS model, which has a completely different curve. The GTRS data provided by Ferguson [6] shows the total airframe (including fuselage, wing, stabilizers) contributes positively to M_u which is definitely not the case for the 3-DoF and 6-DoF models.

In conversion mode the results of the models look a lot more comparable than in helicopter mode, but there are still quite some significant differences. The plot of the 3-DoF shows that M_u starts at a positive value but decreases and becomes negative when airspeed increases. Similar as in helicopter mode this is caused by the horizontal stabilizer. The negative moment induced by this horizontal surface dominates the speed stability derivative at high airspeeds. The 6-DoF model derivative shows a similar trend but has a higher value and remains positive. The rotor system creates a positive pitching up moment which outweighs the negative pitching moment induced by the horizontal stabilizers for this model. For the GTRS model the airframe pitching moment is still very dominant, hence its relatively higher derivative values.

In airplane mode the M_u derivative is positive for all models at all airspeeds. According to Berger et al. [3], M_u should approach zero in airplane mode as airspeed increases. However, this is the case for none of the models. The GTRS and 6-DoF models show an increase in M_u with speed. For the 3-DoF and 6-DoF models it is found that the positive pitching moment induced by the rotor system is very dominant in airplane mode when u is disturbed, preventing the derivative from approaching zero.

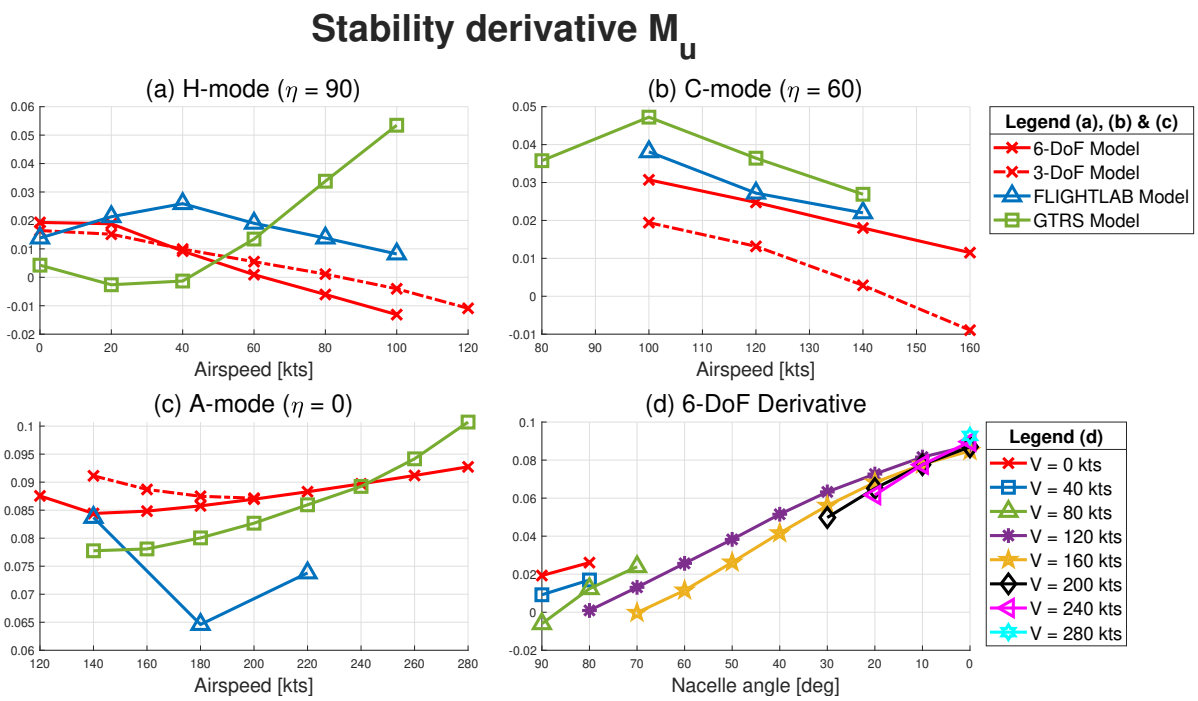

Figure 4.11: Stability derivative M_u in helicopter mode, conversion mode and airplane mode, and as a function of nacelle angle η

From subfigure (d) is becomes apparent that the speed stability derivative increases in magnitude with decreasing nacelle angle. This happens mainly because the thrust force is rotated towards the positive x-axis. The thrust force decreases in magnitude when a positive perturbation in the horizontal velocity component u occurs. Since the thrust force creates a negative pitching moment, this moment also decreases resulting in a positive resultant moment M. The thrust force is increasingly sensitive to disturbances in u when the η decreases, which leads to an increase of M_u when rotating towards the airplane configuration.

Stability Derivative M_w

The incidence static derivative, also called the longitudinal static stability derivative M_w represents the change of pitching moment about the centre of mass of an aircraft due to a perturbation in the vertical velocity component w. Together with M_u this derivative largely affects the longitudinal stability of an aircraft [2]. If a positive perturbation in w causes a positive pitching moment, then M_w is positive and the aircraft is said to be statically unstable. For a conventional airplane this derivative is extremely important. Helicopters, however, are often inherently unstable in pitch. If a positive incidence occurs, the advancing blade creates more lift than the retreating blade. As a result of this differential lift in combination with the 90 deg phase shift, the rotor disc will flap back creating a positive pitching moment around the centre of gravity. This effect increases with increasing speed. For a tiltrotor, M_w is usually negative along the entire velocity range and thus the aircraft is statically stable. According to Lu et al.[4] the wing and the fuselage of a tiltrotor have a destabilizing contribution to M_w because the centre of gravity is located after the aerodynamic center. However, the aircraft is still stable due to the stabilizing effect of the large tailplane.

Figure 4.12 shows the M_w curves for the different models. In hover, M_w is approximately zero, but the derivative decreases with speed increasing the static stability. This is the case for all four models meaning that they are statically stable. A linear trend can be observed for the FLIGHTLAB, 3-DoF and 6-DoF model, although the slopes are significantly different. For the 3-DoF model the aerodynamic centre and the centre of gravity of the fuselage are assumed to coincide, which means that the fuselage is not stabilizing nor destabilizing for this model. For the other models the fuselage is destabilizing which partly explains the steeper curve of the 3-DoF model. Besides that, the destabilizing effect of the wings is very small compared to the stabilizing effect of horizontal stabilizers for the 3-DoF model which also results in a steeper curve.

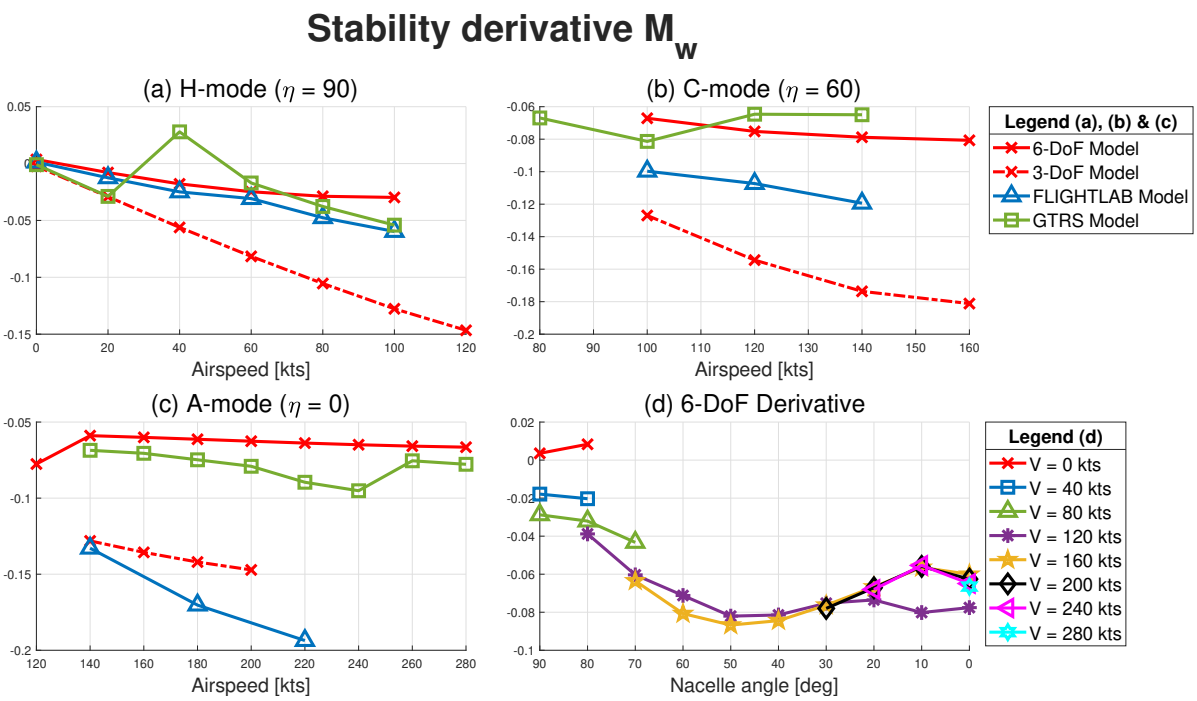

Figure 4.12: Stability derivative M_w in helicopter mode, conversion mode and airplane mode, and as a function of nacelle angle η

The GTRS model shows a statically unstable aircraft at 40 knots with an M_u of 0.027. While the airframe as a whole has a stabilizing effect for all other velocities, it appears to be destabilizing at 40 knots.

In conversion mode M_w is negative for all models at all airspeeds, meaning that they are statically stable in this configuration. Just as we saw in helicopter mode, the derivative of the 3-DoF model has a larger magnitude than the other three models because the model does not consider the destabilizing effect of the fuselage. The tailplane of the aircraft has a big stabilizing effect, which increases with flight speed. The wings are destabilizing, while the rotors provide a stabilizing contribution.

In airplane mode the M_w derivative of the 3-DoF model and FLIGHTLAB model look quite similar. The derivative is negative and decreases with speed. The wings have a destabilizing effect, but the stabilizing effect of the horizontal stabilizer makes the aircraft overall statically stable. The 6-DoF model derivative looks more similar to the GTRS model derivative and has relatively small values compared to the other two models. In airplane mode the rotors have a destabilizing contribution to M_w.

In subfigure (d) the 6-DoF derivative is plotted as a function of nacelle angle. At low airspeeds the nacelle angle does not significantly affect the speed stability derivative. At higher airspeeds the curves decrease slightly with nacelle angle, which means that the aircraft becomes more statically stable. The trim angle of attack increases with nacelle angle, meaning that the horizontal stabilizers create more lift and have a larger stabilizing contribution to the static stability derivative. This causes the negative slope with decreasing nacelle angle at high nacelle angle configurations. When the nacelles rotated further towards A-mode, the rotor contribution changes from negative to positive. This causes the increase in slope at low values of η.

Stability Derivative M_q

The pitch damping derivative M_q plays a very important role in the longitudinal short-term handling characteristics, which means that the derivative hugely affects the short-period of the aircraft. A positive perturbation in q should always results in a restoring pitching down moment, meaning that M_q should be negative [3]. The magnitude of the pitch damping derivative usually increases linearly with airspeed. Lu et al. [4] mention that this is due to the tailplane, which is the main source contribution to this derivative. According to Padfield [2], M_q reduces in magnitude as the rotors are being tilted from helicopter to airplane mode.

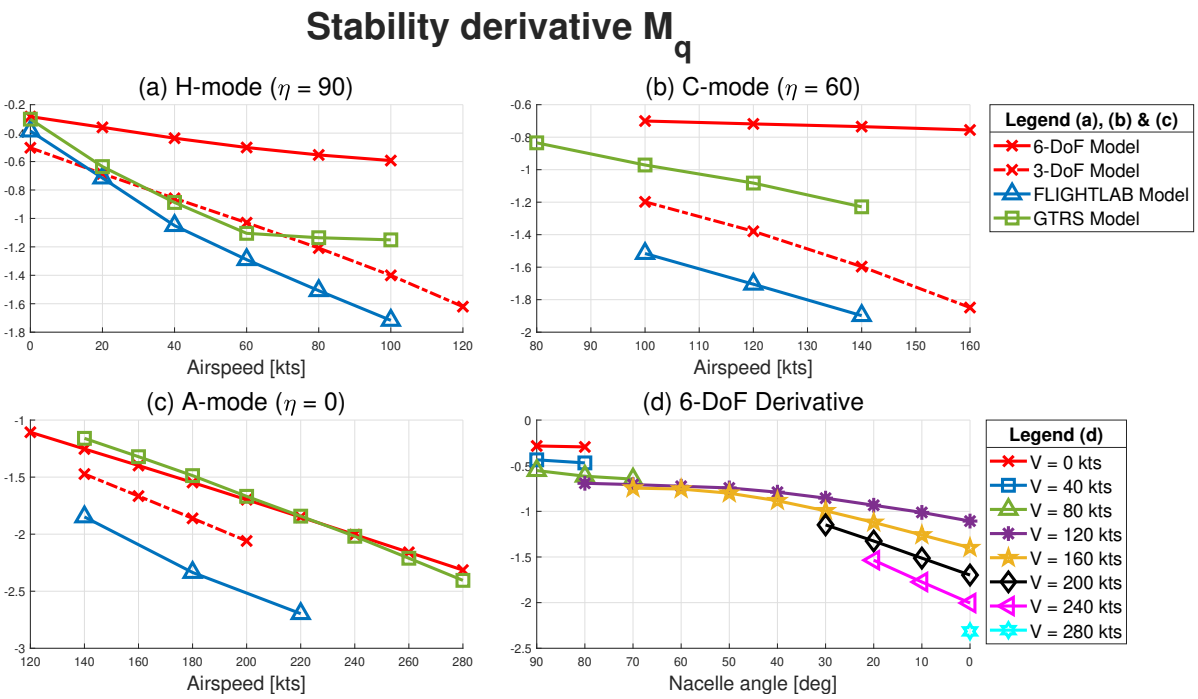

Figure 4.13: Stability derivative M_q in helicopter mode, conversion mode and airplane mode, and as a function of nacelle angle η

This is due to in-plane lift components of the proprotors, which have a positive contribution to the derivative.

The pitch damping derivative M_q is shown in Figure 4.13. For all four models the derivative is negative along the entire velocity range, which is desirable for stability. In hover (subfigure (a)) the pitch damping derivative is almost entirely determined by the rotor system, which is stabilizing. When the airspeed increases the horizontal stabilizer also creates a stabilizing contribution to M_q, leading to a linear decrease in value. In subfigure (b) the conversion mode derivatives are shown. All four models show a linear decrease in value with airspeed. The 6-DoF curve is significantly less steep than the other three model curves. The rotor forces which are stabilizing for the other models are destabilizing for the 6-DoF model in conversion mode with airspeed. This destabilizing contribution is still present in airplane in airplane mode. The biggest contributor to the derivative is however still the horizontal stabilizer system which is stabilizing.

According to Padfield [2] the derivative should decrease in magnitude when the proprotors are tilted towards airplane mode, because the destabilizing effects of the in-plane rotor forces increase. From subfigure (d) it can be concluded that M_q increases in magnitude with nacelle angle for the 6-DoF model. The destabilizing effect of the rotor indeed increases when rotating towards airplane mode, but so does the trim angle of attack. This means that the horizontal stabilizers create more lift and as a result the stabilizing contribution to M_q increases as well. This stabilizing effect by the horizontal stabilizers is bigger than the destabilizing effect of the rotor causing the negative slope. One possible explanation for this difference could be the difference in modelled rotor hub. The FXV-15 is modelled with a gimballed rotor hub which has usually larger in-plane forces than an articulated rotor hub [2].

4.2.2. Lateral/directional Stability Derivatives

In this subsection, the lateral/directional stability derivatives are discussed. These are the derivatives with respect to the lateral velocity component v, the roll rate p and the yaw rate r. Similarly as the longitudinal stability derivatives the lateral/directional derivatives will be compared with the GTRS model and FLIGHTLAB model data. The 3-DoF model data is not included in the comparison as this model is limited to symmetrical motion.

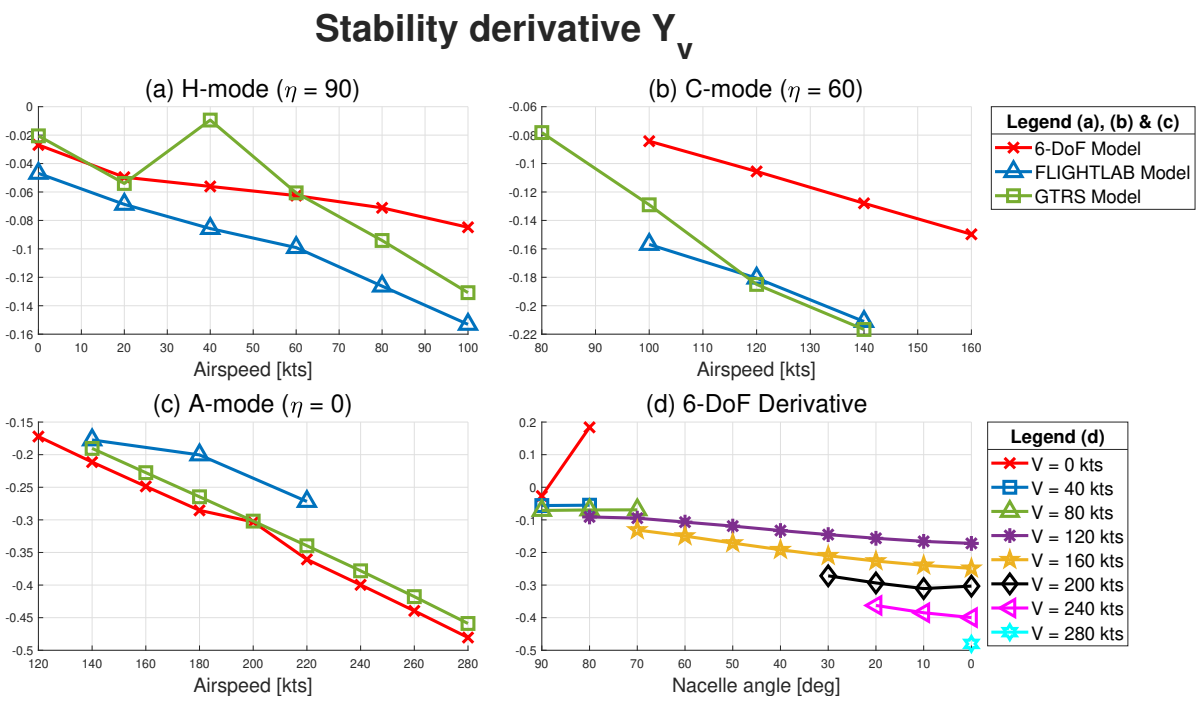

Figure 4.14: Stability derivative Y_v in helicopter mode, conversion mode and airplane mode, and as a function of nacelle angle η

Stability Derivative Y_v

The direct side force damping derivative Y_v derivative is depicted in Figure 4.14. The behavior of this derivative should be similar to the drag damping derivative X_u and the heave damping derivative Z_w, and thus should always be negative in order to have stable side force damping [2]. Subfigure (a), (b) and (c) show that this requirement is satisfied at a 90, 60 and 0 nacelle angle for all three models. During hover in H-mode the derivative is mainly determined by the rotor system which has a stabilizing contribution. There is however also a small destabilizing contribution from the wings due to rotor wake induced velocities. This contribution is significantly higher in hover when the nacelles are at a 80 degrees inclination. This causes an unstable side force damping at these conditions as seen in subfigure (d). When the airspeed increases the contribution of the vertical stabilizers increases which is stabilizing as well. The GTRS model shows an unexpected bump in the helicopter mode plot at 40 kts, which we also saw for the M_w derivative. The GTRS data shows that both the rotor and vertical stabilizers are stabilizing at this airspeed, but their contribution to the derivative is much smaller than at other airspeeds. It is hard to find an explanation for the bump in the graph and unfortunately no explanation about the data is given by Ferguson [6]. In conversion and airplane a similar linear trend is observable. The contribution of both the rotor system and the vertical stabilizers increases linearly with airspeed.

Besides the instability in hover, subfigure (d) shows that the Y_v derivative is barely affected by the nacelle angle. At high airspeeds a small decrease in value can be observed. The influence of the vertical stabilizers is barely affected by the nacelle angle, meaning that this small decrease is due to the rotor system side force component which increases with nacelle angle.

Stability Derivative Y_p

In Figure 4.15 the Y_p derivative has been plotted. Similar to X_q, the inertial trim velocity component w_0 contributes to the derivative and is also included in the graph. In helicopter mode the aircraft is trimmed at a negative angle of attack, which also means that w_0 is negative. As airspeed increases the velocity vector increases in magnitude and the angle of attack decreases resulting in an exponential grow of the w_0 component. This is also clearly visible for all three models in subfigure (a). The differences between the models are mainly due to the differences in trim angle of attack. For example, the trim angle of attack of the GTRS model at 100 kts is slightly lower than for the 6-DoF model (-12.6 versus -11.2 degrees). This

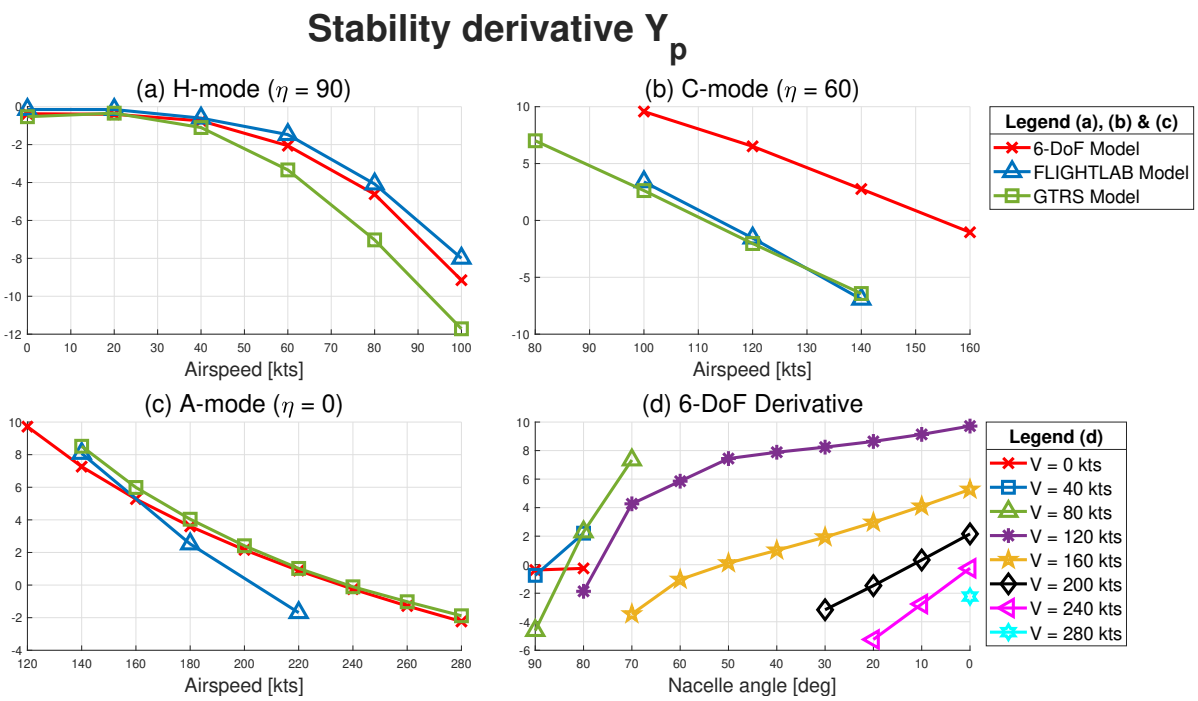

Figure 4.15: Stability derivative Y_p in helicopter mode, conversion mode and airplane mode, and as a function of nacelle angle η

means that the w_0 component of the former model is obviously significantly bigger than the latter, which explains the somewhat steeper curve of the GTRS model.

In conversion mode Y_p decreases with airspeed for the same reason as we saw in helicopter mode. The graphs all start at a positive value but cross the zero border at some point. At this point the angle of attack changes from positive to negative. For every model this moment happens at a different airspeed, hence the differences between them. Because the angle of attack is not constantly increasing in magnitude a linear trend can be observed instead of a exponential one. The 6-DoF curve is significantly higher than the GTRS curve. This could be expected because we saw in section 3.4 that the trim angle of attack at a 60 degrees nacelle angle of the model was also significantly higher than for the GTRS model. In airplane mode the three models show a lot of overlap.

As mentioned before, the angle of attack of the aircraft increases when the nacelles are tilted towards airplane mode while the airspeed is kept constant. Consequently, w_0 increases hence the positive slope observable in subfigure (d). At zero airspeed w_0 is obviously zero thus the graph merely shows the aerodynamic effects of Y_p which are relatively small.

Stability Derivative Y_r

The inertial velocity component u_0 completely dominates the Y_r derivative, making the aerodynamic effects almost negligible, as shown in Figure 4.16. In all flight modes a strong linear relationship with airspeed can be observed and the results of the three models almost perfectly coincide. When the nacelles are rotated towards airplane mode the contribution of the rotor system to Y_r increases. However, the inertial effect of u_0 is very dominant thus although there is small increase in value with decreasing nacelle angle this is barely visible in subfigure (d).

Stability Derivative L_v

One of the two most important sideslip derivatives is L_v, also called the dihedral stability derivative. If the aircraft is disturbed by a positive v perturbation the aircraft is deflected from its path to the right. This means that a negative roll response is required to bring the aircraft back on its path. Therefore it is desirable for stability that L_v is negative. This is the case for both convectional helicopters and airplanes, thus logically

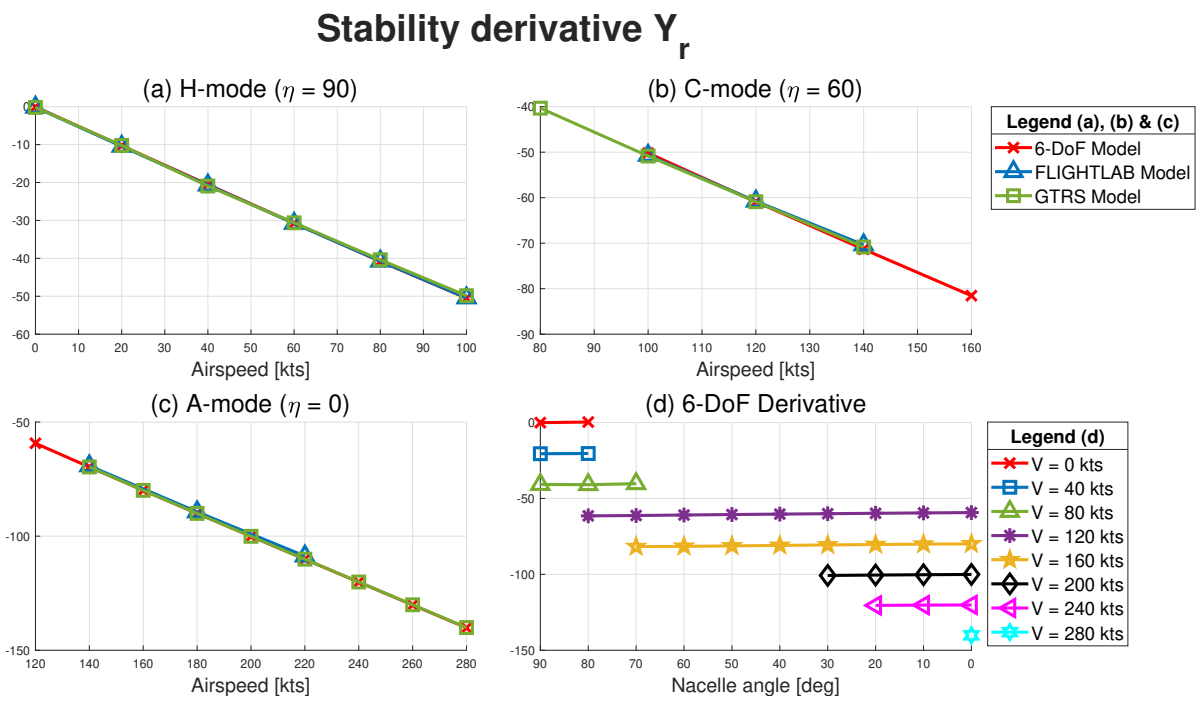

Figure 4.16: Stability derivative Y_r in helicopter mode, conversion mode and airplane mode, and as a function of nacelle angle η

this also applies to tiltrotor aircraft. The L_v curves of the models are shown in Figure 4.17. From subfigure (a) it can be concluded that the derivative is indeed negative in helicopter mode. The GTRS derivative curve has an unexpected peak at 40 kts which we also saw for the M_w and Y_v derivatives. For helicopters the main rotor is usually the main contributor to L_v [2]. This is also the case for the tiltrotor in H-mode according to the 6-DoF model results. The rotor contribution is the most dominant, while the vertical stabilizers also have a significant contribution. Both contributions are stabilizing. The rotor contribution remains fairly constant with airspeed, while the contribution of the vertical stabilizers increases. For the GTRS and FLIGHTLAB model curves a clear linear decrease with airspeed is found. For these models the contribution of the vertical stabilizers might be larger.

In conversion and airplane mode a similar linear decrease with airspeed is found for all three models. The vertical stabilizer is in these modes the main contributor to L_v. The contribution of the rotor decreases when the nacelle are tilted towards airplane mode. The thrust vector of the rotor which creates a rolling moment in helicopter mode is parallel with the rolling axis in airplane mode, meaning that the induced rolling moment vanishes. The contribution of the vertical stabilizers increases with nacelle angle while the rotor contribution decreases with a similar magnitude.. This explains why the derivative is roughly constant with nacelle angle as seen in subfigure (d).

Stability Derivative L_p

The roll-damping derivative plays an important roll in the short-term handling qualities about the x-axis. A positive perturbation in p should result in a restoring negative rolling moment L, meaning that L_p should be negative. The roll-damping derivatives have been plotted in Figure 4.18. Although this derivative is insensitive to speed for a conventional helicopter, the speed highly affects the tiltrotor roll damping derivative in all flight modes [4]. In subfigure (a) a clear decrease in L_p with airspeed is visible. In helicopter mode the two rotors are the dominant contributors to L_p. The contribution from the wings becomes increasingly more important with increasing airspeed which explains the decrease of the L_p curves.

In conversion mode the contribution of the wings becomes more important while the contribution of the rotor system decreases. This happens because the rotors become less aligned with the airflow resulting from a rolling motion. At a nacelle angle of 60 degrees the rotor system however still remains the biggest

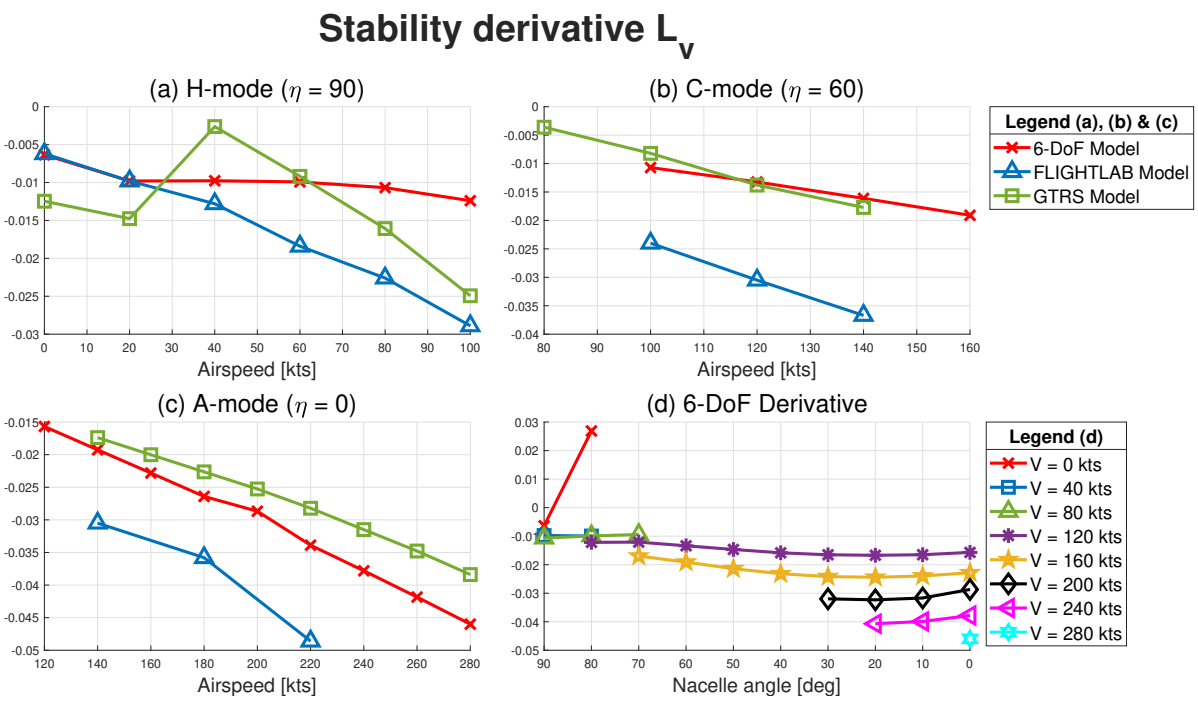

Figure 4.17: Stability derivative L_v in helicopter mode, conversion mode and airplane mode, and as a function of nacelle angle η

contributor. According to Lu et al. [4] and Berger et al. [3] the contribution of the rotor system is much smaller than the contribution of the wing in airplane mode. Johnson [23] however states that the rotor contributions to the roll damping derivative during cruise is of the same order as the contributions of the wings. Both the H-force and torque of the rotors have the same sign and contribute significantly to the roll damping in airplane mode. The latter claim is more in alignment with the results found for the 6-DoF model in A-mode. Although the contribution is the biggest in A-mode, the contribution of the rotor is still of the same order of magnitude. Even though the influence of the rotors on L_p is significant the entire flight envelope, its decrease of influence with nacelle angle is clearly visible subfigure (d). The derivative decreases in absolute value with decreasing nacelle angle.

Stability Derivative L_r

The stability derivative L_r couples the roll and yaw motions together with N_p. This derivative is positive in helicopter mode, mainly due to the contribution of the rotor system. Why the rotors have a positive contribution to N_r can be explained with the help of Figure 4.19. If the yaw rate r is positive the advancing blade of the left rotor has a higher velocity than the advancing blade of the right rotor. Therefore, the left rotor creates more lift than the right rotor, causing a positive rolling moment to the right. In Figure 4.20(a) the derivatives of the different models in helicopter mode are shown, which confirms that L_r is indeed possible in helicopter mode. The models show a very similar trend in this configuration. In hover the roll response to a perturbation in r is quite small, but as soon as the airspeed increases the derivative stabilizes around a value of 0.35. The contribution of the rotor decreases with airspeed while the the contribution of the vertical stabilizers increases at the same rate.

When the nacelles are tilted the rotor response to a positive yaw rate becomes a negative rolling moment instead of a positive one. Subfigure (b) shows that L_r is already negative at a nacelle angle angle of 60 degrees. There are some differences between the models in this configuration. The FLIGHTLAB curve decreases with airspeed while the other two models show an increase. For the 6-DoF model the negative rotor contribution significantly decreases when airspeed increases, causing an increase in L_r.

In airplane mode the opposite happens. The FLIGHTLAB curve is increasing while the other two curves are decreasing. The 6-DoF curve shows quite a steep decrease with airspeed. The wing and vertical stabilizers

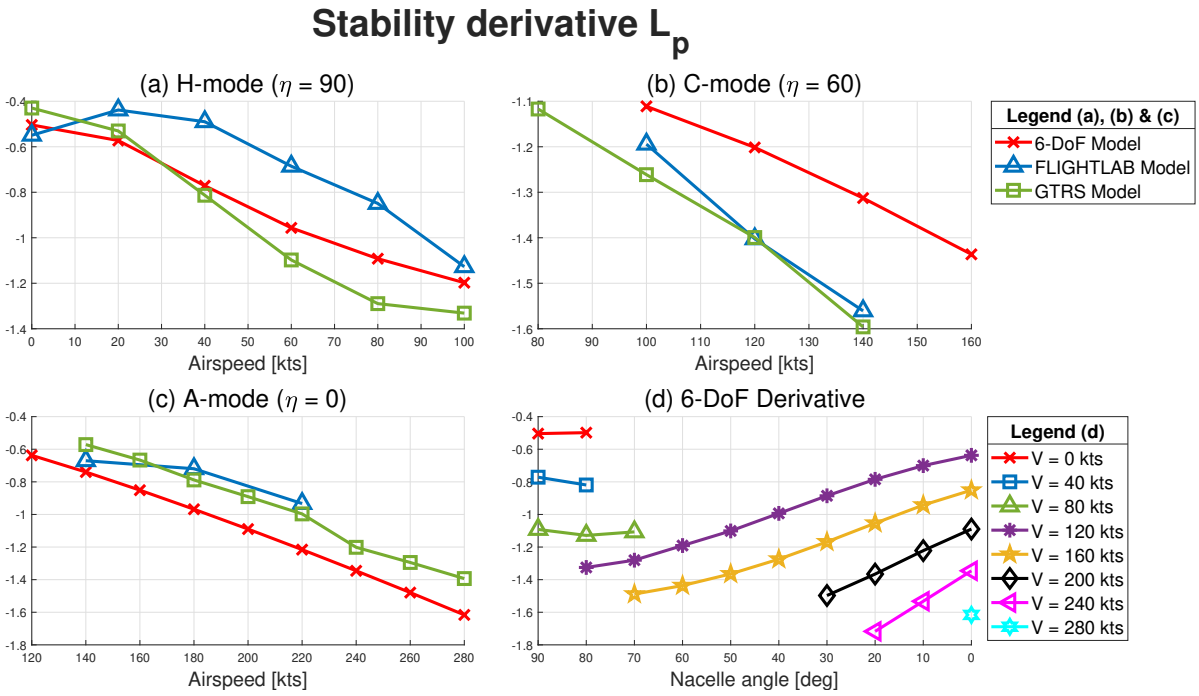

Figure 4.18: Stability derivative L_p in helicopter mode, conversion mode and airplane mode, and as a function of nacelle angle η

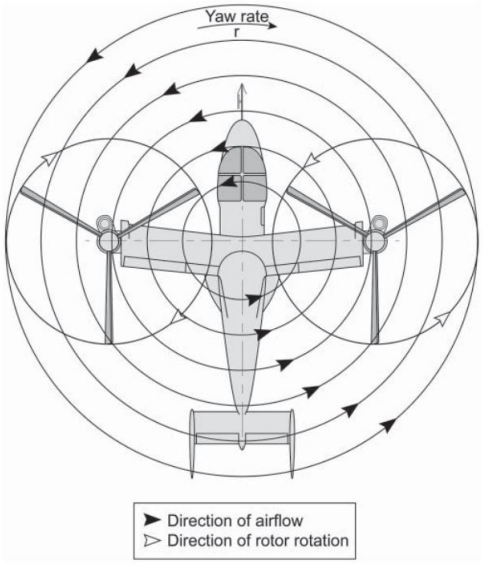

Figure 4.19: The in-plane velocity distribution of the tiltrotor in helicopter mode with a positive yaw rate leads to a positive L_r

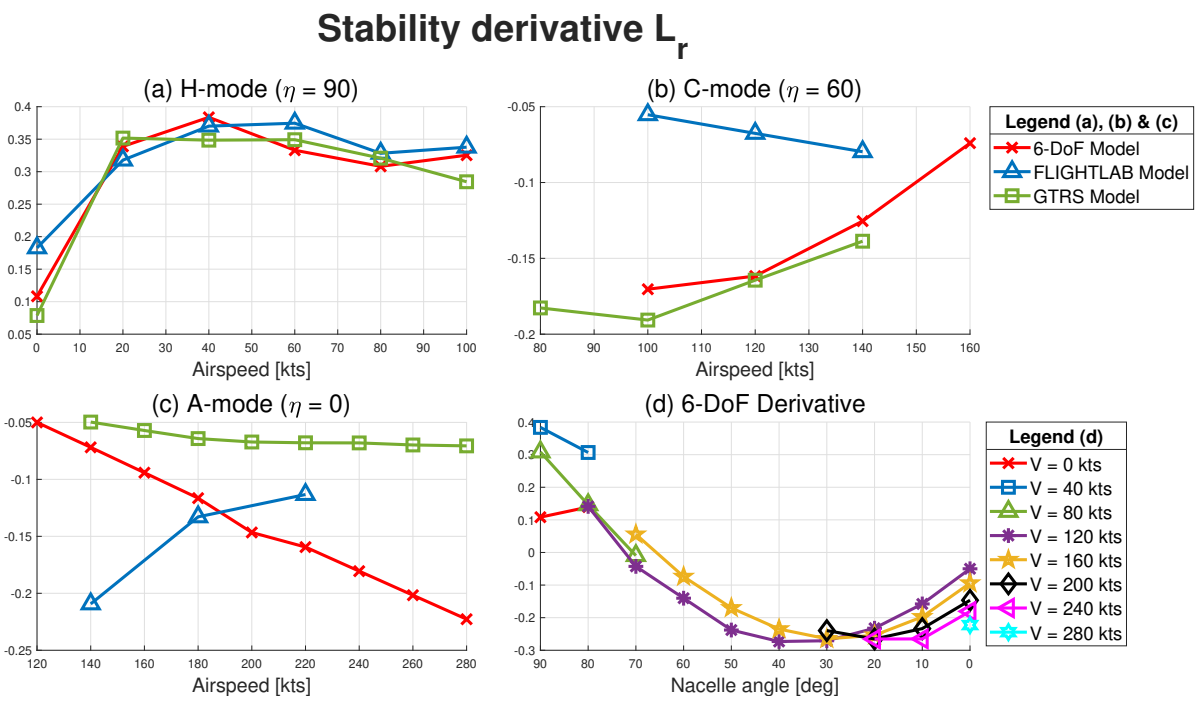

Figure 4.20: Stability derivative L_r in helicopter mode, conversion mode and airplane mode, and as a function of nacelle angle η

have a positive contribution to L_p, but the negative contribution of the rotors is dominant for the 6-DoF model. The influence of the rotors increases significantly with airspeed and this causes the decreasing L_p. In subfigure (d) the decrease of the positive rotor contribution with nacelle tilt is clearly visible. When the nacelles are almost in airplane mode the derivative starts increasing again. This mainly happens due to the increase in angle of attack with decreasing nacelle angle. An increase in angle of attack means that the lift force created by the wings increases and thus also its positive induced resultant moment.

Stability Derivative N_v

According to Padfield [2], the weathercock stability derivative N_v is critically important for both static and dynamic stability. This derivative basically defines the ability of the aircraft to turn in to the wind in order to maintain directional equilibrium [33]. Together with L_v they form the most important sideslip derivatives. A positive perturbation in the lateral velocity component v should result in restoring positive yawing moment meaning that N_v should be positive. Up to moderate airspeeds the derivative should be linear with airspeed [2]. Looking at Figure 4.21(a) this is indeed the case for the 6-DoF and FLIGHTLAB model in helicopter mode. The GTRS model once again shows a unexpected unstable derivative at 40 kts. The negative weathercock stability derivative value at this airspeed would mean that the aircraft is directionally/laterally unstable. For a helicopter this derivative is mainly determined by the tail rotor, the vertical fins and the fuselage. Since a tiltrotor does not have a tail rotor the latter two remain. Additionally, the rotors of the tiltrotor have a relatively large moment arm compared to a conventional helicopter which means that they could also have a significant contribution to N_v. The results of the 6-DoF model in helicopter mode indeed show that the weathercock stability derivative is dependent on the rotor system and the vertical stabilizers which are both stabilizing. The yawing moment created by the fuselage has not been modelled in the 6-DoF model so its contribution to N_v is missing.

In conversion mode a similar linear trend is apparent. The vertical stabilizers have a contribution of approximately 90%, while the rotor system covers the other 10%. The former has a stabilizing effect while the latter in this configuration is destabilizing. In airplane mode the destabilizing contribution of the rotor increases to up to 20%. While the induced negative yawing moment by the rotor system increases when the nacelles are rotated towards airplane mode, the positive moment created by the vertical stabilizers increases as well. The latter increases slightly more which causes an increase of N_v with decreasing nacelle angle. This explains the

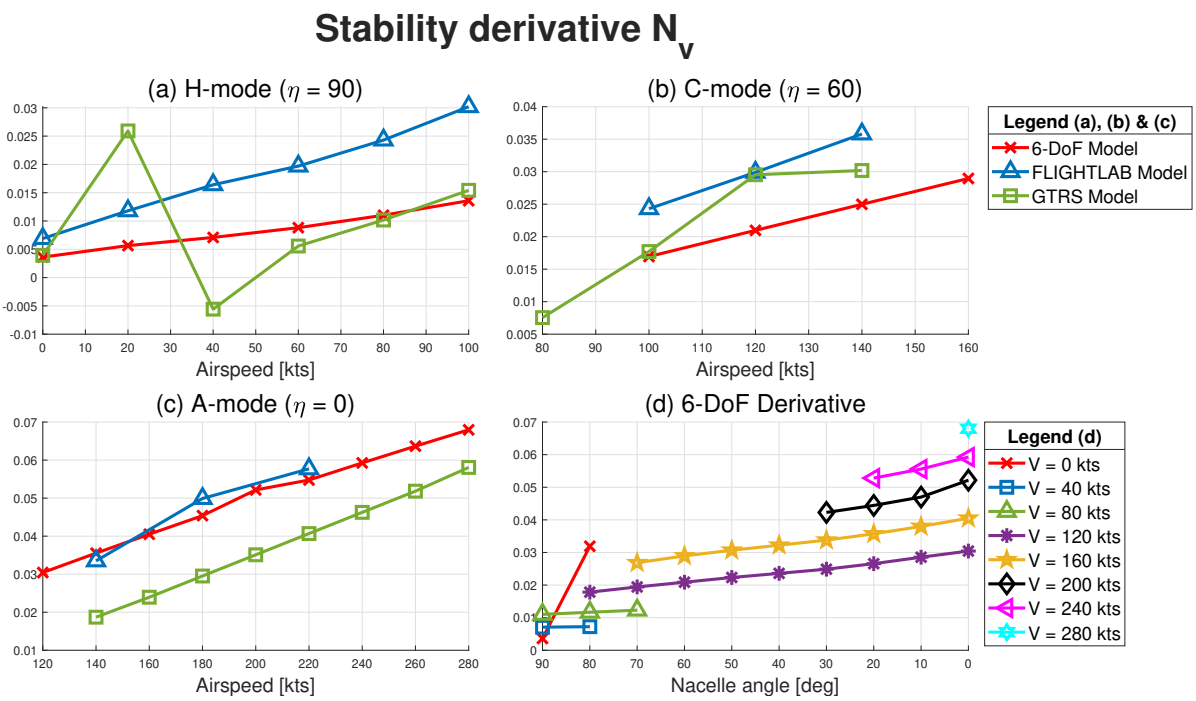

Figure 4.21: Stability derivative N_v in helicopter mode, conversion mode and airplane mode, and as a function of nacelle angle η

increasing curves in Figure 4.21(d).

Stability Derivative N_p

The second derivative that couples roll and yaw motions is the N_p derivative. The coupling effects of N_p are more significant than those of L_r according to Padfield [2]. For a conventional helicopter we know that N_p is negative. Large negative values of N_p causes strong adverse yaw effects. Adverse yaw is the tendency to yaw into the opposite direction of the roll. In Figure 4.22(a) the N_p curves of the three different models in helicopter mode are compared. The tiltrotor derivative is positive for all models, which is different than what we know from conventional helicopters. The rotors and vertical stabilizers mainly determine the value of N_p, and both have a positive contribution in H-mode. The 6-DoF model curve shows significantly lower values of N_p than the other two models.

In conversion mode the derivative is negative instead of positive. The rotors have a negative contribution to N_p and mainly determine its value. The wings also have a negative contribution while the vertical stabilizers contribution is positive. The FLIGHTLAB and 6-DoF derivatives are roughly constant with airspeed while the GTRS shows quite a strong increase. In airplane mode the contribution of the vertical stabilizers has increased. The negative contribution of the rotors and the positive contribution of the vertical stabilizers grow at the same rate with airspeed which explains the roughly constant N_p. In subfigure (d) it is clearly visible that the rotor contribution decreases in value when the nacelles are tilted towards A-mode. Up to 30 degrees N_p decreases due to the rotor influence. Thereafter the rotor contribution increases again, which is why N_p increases as well.

Stability Derivative N_r

The yaw damping derivative is depicted in Figure 4.23. A positive yawing rate r should create a negative restoring yawing moment N, thus N_r should be negative. In subfigure (a) it can be seen that the yaw damping derivative decreases linearly with speed. The GTRS model has an unstable yaw-damping derivative at 40 kts. For a conventional helicopter the tail rotor is the main contributor to the yaw damping, especially at low velocities. Since the tiltrotor has no tail rotor the magnitude of the yaw damping is very small at low airspeeds causing an unstable spiral mode [3]. The stabilizing contribution of the vertical stabilizers increases

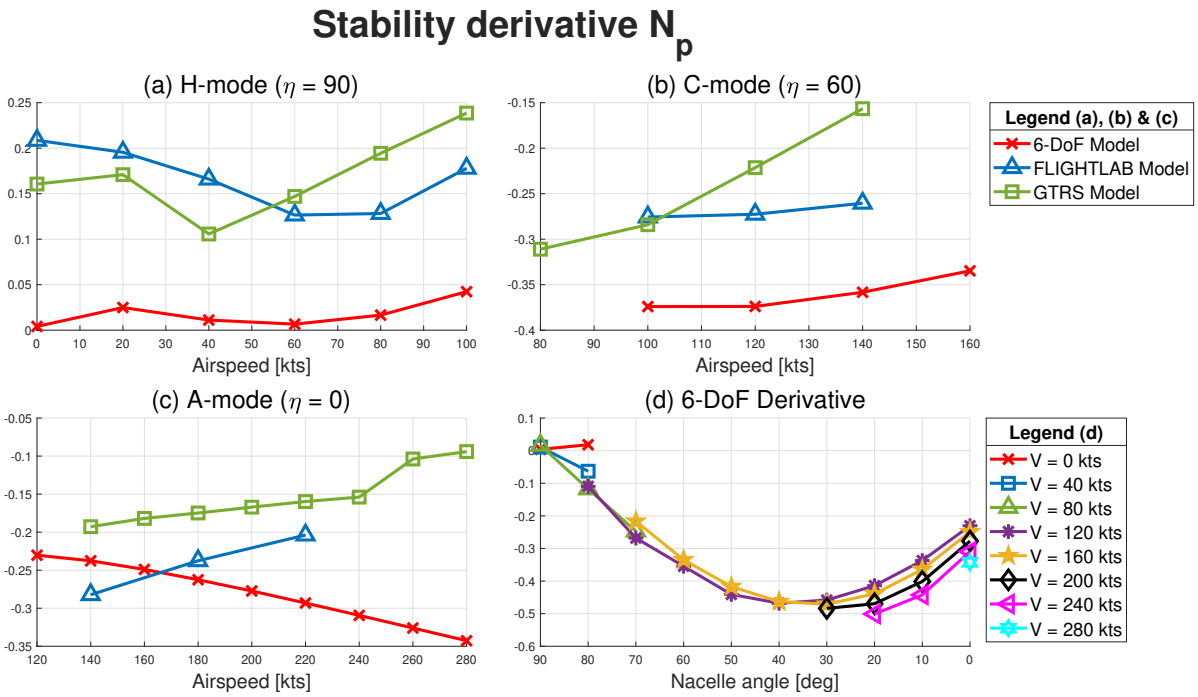

Figure 4.22: Stability derivative N_p in helicopter mode, conversion mode and airplane mode, and as a function of nacelle angle η

when the airspeed increases.

In airplane mode yawing moment created by the rotors is almost constant with airspeed. The negative moment created by the vertical stabilizers increases however, which explains the decrease of N_r with airspeed. The GTRS curve shows a similar rate of decrease with airspeed. The FLIGHTLAB curve remains fairly constant. In general, when the nacelles are tilted forward the stabilizing effect of the proprotors to the yaw damping increases as the thrust force becomes aligned with the airflow resulting from a yawing motion. This increase in yaw damping with decreasing nacelle angle is clearly visible in subfigure (d).

4.3. The Control Derivatives

In this subsection the control derivatives of the linearized 6-DoF model are elaborated upon. The control derivatives are shown in the B matrix of Equation 4.12 Similar to the stability derivatives the control derivatives are analysed as a function of airspeed and nacelle angle. In order to see whether the results make sense, they are compared to the FLIGHTLAB results [2]. All control derivatives have been converted to the units shown in Table 4.2. Firstly the longitudinal control derivatives are analysed. Thereafter, the lateral/directional control derivatives.

Force/control angle	e.g. X_{θ_0}	$m/s^2/rad$
Moment/control angle	e.g. M_{θ_0}	$1/s$

Table 4.2: Units of the control derivatives

4.3.1. Longitudinal Control Derivatives

In this section the longitudinal control derivatives of the XV-15 are discussed. The outcomes of the 6-DoF model are compared with those of the FXV-15 [2]. The collective stick and longitudinal movement of the cyclic stick provide the longitudinal control in the XV-15. Collective pitch control is used in helicopter mode to ascent or descent while longitudinal cyclic control is used to alter the tip-path plane and move the aircraft horizontally. When the nacelles are tilted towards airplane mode the longitudinal cyclic control vanishes

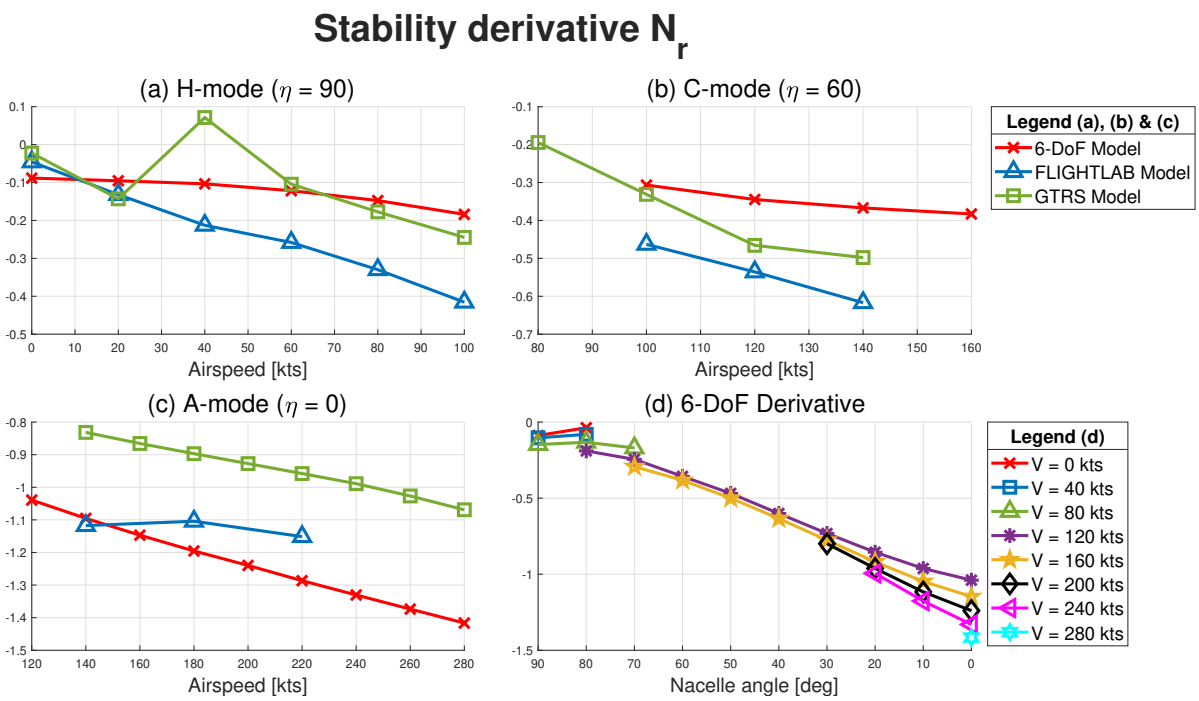

Figure 4.23: Stability derivative N_r in helicopter mode, conversion mode and airplane mode, and as a function of nacelle angle η

and elevators are used instead for pitch control. The longitudinal derivatives with respect to the blade-root collective pitch angle θ_0, the longitudinal cyclic angle θ_{1s} and the elevator deflection δ_e are discussed respectively.

Control Derivatives with respect to θ_0

By increasing the blade-root pitch angle θ_0 the total average blade pitch increases. This means that the blades create more lift and thus the total rotor thrust force is increased. In Figure 4.24 the longitudinal derivatives with respect to θ_0 are shown. On the left side the derivatives are shown as a function of airspeed with the nacelle angle kept constant. The results for both the 6-DoF model and the FLIGHTLAB model are shown in H-mode ($\eta = 90\text{deg}$), C-mode ($\eta = 60\text{deg}$) and A-mode ($\eta = 0\text{deg}$). In helicopter mode the thrust vector points in negative Z-direction. The thrust force increases when θ_0 increases, so Z_{θ_0} should be negative in H-mode. This is indeed the case, as shown in subfigure (b1). The derivatives for both models look very alike. At a nacelle angle of 60 degrees the Z-component of the thrust force is still dominant. When the nacelles are however rotated to A-mode, the thrust is more aligned with the X-axis. This explains the smaller value of Z_{θ_0} and bigger value of X_{θ_0} in this configuration. On the right figures the same derivatives of the 6-DoF model are shown as a function of nacelle angle with the airspeed V kept constant. The decrease of Z_{θ_0} and increase of X_{θ_0} is also clearly visible in these figures.

The M_{θ_0} derivative seems to be almost independent of airspeed, but quite dependent on nacelle angle. The derivative is positive in H-mode, but becomes increasingly negative with decreasing nacelle angle. An increase in thrust results in a positive pitching up moment when η equals 0 degrees. When the nacelles are rotated the moment arm of the thrust force decreases until the line of action passes through the centre of gravity of the aircraft and the induced moment equals zero. When the nacelles are rotated further and negative pitching moment is created and while the moment arm increases M_{θ_0} decreases.

Control Derivatives with respect to θ_{1s}

Symmetric longitudinal cyclic control is used in helicopter mode to move the aircraft horizontally. Simultaneously increasing the longitudinal cyclic angle on both rotors causes the tip-path plane to tilt forward resulting in an increase in forward speed [31]. This means that the resultant force along the X-axis increases, thus $X_{\theta_{1s}}$ should be positive. In the top left corner of Figure 4.25 it can be seen that this is indeed the

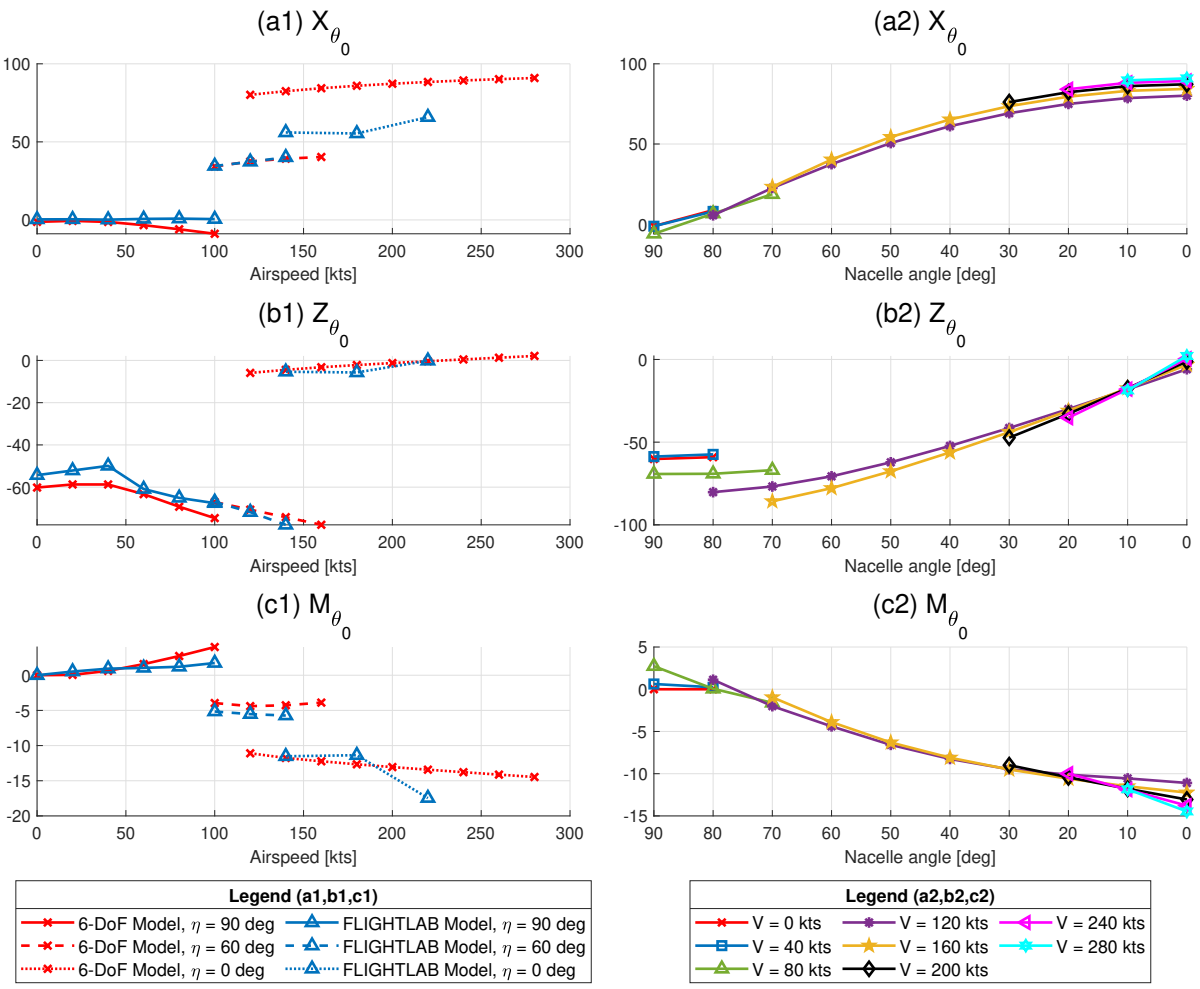

Figure 4.24: Control derivatives with respect to the collective pitch angle θ_0

case for both models in H-mode. The derivative appears to be almost independent of airspeed. At a nacelle incidence of 60 degrees we suddenly see a negative value for this derivative. An increase in θ_{1s} still causes the thrust vector to tilt forward but simultaneously the total thrust force drops. This results in a negative derivative for the 6-DoF model in this configuration and the FLIGHTLAB curve shows similar behavior. In airplane mode the derivative is negative at low airspeeds but increases with airspeed. The derivatives with respect to θ_{1s} are however meaningless in airplane mode, because the longitudinal cyclic angle is fixed in this configuration.

By tilting the tip-path plane forward in helicopter mode the Z-component of the the rotor which is negative decreases in magnitude. This causes the resultant Z-force to increases which means that $Z_{\theta_{1s}}$ is positive. A clear increase in value with airspeed is seen in subfigure (b1). The results for this derivative in helicopter mode and conversion mode look very similar. In airplane mode the models show clearly different results. These curves are however meaningless because θ_{1s} is fixed in A-mode. Graph (b2) shows that the derivative is almost constant with nacelle angle at low speeds. At higher speeds in a low nacelle angle configuration a small decrease can be observed.

Looking at the $M_{\theta_{1s}}$ curves we see that a negative pitching is induced when θ_{1s} increases. This pitching moment is approximately constant with airspeed but gets smaller when the nacelles are rotated towards A-mode. When the nacelles are almost aligned with the wings the derivative decreases again.

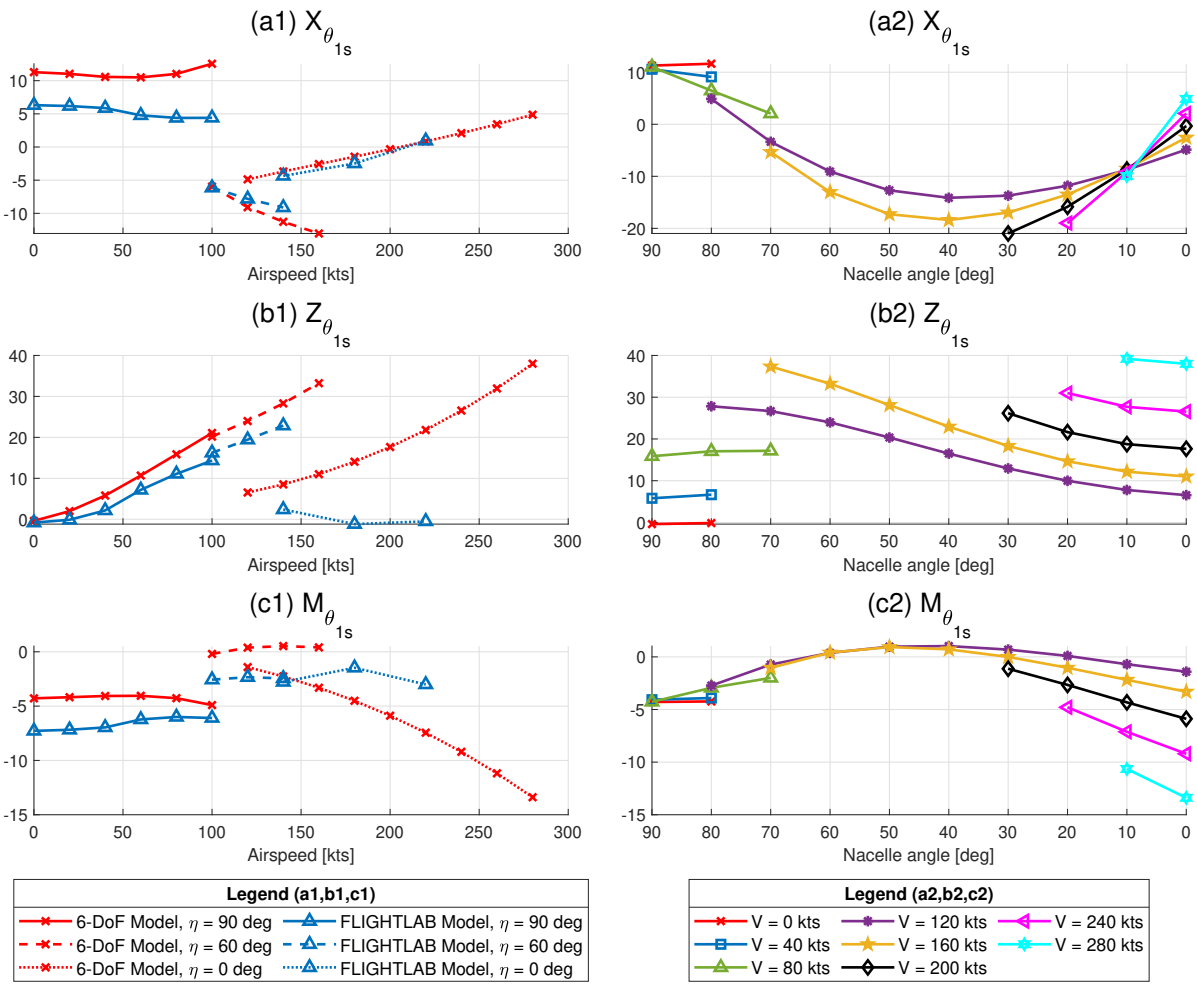

Figure 4.25: Control derivatives with respect to the longitudinal cyclic angle θ_{1s}

Control Derivatives with respect to δ_e

The longitudinal control derivatives with respect to the elevator deflection are shown in Figure 4.26. Downward deflection of the elevator is defined as positive. The 6-DoF and FLIGHTLAB model X_{δ_e} derivative clearly deviate a lot; the FLIGHTLAB derivative is approximately a factor 10 larger. The drag of the elevator is not incorporated in the 6-DoF model which is most likely the reason for this distinction. This means that the change in lift force created by the elevator is the only contributor to this derivative. The change in lift force due to the elevator increases with airspeed, which is also clearly visible in the graphs. The following relationship for Z_{δ_e} can be derived from the 6-DoF model:

$$\frac{dZ}{d\delta_e} = -\frac{1}{2}\rho V_{hs}^2 S_{hs} \frac{dC_{L,hs}}{d\delta_e} \cos\alpha_{hs} \tag{4.20}$$

The derivative grows proportionally with V^2. The same goes for the M_{δ_e} derivative. The nacelle angle has no influence on the derivative at all.

4.3.2. Lateral/directional Control Derivatives

The lateral/directional control derivatives will be analysed in a very similar manner as the longitudinal ones which were treated in the previous section. In helicopter mode, differential collective pitch θ_{0d} is used to control roll and differential cyclic pitch θ_{1s} to control yaw. In airplane mode the ailerons and rudders are used to control roll and yaw respectively. All lateral/directional control derivatives with respect to these four controls are discussed in this section.

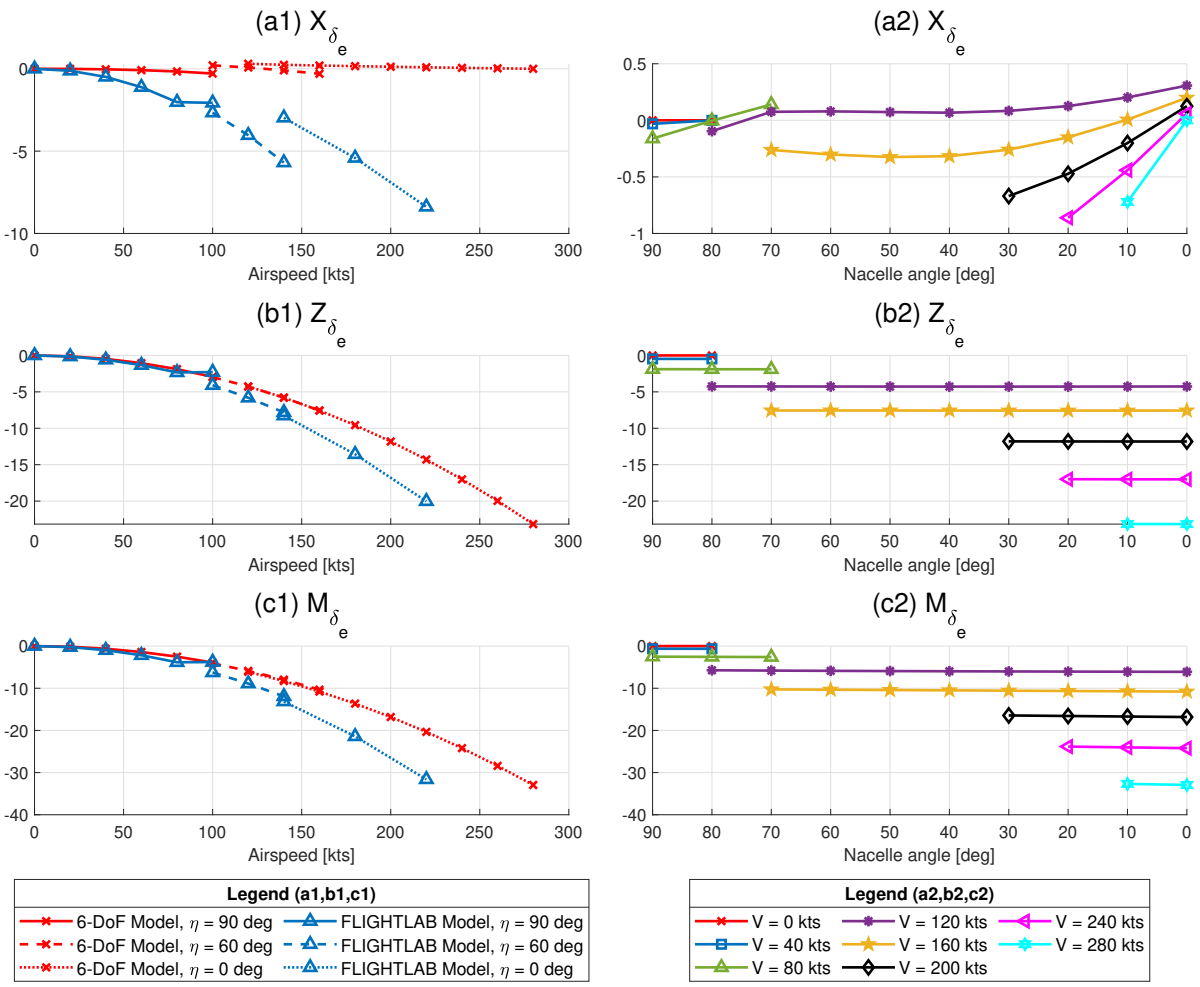

Figure 4.26: Control derivatives with respect to the elevator deflection angle δ_e

Control Derivatives with respect to θ_{0d}

Differential collective θ_{0d} is used to generate a rolling motion in helicopter mode. An increase and decrease of the collective pitch on the right and left rotor respectively is defined as a positive differential collective control input. The top two figures of Figure 4.27 represent the $Y_{\delta_{0d}}$ derivative. A clear difference in derivative magnitude between the models can be observed. The FLIGHTLAB derivative is between a factor 10 and 100 larger than the 6-DoF derivative. The FLIGHTLAB model has implemented a gimballed rotor hub while the 6-DoF assumes an articulated rotor hub. The lateral hub forces are significantly higher for a gimballed hub compared to an articulated hub [2], which could explain this difference in magnitude.

The middle two figures of Figure 4.27 show the rolling moment as a response to a differential collective input. If the right rotor collective is higher than the left rotor collective the right rotor creates more lift. This leads to a negative rolling moment L which is why $L_{\theta_{0d}}$ is negative. When the nacelles rotate towards A-mode the derivative significantly decreases in magnitude. The FLIGHTLAB derivative is approximately three times larger than the 6-DoF model derivative. This difference is also most likely due to the higher in-plane forces of the gimballed rotor hub which also create a significant rolling moment.

The bottom two plots show the yawing moment due to differential collective derivative $N_{\theta_{0d}}$. This derivative has a similar order of magnitude as $L_{\theta_{0d}}$ but is small in H-mode and large in A-mode. This makes sense because in airplane mode the thrust vector is more aligned with the yawing motion. This derivative however appears to be less dependent on airspeed, concluding from the horizontal trends in the left graph.

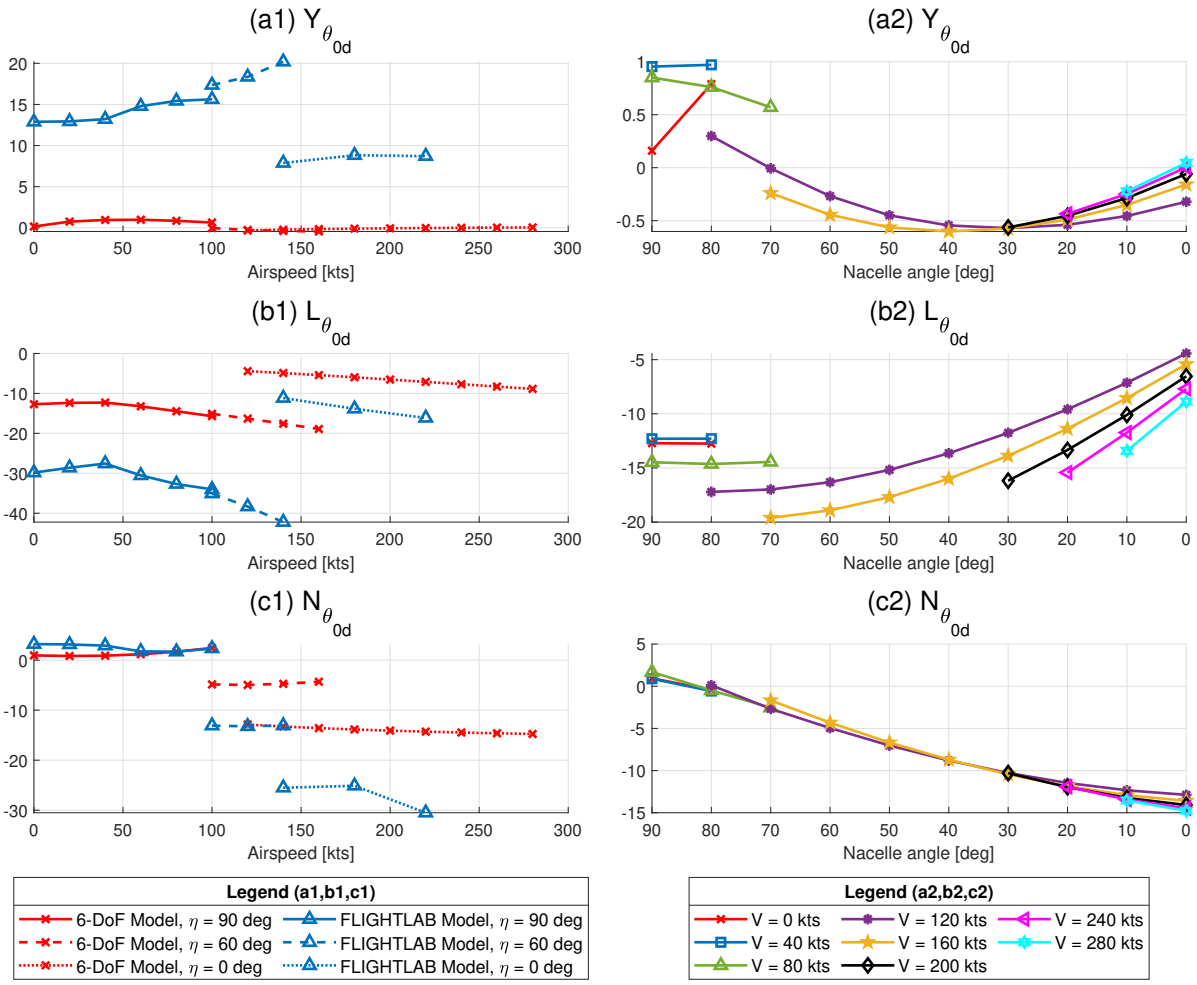

Figure 4.27: Control derivatives with respect to differential collective pitch angle θ_{0d}

Control Derivatives with respect to δ_a

In airplane mode the rolling motion of the XV-15 can be controlled using the ailerons. If the right aileron is deflected downward and the left aileron upward δ_a is defined positive. In the top left corner of Figure 4.28 Y_{δ_a} is shown as a function of airspeed. The lateral force created by aileron deflection is approximately zero for straight wings [34], but since the XV-15 has a swept wing this derivative is nonzero. There are some clear differences between the 6-DoF and FLIGHTLAB derivative. First of all, in hover the FLIGHTLAB derivative is zero while the 6-DoF derivative is nonzero. The flight speed is equal to zero but the rotor wake interference with the wing induces aerodynamic forces. Therefore it makes perfect sense that the 6-DoF derivative is nonzero. When airspeed increases the FLIGHTLAB derivative increases wile the 6-DoF derivative decreases. The Y-component of the lift forces created by the ailerons has a negative contribution to the derivative which is why the 6-DoF derivative is negative. The drag of the aileron is not incorporated in the 6-DoF model but most likely is in the FLIGHTLAB model. This could be a possible explanation for the differences in sign between the models. Nevertheless, the influence of Y_{δ_a} on the flight dynamics is very small and often is usually neglected [34].

A much more important derivative is L_{δ_a}. As mentioned earlier, a positive aileron deflection means that the right aileron is deflected downward and the left aileron upward. The result of this deflection is that the right wing will produce more lift than the left wing, resulting in a negative rolling moment L. The derivative can analytically be defined as:

$$L_{\delta_a} = \frac{\delta L}{\delta ail} = \frac{\delta C_L}{\delta_a} \frac{1}{2} \rho V^2 S_a b_a \tag{4.21}$$

This equation shows that L_{δ_a} decreases proportionally with V^2, which is also clearly visible in subfigure (b1) for both models. The magnitude of the derivative is also dependent on $\frac{\delta C_L}{\delta_a}$, which is defined as the aileron effectiveness. The magnitude of $\frac{\delta C_L}{\delta_a}$ strongly depends on the dimensions and the spanwise location of the ailerons [34]. Since both models consider the XV-15 as reference aircraft the aileron effectiveness should be equal. The fact that there is a clear distinction between the steepness of the curves, primarily at high airspeeds indicates that most likely different values for the aileron effectiveness are used.

If the lift over the right wing increases the drag increases on that side as well, while both aerodynamic forces at the left wing decrease. Consequently, the right wing is pulled back and a positive yawing moment is created. If the pilot wants to turn left he/she deflects the lateral cyclic stick to the left which creates a positive aileron deflection. This initiates a negative rolling moment but simultaneously a positive yawing moment. This unwanted yawing response of the aircraft is called 'adverse yaw'. Since the drag of the aileron is not modelled in the 6-DoF model this adverse yaw effect is not expected to be visible in simulations. In subfigure (c1) the yaw derivative with respect to aileron deflection N_{δ_a} is plotted as a function of airspeed. The 6-DoF derivative is small compared to the FLIGHTLAB one which is expected since it is only dependent on the lift force created by the aileron. The behavior of the FLIGHTLAB derivative is also somewhat unexpected. The derivative appears to be heavily dependent on the nacelle angle and increases from negative to positive in C-mode and A-mode.

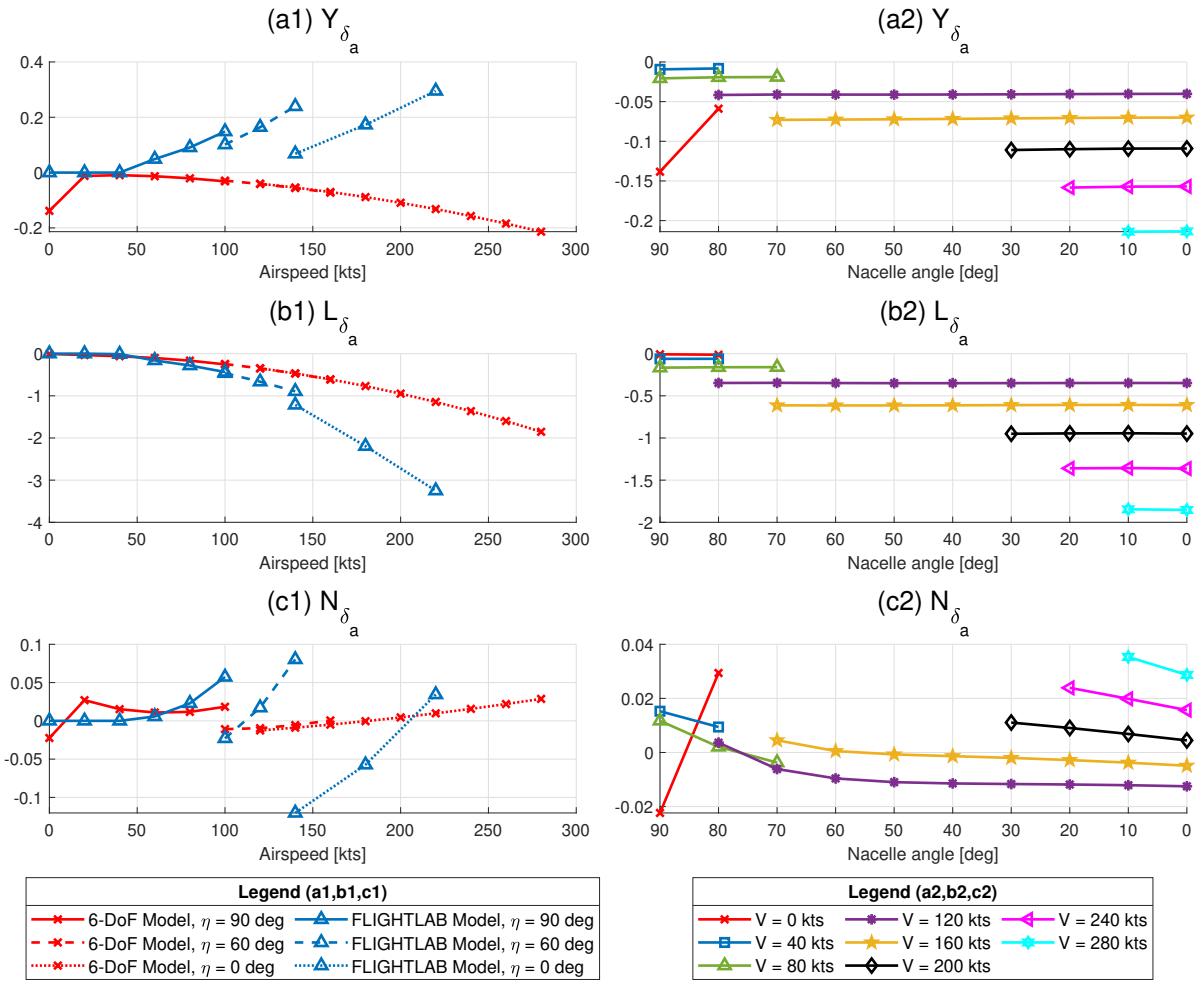

Figure 4.28: Control derivatives with respect to the aileron deflection angle δ_a

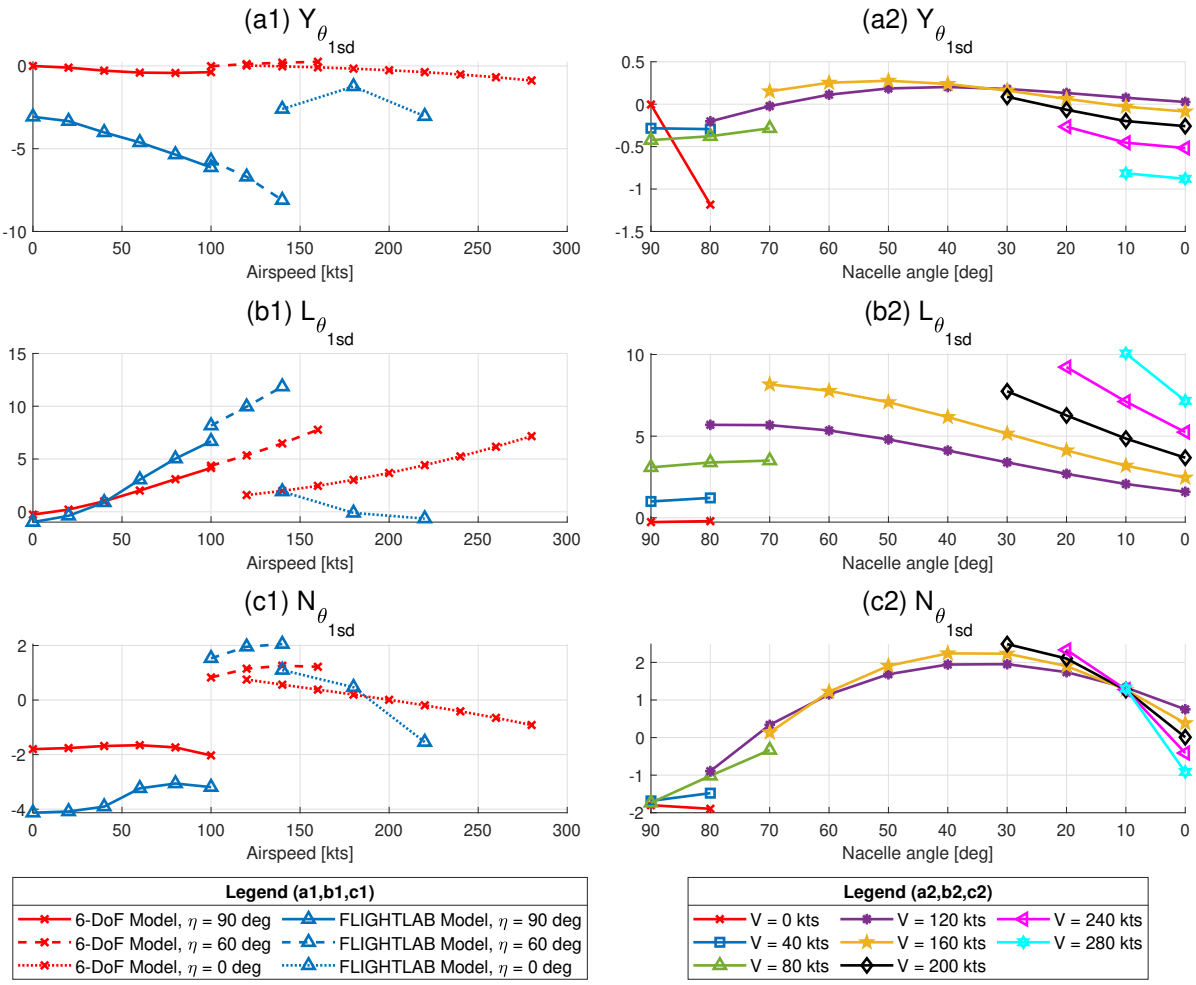

Figure 4.29: Control derivatives with respect to differential longitudinal cyclic angle θ_{1sd}

Control Derivatives with respect to θ_{1sd}

In Figure 4.29 the derivatives with respect to differential longitudinal cyclic θ_{1sd} are plotted. Differential longitudinal cyclic is used at low airspeeds to control yaw. An increase and decrease of the longitudinal cyclic on the right and left rotor respectively is defined as a positive differential longitudinal cyclic input. In the top two figures $Y_{\theta_{1sd}}$ is shown. Similar to $Y_{\theta_{0d}}$ there is huge discrepancy between the two models. The FLIGHTLAB derivative is a factor 10-100 larger in magnitude. The most logical explanation for this difference is the different hub incorporated in the models. The gimballed hub modelled in FLIGHTLAB is expected to create larger in-plane forces than the articulated hub used in the 6-DoF model.

The $L_{\theta_{1sd}}$ curve shows some similarities between the models. In helicopter and conversion mode the derivative is positive and increases with airspeed. When the right rotor increases its longitudinal cyclic its thrust vector is tilted forward while the left rotor thrust vector is tilted aft. An increase in longitudinal cyclic however decreases the total force created by the rotor. Therefore the left rotor creates a larger thrust force than the right rotor which results in a positive rolling moment. In airplane mode the longitudinal cyclic angle is fixed so the airplane curves can be neglected. From graph (b2) it can be concluded that the derivative is somewhat constant as a function of nacelle angle. At high nacelle angles a small decrease can be observed.

Since the main purpose of differential longitudinal cyclic is to control the yawing motion of the aircraft $N_{\theta_{1sd}}$ is its primary derivative. When a positive θ_{1sd} input is initiated the thrust vector on the right side is tilted forward and decreases in magnitude. Simultaneously the thrust vector on the left rotor is tilted aft and increases in magnitude. In helicopter mode the thrust vectors have a negative X-component thus both the tilting and change in magnitude of the vectors contribute to a negative yawing moment. It can be seen that

the curves of both models for $N_{\theta_{1sd}}$ are indeed negative in H-mode. When the nacelles are tilted forward the thrust vectors are also tilted forward resulting in a positive X-component. The consequence of this change in sign is that the change in thrust magnitude of the rotors now has a positive contribution to $N_{\theta_{1sd}}$. The tilting of the vectors still has a negative contribution to the derivative but the former mentioned contribution is larger, resulting in a positive $N_{\theta_{1sd}}$ after a certain nacelle tilt. This effect is also clearly visible in subfigure (c2). At low nacelle angle configurations the derivative decreases again, but $N_{\theta_{1sd}}$ is less meaningful at low values of η because differential longitudinal cyclic control is phased out towards A-mode.

Control Derivatives with respect to δ_r

In airplane mode directional control of the XV-15 is achieved using rudders. The XV-15 has two vertical stabilizers which both have a rudder mounted on the top half. A positive rudder deflection creates a lateral force in positive Y-direction. Therefore Y_{δ_r} is positive. The derivative (before normalization) can be computed using [34]:

$$Y_{\delta_r} = \frac{\delta Y}{\delta_r} = \frac{\delta C_L}{\delta_r}\frac{1}{2}\rho V^2 S \tag{4.22}$$

This equation shows that the derivative grows proportionally with V^2 and this is also clearly visible in Figure 4.30 (a1). The FLIGHTLAB curve is a bit steeper than the 6-DoF model curve which indicates that a different $\frac{\delta C_L}{\delta_r}$ is used. A similar difference is visible for the L_{δ_r} derivative. This is not surprising since L_{δ_r} (before normalization) can be approximated using:

$$L_{\delta_r} = Y_{\delta_r} d_{z,vs} \tag{4.23}$$

We know Y_{δ_r} is positive and since the vertical stabilizers are located higher than the body centre of gravity $d_{z,vs}$ is also positive. Therefore L_{δ_r} is logically also positive. Since the rudders are used for yaw control N_{δ_r} is the primary rudder derivative. This derivative (before normalization) can be approximated using:

$$N_{\delta_r} = -Y_{\delta_r} d_{x,vs} \tag{4.24}$$

Both Y_{δ_r} and $d_{x,vs}$ are positive so N_{δ_r} is negative. Furthermore, from the three graphs on the right hand side of Figure 4.30 it can be concluded that the nacelle angle does not affect the rudder control derivatives.

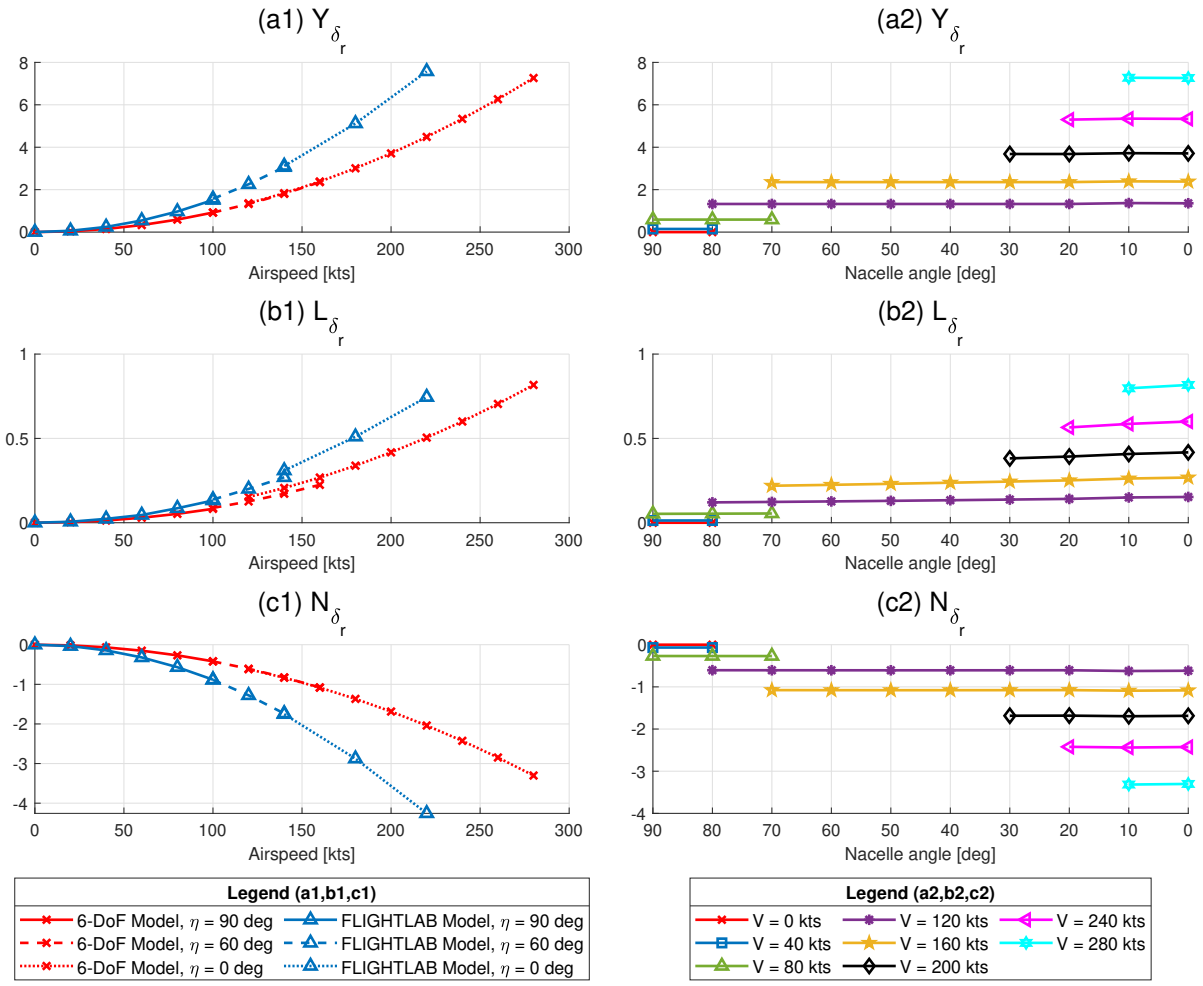

Figure 4.30: Control derivatives with respect to the rudder deflection angle δ_r

5

Natural Eigenmodes

The dynamic stability of an aircraft can usually be described by two different subsets. The first subset contains the longitudinal motions, which can be described using the surge (u), heave (w) and pitch (q) states of the aircraft. The second subset contains the lateral/directional modes, described by the sway (v), roll (p) and yaw (r) states. The coupling between these two subsets is usually small for conventional aircraft and can thus be neglected. Helicopters are much more affected by this coupling, primarily at low speeds. Nevertheless, for describing the dynamic modes of both type of aircraft the assumption that the coupling between the subsets is small is usually made. This allows the simplification of the linearized equations of motion.

For a tiltrotor the uncoupling of the two types of modes is also assumed to be valid. In section 5.1 the longitudinal eigenmodes are analysed. The variation of the eigenvalues with airspeed and nacelle angle are investigated and how this variation affects the stability of the aircraft. In section 5.2 a similar analysis is conducted on the lateral/directional modes. To verify the validity of the uncoupling of the modes the results of the full linear model are compared with the uncoupled models in section 5.3. Furthermore, the results of the 6-DoF model are compared with data from the FLIGHTLAB model for validation purposes.

5.1. Uncoupled Longitudinal Modes

It is assumed that the longitudinal eigenmodes can be described by using only the longitudinal aircraft states. This means that the state vector can be simplified to the following form

$$x = [u, w, \theta, q]^T \tag{5.1}$$

This reduces the full 8x8 state space system given by Equation 4.12 to the following simplified 4x4 form

$$\begin{bmatrix} \dot{u} \\ \dot{w} \\ \dot{\theta}_f \\ \dot{q} \end{bmatrix} = \begin{bmatrix} X_u & X_w & -g\cos(\theta_0) & X_q - w_0 \\ Z_u & Z_w & -g\sin(\theta_0) & Z_q + u_0 \\ 0 & 0 & 0 & 1 \\ M_u & M_w & 0 & M_q \end{bmatrix} \begin{bmatrix} u \\ w \\ \theta \\ q \end{bmatrix} + \begin{bmatrix} X_{X_{COL}} & X_{X_{LON}} \\ Z_{X_{COL}} & Z_{X_{LON}} \\ 0 & 0 \\ M_{X_{COL}} & M_{X_{LON}} \end{bmatrix} \begin{bmatrix} X_{COL} \\ X_{LON} \end{bmatrix} \tag{5.2}$$

For the analysis of the natural modes the free response of the aircraft is of interest meaning a disturbance to one of the aircraft states. Therefore the controls are assumed fixed and only the first matrix is of interest. This reduces the system to the following from

$$\dot{\mathbf{x}} = \mathbf{A}\mathbf{x} \tag{5.3}$$

To analyse the stability of this system the eigenvalues have to be computed. The eigenvalues can be found using

$$\mathbf{A} - \lambda\mathbf{I} = \mathbf{0} \tag{5.4}$$

The eigenvalues of the longitudinal state space model represent the phugoid, the short-period and the heave and pitch modes. The heave and pitch mode merge together to form the short period when the airspeed increases. Firstly, this short period will be discussed, after which the phugoid will be analysed.

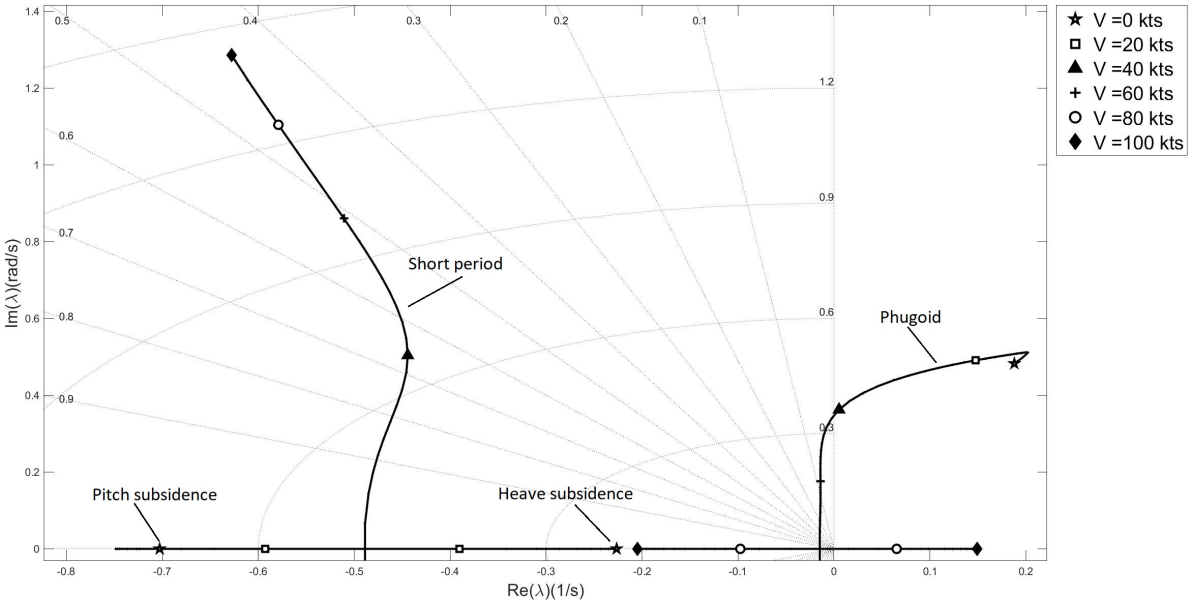

Figure 5.1: XV-15 uncoupled longitudinal eigenmodes in helicopter mode ($\eta = 90\text{deg}$)

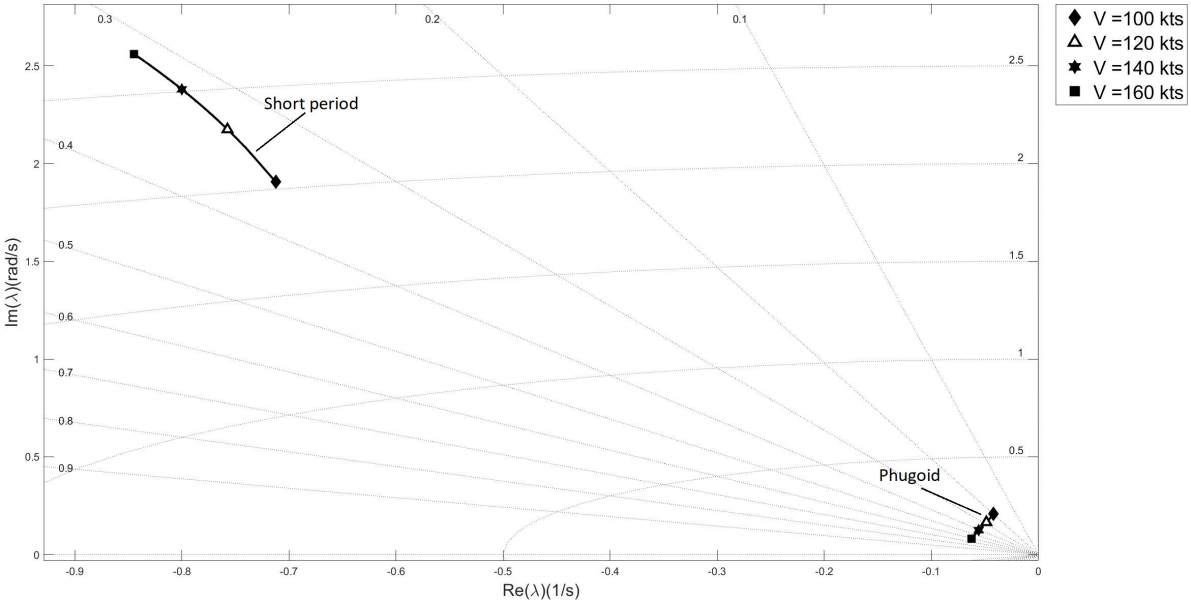

Figure 5.2: XV-15 uncoupled longitudinal eigenmodes in conversion mode ($\eta = 60\text{deg}$)

5.1.1. Short period

The short period is a relatively highly damped oscillatory dynamic mode, which consists of a pitching and heaving motion [35]. At low airspeeds in helicopter mode the short period is split up in these two subsidences. Their eigenvalues are located on the real axis. In Figure 5.1 the eigenvalues in helicopter mode are shown. The different dynamic modes are indicated in the figure. The real eigenvalue on the left is the pitch subsidence, the one on the right the heave subsidence. In order to validate the results, the 6-DoF model eigenvalues of these motions in hover are compared to the results of other models in Table 5.1.

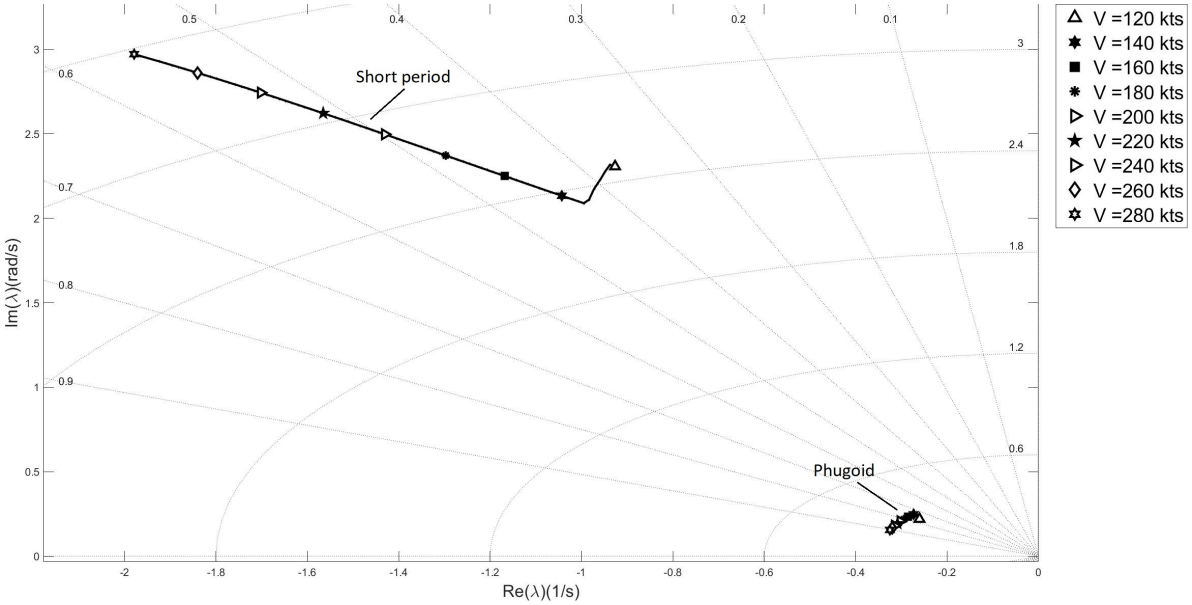

Figure 5.3: XV-15 uncoupled longitudinal eigenmodes in airplane mode ($\eta = 0\text{deg}$)

Table 5.1: Pitch and heave subsidence eigenvalues validation in hover

Model	Pitch subsidence	Heave subsidence
6-DoF model	-0.703	-0.227
3-DoF model	-0.794	-0.212
GTRS model[6]	-0.373	-0.201
FLIGHTLAB model [2]	-0.681	-0.141
Flight test [4]	-1.320	-0.105

The pitch subsidence is stable for all models. The eigenvalue of the 6-DoF model is quite comparable to the 3-DoF model and FLIGHTLAB eigenvalue. The GTRS model value is significantly smaller while none of the models come really close to the flight test value. The heave subsidence eigenvalue looks more comparable between the models. The FLIGHTLAB model eigenvalue comes closest to the flight test data. To analyse what causes the differences between the results the modes can be approximated analytically. This allows us to see which derivatives affect the modes and get a better physical understanding of the results. The short period typically occurs so quickly that the velocity of the aircraft is approximately constant throughout the motion [35]. For this reason u can be set equal to zero. This allows us to simplify the linear state space model to:

$$\begin{bmatrix} \dot{w} \\ \dot{q} \end{bmatrix} = \begin{bmatrix} Z_w & Z_q + u_0 \\ M_w & M_q \end{bmatrix} \begin{bmatrix} w \\ q \end{bmatrix} \tag{5.5}$$

This leads to the following characteristic equation for the short period:

$$\lambda_{sp}^2 - (Z_w + M_q)\lambda_{sp} + Z_w M_q - M_w u_0 = 0 \tag{5.6}$$

Where the damping and frequency are given by:

$$2\zeta_{sp}\omega_{sp} = -(Z_w + M_q) \tag{5.7}$$

$$\omega_{sp}^2 = Z_w M_q - M_w u_0 \tag{5.8}$$

The short period eigenvalues can then be computed using:

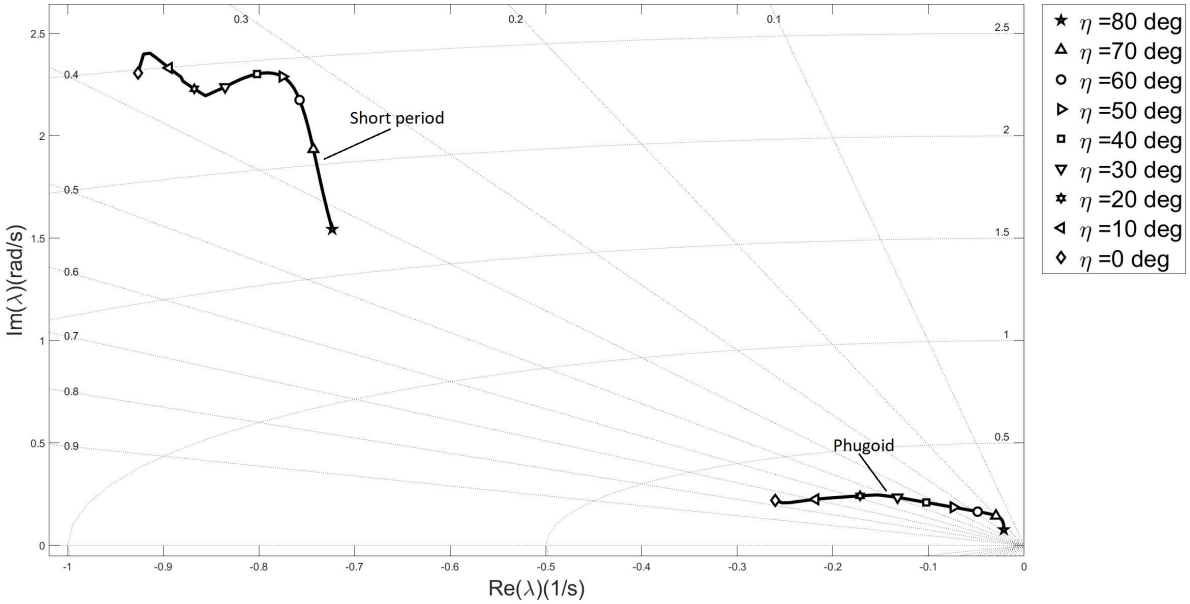

Figure 5.4: XV-15 uncoupled longitudinal eigenmodes in airplane mode as a function of nacelle angle (V = 120 kts)

$$\lambda_{sp} = -\zeta_{sp}\omega_{sp} \pm \omega_{sp}\sqrt{1-\zeta_{sp}^2}i \tag{5.9}$$

In order to verify whether this approximation is valid for tiltrotor aircraft the numerical eigenvalues are compared with the approximated eigenvalues. This is done for different combinations of V and η. The results are shown in Table 5.2. In the last two columns of the table the errors of the approximations are shown. It can be concluded that the approximation is not completely valid in hover. The approximation equation results in two eigenvalues which are close to the heave subsidence eigenvalue but far away from the pitch subsidence eigenvalue. This is not surprising, while we know that both modes are critically damped, which means that the damping ratio $\zeta = 1$. Substituting this in Equation 5.9 leads to λ_{sp} = -ω_{sp}, which gives only one eigenvalue. Instead of using Equation 5.9, the following approximation equations should be valid for the heave and pitch subsidences [2]:

$$\lambda_h = Z_w \tag{5.10}$$
$$\lambda_p = M_q \tag{5.11}$$

This means that the subsidence eigenvalues can be assumed approximately equal to their damping derivatives. Derivatives Z_w and M_q equal -0.226 and -0.284 respectively in hover. This shows that the heave damping derivative very accurately represents the heave subsidence (-0.227). The pitch subsidence (-0.703) has a lot more damping than the pitch damping derivative would suggest. The relatively low value of M_q results in translational velocities building up during pitching motion, resulting in a strongly coupled pitch-surge mode [2]. Going back to Table 5.1 we saw that the GTRS heave mode eigenvalue in hover equals -0.373, while a value of -0.3017 was found for M_q. According to this data there is not that much coupling between the pitch and surge mode as the 6-DoF model results would suggest. However, it should be mentioned that the GTRS data are extracted from two different references [12][6], meaning that the model setup could be not completely similar. When the airspeed is nonzero and the modes are coupled Equation 5.9 leads to quite accurate results, with errors below 10%. This shows that the short period is indeed mainly dependent on Z_w, M_w and M_q.

A sensitivity analysis on the stability derivatives has also been conducted for all dynamic modes. The results of this analysis can be found in Appendix D. Each derivative of the 4x4 reduced system has been varied from 0 to twice the value of the original. The effect of this variation on the frequency and damping of each mode has been plotted. The purpose of this sensitivity analysis is to shows which derivatives are the most

Table 5.2: Comparison of exact and approximation short period eigenvalues

η [deg]	Airspeed [kts]	λ_{sp} (model)	λ_{sp} (approximation)	error Re(λ_{sp}) [%]	error Im(λ_{sp}) [%]
90	0	-0.703, -0.227	-0.287, -0.223	138.2	1.7
90	100	-0.628 $\pm$ 1.287i	-0.630 $\pm$ 1.228i	0.4	4.5
60	100	-0.713 $\pm$ 1.907i	-0.694 $\pm$ 1.836i	2.6	3.7
60	140	-0.800 $\pm$ 2.380i	-0.784 $\pm$ 2.370i	2.1	0.4
0	140	-1.043 $\pm$ 2.134i	-1.051 $\pm$ 2.019i	0.8	5.4
0	240	-1.702 $\pm$ 2.744i	-1.724 $\pm$ 2.781i	1.3	1.4

prominent for each mode [36]. The derivatives which are mainly determined by inertial effects such as Z_q are left out of this analysis. The variations in short period frequency and damping due to the variation of the derivatives are shown in Figure D.1 and Figure D.2. From the graphs showing the derivatives with respect to u it can be concluded that the short period is indeed almost independent on variations in u. The graphs verify that Z_w, M_w and M_q are the most important derivatives for the short period. Primarily the effect of M_w on the frequency is very dominant at high airspeeds. This is not surprising when we look back at Equation 5.8; the contribution of M_w to the frequency is amplified by u_0.

In general, from the eigenvalue figures and Table 5.2 it can be concluded that the frequency of the short period increases with airspeed. The damping of the modes behaves less predictable with airspeed. In helicopter mode (Figure 5.1) and conversion mode (Figure 5.2) the damping decreases slightly with airspeed. In airplane mode (Figure 5.3) the damping increases slightly with airspeed. The more significant jump in damping between 120 and 140 kts can be explained by looking back at the M_w derivative, which also jumped from approximately -0.75 to -0.6 between these speeds and then remained constant with increasing airspeed.

Lastly, the variation of the short period eigenvalues with decreasing nacelle angle is shown in Figure 5.4. The airspeed is kept constant at 120 kts. This speed has been chosen because it has the largest range of possible nacelle angle configurations at which a trim solution exists. According to the 6-DoF model conversion corridor the XV-15 can be trimmed at 120 kts in a 80deg nacelle angle configuration as well as in a 0deg configuration. The figure shows that at high nacelle angles the short period frequency increases when the rotors are tilting towards airplane mode. It can be determined from Figure 4.12 that the incidence static stability derivative M_w decreases with nacelle angle up to 40 degrees after which it remains somewhat constant. This is also the point at which the frequency in Figure 5.4 stops increasing rapidly. The damping ratio of the short period is less affected by the rotations of the rotors. Along the η range the damping is constantly between 0.3 and 0.4 at an airspeed of 120 kts.

5.1.2. Phugoid

The phugoid is an oscillatory mode with a variation of airspeed, pitch angle and altitude over time [35]. The mode has a large period because of which the angle of attack remains almost constant over time. There is a very slow interchange between kinetic and potential energy during the mode, while the aircraft attempts to restore the steady horizontal equilibrium state. From Figure 5.1 it can be concluded that in hover the phugoid is unstable. To validate this conclusion, the hover eigenvalues are compared with results from other models in Table 5.3. We see that indeed the phugoid is unstable in hover for all models. Compared to the GTRS, FLIGHTLAB and 3-DoF model the 6-DoF model most accurately reproduces the flight test eigenvalues.

When the airspeed increases the phugoid becomes stable and the damping increases. The damping increases so fast that at approximately 70 kts the phugoid becomes non-oscillatory. This non-oscillatory behavior of the phugoid is not something that is found in literature. To analyse what causes this behavior, a closer look has to be taken at the derivatives affecting the phugoid. Constructing an accurate approximation equation for the phugoid is less straightforward for tiltrotor aircraft than for helicopters or conventional airplanes. For helicopters, the heave velocity component w contribution to the phugoid is small so all derivatives with respect to this state are set to zero. For an airplane M_w heavily affects the longitudinal stability due to wing and large fuselage thus its contribution to the phugoid is not negligible [2]. The same goes for the

Table 5.3: Phugoid eigenvalue validation in hover

Hover	Phugoid
6-DoF model	0.1880 ± 0.4827i
3-DoF model	0.1281 ± 0.4335i
GTRS [6]	0.0810 ± 0.2352i
FLIGHTLAB [2]	0.1471 ± 0.4208i
Flight test [4]	0.2681 ± 0.5132i

tiltrotor. The Lanchester approximation which is often used for conventional airplanes assumes that the phugoid is simply an exchange between height and speed with $\dot{q}$ equal to zero [28]. Derivative M_u, which couples the phugoid with pitch is usually zero for conventional airplanes but nonzero for tiltrotors as we saw in subsection 4.2.1. Therefore the Lanchester approximation does not hold in this case. Padfield suggests the following approximation for tiltrotor aircraft [2]

$$\lambda_{ph}^2 - (X_u - X_w \frac{M_u}{M_w})\lambda_{ph} - \frac{g}{u_0}(Z_u - Z_w \frac{M_u}{M_w}) = 0 \tag{5.12}$$

The damping of and the frequency of the phugoid mode can then be computed using

$$2\zeta_{ph}\omega_{ph} = -(X_u - X_w \frac{M_u}{M_w}) \tag{5.13}$$

$$\omega_{ph}^2 = -\frac{g}{u_0}(Z_u - Z_w \frac{M_u}{M_w}) \tag{5.14}$$

Using these two expressions, the eigenvalues of the phugoid can be found

$$\lambda_{ph} = -\zeta_{ph}\omega_{ph} \pm \omega_{ph}\sqrt{1 - \zeta_{ph}^2}i \tag{5.15}$$

In order to verify the accuracy of this approximation equation the exact values and the approximation values are compared for all three configurations in Table 5.4. The first conclusion that can be drawn from the equation itself is that it can not be used to approximate the hover eigenvalues. The trim horizontal velocity component u_0 is zero in hover which gives an undefined solution. At low airspeeds the approximation will also lead to inaccurate high values of the frequency. When the airspeed increases the equation becomes reasonably accurate with errors around ± 50%. Equation 5.15 is also able to approximate the critically damped phugoid at high airspeeds in H-mode. According to the approximation the damping ratio can be computed using:

$$\zeta_{ph} = \frac{-(X_u - X_w \frac{M_u}{M_w})}{2\sqrt{-\frac{g}{u_0}(Z_u - Z_w \frac{M_u}{M_w})}} \tag{5.16}$$

The eigenvalues of the phugoid are located on the real axis when the damping is equal to 1. According to this equation the damping is dependent on X_u, X_w, Z_w, Z_q, M_u and M_w. To see which of these derivatives causes the phugoid to become non-oscillatory the sensitivity analysis results in Appendix D can be used. Figure D.4 shows how the damping of the phugoid varies when the stability derivatives are varied from 0 to 2 times the original value.

From the graphs it can be concluded that the high damping in airplane mode is mainly due to the large magnitudes of X_u and M_w. The same holds for the conversion mode, although Z_u, Z_w and M_u also affect the damping. If M_u or Z_w would be one fourth of their magnitudes the phugoid would be critically damped as well. In helicopter mode X_u is relatively small because the rotor contribution to the drag damping is insignificant. Therefore doubling or halving its value does not do much to the damping. Derivatives Z_u and

Table 5.4: Comparison of exact and approximation phugoid eigenvalues

η [deg]	Airspeed [kts]	λ_{ph} (model)	λ_{ph} (approximation)	error Re(λ_{ph}) [%]	error Im(λ_{ph}) [%]
90	0	0.1880 $\pm$ 0.4827i	-	-	-
90	100	0.1490, -0.2050	0.1865 -0.2342	25.1	14.3
60	100	-0.0418 $\pm$ 0.2094i	0.0007 $\pm$ 0.2389i	101.6	14.1
60	140	-0.0558 $\pm$ 0.1247i	-0.0415 $\pm$ 0.1402i	25.6	12.4
0	140	-0.2731 $\pm$ 0.2479i	-0.1748 $\pm$ 0.4024i	36.0	62.3
0	240	-0.3145 $\pm$ 0.1806i	-0.2862 $\pm$ 0.3061i	9.0	69.5

Z_w are also important for the phugoid damping in H-mode. However, the primary reason why the phugoid is non-oscillatory in H-mode is not visible in the sensitivity analysis graphs. Comparing the 6-DoF M_u derivative in H-mode with other models in Figure 4.11 leads to the observation that the 6-DoF model derivative is the only derivative that is negative at high airspeeds. This means that the second term in Equation 5.16 increases the damping instead of decreasing it. This results in damping values reaching 1.

In Figure D.3 the sensitivity analysis results on the frequency of the phugoid are shown. In A-mode and C-mode the frequency appears to be mostly affected by M_w, Z_w and M_u also have a contribution. In H-mode the frequency is unaffected by the X derivatives. Derivatives Z_u, Z_w, M_u and M_w all affect the ω_{ph} according to the approximation:

$$\omega_{ph} = \sqrt{-\frac{g}{U_e}(Z_u - Z_w \frac{M_u}{M_w})} \tag{5.17}$$

(5.18)

The pitch damping derivative M_q is not considered in the approximation equation but significantly affects the phugoid frequency at low airspeeds in H-mode according to the sensitivity analysis plot.

The variation of the phugoid eigenvalues with nacelle angle is shown in Figure 5.4. The airspeed is kept at 120 kts while the nacelles are tilted from 80 to 0 degrees. The fact that the phugoid is oscillatory at at nacelle angles between 80 and 0 degrees shows that the mode is only non-oscillatory at nacelle angles very close to hover. As the nacelle are rotating away from helicopter mode the M_u derivative increases as shown in Figure 4.11(d). At the same time the drag damping X_u becomes larger and X_w increases. The combination of these three results in an increase in damping with decreasing nacelle angle. At the same time the frequency of the phugoid increases slightly.

5.2. Uncoupled Lateral/directional Modes

For the analysis of the lateral/directional modes of the tiltrotor it will be assumed that the contribution of the longitudinal states to the modes is negligible. This means that the state vector can be reduced to the following form:

$$x = [v, p, \phi, r]^T \tag{5.19}$$

Furthermore, only the free response of the aircraft will be analysed meaning that only the A-matrix is of interest. The reduced 4x4 lateral/directional state space system is given by:

$$\begin{bmatrix} \dot{v} \\ \dot{p} \\ \dot{\phi} \\ \dot{r} \end{bmatrix} = \begin{bmatrix} Y_v & Y_p + w_0 & g\cos\phi_0 & Y_r - u_0 \\ L'_v & L'_p & 0 & L'_r \\ 0 & 1 & 0 & \cos\phi_0 \\ N'_v & N'_p & 0 & N'_r \end{bmatrix} \begin{bmatrix} v \\ p \\ \phi \\ r \end{bmatrix} \tag{5.20}$$

The aircraft response to the lateral/directional perturbations consists of three different modes; one oscillatory mode and two non-oscillatory modes. The non-oscillatory modes are the spiral mode and the rolling mode, of which the former is usually unstable and the latter is heavily damped. The oscillatory mode is the Dutch Roll mode, which consists of a combination of rolling, yawing and sideslipping. Firstly the roll mode will be discussed, whereafter the spiral mode and Dutch Roll mode will be elaborated upon.

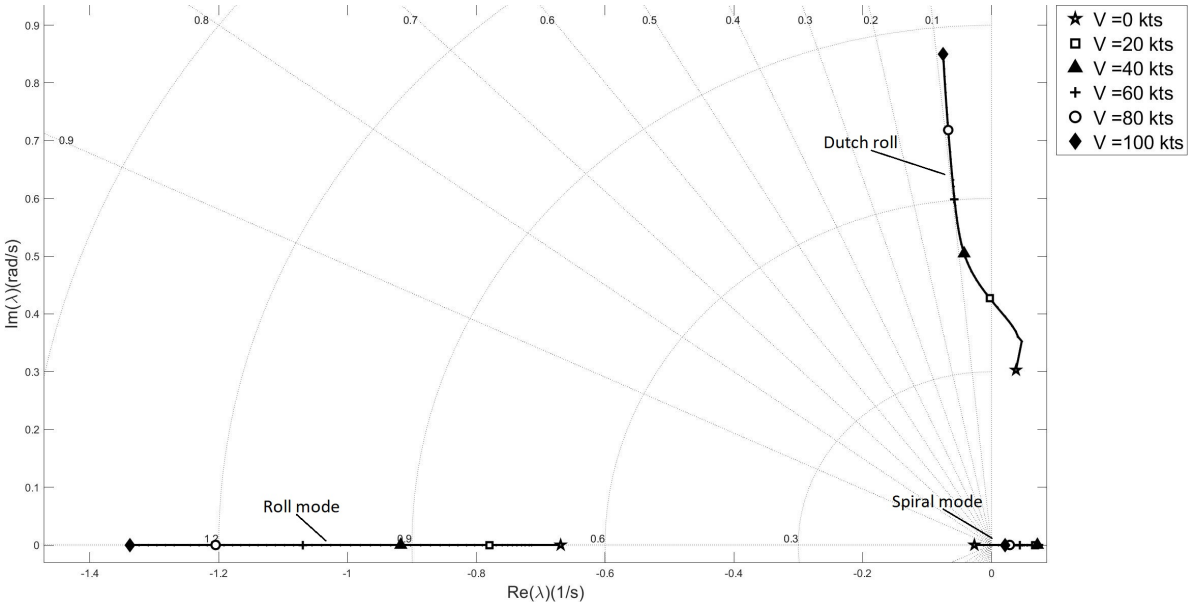

Figure 5.5: XV-15 uncoupled lateral eigenmodes in helicopter mode as a function of airspeed ($\eta = 90\text{deg}$)

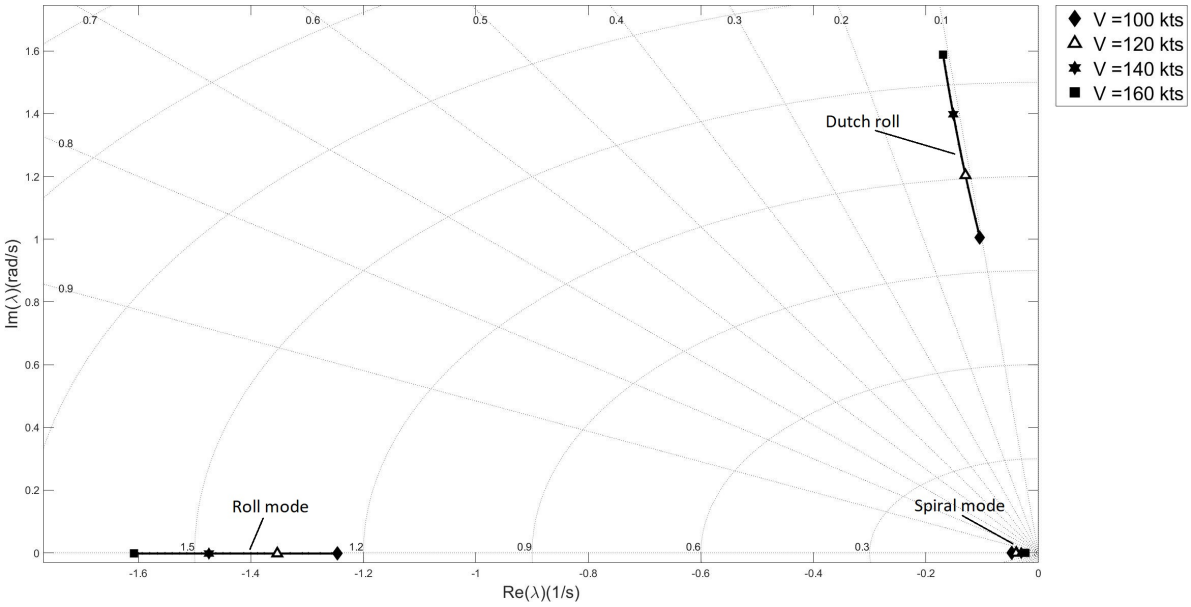

Figure 5.6: XV-15 uncoupled lateral eigenmodes in conversion mode as a function of airspeed ($\eta = 60\text{deg}$)

5.2.1. Rolling mode

The rolling mode is usually a pure roll subsidence, which is stable, highly damped and non-oscillatory. In Figure 5.5 the lateral/directional eigenmodes in helicopter configuration are shown. The roll subsidence eigenvalues are located on the real axis, meaning that the mode is critically damped. When airspeed increases the roll mode eigenvalue moves to the left which indicates that the frequency of the mode increases. The roll motion can be written in the first-order differential form of a rate response type :

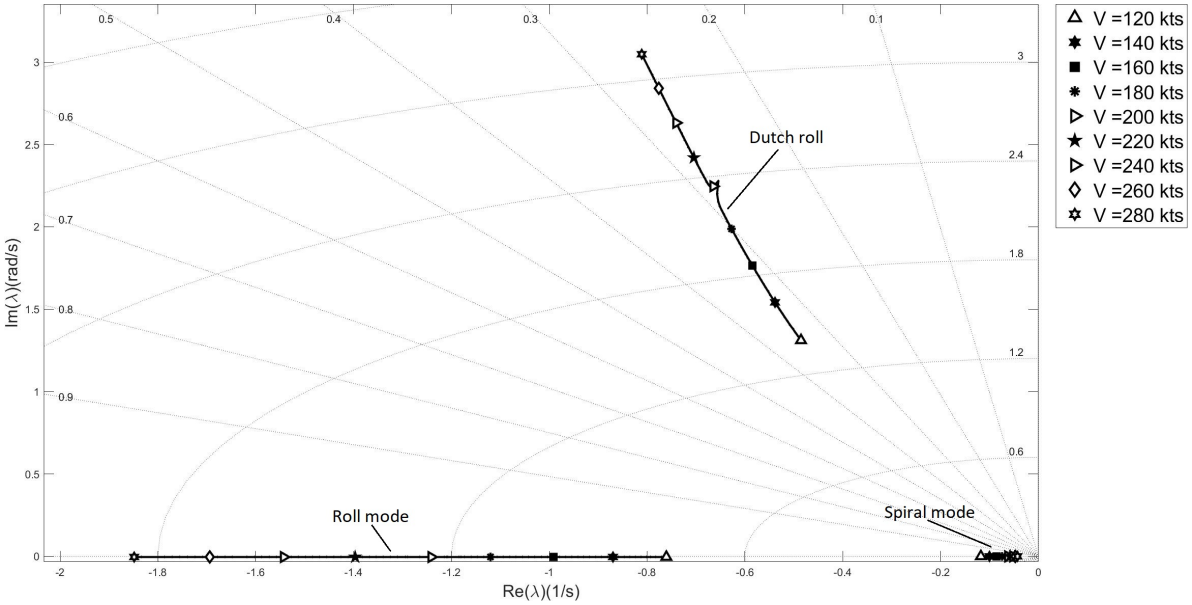

Figure 5.7: XV-15 uncoupled lateral eigenmodes in airplane mode as a function of airspeed ($\eta = 0\text{deg}$)

$$\dot{p} = L_p p \tag{5.21}$$

Which simply leads to the following approximation for the roll mode eigenvalue:

$$\lambda_r = L_p \tag{5.22}$$

The accuracy of this approximation is investigated in Table 5.5. The error is below 25 % for all conditions, so the approximation can be assumed to be reasonable. The relatively lower value of L_p shows that there is some coupling with the sway motion, meaning that there are translational velocities building up along the y-axis during the rolling motions. The sensitivity analysis results for the roll mode frequency are shown in Figure D.5. As expected the figures show that the roll mode frequency is mainly dependent on the value of L_p. In helicopter mode the derivatives with respect to the yawing moment N have a negligible effect on the roll. Higher values of L_r and L_v would increase the frequency of the roll mode. In conversion mode and airplane mode the rotors are tilted so the thrust force is more aligned with the x-axis. This results in more coupling between roll and yaw when a perturbation in p occurs. This is also clearly visible in the yawing moment derivatives, which all have some effect on the roll mode eigenvalue.

Table 5.5: Comparison of exact and approximation roll mode eigenvalues

η [deg]	Airspeed [kts]	λ_r (exact)	λ_r (approximation)	error [%]
90	0	-0.6691	-0.5041	24.7
90	100	-1.3380	-1.1976	10.5
60	100	-1.2465	-1.1111	10.9
60	140	-1.4745	-1.3127	11.0
0	140	-0.8697	-0.7397	14.9
0	240	-1.5428	-1.3457	12.8

In conversion and airplane mode the roll mode frequency similarly increases with airspeed as seen in Figure 5.6 and Figure 5.7, which mainly happens because L_p increases in magnitude. In Figure 5.8 the variation of the lateral eigenvalues with nacelle angle are shown. The airspeed is again kept constant at 120 kts. The roll mode eigenvalue moves moves to the right on the real axis when the nacelle angle decreases. In

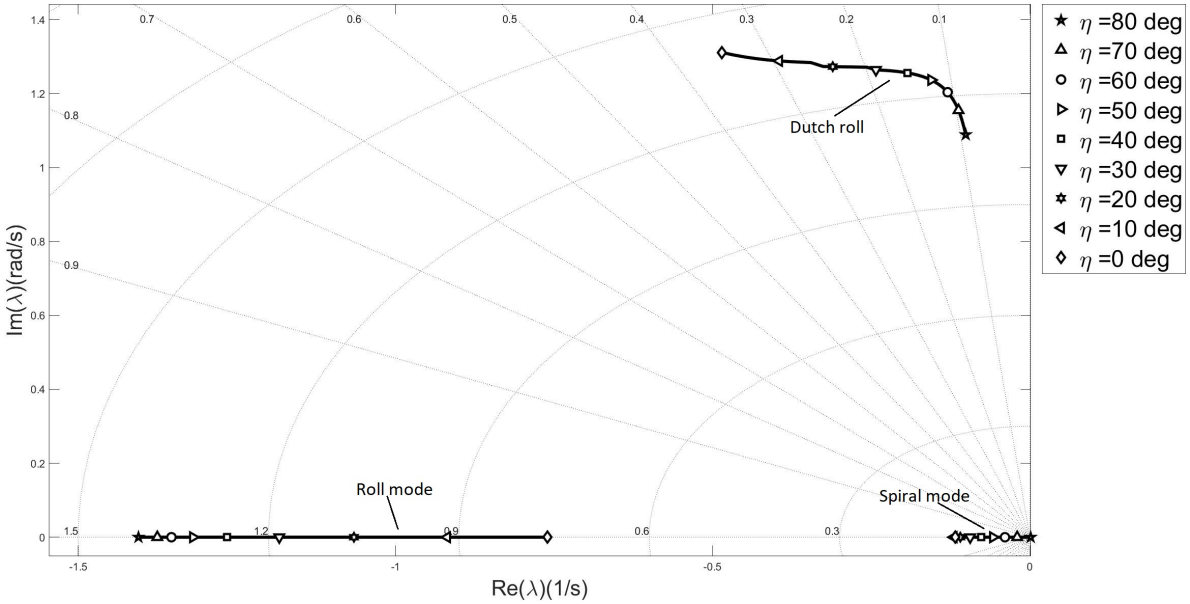

Figure 5.8: XV-15 uncoupled lateral eigenmodes in airplane mode as a function of nacelle angle (V = 120 kts)

Figure 4.18(d) it is shown that L_p decreases in magnitude with decreasing nacelle angle. The rotors have a smaller contribution to the roll damping derivative when the thrust vectors are oriented more horizontally.

5.2.2. Spiral mode

The spiral mode is the second non-oscillatory mode and is determined by the other real root from the 4x4 lateral state space system. The mode is usually developed very slowly and involves a combination of roll, yaw and sideslip. The spiral mode for conventional helicopters at low speeds is usually primarily a yawing motion, meaning $\lambda_s = N_r$. Since N_r is a damping derivative the spiral is a stable mode and equilibrium is restored by the helicopter itself [2]. The dihedral effect is destabilizing the spiral mode [29], and this effect is much more prominent for tiltrotors than for conventional helicopters. In Figure 5.5 we see a negative real eigenvalue for the spiral mode in hover, meaning that the mode is stable. The hover eigenvalue is validated with data from other models in Table 5.6. The GTRS model and flight test data show a stable eigenvalue in hover as well, while the FLIGHTLAB model finds an unstable spiral mode. The differences in magnitude between the eigenvalues are quite significant.

Table 5.6: Spiral mode eigenvalue validation in hover

Hover	Roll mode
6-DoF model	-0.0265
GTRS [6]	-0.0008
FLIGHTLAB [2]	0.136
Flight test [4]	–0.105

To get a better understanding what could cause these differences it can help to look at a spiral mode approximation equation. Padfield gives the following approximation equation for the spiral mode [2]

$$\lambda_s = \frac{g}{L_p} \frac{(L_v N_r - N_v L_r)}{(u_0 N_v + \sigma_s L_v)} \tag{5.23}$$

with

$$\sigma_s = \frac{g - N_p u_0}{L_p} \tag{5.24}$$

In table Table 5.7 the results of this approximation are compared with the real spiral eigenvalues and it can be concluded that the approximation is quite accurate. The approximation can be simplified in hover when u_0 is equal to zero, leading to

$$\lambda_s = N_r - \frac{N_v}{L_v} L_r \tag{5.25}$$

The first term in this approximation is the yaw damping derivative, which is negative and thus stabilizing. In subsection 4.2.2 it was mentioned that the yaw damping derivative for tiltrotor in H-mode is significantly lower than for helicopters due to the absence of a tail rotor. The second term consist of the dihedral effect L_v and weathercock stability derivative N_v which are negative and positive respectively. Besides the two sideslip derivatives the yaw-roll coupling derivative L_r is included in the equation which is positive in H-mode. This means that the second term of the approximation equation is destabilizing. For the 6-DoF model the stabilizing N_r term is bigger than the destabilizing second term, although they are not far off (-0.0883 and 0.0618 respectively). In Figure 4.2.2(a) it is shown that the 6-DoF model finds a larger N_r than the FLIGHTLAB and GTRS models, which explains why its spiral mode is the most stable. When the airspeed increases to moderate airspeeds N_r does not significantly increase, while the other derivatives affecting the spiral do. This causes the 6-DoF model spiral mode to become unstable as seen in Figure 5.5. The peak of instability is reached at approximately 30 kts, where the real positive eigenvalue is at its largest. Thereafter the eigenvalue moves towards the stable axis again which mainly happens because N_r starts increasing in magnitude.

Table 5.7: Comparison of exact and approximation spiral mode eigenvalues

η [deg]	Airspeed [kts]	λ_s (exact)	λ_s (approx eq1)	error [%]
90	0	-0.0265	-0.0265	0.0
90	100	0.0216	0.0229	6.2
60	100	-0.0476	-0.0484	1.7
60	140	-0.0304	-0.0305	0.2
0	140	-0.1000	-0.0991	0.9
0	240	-0.0519	-0.0527	1.5

In Figure 5.6 the spiral mode eigenvalues as a function of airspeed in C-mode are shown. In this configuration the spiral mode is barely affected by the airspeed. The frequency remains fairly constant over the airspeed range. The yaw damping in this configuration is higher than in helicopter mode and the destabilizing positive L_r in H-mode is now negative. The result is a stable spiral mode. In airplane mode (Figure 5.7) the spiral mode is also stable but the frequency decreases with airspeed. The roll damping derivative L_p increases in magnitude with airspeed which contributes to the decrease in magnitude of λ_s.

Looking at the frequency plots of the sensitivity analysis results for the spiral in Figure D.7 also confirms the influence of L_p on the spiral mode. Furthermore the dependency of the spiral mode on the yaw moment N other roll moment L derivatives is clearly visible, primarily in airplane mode. In helicopter mode the derivatives from Equation 5.25 mainly influence the spiral frequency. The roll-yaw coupling derivative contribution is amplified by the horizontal trim velocity component u_0 which explains the small contribution in H-mode and large contribution in A-mode. In Figure D.8 a sensitivity analysis on the damping of the spiral has been conducted. In helicopter mode the destabilizing effects of N_v and L_r are visible. If these derivatives would be significantly smaller the spiral mode would be stable at 40 kts. It is also interesting to see what would happen if L_p would decrease in magnitude in airplane mode. This would result in slow roll damping causing other angular rates and translational airspeeds to build up, eventually resulting in an oscillatory mode.

In Figure 5.8 the spiral eigenvalues as a function of nacelle angle are shown. It can be concluded from the figure that the spiral mode becomes more stable when the nacelles are rotated towards airplane mode. The positive roll-yaw coupling derivative L_r is destabilizing at high nacelle angles. The derivative decreases and becomes negative when the nacelles are rotated towards 0 degrees. This contributes to the stabilization of the spiral mode. Simultaneously the roll damping derivative L_p decreases in size which also contributes to the spiral becoming more stable.

5.2.3. Dutch roll

The Dutch roll mode is an oscillatory lateral/directional mode which consists of a combination of yawing, rolling and sidesliping motion. The Dutch roll has quite a short period and is usually lightly damped. The Dutch roll is often considered an undesirable mode since it interferes with the pilot's ability to hold a trim. Besides this, the mode is quite unpleasant for passengers [27]. In Figure 5.5 the Dutch roll eigenvalues in helicopter mode as a function of airspeed are shown. In hover the mode is unstable which is also sometimes the case for conventional helicopters [2]. If we compare the 6-DoF model hover eigenvalues with the the values found by the GTRS model and the one measured during a flight test we find a similar instability. The comparison is shown in Table 5.8. The real part of the Dutch roll eigenvalue found by 6-DoF model is significantly lower than the other two eigenvalues. The imaginary part however comes quite close to the flight test value.

Table 5.8: Eigenvalue validation in hover

6-DoF model	$0.0381 \pm 0.3028i$
Flight test [4]	$0.1868 \pm 0.4061i$
GTRS [6]	$0.1866 \pm 1.0826i$

When the airspeed increases the Dutch roll becomes a very lightly damped stable mode. The frequency increases with airspeed, while the damping remains roughly constant. The eigenvalues in conversion mode and airplane mode show a similar trend, as shown in Figure 5.6 and Figure 5.7. The frequency increases linearly with airspeed.

To get a better understanding of which derivatives affect the mode it is useful to have a look at how the Dutch roll is often approximated. Padfield proposes the following first-order approximation characteristic equation for the Dutch roll eigenvalues for conventional helicopters[2]:

$$\lambda_d^2 - (N_r + Y_v + \sigma_d \frac{L_r}{u_0})\lambda_p + (u_0 N_v + \sigma_d L_v) = 0 \tag{5.26}$$

with

$$\sigma_d = \frac{g - N_p u_0}{L_p} \tag{5.27}$$

The damping of and the frequency of the Dutch roll can then be computed using

$$\zeta_d = \frac{-(N_r + Y_v + \sigma_d \frac{L_r}{u_0})}{2\sqrt{(u_0 N_v + \sigma_d L_v)}} \tag{5.28}$$

$$\omega_d = \sqrt{u_0 N_v + \sigma_d L_v} \tag{5.29}$$

Leading to the following approximation for the Dutch roll eigenvalues

$$\lambda_d = -\zeta_d \omega_d \pm \omega_d \sqrt{1 - \zeta_d^2} i \tag{5.30}$$

There are many different Dutch roll approximations used in literature for both airplanes and helicopters. This first-order approximation for helicopters proved to be one of the most accurate ones for applications to

Table 5.9: Comparison of exact and approximation Dutch roll mode eigenvalues using the first-order approximation equation

η [deg]	Airspeed [kts]	λ_{dr} (exact)	λ_{dr} (approx)	error Re(λ_{dr})[%]	error Im(λ_{dr}) [%]
90	0	0.0381 $\pm$ 0.3028i	-0.0576 $\pm$ 0.3466i	251.1	14.4
90	100	-0.0749 $\pm$ 0.8499i	-0.1550 $\pm$ 0.8611i	106.9	1.3
60	100	-0.1040 $\pm$ 1.0050i	-0.1518 $\pm$ 1.0501i	45.9	4.5
60	140	-0.1513 $\pm$ 1.3983i	-0.2238 $\pm$ 1.4719i	47.9	5.3
0	140	-0.5384 $\pm$ 1.5416i	-0.6350 $\pm$ 1.6613i	17.9	7.8
0	240	-0.7405 $\pm$ 2.6312i	-0.8388 $\pm$ 2.7812i	13.3	5.7

the tiltrotor, surprisingly primarily in C-mode and A-mode. The approximations are compared with the exact values in Table 5.9. Unfortunately this approximation is unable to capture the instability of the Dutch roll in hover. N_r and Y_v are both damping derivatives which are negative, so they have a positive contribution to the damping. The third term in the numerator contains the inertial velocity component u_0 which is zero in hover, so this term can be disregarded. To see which derivatives are destabilizing at low airspeeds we have to extend the analysis to second-order terms. This leads to the following characteristic equation [2]:

$$\lambda_d^2 - (N_r + Y_v + \sigma_d(\frac{L_r}{u_0} - \frac{L_v}{L_p})/(1 - \frac{\sigma_d L_r}{L_p u_0}))\lambda_p + (u_0 N_v + \sigma_d L_v)/(1 - \frac{\sigma_d L_r}{L_p u_0}) = 0 \tag{5.31}$$

with

$$\sigma_d = \frac{g - N_p u_0}{L_p} \tag{5.32}$$

The damping of and the frequency of the Dutch roll can then be computed using

$$\zeta_d = \frac{-(N_r + Y_v + \sigma_d(\frac{L_r}{u_0} - \frac{L_v}{L_p})/(1 - \frac{\sigma_d L_r}{L_p u_0}))}{2\sqrt{u_0 N_v + \sigma_d L_v)/(1 - \frac{\sigma_d L_r}{L_p u_0})}} \tag{5.33}$$

$$\omega_d = \sqrt{u_0 N_v + \sigma_d L_v)/(1 - \frac{\sigma_d L_r}{L_p u_0}} \tag{5.34}$$

In hover, these equations can be simplified using $u_0 = 0$

$$\zeta_d = \frac{-(N_r + Y_v - \frac{L_v}{L_p^2})}{2\sqrt{\sigma_d L_v)}} \tag{5.35}$$

$$\omega_d = \sqrt{\sigma_d L_v} \tag{5.36}$$

A comparison between this second-order approximation and the exact results is made in Table 5.10. The results show that this approximation is able to capture the unstable Dutch roll mode at low airspeeds. According to the approximation, the Dutch roll damping is also affected by the dihedral effect L_v. In subsection 4.2.2 it was explained that the dihedral derivative is preferably negative, which is also the case in H-mode. According to Equation 5.35 this has a destabilizing effect to the Dutch roll mode. At low airspeed the damping derivatives are quite small which is why the destabilizing L_v is dominant for the mode. When airspeed increases the damping derivatives increase in magnitude while the dihedral effect remains roughly constant. Therefore the Dutch roll is stable after a certain airspeed (approx. 20kts) is reached. At high airspeeds the second-order approximation produces less accurate results than the first-order approximation. Primarily in A-mode the first-order approximation shows more coherence with the exact eigenvalues.

Table 5.10: Comparison of exact and approximation Dutch roll mode eigenvalues using the second-order approximation equation

η [deg]	Airspeed [kts]	λ_{dr} (exact)	λ_{dr} (approx)	error Re(λ_{dr})[%]	error Im(λ_{dr}) [%]
90	0	0.0381 $\pm$ 0.3028i	0.0648 $\pm$ 0.3453i	70.0	14.0
90	100	-0.0749 $\pm$ 0.8499i	-0.1262 $\pm$ 0.8815i	68.4	3.7
60	100	-0.1040 $\pm$ 1.0050i	-0.0259 $\pm$ 1.0213i	75.1	1.6
60	140	-0.1513 $\pm$ 1.3983i	-0.0563 $\pm$ 1.4616i	62.8	4.5
0	140	-0.5384 $\pm$ 1.5416i	-0.1629 $\pm$ 1.7282i	69.7	12.1
0	240	-0.7405 $\pm$ 2.6312i	-0.3353 $\pm$ 2.8301i	54.7	7.6

In Figure D.10 the sensitivity analysis results on the Dutch roll damping are shown. The stabilizing contributions of the damping derivatives Y_v, L_p and N_r in H-mode are clearly visible. Primarily L_p which reduces the destabilizing effect of the dihedral effect L_v plays an important role. The weathercock stability derivative N_v and the roll-yaw coupling derivative L_r also seem to have a significant stabilizing effect on the damping. When the nacelles are rotated towards airplane mode the importance of N_r and L_p on the damping increases and reduces respectively. The coupling derivative L_r becomes less important while the importance of the other coupling derivative N_p increases. Derivatives N_v and N_p have a destabilizing effect to the Dutch roll of the same order as L_v in airplane mode. From Equation 5.29 and Equation 5.34 and the eigenvalue figures it could already be concluded that the frequency of the mode is very dependent on the horizontal speed component. From Figure D.9 a similar conclusion can be drawn; the derivatives barely affect the frequency. Only N_v which is amplified by u_0 clearly affects the frequency. The higher the velocity, the higher the sensitivity to changes in N_v.

Figure 5.8 shows the Dutch roll eigenvalues as a function of nacelle angle. From the figure it can be concluded that the frequency of the mode slowly increases with decreasing nacelle angle. It was established that the tiltrotor Dutch roll frequency was mainly determined by N_v and u_0. Since the forward speed is kept constant the effect of u_0 can be neglected. From Figure 4.21 it can be concluded that N_v slightly increases with decreasing nacelle which explains the slight increase in frequency. The increase of the damping slowly builds up with decreasing nacelle. This mainly happens due to the increase in yaw damping N_r. Furthermore, the roll-yaw coupling derivative N_p first increases in magnitude up to ≈30 degrees which withholds the damping from increasing faster. Thereafter the derivative decreases again, which explains why the damping suddenly increases faster with nacelle angle.

5.3. Coupled Modes

In the previous two sections the longitudinal and lateral eigenmodes of the tiltrotor have been analysed by using a reduced state space system. The assumption has been made that the longitudinal modes can be decoupled from the lateral modes. In this section the validity of this assumption will be investigated. The eigenvalues of the full 8x8 state space A-matrix will be analysed and compared with the results of the reduced systems. The comparison is elaborated upon in subsection 5.3.1. The full uncoupled A-matrix is shown below.

$$\begin{bmatrix} \dot{u} \\ \dot{w} \\ \dot{q} \\ \dot{\theta} \\ \dot{v} \\ \dot{p} \\ \dot{\phi} \\ \dot{r} \end{bmatrix} = \begin{bmatrix} X_u & X_w - q_0 & X_q - w_0 & -g\cos\theta_0 & X_v + r_0 & X_p & 0 & X_r + v_0 \\ Z_u + q_0 & Z_w & Z_q + u_0 & -g\cos\phi_0\sin\theta_0 & Z_v - p_0 & Z_p - v_0 & -g\sin\phi_0\cos\theta_0 & Z_r \\ M_u & M_w & M_q & 0 & M_v & \begin{matrix} M_p - 2p_0 I_{xz} I_y \\ -r_0(I_x - I_z)I_y \end{matrix} & 0 & \begin{matrix} M_r - 2r_0 I_{xz} I_y \\ -2p_0(I_x - I_z)I_y \end{matrix} \\ 0 & 0 & \cos\theta_0 & 0 & 0 & 0 & -\Omega_0\cos\theta_0 & -\sin\theta_0 \\ Y_u - r_0 & Y_w + p_0 & Y_q & -g\sin\phi_0\sin\theta_0 & Y_v & Y_p + w_0 & g\cos\phi_0\cos\theta_0 & Y_r - u_0 \\ L'_u & L'_w & L'_q + k_1 p_0 - k_2 r_0 & 0 & L'_v & L'_p + k_1 q_0 & 0 & L'_r - k_2 q_0 \\ 0 & 0 & \sin\phi_0\tan\theta_0 & \Omega_0\sec\theta_0 & 0 & 1 & 0 & \cos\phi_0\tan\theta_0 \\ N'_u & N'_w & N'_q - k_1 r_0 - k_3 p_0 & 0 & N'_v & N'_p - k_3 q_0 & 0 & N'_r - k_1 q_0 \end{bmatrix} \begin{bmatrix} u \\ w \\ q \\ \theta \\ v \\ p \\ \phi \\ r \end{bmatrix} \quad (5.37)$$

Furthermore, the validity of the whole linear 6-DoF model will be tested by comparing the uncoupled eigenvalues results with the FLIGHTLAB results. The differences between the two models will be analysed and

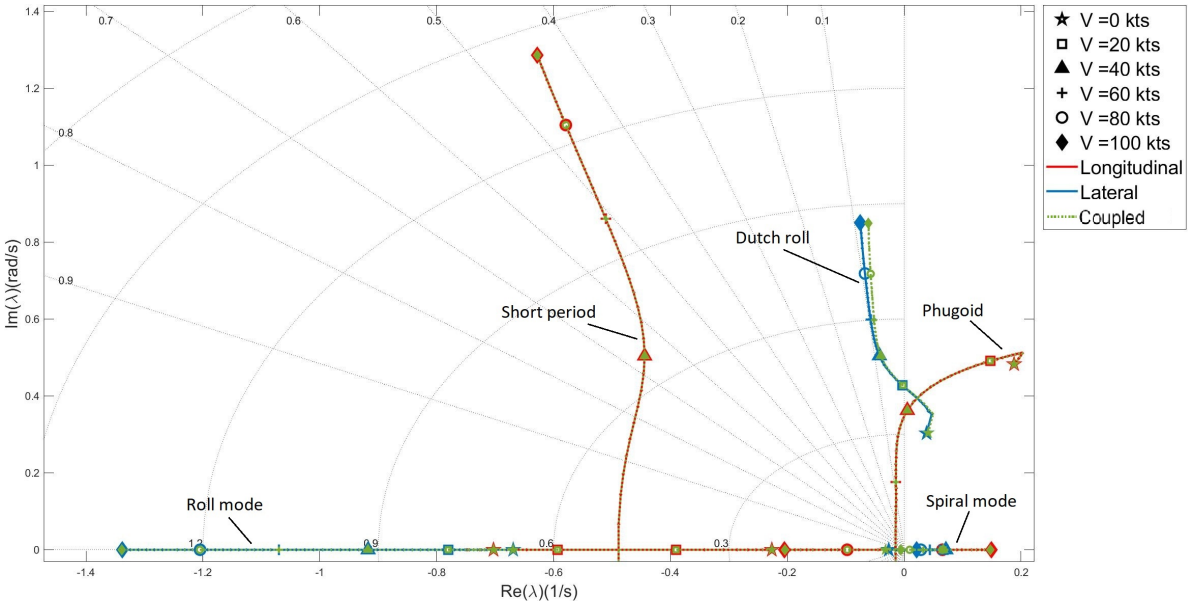

Figure 5.9: XV-15 coupled longitudinal eigenmodes compared with the uncoupled modes in helicopter mode

explained by looking at the differences in modelling approaches and stability derivatives. This is done in subsection 5.3.2.

5.3.1. Comparison with Uncoupled Modes

In order to verify whether the uncoupling of the longitudinal and lateral eigenmodes is valid for tiltrotor aircraft the coupled system eigenvalues are compared with those of the uncoupled systems. The eigenvalues of the three different systems have been plotted in the three different configurations, as a function of airspeed. The comparison in helicopter mode is shown in Figure 5.9. It can be observed that there is a lot of overlap between the uncoupled models and the coupled model. The longitudinal modes (phugoid and short period) show an almost perfect resemblance, meaning that there is little to no coupling with lateral motion. For the lateral modes there appears to be slightly less overlap. The coupled Dutch Roll is a little bit less damped than the uncoupled one. Investigation of the longitudinal-lateral coupling derivatives shows that none of the derivatives in helicopter mode has a significant magnitude that could influence the dynamic modes. The differences are caused by the assumption for the uncoupled lateral/directional system that the modes are independent of the pitch angle. This means that $\cos\theta_0$ and $\tan\theta_0$ are assumed to be equal to 1 and 0 respectively. This assumption is not made for the uncoupled system and is mainly the reason for the observed differences.

In conversion mode the eigenvalues are also very similar. This is shown in Figure 5.10. The longitudinal eigenvalues have an almost perfect overlap, while the lateral eigenvalues have a small discrepancy. This shows that the longitudinal-lateral coupling is also negligible in conversion mode. At an airspeed of 100 kts the Dutch Roll eigenvalues are clearly not perfectly equal while at 160 there is a perfect overlap. This can be related to the the absence of the pitch angle influence to the uncoupled lateral eigenmodes. At an airspeed of 100 kts the pitch angle is approximately 10 degrees while at 160 kts the angle is around zero Figure 3.7. Therefore the assumption that $\cos\theta_0 = 1$ and $\tan\theta_0 = 0$ for the uncoupled lateral/directional modes is less valid at 100 kts.

In airplane mode there are also no noteworthy differences between the coupled model and the uncoupled models (Figure 5.11). There is even more overlap than in helicopter and conversion mode. Generally, the conclusion can be drawn that for the 6-DoF model the uncoupling of the modes is valid for the entire flight envelope. There appears to be little to no coupling between the longitudinal and lateral motion in these flight conditions. However, the results of the FLIGHTLAB model show quite some coupling between the subsets, primarily in helicopter mode. The following A-matrix is found by the FLIGHTLAB model for the XV-15 at a 20 kts H-mode horizontal trim condition [2]:

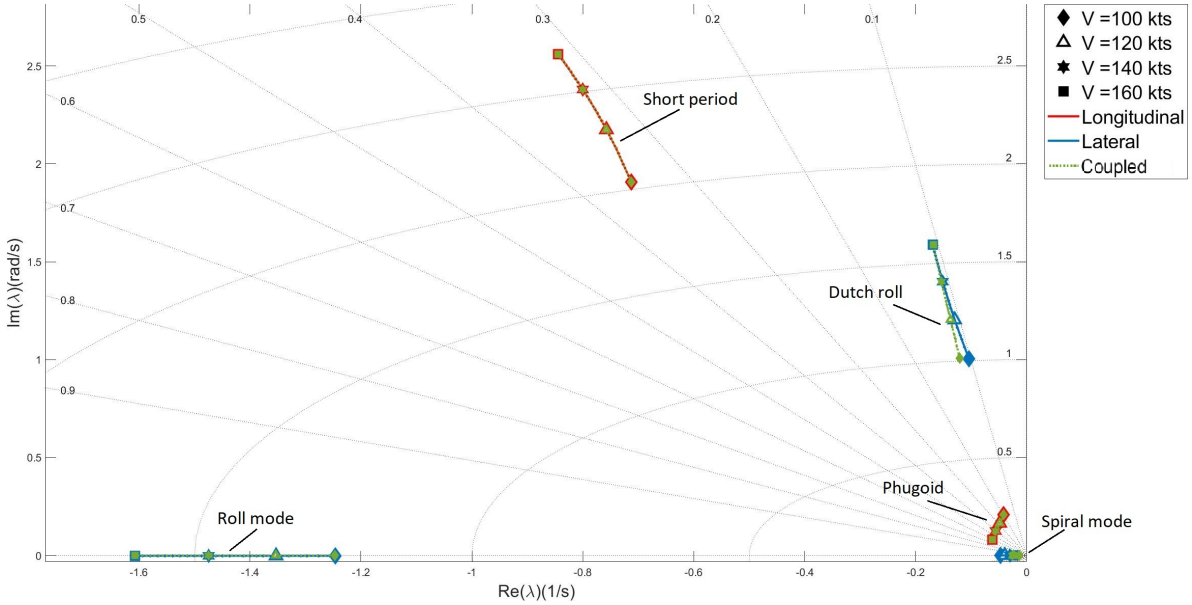

Figure 5.10: XV-15 coupled longitudinal eigenmodes compared with the uncoupled modes in conversion mode

$$\begin{bmatrix} \dot{u} \\ \dot{w} \\ \dot{q} \\ \dot{\theta} \\ \dot{v} \\ \dot{p} \\ \dot{\phi} \\ \dot{r} \end{bmatrix} = \begin{bmatrix} -0.0272 & -0.005 & 0.0241 & -9.8136 & 0 & 0.0363 & 0 & 0.0058 \\ -0.0741 & -0.2071 & 10.0337 & -0.0727 & 0.0004 & 0.3163 & -0.0001 & 0.0506 \\ 0.0213 & -0.0125 & -0.7157 & 0 & 0 & -0.0433 & 0 & -0.0069 \\ 0 & 0 & 1 & 0 & 0 & 0 & 0 & 0 \\ 0 & 0 & 0 & 0 & -0.0687 & -0.1496 & 10.4343 & -10.4567 \\ 0 & 0 & 0 & 0 & -0.0098 & -0.4383 & 0.0303 & 0.3178 \\ 0 & 0 & 0 & 0 & 0 & 1 & 0 & 0.0074 \\ 0 & 0 & 0 & 0 & 0.0118 & 0.1955 & 0.0111 & -0.132 \end{bmatrix} \begin{bmatrix} u \\ w \\ q \\ \theta \\ v \\ p \\ \phi \\ r \end{bmatrix} \tag{5.38}$$

At the same conditions the following A-matrix is found by the 6-DoF model:

$$\begin{bmatrix} \dot{u} \\ \dot{w} \\ \dot{q} \\ \dot{\theta} \\ \dot{v} \\ \dot{p} \\ \dot{\phi} \\ \dot{r} \end{bmatrix} = \begin{bmatrix} -0.052937 & 0.000936697 & 0.558781 & -9.80988 & 0 & -4.81993e{-}17 & 0 & -4.81993e{-}17 \\ -0.0974182 & -0.265395 & 10.396 & 0.0489084 & 0 & 0 & 0 & 0 \\ 0.022537 & -0.00721859 & -0.408926 & 0 & 3.92561e{-}17 & 2.3063e{-}16 & 0 & -1.17768e{-}16 \\ 0 & 0 & 0.999988 & 0 & 0 & 0 & 0 & 0.00498556 \\ 1.30025e{-}34 & -2.34908e{-}16 & 0 & 0 & -0.0577036 & -0.454964 & 9.80988 & -10.3117 \\ -1.2369e{-}17 & 0 & -1.47791e{-}19 & 0 & -0.0116449 & -0.555316 & 0 & 0.334559 \\ 0 & 0 & 0 & 0 & 0 & 1 & 0 & -0.00498562 \\ -8.44383e{-}19 & 0 & -6.32303e{-}18 & 0 & 0.00665441 & 0.0312379 & 0 & -0.10829 \end{bmatrix} \begin{bmatrix} u \\ w \\ q \\ \theta \\ v \\ p \\ \phi \\ r \end{bmatrix} \tag{5.39}$$

While the coupling derivatives of the 6-DoF are almost infinitesimally small the FLIGHTLAB model has quite some significant coupling derivatives e.g. Z_p, M_p and Z_r. These nonzero coupling derivatives are mostly the result of the rotor wake interference with the wing [2]. The aerodynamics for the rotor wake on the wing and empennage used in the FLIGHTLAB model are derived from wind tunnel tests conducted in support of the preflight simulation development. The 6-DoF model uses the rather simplistic method described in subsection 3.3.4 to compute this interaction. In order to better predict the longitudinal-lateral coupling effects a better interaction model should be incorporated in the 6-DoF model.

5.3.2. Comparison with FLIGHTLAB Results

In this subsection the results obtained by the 6-DoF model will be validated by comparing them with the FLIGHTLAB model (FXV-15) results. The eigenvalues of the two linearized models will be compared by plotting them together in the same figure as a function of airspeed. This will be done for three different nacelle configurations; H-mode (90deg), C-mode (60deg) and A-mode (0deg). For both models the coupled state space systems are used. The FLIGHTLAB eigenvalues are plotted with steps of 20 kts, while the 6-DoF model uses steps of 2 kts.

Figure 5.12 presents the eigenvalues of the two models in helicopter mode. The airspeed of both models ranges from 0 to 100 kts. Subfigure (a) presents the full set of eigenmodes while in subfigure (b) the low frequency modes are expanded. Some eigenvalues which are located on the real axis have been plotted

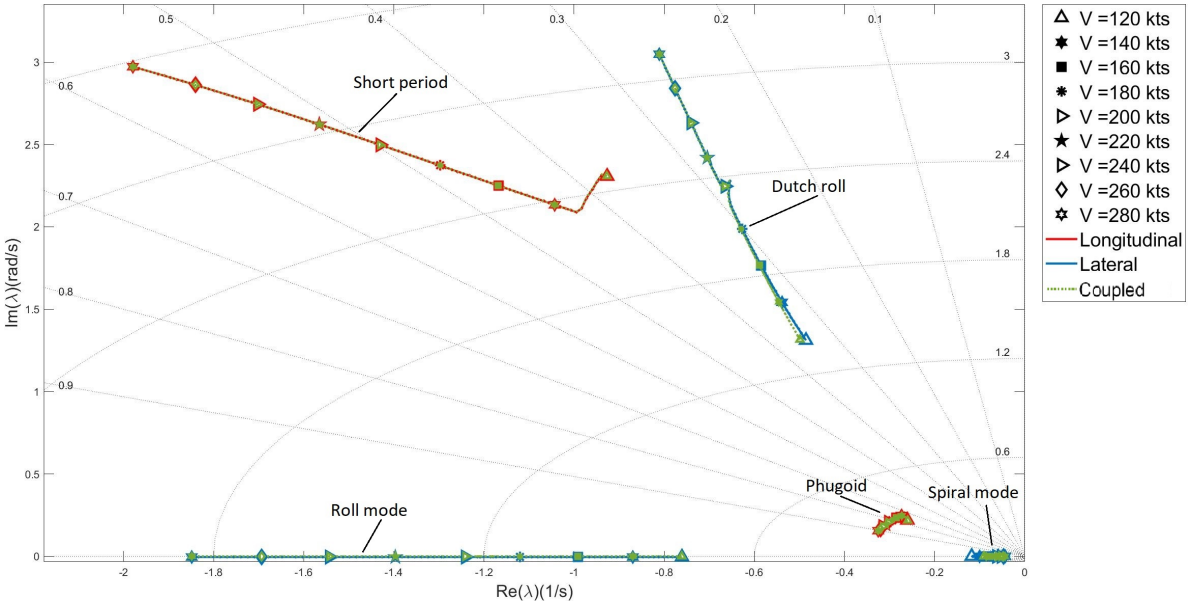

Figure 5.11: XV-15 coupled longitudinal eigenmodes compared with the uncoupled modes in airplane mode

with some vertical offset in order to distinguish between the different modes and models in the figures. In hover, the phugoid and the Dutch Roll are unstable for both models. The roll mode, spiral mode and heave and pitch subsidences take their place on the real axis. The frequency of the roll mode increases with airspeed. The spiral mode is unstable for both models at moderate airspeeds. The 6-DoF model spiral mode is however stable in hover while the FLIGHTLAB model mode is unstable. Both eigenvalues move to right on real axis up until 20-30 kts, after which they move towards the stable side of the graph again. The spiral stabilizes at around 80 kts for both models. According to Padfield, the increase in instability up to 20-30 kts can be attributed to the increasing interaction of the rotor wakes with the wings [2]. There is a significant increase in the destabilizing derivative L_r which is captured by both models (Figure 4.20). The weathercock stability derivative N_v is the second derivative that destabilizes the spiral mode according to Equation 5.25. In Figure 4.21 we saw that the FLIGHTLAB weathercock stability derivative is a factor 2 or 3 larger than the 6-DoF derivative. The most obvious reason for this difference was explained to be the fuselage contribution to the yawing moment which is not modelled in the 6-DoF model. Consequently, this also explains the differences in spiral eigenvalues at low airspeeds.

The Dutch Roll mode stabilizes shortly after the airspeed is increased from hover according to both models. The Dutch Roll damping is also quite similar while the frequency of the FLIGHTLAB model increases faster with speed. In subsection 5.2.3 it became clear that the frequency of the mode is mainly dependent on u_0 and N_v. Trim velocity component u_0 is obviously almost equal for both models at the same speed. The larger weathercock stability of the FLIGHTLAB model thus causes the bigger increase in frequency. The short period of both models show a similar trend. The frequency increases with airspeed while the damping decreases. However, the FLIGHTLAB mode presents a stronger increase in frequency and is more heavily damped. The damping and frequency of the short period are both heavily dependent on M_q (Equation 5.9). From Figure 4.13 it became clear that the pitch damping derivative is significantly higher for the FLIGHTLAB model than for the 6-DoF model. This was mainly attributed to the destabilizing rotor contribution for the latter model which is stabilizing for the former. Lastly, the most striking difference between the models in helicopter mode is the phugoid mode. In subsection 5.1.2 we saw that the phugoid damping increases with airspeed until the mode is critically damped and decouples. From Figure 5.12 it can be concluded that this is only the case for the 6-DoF model. The FLIGHTLAB model phugoid damping increases as well but the mode remains oscillatory. This happens because the speed stability derivative M_u is positive for the FLIGHTLAB derivative while for the 6-DoF model the derivative is negative at high airspeeds. A negative M_u amplifies the damping according to Equation 5.16.

A similar comparison between the models is presented in Figure 5.13 for the XV-15 in conversion mode with

a 60 degrees nacelle angle configuration. The 6-DoF model eigenvalues range from 100 to 160 kts while those of the FLIGHTLAB model range from 100 to 140 kts. The roll mode eigenvalue are quite comparable. The frequency of the mode increases with airspeed for both models. The FLIGHTLAB roll damping derivative is larger than the 6-DoF derivative in this configuration which also explains why the former model its eigenvalues are located more to the left on the real axis. Similarly as in helicopter mode the FXV-15 short period is more heavily damped than the 6-DoF model mode, which is caused by the larger M_q value. The FLIGHTLAB Dutch Roll mode is also slightly more damped, but the results look already more comparable than in helicopter mode. This is because the differences between the N_v derivatives have decreased. In subfigure (b) the low frequency modes are expanded. The spiral mode of both models is stable and the frequency increases slightly with airspeed. The FLIGHTLAB spiral mode frequency is however roughly double the frequency of the 6-DoF model. From Figure D.7 it can be concluded that larger N_r and L_v increase the spiral frequency. These two derivatives are significantly larger for the FLIGHTLAB model. In contrary to the H-mode both models have an oscillatory phugoid along the entire airspeed range. In this configuration the M_u derivative is positive for both models. The phugoid damping increases with speed for both models while the frequency slightly decreases.

In Figure 5.14 the eigenvalues of the models in airplane mode are compared. The 6-DoF model has an airspeed range of 120 to 280 kts in this configuration. For the FLIGHTLAB model data was available at 140, 180 and 220 kts so this has been used for this comparison. In subsection 5.2.1 we already saw that the roll mode frequency of the 6-DoF model increases with airspeed. This is also the case for the FXV-15. The short period of the 6-DoF model is more heavily damped than the FLIGHTLAB model while the latter model has a higher frequency. Both observations can be explained by looking at differences in static stability derivative M_w in airplane mode (Figure 4.12(c)). The 6-DoF model derivative is a factor 2-3 smaller. A smaller value of M_w increases the damping of the short period while it decreases the frequency, according to Equation 5.7 and Equation 5.8. The Dutch roll modes look quite comparable. In contrary to H-mode and C-mode the 6-DoF model now has a more highly damped Dutch roll. Both N_r and Y_v which influence the Dutch roll damping significantly according to Equation 5.28 have increased more for the 6-DoF model compared to the FLIGHTLAB model. In Figure 5.14b the spiral mode is shown, which becomes less stable with airspeed for both models. According to Padfield, this happens due to the reduction in yaw damping (N_r) and increase in the roll-yaw coupling (N_p). However, the 6-DoF yaw damping increases while N_p decreases so this does not explain the behavior of the 6-DoF model. The roll damping L_p significantly influences the spiral frequency which causes its decrease with airspeed. The phugoid damping mode in A-mode increases slightly with airspeed for both models. The frequency is more or less constant with airspeed.

In general, the XV-15 stability characteristics obtained by both models are quite similar. Both models have an unstable phugoid and Dutch roll in hover. The spiral mode is unstable at moderate airspeed in helicopter mode. The curves of the eigenvalues with airspeed also show a lot of similarities. The trends of the frequency and damping of the modes with speed are more or less the same for both models. The main discrepancy between the two models is phugoid in helicopter mode. The 6-DoF model phugoid is non-oscillatory at high airspeeds, which is caused by the negative speed stability derivative M_u. Other than that, the 6-DoF model has proved to be a valid model for stability research.

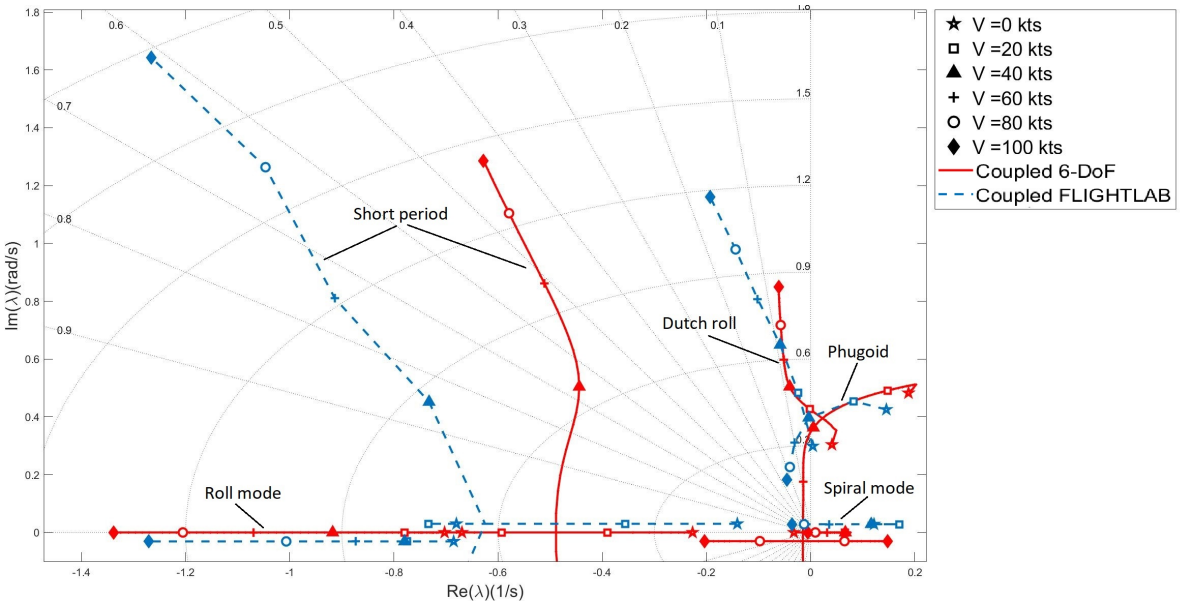

(a) Full picture

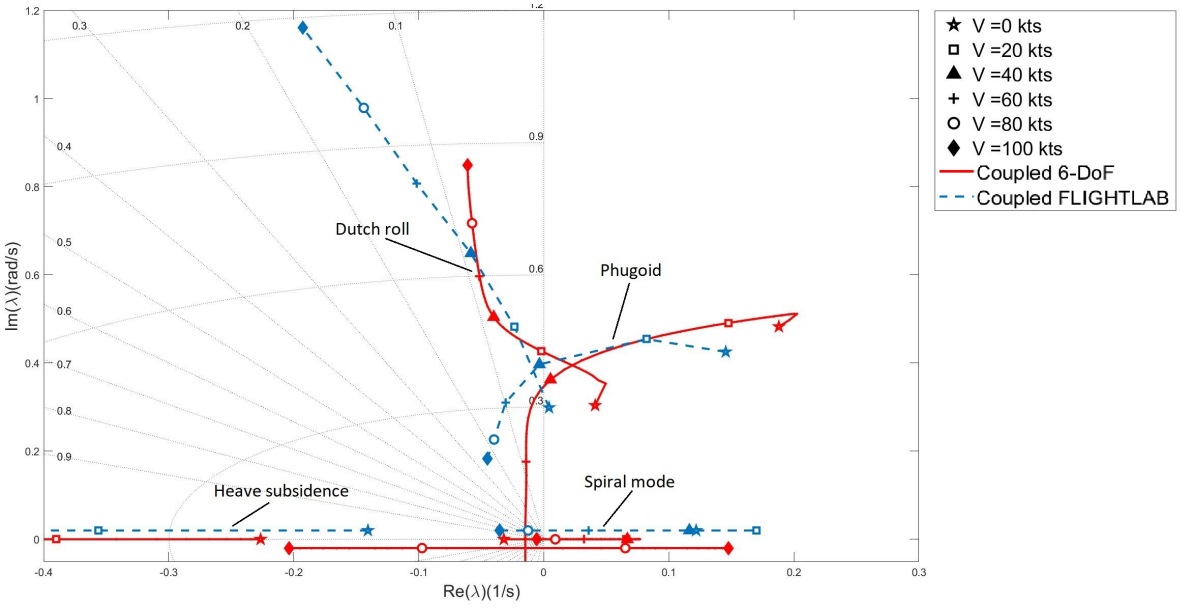

(b) Low frequency modes

Figure 5.12: XV-15 6-DoF model coupled eigenmodes in helicopter mode compared with the FLIGHTLAB eigenmodes

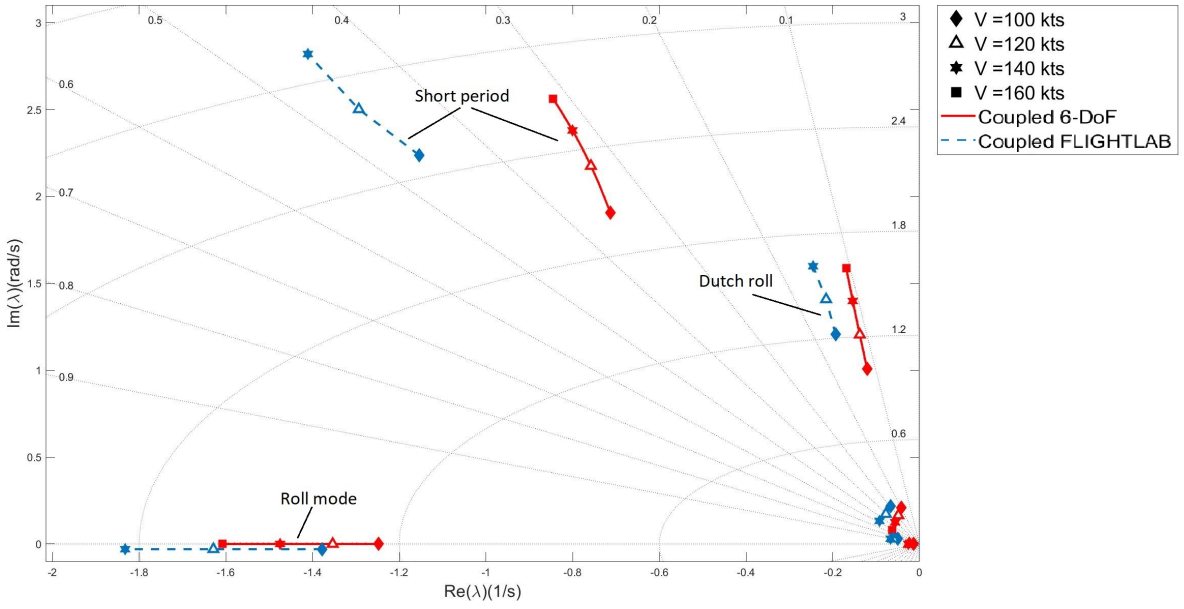

(a) Full picture

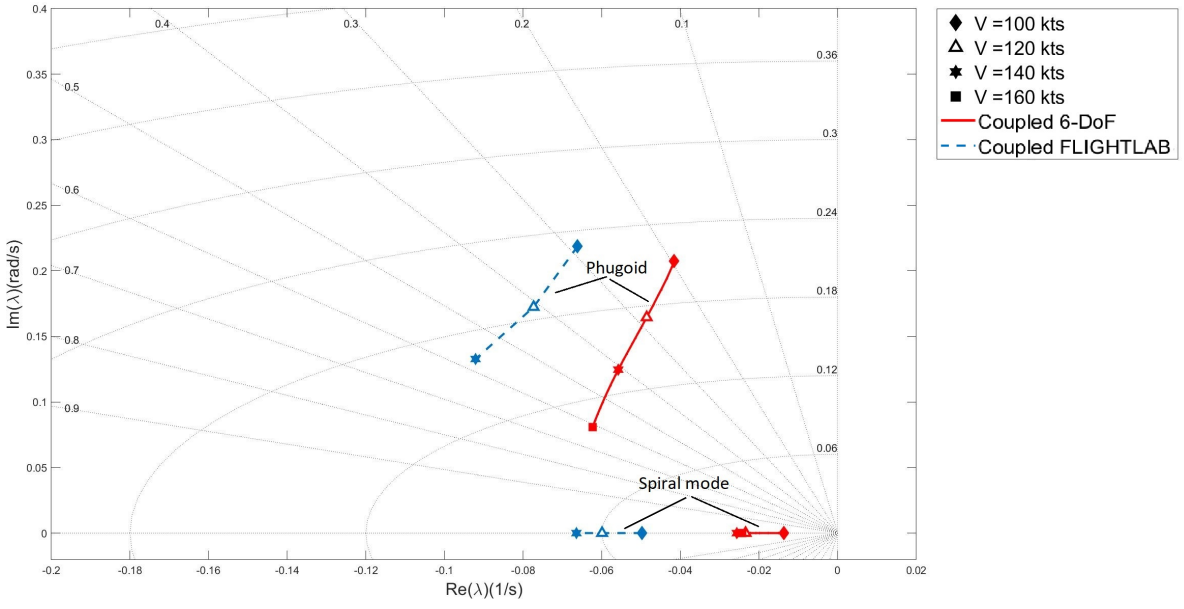

(b) Low frequency modes

Figure 5.13: XV-15 6-DoF model coupled eigenmodes in conversion mode compared with the FLIGHTLAB eigenmodes

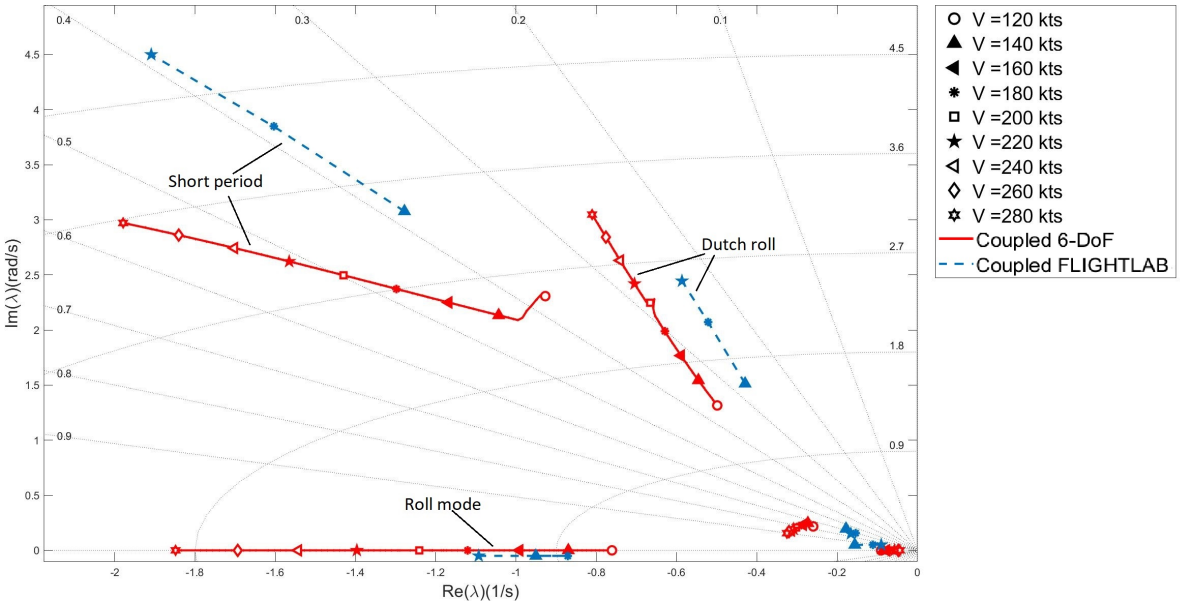

(a) Full picture

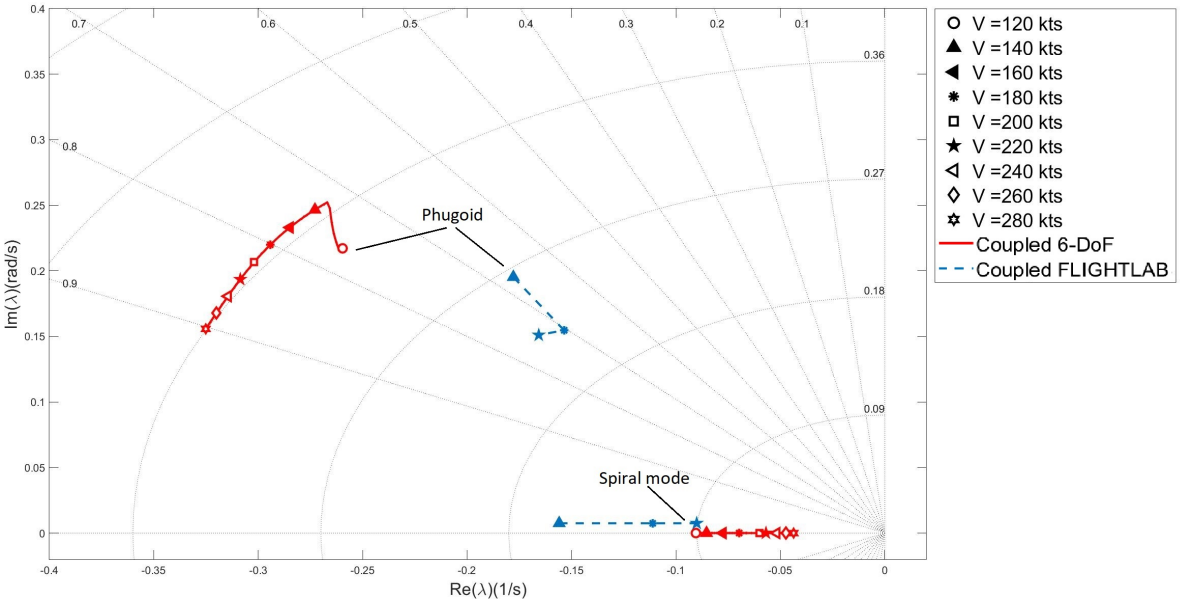

(b) Low frequency modes

Figure 5.14: XV-15 6-DoF model coupled eigenmodes in airplane mode compared with the FLIGHTLAB eigenmodes

6

Conclusions and Recommendations

In this final chapter the research conducted is concluded. The research questions are answered and conclusions are drawn following from the research objective. Lastly, recommendations are provided for future work about this topic.

6.1. Conclusions

The objective of this research was to to investigate the stability characteristics of tiltrotor aircraft theoretically by using the technique of linearized stability derivatives on a six-degrees-of-freedom tiltrotor flight dynamics model. In order to reach this objective several research subquestions were posed in the introduction of this report, which answers together serve as an answer to the main research question. The answers to these subquestions can be find below. Afterwards, a general conclusion about the research is drawn.

1. *Which features characterize a tiltrotor aircraft?*
The most promising feature of the tiltrotor aircraft is its capability of performing vertical manoeuvres like a conventional helicopter as well as reaching high flight speeds and long ranges like a fixed-wing airplane. This can be achieved by tilting the rotors which are located at the tips of the wing. Because of this capability, the tiltrotor also requires a special control strategy. Both helicopter and airplane control strategies are combined to have good control at both very low and very high flight speeds. A tail rotor which is a necessity for a conventional helicopter has become redundant as the two counter rotating rotors cancel out each others torque. Longitudinal cyclic is used to control the pitch motion in helicopter mode. In the same mode differential collective and cyclic pitch is used to control yawing and rolling motions. Ailerons, elevators and rudders are also included to control the tiltrotor in airplane mode. The controls in helicopter mode are gradually phased out while the airplane controls are phased in when rotating the nacelles towards the horizontal axis. In all flight modes the pilot uses a center cyclic stick to control pitch and roll while pedals are used to control yaw. A collective stick is included to control the collective pitch of the blades in helicopter mode, and the same stick functions are a power lever in airplane mode.

2. *How can the dynamic behavior of the tiltrotor most accurately be predicted by modelling its principles into a flight dynamics model?* In order to investigate the stability characteristics of a tiltrotor a flight dynamics model has to be developed. In prior research conducted at Delft University of Technology a six-degrees-of-freedom tiltrotor flight dynamics model has been developed (6-DoF model). This model describes the motion of the tiltrotor using 9 different states; 3 translational velocity states, 3 rotational velocity states and three Euler angles describing the orientation of the aircraft with respect to the earth. Furthermore, the motion of the aircraft can be controlled using 4 different inputs; the longitudinal and lateral cyclic stick deflection, the collective stick deflection and the pedal deflection. The 6-DoF model divides the tiltrotor into 15 different components and the forces and moments acting on each component are computed and converted to the same reference frame. In order to improve the prediction of the dynamic behavior of the aircraft some important additions are made to the model. The aerodynamic coefficients of the lifting surfaces are computed using a combination of flat plate area theory and linear aerodynamics, solving issues with the rotor wake-wing interference. Furthermore, the centre of gravity and moments of inertia of the aircraft are

made dependable on the nacelle angle. This improves primarily the prediction of the pitching moments. Look-up tables have been implemented to the model to add the aerodynamic contributions of the fuselage. Moreover, the interference between the wing wake and the empennage has been implemented into the model. The effective angle of attack of the horizontal stabilizers is influenced by this interference and results in a more accurate prediction of the empennage aerodynamic forces.

3. *Which conclusions can be drawn about the stability characteristics of the tiltrotor from the linearized stability and control derivatives?* The nonlinear 6-DoF model has been linearized and the stability and control derivatives following from the linearization have been analysed as a function of airspeed and nacelle angle. The derivatives are also compared with data obtained from other models. This serves as validation for the results, but the differences between the models can also say a lot about the effects of the different assumptions made during the modelling process. Generally, most of the derivatives in H-mode have conventional helicopter characteristics while in A-mode they have fixed-wing airplane characteristics. There are however some exceptions, such as X_u in helicopter mode for example. The drag damping derivative of a tiltrotor in this mode is much larger than for a conventional helicopter due to the extra drag of the wings and the second rotor. Furthermore, the damping derivatives (X_u, Z_w, L_p etc.) are all negative along the entire flight envelope which is required for the stability of the subsidences. The rotor contribution to Z_w is large in helicopter mode and large to X_u in airplane mode. The heave-surge coupling derivatives Z_u and X_w are the largest when the nacelle angles are approximately at a 45 degrees inclination. The same goes for the roll-yaw coupling derivatives N_p and L_r. The models' stability derivatives show a lot of similarities. The speed stability derivative M_u curves look less similar. The 6-DoF model derivative is negative at high airspeeds in H-mode while the derivatives of the GTRS and FLIGHTLAB models remain positive. The negative contribution of the horizontal stabilizers to M_u is very dominant for the 6-DoF model, which seems to be not the case for the other models. Furthermore, the weathercock stability derivative N_v and dihedral effect L_v are positive and negative respectively. Lastly, the yaw damping derivative N_r is relatively small at low airspeeds compared to conventional helicopters due to the absence of a tail rotor. The control derivatives of the 6-DoF model show a lot of similarities with the FXV-15 and the control inputs lead to the desired responses. The assumption that elevators, ailerons and rudders create no drag results in differences between the curves of the models. The effectiveness's of the control surfaces of the models seem to be dissimilar while they should be equal.

4. *Which conclusions can be drawn about the stability characteristics of the tiltrotor from the eigenvalues of the dynamic modes?* Firstly, the dynamic modes have been evaluated by uncoupling the longitudinal and lateral modes. In hover, the heave and pitch subsidences are both non-oscillatory but stable. As airspeed increases, the heave an pitch subsidence couple together and form the short period. The frequency of the short period increases with airspeed while the damping slightly decreases at high nacelle angle configurations. At low nacelle angle configurations the damping increases with airspeed. When the airspeed is kept constant and the nacelle angle decreases the frequency slowly increases while the damping remains roughly constant. In hover the phugoid is oscillatory but unstable. The mode stabilizes when the airspeed increases and becomes at some point non-oscillatory. This can be attributed to the negative value of M_u which amplifies the phugoid damping. In C-mode and A-mode the phugoid is oscillatory and stable. At constant airspeed and decreasing nacelle angle the phugoid damping increases. At the same time the frequency of the mode increases slightly. The roll mode is mostly a pure roll subsidence which is stable, highly damped an non-oscillatory. Its frequency increases with airspeed but decreases with decreasing nacelle angle. The coupling with yaw increases with decreasing nacelle angle. The spiral mode is mostly unstable in helicopter mode. In hover the mode is stable, but as airspeed increases the mode destabilizes. The instability increases with airspeed up to $\pm$ 30 kts, after which it decreases again. At airspeeds higher than $\pm$ 80kts in H-mode the spiral is again stable. The spiral mode also becomes more stable with decreasing nacelle angle. In hover the Dutch roll is also unstable, but becomes stable after airspeed increases. The dutch roll frequency increases with airspeed while the damping remains constant. Decreasing the nacelle angle however clearly increases the damping of the mode. Furthermore it was found that the uncoupling of the modes is valid for the 6-DoF model since the coupling derivatives are approximately zero. The 6-DoF model eigenmodes results showed a lot of similarities with the FXV-15. Both models have an unstable phugoid and Dutch roll in hover. The spiral modes are often unstable in helicopter mode and have similar trends with airspeed. The FXV-15 spiral is however already unstable in hover, due to its lower value of N_r. The FXV-15 short period in H-mode and C-mode is relatively more damped due to its higher pitch damping M_q. The biggest difference in modes

between the two models is the phugoid in helicopter mode. The 6-DoF model phugoid is non-oscillatory at high airspeeds because of the negative M_u at those flight conditions. In the same flight conditions the FLIGHTLAB M_u is positive and thus the phugoid remains oscillatory.

In general, the 6-DoF model shows good agreement with previously published data from other tiltrotor models. The trim data of the 6-DoF model looked similar to the GTRS trim data. The linearized model derivatives also showed a lot of resemblance with derivatives from other models with a few exceptions such as M_u. This gives confidence in using the model for future research related to flight dynamics, stability, control or handling qualities.

6.2. Recommendations for Future Work

Now that the thesis research is concluded and the research questions have been answered, there are still some recommendations for future research. These recommendations are mainly focused on improvement of the nonlinear model, since the accuracy of the predicted stability characteristics heavily depends on the accuracy of the nonlinear model.

The first recommendation I would propose is a further investigation into the M_u derivative. The negative value of the speed stability derivative at high airspeeds in helicopter mode is not in line with what is found in literature. This negative M_u amplifies the phugoid damping, which results in a non-oscillatory phugoid. The negative contribution of the airframe, with in particular the horizontal stabilizers, causes the negative value of M_u. According to the GTRS model data the airframe should have a positive contribution to the derivative, but what the actual cause is for this difference has not been discovered during this research.

Furthermore, the comparison between the eigenmodes of the coupled and uncoupled linear state space systems showed that there is almost no coupling at all between the longitudinal and lateral modes. The FXV-15 however showed quite some significant values for the coupling derivatives, primarily at low airspeeds in helicopter mode. This was mainly attributed by Padfield to the interference between the rotor wake and the airframe. For example, any perturbation in yaw or sideslip should lead to variations in rotor downwash at the horizontal stabilizers resulting in a pitching moment. For this reason, the M_r and M_v derivatives are non-zero for the FXV-15. Rotor wake-empennage interference has not been implemented in the 6-DoF model which is most likely the cause why these derivatives are zero for the 6-DoF model. The interference between the rotor wake and the wing of the 6-DoF model is modelled rather simplistic and far away from reality. The interference model is also dependent on the the induced velocity which is computed using basic momentum theory. This theory assumes that the induced velocity is constant along the rotor disc, which is a rather big assumption. An improved induced flow model which does not make this assumption is expected to give more realistic results. In order to more accurately investigate the coupling between longitudinal and lateral motions, the interference models between the rotors and airframe should be improved.

Lastly, in the introduction of this report the accident of the AW609 during flight testing was mentioned. The accident happened after diverging yaw- and roll oscillations were experienced. The accident was described as an unstable Dutch Roll. During the dynamic stability analysis conducted in this research no stability issues were found for the Dutch Roll. However, the research was limited to steady, horizontal, symmetrical flight. The accident occured while exiting a turn after a high-speed test dive was performed. This means that the aircraft was probably not flying level. The effect of for example the glide slope angle or sideslip angle on the Dutch Roll stability was not investigated. It would be interesting to further investigate what the effect is of these two angles on the Dutch roll stability and investigate more deeply what caused the instability before the accident.

Bibliography

[1] M. D. Maisel, D. J. Giulianetti, and D. C. Dugan, *The Histort of The XV-15 Tilt Rotor Research Aircraft: From Concept to Flight* (National Aeronautics and Space Administration, 2000).

[2] G. D. Padfield, *Helicopter Flight Dynamics, Including a Treatment of Tiltrotor Aircraft*, 3rd ed. (Wiley, 2018).

[3] T. Berger, O. Juhasz, M. J. S. Lopez, M. B. Tischler, and J. F. Horn, *Modeling and control of lift offset coaxial and tiltrotor rotorcraft,* CEAS Aeronautical Journal **vol. 11**, pp. 191 (2020).

[4] K. Lu, C. Liu, C. Li, and R. Chen, *Flight dynamics modeling and dynamic stability analysis of tilt-rotor aircraft,* International Journal of Aerospace Engineering **vol. 2019**, 1 (2019).

[5] Y. Yuan, D. Thomson, and D. Anderson, *Manoeuvrability investigation for tiltrotor aircraft with an integrated simulation engine,* 47th European Rotorcraft Forum (2021).

[6] S. W. Ferguson, *Development and Validation of a Simulation for a Generic Tilt-Rotor Aircraft*, Tech. Rep. (NASA CR-166537, 1989).

[7] J. H. Taylor and A. J. Antoniotti, *Linearization algorithm for computer-aided control engineering,* in *IEEE Symposium on Computer-Aided Control Systems Design* (IEEE Control Systems Society, Napa, CA, 1992).

[8] S. W. Ferguson, *A mathematical model for real time flight simulation of a generic tilt-rotor aircraft*, Tech. Rep. (NASA CR-166536, 1988).

[9] L. A. Young, W. W. Chung, A. Paris, D. Salvano, R. Young, H. Gao, K. Wright, D. Miller, and V. Cheng, *A study of civil tiltrotor aircraft in nextgen airspace,* in *10th AIAA Aviation Technology, Integration, and Operations (ATIO) Conference* (American Institute of Aeronautics and Astronautics, Forth Worth, Texas, 2010) pp. 1–18.

[10] O. Johnson, *Aw609 crash: final report points to oscillations and flight control laws,* vertical (2017).

[11] D. Perry, *Aw609 control laws initiated 'dutch roll': investigators,* Flight Global (2016).

[12] K. M. Kleinhesselink, *Stability and Control Modeling of Tiltrotor Aircraft*, Master's thesis, University of Maryland, Department of Aerospace Engineering (2007).

[13] R. Fortenbaugh and L. Lazaric, *Ba609 tiltrotor handling qualities; development flight test results, proc. raes conference 'rotorcraft handling qualities',* (Liverpool, 2008).

[14] R. Fortenbaugh, D. W. King, and M. Peryea, *Flight control features of the bell-agusta ba-609 tiltrotor: a handling qualities perspective,* 25th European Rotorcraft Forum , 1 (1999).

[15] P. Sokolowski, *Literature study: Flight Dynamics Modelling of a Tiltrotor Aircraft*, Master's thesis, Delft University of Technology (2020).

[16] P. B. Harendra, M. Joglekar, T. M. Gaffey, and R. L. Marr, *V/STOL Tilt Rotor Study-Volume 5: A Mathematical Model for Real Time Flight Simulation of the Bell Model 301 Tilt Rotor Research Aircraft*, Tech. Rep. (NASA CR-114614, 1973).

[17] M. B. Tischler, *Identification and verification of frequency domain models for XV-15 tilt-rotor aircraft dynamics*, Tech. Rep. (NASA-TM-86009, 1984).

[18] G. D. Padfield and M. M. Meyer, *First steps in the development of handling qualities criteria for a civil tiltrotor,* Journal of the American Helicopter Society **50**, 33–46 (2005).

[19] D. Walker and P. Perfect, *Longitudinal Stability and Control of Large Tilt-Rotor Aircraft*, Tech. Rep. (Engineering Department, Liverpool University, 2007).

[20] G. D. Klein, *Linear Modelling of Tiltrotor Aircraft (in Helicopter and Airplane Modes) for Stability Analysis and Preliminary Design*, Master's thesis, Naval Post Graduate School, Monterey, CA (1996).

[21] C. W. Acree Jr., H. Yeo, and J. Sinsay, *Performance optimization of the nasa large tiltrotor,* NASA/TM-2008-215359 (2008).

[22] M. B. Tischler and R. K. Remple, *Aircraft and Rotorcraft System Identification: Engineering Methods with Flight Test Examples*, 2nd ed. (AIAA, Reston, 2012).

[23] W. Johnson, *Dynamics of Tilting Proprotor Aircraft in Cruise Flight*, Tech. Rep. (Ames Research Center and U.S. Army Air Mobility R&D Laboratory, Moffett Field, Carlif., 1974).

[24] R. K. Heffley and M. A, *Minimum-Complexity Helicopter Simulation Math Model*, Tech. Rep. (Manudyne Systems Inc. Los Altos, CA. April, 1988).

[25] Anonymous, *Handling qualities requirements for military rotor- craft. aeronautical design standard ads-33e-prf,* United States Army Aviation and Troop Command (2000).

[26] O. Juhasz, R. Celi, C. M. Ivler, M. B. Tischler, and T. Berger, *Flight dynamic simulation modeling of large flexible tilt- rotor aircraft,,* American Helicopter Society 68th Annual Forum (2012).

[27] M. Pavel, *Rotorcraft mechanics course ae4314, lecture slides,* (2020).

[28] M. V. Cook, *Flight Dynamics Principles*, 2nd ed. (Arnold (Wiley), 1997).

[29] R. Prouty, *Helicopter Performance, Stability and Control* (PWS Publishers, 1986).

[30] P. Sokolowski, *MSc. Thesis: Flight Dynamics Modelling of a Tiltrotor Aircraft*, Master's thesis, Delft University of Technology (2021).

[31] T. van Holten, J. A. Melkert, B. Marrant, and M. Pavel, *Helicopter performance, stability and control lecture notes,* (2002).

[32] M. D. Pavel, *Six Degrees of Freedom Linear Model for Helicopter Trim and Stability Calculation*, Tech. Rep. (Delft University of Technology, Delft, 1996).

[33] J. Fu, J. Huang, L. Song, and D. Yang, *Experimental study of aircraft achieving dutch roll mode stability without weathercock stability,* International Journal of Aerospace Engineering , 1 (2020).

[34] J. A. Mulder, W. van Staveren, J. van der Vaart, E. de Weerdt, C. de Visser, A. in 't Veld, and E. Mooij, *Flight dynamics lecture notes,* (2013).

[35] R. C. Nelson, *Flight Stability and Automatic Control*, 2nd ed. (McGraw-Hill Companies, 1998).

[36] A. Faulkner, *Lateral-directional stability: theoretical analysis and flight test experience,* 9th European Rotorcraft Forum (1983).

A

3-DoF Model Equations

- Equations are shown on next page -

$$a_0 = \frac{\left(3\mu_{cp}^2\theta_0 - 6\mu_{cp}\theta_0\lambda_{qt} + 3\theta_0\lambda_{qt}^2 + 3\theta_0 - 4\lambda_{cp} - 4\lambda_i + 4\lambda_{qp}\right) I_b\gamma\Omega^2}{24\left(I_b\Omega^2 + K_\beta\right)} \tag{A.1}$$

$$\begin{aligned} a_1 = {} & \frac{32\Omega\gamma I_b}{\left(I_b\Omega^2 + K_\beta\right)\left(I_b^2\gamma^2\Omega^4\left(\mu_{cp}^2 - 2\mu_{cp}\lambda_{qt} + \lambda_{qt}^2 + 2\right)\left(\mu_{cp}^2 - 2\mu_{cp}\lambda_{qt} + \lambda_{qt}^2 - 2\right) - 256K_\beta^2\right)}\Bigg(qI_b^2\Omega^4\left(\mu_{cp}^2 - 2\mu_{cp}\lambda_{qt} + \lambda_{qt}^2 + 2\right) + \\ & + \frac{\left(\mu_{cp}^2 - 2\mu_{cp}\lambda_{qt} + \lambda_{qt}^2 + 2\right)\left(\lambda_{qp} + \frac{4\theta_0}{3} - \lambda_{cp} - \lambda_i\right)\left(-\mu_{cp} + \lambda_{qt}\right)\gamma I_b^2\Omega^5}{8} + qI_bK_\beta\left(\mu_{cp}^2 - 2\mu_{cp}\lambda_{qt} + \lambda_{qt}^2 + 3\right)\Omega^2 + K_\beta^2 q + \\ & + \frac{\left(\left(\lambda_{qp} + \frac{8\theta_0}{3} - \lambda_{cp} - \lambda_i\right)\lambda_{qt}^2 - 2\mu_{cp}\left(\lambda_{qp} + \frac{8\theta_0}{3} - \lambda_{cp} - \lambda_i\right)\lambda_{qt} + \left(\lambda_{qp} + \frac{8\theta_0}{3} - \lambda_{cp} - \lambda_i\right)\mu_{cp}^2 + \frac{34\left(\lambda_{qp} - \lambda_{cp} - \lambda_i\right)}{9} + 4\theta_0\right)K_\beta\left(-\mu_{cp} + \lambda_{qt}\right)\gamma I_b\Omega^3}{8}\Bigg) \end{aligned} \tag{A.2}$$

$$\begin{aligned} b_1 = {} & \frac{-2\Omega I_b}{\left(I_b\Omega^2 + K_\beta\right)\left(I_b^2\gamma^2\left(\mu_{cp}^2 - 2\mu_{cp}\lambda_{qt} + \lambda_{qt}^2 + 2\right)\left(\mu_{cp}^2 - 2\mu_{cp}\lambda_{qt} + \lambda_{qt}^2 - 2\right)\Omega^4 - 256K_\beta^2\right)}\Bigg(\left(256 + \left(\mu_{cp}^2 - 2\mu_{cp}\lambda_{qt} + \lambda_{qt}^2 - 2\right)\gamma^2\right)qK_\beta I_b\Omega^2 + \\ & + \frac{2\left(\frac{3\lambda_{qt}^2\theta_0}{4} - \frac{3\lambda_{qt}\mu_{cp}\theta_0}{2} + \frac{3\mu_{cp}^2\theta_0}{4} + \lambda_{qp} + \frac{3\theta_0}{4} - \lambda_{cp} - \lambda_i\right)\left(\mu_{cp}^2 - 2\mu_{cp}\lambda_{qt} + \lambda_{qt}^2 - 2\right)\left(-\mu_{cp} + \lambda_{qt}\right)\gamma^3 I_b^2\Omega^5}{9} + qI_b^2\gamma^2\left(\mu_{cp}^2 - 2\mu_{cp}\lambda_{qt} + \lambda_{qt}^2 - 2\right)\Omega^4 + \\ & + 32\left(\lambda_{qp} + \frac{4\theta_0}{3} - \lambda_{cp} - \lambda_i\right)K_\beta\left(-\mu_{cp} + \lambda_{qt}\right)\gamma I_b\Omega^3 + 32\left(\lambda_{qp} + \frac{4\theta_0}{3} - \lambda_{cp} - \lambda_i\right)\Bigg)K_\beta^2\left(-\mu_{cp} + \lambda_{qt}\right)\gamma\Omega + 256K_\beta^2 q\Bigg) \end{aligned} \tag{A.3}$$

$$
\begin{aligned}
H = &-\frac{\Omega N_b}{96R}\left(-b_1\left(c_{d_2,b}\theta_0-\frac{c_{d_1,b}}{2}\right)^2 a_0\lambda_{qt}^3+3\left(\mu_{cp}a_0b_1-\frac{a_0^2}{3}-\frac{a_1^2}{6}-\frac{b_1^2}{6}\right)\left(c_{d_2,b}\theta_0-\frac{c_{d_1,b}}{2}\right)^2\lambda_{qt}^2+\right.\\
&+\left(-3b_1\left(c_{d_2,b}\theta_0-c_{d_1,b}\frac{1}{2}\right)^2 a_0\mu_{cp}^2+2\left(c_{d_2,b}\theta_0-c_{d_1,b}\frac{1}{2}\right)^2\left(a_0^2+\frac{1}{2}a_1^2+\frac{1}{2}b_1^2\right)\mu_{cp}-\right.\\
&-2\left(\frac{1}{4}a_0b_1+a_1\left(\lambda_{cp}+\lambda_i-\lambda_{qp}\right)\right)c_{d_2,b}^2\theta_0^2+2c_{d_1,b}\left(\frac{1}{4}a_0b_1+a_1\left(\lambda_{cp}+\lambda_i-\lambda_{qp}\right)\right)c_{d_2,b}\theta_0-12c_{d_2,b}\Omega a_0b_1+\\
&+\left(-\frac{1}{8}a_0b_1-\frac{1}{2}a_1\left(\lambda_{cp}+\lambda_i-\lambda_{qp}\right)\right)c_{d_1,b}^2+12\Omega C_{l_\alpha,bl}a_0b_1\Big)\lambda_{qt}+b_1\left(c_{d_2,b}\theta_0-c_{d_1,b}\frac{1}{2}\right)^2 a_0\mu_{cp}^3-\left(c_{d_2,b}\theta_0-c_{d_1,b}\frac{1}{2}\right)^2\left(a_0^2+\frac{1}{2}a_1^2+\frac{1}{2}b_1^2\right)\mu_{cp}^2+\\
&+\left(2\left(\frac{1}{4}a_0b_1+a_1\left(\lambda_{cp}+\lambda_i-\lambda_{qp}\right)\right)c_{d_2,b}^2\theta_0^2-2c_{d_1,b}\left(\frac{1}{4}a_0b_1+a_1\left(\lambda_{cp}+\lambda_i-\lambda_{qp}\right)\right)c_{d_2,b}\theta_0+12c_{d_2,b}\Omega a_0b_1+\right.\\
&+\left(\frac{1}{8}a_0b_1+\frac{1}{2}a_1\left(\lambda_{cp}+\lambda_i-\lambda_{qp}\right)\right)c_{d_1,b}^2-12\Omega C_{l_\alpha,bl}a_0b_1\Big)\mu_{cp}-4c_{d_2,b}\left(\left(\lambda_{cp}+\lambda_i-\lambda_{qp}\right)^2 c_{d_2,b}+\Omega\frac{1}{2}\right)\theta_0^2+4c_{d_1,b}\left(\left(\lambda_{cp}+\lambda_i-\lambda_{qp}\right)^2 c_{d_2,b}+\Omega\frac{1}{2}\right)\theta_0-\\
&-6c_{d_2,b}b_1\Omega\hat{q}-\left(\lambda_{cp}+\lambda_i-\lambda_{qp}\right)^2 c_{d_1,b}^2+6\left(\hat{q}C_{l_\alpha,bl}b_1-c_{d_0,b}\frac{1}{3}\right)\Omega\Big)\rho c\left(\mu_{cp}-\lambda_{qt}\right)R^4+\\
&+12\gamma I_b\left(\Omega a_0b_1\lambda_{qt}^2+\left(-2b_1\Omega\mu_{cp}a_0+2\Omega\left(\lambda_{cp}+\lambda_i-\lambda_{qp}\right)\theta_0+\frac{1}{4}\Omega b_1^2+\frac{1}{4}qb_1+\Omega\left(a_0^2+\frac{3}{4}a_1^2\right)\right)\lambda_{qt}+\Omega a_0b_1\mu_{cp}^2+\right.\\
&+\left.\left(-2\Omega\left(\lambda_{cp}+\lambda_i-\lambda_{qp}\right)\theta_0-\frac{1}{4}\Omega b_1^2-\frac{1}{4}qb_1-\Omega\left(a_0^2+\frac{3}{4}a_1^2\right)\right)\mu_{cp}-2\frac{1}{3}\Omega a_1\theta_0+2\frac{1}{3}qa_0+\Omega a_1\left(\lambda_{cp}+\lambda_i-\lambda_{qp}\right)\right)
\end{aligned}
\tag{A.4}
$$

B

6-DoF Model Equations

B.1. Equation a_0

Simplified equation

$$a_0 = \frac{\Omega^2 I_{bl}}{\Omega^2 I_{bl} + K_\beta} \frac{\gamma_{bl}}{8} \left(\left(1 + \mu_c^2\right) \theta_0 - \frac{4}{3}(\lambda_i - \lambda_c) + \left(\frac{4}{5} + \frac{2}{3}\mu_c^2\right) \theta_{bl_1} R \right) \tag{B.1}$$

Full equation

$$\begin{aligned}
a_0 = \frac{0.0083}{I_{bl}\Omega^2 \bar{\Omega}_{RZR}^2 + K_\beta} (& 120 \cos\theta_{1s} M_{bl} a_{z,h} \\
& - 120 M_{bl} \sin\theta_{1s} a_{x,h} \\
& + 60 M_{bl} \sin\delta a_1 a_{y,h} \\
& - 20 I_{bl}\Omega^2 \gamma_{bl} \lambda_i \\
& + 20 I_{bl}\Omega^2 \gamma_{bl} \hat{\lambda}_c \\
& + 15 I_{bl}\Omega^2 \gamma_{bl} \theta_{bl0} \\
& + 60 \cos\delta M_{bl} \sin\theta_{1s} a_1 a_{z,h} \\
& + 12 I_{bl}\Omega^2 R \gamma_{bl} \theta_{bl1} \\
& + 10 I_{bl}\Omega^2 a_1 \gamma_{bl} \hat{\mu}_c \\
& + 15 I_{bl}\Omega^2 \gamma_{bl} \hat{\mu}_c^2 \theta_{bl0} \\
& + 60 \cos\delta \cos\theta_{1s} M_{bl} a_1 a_{x,h} \\
& + 10 I_{bl}\Omega^2 R \gamma_{bl} \hat{\mu}_c^2 \theta_{bl1} \\
& + 15 \cos{\theta_{1s}}^2 I_{bl}\Omega^2 \sin\eta^2 \gamma_{bl} \overline{p}^2 \theta_{bl0} \\
& - 10 I_{bl}\Omega^2 \Omega_{sgn} \bar{\Omega}_{RZR} a_1 \gamma_{bl} \hat{\mu}_c \\
& + 15 \cos\eta^2 \cos{\theta_{1s}}^2 I_{bl}\Omega^2 \gamma_{bl} \overline{r}^2 \theta_{bl0} \\
& + 10 I_{bl}\Omega^2 \Omega_{sgn} \sin\delta \gamma_{bl} \hat{\mu}_c \overline{q}
\end{aligned}$$

$$
\begin{aligned}
&+ 20\cos\eta\cos\theta_{1s} I_{bl}\Omega^2\Omega_{sgn}\gamma_{bl}\lambda_i\overline{r}\\
&- 20\cos\eta\cos\theta_{1s} I_{bl}\Omega^2\Omega_{sgn}\gamma_{bl}\hat{\lambda}_c\overline{r}\\
&- 30\cos\eta\cos\theta_{1s} I_{bl}\Omega^2\Omega_{sgn}\gamma_{bl}\overline{r}\theta_{bl0}\\
&+ 12\cos\eta^2\cos{\theta_{1s}}^2 I_{bl}\Omega^2 R\gamma_{bl}\overline{r}^2\theta_{bl1}\\
&- 20\cos\eta I_{bl}\Omega^2\Omega_{sgn}\sin\theta_{1s}\gamma_{bl}\lambda_i\overline{p}\\
&+ 20\cos\theta_{1s} I_{bl}\Omega^2\Omega_{sgn}\sin\eta\gamma_{bl}\lambda_i\overline{p}\\
&+ 20\cos\eta I_{bl}\Omega^2\Omega_{sgn}\sin\theta_{1s}\gamma_{bl}\hat{\lambda}_c\overline{p}\\
&- 20\cos\theta_{1s} I_{bl}\Omega^2\Omega_{sgn}\sin\eta\gamma_{bl}\hat{\lambda}_c\overline{p}\\
&+ 30\cos\eta I_{bl}\Omega^2\Omega_{sgn}\sin\theta_{1s}\gamma_{bl}\overline{p}\theta_{bl0}\\
&- 30\cos\theta_{1s} I_{bl}\Omega^2\Omega_{sgn}\sin\eta\gamma_{bl}\overline{p}\theta_{bl0}\\
&+ 12\cos{\theta_{1s}}^2 I_{bl}\Omega^2 R\sin\eta^2\gamma_{bl}\overline{p}^2\theta_{bl1}\\
&- 20 I_{bl}\Omega^2\Omega_{sgn}\sin\eta\sin\theta_{1s}\gamma_{bl}\hat{\lambda}_c\overline{r}\\
&- 30 I_{bl}\Omega^2\Omega_{sgn}\sin\eta\sin\theta_{1s}\gamma_{bl}\overline{r}\theta_{bl0}\\
&- 10 I_{bl}\Omega^2\Omega_{sgn}\sin\delta a_1\gamma_{bl}\hat{\lambda}_c\overline{q}\\
&- 15 I_{bl}\Omega^2\Omega_{sgn}\sin\delta a_1\gamma_{bl}\overline{q}\theta_{bl0}\\
&+ 10\cos\delta\cos\eta\cos\theta_{1s} I_{bl}\Omega^2\Omega_{sgn}\gamma_{bl}\hat{\mu}_c\overline{p}\\
&+ 10\cos\delta\cos\eta I_{bl}\Omega^2\Omega_{sgn}\sin\theta_{1s}\gamma_{bl}\hat{\mu}_c\overline{r}\\
&- 10\cos\delta\cos\theta_{1s} I_{bl}\Omega^2\Omega_{sgn}\sin\eta\gamma_{bl}\hat{\mu}_c\overline{r}\\
&- 24\cos\eta\cos\theta_{1s} I_{bl}\Omega^2\Omega_{sgn}R\gamma_{bl}\overline{r}\theta_{bl1}\\
&- 30\cos\eta\cos\theta_{1s} I_{bl}\Omega^2\sin\eta\sin\theta_{1s}\gamma_{bl}\overline{p}^2\theta_{bl0}\\
&- 10\cos\eta\cos\theta_{1s} I_{bl}\Omega^2\Omega_{sgn}a_1\gamma_{bl}\hat{\mu}_c\overline{r}\\
&+ 10\cos\delta I_{bl}\Omega^2\Omega_{sgn}\sin\eta\sin\theta_{1s}\gamma_{bl}\hat{\mu}_c\overline{p}\\
&+ 24\cos\eta I_{bl}\Omega^2\Omega_{sgn}R\sin\theta_{1s}\gamma_{bl}\overline{p}\theta_{bl1}\\
&- 24\cos\theta_{1s} I_{bl}\Omega^2\Omega_{sgn}R\sin\eta\gamma_{bl}\overline{p}\theta_{bl1}\\
&- 10\cos\theta_{1s} I_{bl}\Omega^2\Omega_{sgn}\sin\eta a_1\gamma_{bl}\hat{\mu}_c\overline{p}\\
&- 24 I_{bl}\Omega^2\Omega_{sgn}R\sin\eta\sin\theta_{1s}\gamma_{bl}\overline{r}\theta_{bl1}\\
&+ 30\cos\eta\cos{\theta_{1s}}^2 I_{bl}\Omega^2\sin\eta\gamma_{bl}\overline{pr}\theta_{bl0}\\
&- 12 I_{bl}\Omega^2\Omega_{sgn}R\sin\delta a_1\gamma_{bl}\overline{q}\theta_{bl1}\\
&- 10\cos\delta\cos\eta\cos\theta_{1s} I_{bl}\Omega^2\Omega_{sgn}a_1\gamma_{bl}\hat{\lambda}_c\overline{p}\\
&- 15\cos\delta\cos\eta\cos\theta_{1s} I_{bl}\Omega^2\Omega_{sgn}a_1\gamma_{bl}\overline{p}\theta_{bl0}\\
&+ 10\cos\delta\cos\theta_{1s} I_{bl}\Omega^2\Omega_{sgn}\sin\eta a_1\gamma_{bl}\hat{\lambda}_c\overline{r}\\
&- 15\cos\delta\cos\eta I_{bl}\Omega^2\Omega_{sgn}\sin\theta_{1s}a_1\gamma_{bl}\overline{r}\theta_{bl0}\\
&+ 15\cos\delta\cos\theta_{1s} I_{bl}\Omega^2\Omega_{sgn}\sin\eta a_1\gamma_{bl}\overline{r}\theta_{bl0}\\
&- 15\cos\delta I_{bl}\Omega^2\Omega_{sgn}\sin\eta\sin\theta_{1s}a_1\gamma_{bl}\overline{p}\theta_{bl0}\\
&+ 24\cos\eta\cos{\theta_{1s}}^2 I_{bl}\Omega^2 R\sin\eta\gamma_{bl}\overline{pr}\theta_{bl1}\\
&- 12\cos\delta\cos\eta\cos\theta_{1s} I_{bl}\Omega^2\Omega_{sgn}Ra_1\gamma_{bl}\overline{p}\theta_{bl1}\\
&- 12\cos\delta\cos\eta I_{bl}\Omega^2\Omega_{sgn}R\sin\theta_{1s}a_1\gamma_{bl}\overline{r}\theta_{bl1}\\
&+ 12\cos\delta\cos\theta_{1s} I_{bl}\Omega^2\Omega_{sgn}R\sin\eta a_1\gamma_{bl}\overline{r}\theta_{bl1}\\
&- 12\cos\delta I_{bl}\Omega^2\Omega_{sgn}R\sin\eta\sin\theta_{1s}a_1\gamma_{bl}\overline{p}\theta_{bl1})
\end{aligned}
$$

B.2. Equation a_1

Simplified equation

$$a_1 = \frac{-\frac{16}{\gamma_{bl}}\frac{q}{\Omega} - \frac{p}{\Omega}\Omega_{sgn}\cos\eta - \frac{r}{\Omega}\Omega_{sgn}\sin\eta - 2\mu_c(\lambda_i - \lambda_c) + \frac{8}{3}\theta_0\mu_c + 2\theta_{bl_1}\mu_c R}{1 - \frac{1}{2}\mu_c^2} \tag{B.2}$$

Full equation

$$\begin{aligned}
a_1 = 0.4000(&30I_{bl}\Omega^2\gamma_{bl}\lambda_i\hat{\mu}_c \\
&- 120\cos\delta M_{bl}\Omega_{sgn}a_0 a_{y,h} \\
&- 120I_{bl}\Omega_{sgn}\sin\delta\dot{q} \\
&- 30I_{bl}\Omega^2\gamma_{bl}\hat{\lambda}_c\hat{\mu}_c \\
&- 40I_{bl}\Omega^2\gamma_{bl}\hat{\mu}_c\theta_{bl0} \\
&- 120\cos\delta\cos\eta\cos\theta_{1s}I_{bl}\Omega_{sgn}\dot{p} \\
&+ 240\cos\delta I_{bl}\Omega^2\Omega_{sgn}\bar{\Omega}_{RZR}\dot{\bar{\eta}} \\
&+ 120\cos\delta\cos\theta_{1s}I_{bl}\Omega_{sgn}\sin\eta\dot{r} \\
&+ 240\cos\delta I_{bl}\Omega^2\Omega_{sgn}\bar{\Omega}_{RZR}\overline{q} \\
&- 120\cos\delta I_{bl}\Omega_{sgn}\sin\eta\sin\theta_{1s}\dot{p} \\
&+ 120\cos\theta_{1s}M_{bl}\Omega_{sgn}\sin\delta a_0 a_{x,h} \\
&- 15I_{bl}\Omega^2\Omega_{sgn}\sin\delta\dot{\bar{\eta}}\gamma_{bl} \\
&- 15I_{bl}\Omega^2\Omega_{sgn}\sin\delta\gamma_{bl}\overline{q} \\
&- 30I_{bl}\Omega^2 R\gamma_{bl}\hat{\mu}_c\theta_{bl1} \\
&+ 30\cos\delta I_{bl}\Omega^2 a_0\gamma_{bl}\overline{q}\theta_{bl0} \\
&- 240I_{bl}\Omega^2\Omega_{sgn}\bar{\Omega}_{RZR}\sin\delta\sin\eta\sin\theta_{1s}\overline{p} \\
&- 15\cos\delta I_{bl}\Omega^2\Omega_{sgn}\sin\eta\sin\theta_{1s}\gamma_{bl}\overline{p} \\
&+ 15\cos\delta\cos\eta^2\cos{\theta_{1s}}^2 I_{bl}\Omega^2\gamma_{bl}\overline{pr} \\
&+ 15\cos\eta\cos\theta_{1s}I_{bl}\Omega^2\sin\delta\gamma_{bl}\overline{qr} \\
&+ 15\cos\theta_{1s}I_{bl}\Omega^2\sin\delta\sin\eta\gamma_{bl}\overline{pq} \\
&+ 24\cos\delta I_{bl}\Omega^2 R a_0\gamma_{bl}\overline{q}\theta_{bl1} \\
&+ 15\cos\delta\cos\eta\cos{\theta_{1s}}^2 I_{bl}\Omega^2\sin\eta\gamma_{bl}\overline{p}^2 \\
&- 15\cos\delta\cos\eta\cos{\theta_{1s}}^2 I_{bl}\Omega^2\sin\eta\gamma_{bl}\overline{r}^2 \\
&- 15\cos\delta\cos{\theta_{1s}}^2 I_{bl}\Omega^2\sin\eta^2\gamma_{bl}\overline{pr} \\
&- 240\cos\eta\cos\theta_{1s}I_{bl}\Omega^2\Omega_{sgn}\bar{\Omega}_{RZR}\sin\delta\overline{p} \\
&- 15\cos\delta\cos\eta\cos\theta_{1s}I_{bl}\Omega^2\Omega_{sgn}\gamma_{bl}\overline{p} \\
&- 240\cos\eta I_{bl}\Omega^2\Omega_{sgn}\bar{\Omega}_{RZR}\sin\delta\sin\theta_{1s}\overline{r} \\
&+ 240\cos\theta_{1s}I_{bl}\Omega^2\Omega_{sgn}\bar{\Omega}_{RZR}\sin\delta\sin\eta\overline{r} \\
&- 15\cos\delta\cos\eta I_{bl}\Omega^2\Omega_{sgn}\sin\theta_{1s}\gamma_{bl}\overline{r} \\
&+ 15\cos\delta\cos\theta_{1s}I_{bl}\Omega^2\Omega_{sgn}\sin\eta\gamma_{bl}\overline{r} \\
&- 20\cos\eta\cos\theta_{1s}I_{bl}\Omega^2\sin\delta a_0\gamma_{bl}\hat{\lambda}_c\overline{p} \\
&- 30\cos\eta\cos\theta_{1s}I_{bl}\Omega^2\sin\delta a_0\gamma_{bl}\overline{p}\theta_{bl0}
\end{aligned}$$

$$
\begin{aligned}
&+ 20\cos\theta_{1s} I_{bl}\Omega^2 \sin\delta \sin\eta a_0 \gamma_{bl} \hat{\lambda}_c \overline{r} \\
&+ 40\cos\eta \cos\theta_{1s} I_{bl}\Omega^2 \Omega_{sgn} \gamma_{bl} \hat{\mu}_c \overline{r} \theta_{bl0} \\
&+ 30\cos\theta_{1s} I_{bl}\Omega^2 \sin\delta \sin\eta a_0 \gamma_{bl} \overline{r} \theta_{bl0} \\
&- 40\cos\eta I_{bl}\Omega^2 \Omega_{sgn} \sin\theta_{1s} \gamma_{bl} \hat{\mu}_c \overline{p} \theta_{bl0} \\
&+ 40\cos\theta_{1s} I_{bl}\Omega^2 \Omega_{sgn} \sin\eta \gamma_{bl} \hat{\mu}_c \overline{p} \theta_{bl0} \\
&+ 40 I_{bl}\Omega^2 \Omega_{sgn} \sin\eta \sin\theta_{1s} \gamma_{bl} \hat{\mu}_c \overline{r} \theta_{bl0} \\
&+ 60\cos\delta \cos\eta \cos\theta_{1s} I_{bl}\Omega^2 \sin\eta \sin\theta_{1s} \gamma_{bl} \overline{pr} \\
&- 24\cos\eta \cos\theta_{1s} I_{bl}\Omega^2 R \sin\delta a_0 \gamma_{bl} \overline{p} \theta_{bl1} \\
&+ 30\cos\eta \cos\theta_{1s} I_{bl}\Omega^2 \Omega_{sgn} R \gamma_{bl} \hat{\mu}_c \overline{r} \theta_{bl1} \\
&+ 24\cos\theta_{1s} I_{bl}\Omega^2 R \sin\delta \sin\eta a_0 \gamma_{bl} \overline{r} \theta_{bl1} \\
&- 30\cos\eta I_{bl}\Omega^2 \Omega_{sgn} R \sin\theta_{1s} \gamma_{bl} \hat{\mu}_c \overline{p} \theta_{bl1} \\
&+ 30\cos\theta_{1s} I_{bl}\Omega^2 \Omega_{sgn} R \sin\eta \gamma_{bl} \hat{\mu}_c \overline{p} \theta_{bl1} \\
&+ 30 I_{bl}\Omega^2 \Omega_{sgn} R \sin\eta \sin\theta_{1s} \gamma_{bl} \hat{\mu}_c \overline{r} \theta_{bl1}) \\
&/ \\
&(I_{bl}\Omega^2 (3\gamma_{bl}\hat{\mu}_c^2 \\
&- 6\Omega_{sgn}\bar{\Omega}_{RZR}\gamma_{bl} \\
&+ 6\cos\eta \cos\theta_{1s}\bar{\Omega}_{RZR}\gamma_{bl}\overline{r} \\
&- 6\cos\eta\bar{\Omega}_{RZR}\sin\theta_{1s}\gamma_{bl}\overline{p} \\
&+ 6\cos\theta_{1s}\bar{\Omega}_{RZR}\sin\eta\gamma_{bl}\overline{p} \\
&+ 6\bar{\Omega}_{RZR}\sin\eta\sin\theta_{1s}\gamma_{bl}\overline{r} \\
&- 48\cos\delta\cos\eta^2\cos{\theta_{1s}}^2\Omega_{sgn}\sin\delta\overline{p}^2 \\
&- 4\Omega_{sgn}\sin\delta\gamma_{bl}\hat{\mu}_c\overline{q}\theta_{bl0} \\
&- 3\Omega_{sgn}R\sin\delta\gamma_{bl}\hat{\mu}_c\overline{q}\theta_{bl1} \\
&+ 96\cos\delta\cos\eta\cos{\theta_{1s}}^2\Omega_{sgn}\sin\delta\sin\eta\overline{pr} \\
&- 4\cos\delta\cos\eta\cos\theta_{1s}\Omega_{sgn}\gamma_{bl}\hat{\mu}_c\overline{p}\theta_{bl0} \\
&+ 4\cos\delta\cos\theta_{1s}\Omega_{sgn}\sin\eta\gamma_{bl}\hat{\mu}_c\overline{r}\theta_{bl0} \\
&- 3\cos\delta\cos\eta\cos\theta_{1s}\Omega_{sgn}R\gamma_{bl}\hat{\mu}_c\overline{p}\theta_{bl1} \\
&+ 3\cos\delta\cos\theta_{1s}\Omega_{sgn}R\sin\eta\gamma_{bl}\hat{\mu}_c\overline{r}\theta_{bl1}))
\end{aligned}
$$

B.3. Equation b_1

Simplified equation

$$b_1 = \frac{-8K_\beta}{\gamma_{bl}\Omega_{sgn}\Omega^2 I_{bl}}\left(\frac{-2\mu_c(\lambda_i-\lambda_c)-\frac{8}{3}\mu_c\theta_0+\frac{16}{\gamma_{bl}}\frac{q}{\Omega}-\frac{p}{\Omega}\Omega_{sgn}\cos\eta-2R\mu_c\theta_{bl_1}}{\frac{1}{2}\mu_c^2-1}\right) - \frac{q}{\Omega}\Omega_{sgn}+\frac{16}{\gamma_{bl}}\frac{r}{\Omega}+\frac{4}{3}\mu_c a_0\Omega_{sgn}-\frac{16}{\gamma_{bl}}\frac{p}{\Omega}\cos\eta$$

Full equation

$$\begin{aligned}
b_1 = \frac{0.0333}{I_{bl}\Omega^2\overline{\Omega}_{RZR}\gamma_{bl}}(&240K_\beta a_1\\
&+240\cos\delta I_{bl}\dot{q}\\
&-240M_{bl}\sin\delta a0a_{y,h}\\
&+480I_{bl}\Omega^2\overline{\Omega}_{RZR}\sin\delta\dot{\overline{\eta}}\\
&+240\cos\theta_{1s}I_{bl}\sin\delta\sin\eta\dot{r}\\
&+30\cos\delta I_{bl}\Omega^2\dot{\overline{\eta}}\gamma_{bl}\\
&+480I_{bl}\Omega^2\overline{\Omega}_{RZR}\sin\delta\overline{q}\\
&-180\cos\delta^2 I_{bl}\Omega^2 a_1\overline{p}^2\\
&-240I_{bl}\sin\delta\sin\eta\sin\theta_{1s}\dot{p}\\
&+30\cos\delta I_{bl}\Omega^2\gamma_{bl}\overline{q}\\
&-40I_{bl}\Omega^2 a0\gamma_{bl}\hat{\mu}_c\\
&-240\cos\eta\cos\theta_{1s}I_{bl}\sin\delta\dot{p}\\
&-240\cos\delta\cos\theta_{1s}M_{bl}a0a_{x,h}\\
&+180\cos\delta^2\cos\eta^2 I_{bl}\Omega^2 a_1\overline{p}^2\\
&+180\cos\delta^2\cos{\theta_{1s}}^2 I_{bl}\Omega^2 a_1\overline{p}^2\\
&-120\cos\eta^2\cos{\theta_{1s}}^2 I_{bl}\Omega^2 a_1\overline{p}^2\\
&+480\cos\delta\cos\eta\cos\theta_{1s}I_{bl}\Omega^2\overline{\Omega}_{RZR}\overline{p}\\
&-240\cos\delta^2\cos\eta^2\cos{\theta_{1s}}^2 I_{bl}\Omega^2 a_1\overline{p}^2\\
&+480\cos\delta\cos\eta I_{bl}\Omega^2\overline{\Omega}_{RZR}\sin\theta_{1s}\overline{r}\\
&-480\cos\delta\cos\theta_{1s}I_{bl}\Omega^2\overline{\Omega}_{RZR}\sin\eta\overline{r}\\
&+480\cos\delta I_{bl}\Omega^2\overline{\Omega}_{RZR}\sin\eta\sin\theta_{1s}\overline{p}\\
&-30\cos\eta\cos\theta_{1s}I_{bl}\Omega^2\sin\delta\gamma_{bl}\overline{p}\\
&+240\cos\theta_{1s}I_{bl}\Omega^2\sin\delta\sin\eta\dot{\overline{\eta}}\overline{p}\\
&-30\cos\eta I_{bl}\Omega^2\sin\delta\sin\theta_{1s}\gamma_{bl}\overline{r}\\
&+30\cos\theta_{1s}I_{bl}\Omega^2\sin\delta\sin\eta\gamma_{bl}\overline{r}\\
&-30I_{bl}\Omega^2\sin\delta\sin\eta\sin\theta_{1s}\gamma_{bl}\overline{p}\\
&+360\cos\delta^2\cos\eta^2\cos{\theta_{1s}}^2 I_{bl}\Omega^2 a_1\overline{r}^2\\
&-360\cos\delta^2\cos\eta I_{bl}\Omega^2\sin\eta a_1\overline{pr}\\
&+240\cos\eta\cos{\theta_{1s}}^2 I_{bl}\Omega^2\sin\eta a_1\overline{pr}\\
&+40I_{bl}\Omega^2\Omega_{sgn}\sin\delta a0\gamma_{bl}\hat{\lambda}_c\overline{q}
\end{aligned}$$

$$
\begin{aligned}
&+ 60 I_{bl}\Omega^2\Omega_{sgn}\sin\delta a0\gamma_{bl}\overline{q}\theta_{bl0}\\
&+ 20\cos\delta I_{bl}\Omega^2 a_1\gamma_{bl}\hat{\mu}_c\overline{q}\theta_{bl0}\\
&- 360\cos\delta\cos\eta\cos\theta_{1s}I_{bl}\Omega^2\sin\delta a_1\overline{pq}\\
&+ 480\cos\delta^2\cos\eta\cos{\theta_{1s}}^2 I_{bl}\Omega^2\sin\eta a_1\overline{pr}\\
&- 720\cos\delta^2\cos\eta^2\cos\theta_{1s}I_{bl}\Omega^2\sin\theta_{1s}a_1\overline{pr}\\
&- 30\cos\delta\cos\eta\cos\theta_{1s}I_{bl}\Omega^2\Omega_{sgn}\gamma_{bl}\overline{qr}\\
&+ 360\cos\delta\cos\theta_{1s}I_{bl}\Omega^2\sin\delta\sin\eta a_1\overline{qr}\\
&- 30\cos\delta\cos\theta_{1s}I_{bl}\Omega^2\Omega_{sgn}\sin\eta\gamma_{bl}\overline{pq}\\
&+ 30\cos\eta^2\cos{\theta_{1s}}^2 I_{bl}\Omega^2\Omega_{sgn}\sin\delta\gamma_{bl}\overline{pr}\\
&+ 40\cos\theta_{1s}I_{bl}\Omega^2\Omega_{sgn}\sin\eta a0\gamma_{bl}\hat{\mu}_c\overline{p}\\
&+ 48 I_{bl}\Omega^2\Omega_{sgn}R\sin\delta a0\gamma_{bl}\overline{q}\theta_{bl1}\\
&+ 15\cos\delta I_{bl}\Omega^2 R a_1\gamma_{bl}\hat{\mu}_c\overline{q}\theta_{bl1}\\
&+ 30\cos\eta\cos{\theta_{1s}}^2 I_{bl}\Omega^2\Omega_{sgn}\sin\delta\sin\eta\gamma_{bl}\overline{p}^2\\
&- 30\cos\eta\cos{\theta_{1s}}^2 I_{bl}\Omega^2\Omega_{sgn}\sin\delta\sin\eta\gamma_{bl}\overline{r}^2\\
&- 30\cos{\theta_{1s}}^2 I_{bl}\Omega^2\Omega_{sgn}\sin\delta\sin\eta^2\gamma_{bl}\overline{pr}\\
&+ 40\cos\delta\cos\eta\cos\theta_{1s}I_{bl}\Omega^2\Omega_{sgn}a0\gamma_{bl}\hat{\lambda}_c\overline{p}\\
&+ 60\cos\delta\cos\eta\cos\theta_{1s}I_{bl}\Omega^2\Omega_{sgn}a0\gamma_{bl}\overline{p}\theta_{bl0}\\
&- 40\cos\delta\cos\theta_{1s}I_{bl}\Omega^2\Omega_{sgn}\sin\eta a0\gamma_{bl}\hat{\lambda}_c\overline{r}\\
&- 60\cos\delta\cos\theta_{1s}I_{bl}\Omega^2\Omega_{sgn}\sin\eta a0\gamma_{bl}\overline{r}\theta_{bl0}\\
&+ 60\cos\delta I_{bl}\Omega^2\Omega_{sgn}\sin\eta\sin\theta_{1s}a0\gamma_{bl}\overline{p}\theta_{bl0}\\
&- 20\cos\eta\cos\theta_{1s}I_{bl}\Omega^2\sin\delta a_1\gamma_{bl}\hat{\mu}_c\overline{p}\theta_{bl0}\\
&+ 20\cos\theta_{1s}I_{bl}\Omega^2\sin\delta\sin\eta a_1\gamma_{bl}\hat{\mu}_c\overline{r}\theta_{bl0}\\
&+ 48\cos\delta\cos\eta\cos\theta_{1s}I_{bl}\Omega^2\Omega_{sgn}R a0\gamma_{bl}\overline{p}\theta_{bl1}\\
&+ 120\cos\eta\cos\theta_{1s}I_{bl}\Omega^2\Omega_{sgn}\sin\delta\sin\eta\sin\theta_{1s}\gamma_{bl}\overline{pr}\\
&- 48\cos\delta\cos\theta_{1s}I_{bl}\Omega^2\Omega_{sgn}R\sin\eta a0\gamma_{bl}\overline{r}\theta_{bl1}\\
&+ 48\cos\delta I_{bl}\Omega^2\Omega_{sgn}R\sin\eta\sin\theta_{1s}a0\gamma_{bl}\overline{p}\theta_{bl1}\\
&- 15\cos\eta\cos\theta_{1s}I_{bl}\Omega^2 R\sin\delta a_1\gamma_{bl}\hat{\mu}_c\overline{p}\theta_{bl1}\\
&+ 15\cos\theta_{1s}I_{bl}\Omega^2 R\sin\delta\sin\eta a_1\gamma_{bl}\hat{\mu}_c\overline{r}\theta_{bl1})
\end{aligned}
$$

B.4. Equation $C_{T,BEM}$

Simplified equation

$$C_{T,BEM} = \frac{C_{l_\alpha}\sigma}{4}(\theta_0(\frac{2}{3} + \mu_c^2) + \frac{1}{2}\theta_{bl_1}R(1 + \mu_c^2) - (\lambda_i - \lambda_c)) \tag{B.3}$$

Full equation

$$\begin{aligned}
C_{T,BEM} = \frac{-0.0133 I_{bl} N \gamma_{bl}}{R^5 \rho}(&6\lambda_i \\
&- 6\hat{\lambda}_c \\
&- 4\theta_{bl0} \\
&- 3R\theta_{bl1} \\
&- 3a_1\hat{\mu}_c \\
&- 6\hat{\mu}_c^2\theta_{bl0} \\
&- 3R\hat{\mu}_c^2\theta_{bl1} \\
&+ 3\Omega_{sgn}\bar{\Omega}_{RZR}a_1\hat{\mu}_c \\
&- 4\cos\theta_{1s}{}^2\sin\eta^2\overline{p}^2\theta_{bl0} \\
&- 3\Omega_{sgn}\sin\delta\hat{\mu}_c\overline{q} \\
&- 6\cos\eta\cos\theta_{1s}\Omega_{sgn}\lambda_i\overline{r} \\
&+ 6\cos\eta\cos\theta_{1s}\Omega_{sgn}\hat{\lambda}_c\overline{r} \\
&+ 8\cos\eta\cos\theta_{1s}\Omega_{sgn}\overline{r}\theta_{bl0} \\
&+ 6\cos\eta\Omega_{sgn}\sin\theta_{1s}\lambda_i\overline{p} \\
&- 6\cos\theta_{1s}\Omega_{sgn}\sin\eta\lambda_i\overline{p} \\
&- 6\cos\eta\Omega_{sgn}\sin\theta_{1s}\hat{\lambda}_c\overline{p} \\
&+ 6\cos\theta_{1s}\Omega_{sgn}\sin\eta\hat{\lambda}_c\overline{p} \\
&- 8\cos\eta\Omega_{sgn}\sin\theta_{1s}\overline{p}\theta_{bl0} \\
&+ 8\cos\theta_{1s}\Omega_{sgn}\sin\eta\overline{p}\theta_{bl0} \\
&- 3\cos\theta_{1s}{}^2R\sin\eta^2\overline{p}^2\theta_{bl1} \\
&+ 6\Omega_{sgn}\sin\eta\sin\theta_{1s}\hat{\lambda}_c\overline{r} \\
&+ 8\Omega_{sgn}\sin\eta\sin\theta_{1s}\overline{r}\theta_{bl0} \\
&+ 3\Omega_{sgn}\sin\delta a_1\hat{\lambda}_c\overline{q} \\
&+ 4\Omega_{sgn}\sin\delta a_1\overline{q}\theta_{bl0} \\
&- 3\cos\eta^2\cos\theta_{1s}{}^2R\overline{r}^2\theta_{bl1} \\
&- 3\cos\delta\cos\eta\cos\theta_{1s}\Omega_{sgn}\hat{\mu}_c\overline{p} \\
&- 3\cos\delta\cos\eta\Omega_{sgn}\sin\theta_{1s}\hat{\mu}_c\overline{r} \\
&+ 3\cos\delta\cos\theta_{1s}\Omega_{sgn}\sin\eta\hat{\mu}_c\overline{r} \\
&+ 6\cos\eta\cos\theta_{1s}\Omega_{sgn}R\overline{r}\theta_{bl1} \\
&+ 8\cos\eta\cos\theta_{1s}\sin\eta\sin\theta_{1s}\overline{p}^2\theta_{bl0} \\
&+ 3\cos\eta\cos\theta_{1s}\Omega_{sgn}a_1\hat{\mu}_c\overline{r} \\
&- 3\cos\delta\Omega_{sgn}\sin\eta\sin\theta_{1s}\hat{\mu}_c\overline{p} \\
&- 6\cos\eta\Omega_{sgn}R\sin\theta_{1s}\overline{p}\theta_{bl1}
\end{aligned}$$

$$
\begin{aligned}
&+ 6\cos\theta_{1s}\Omega_{sgn}R\sin\eta\overline{p}\theta_{bl1} \\
&+ 3\cos\theta_{1s}\Omega_{sgn}\sin\eta a_1\hat{\mu}_c\overline{p} \\
&+ 6\Omega_{sgn}R\sin\eta\sin\theta_{1s}\overline{r}\theta_{bl1} \\
&- 8\cos\eta\cos{\theta_{1s}}^2\sin\eta\overline{pr}\theta_{bl0} \\
&+ 3\Omega_{sgn}R\sin\delta a_1\overline{q}\theta_{bl1} \\
&+ 3\cos\delta\cos\eta\cos\theta_{1s}\Omega_{sgn}a_1\hat{\lambda}_c\overline{p} \\
&+ 4\cos\delta\cos\eta\cos\theta_{1s}\Omega_{sgn}a_1\overline{p}\theta_{bl0} \\
&- 3\cos\delta\cos\theta_{1s}\Omega_{sgn}\sin\eta a_1\hat{\lambda}_c\overline{r} \\
&+ 4\cos\delta\cos\eta\Omega_{sgn}\sin\theta_{1s}a_1\overline{r}\theta_{bl0} \\
&- 4\cos\delta\cos\theta_{1s}\Omega_{sgn}\sin\eta a_1\overline{r}\theta_{bl0} \\
&+ 4\cos\delta\Omega_{sgn}\sin\eta\sin\theta_{1s}a_1\overline{p}\theta_{bl0} \\
&- 6\cos\eta\cos{\theta_{1s}}^2R\sin\eta\overline{pr}\theta_{bl1} \\
&+ 3\cos\delta\cos\eta\cos\theta_{1s}\Omega_{sgn}Ra_1\overline{p}\theta_{bl1} \\
&+ 3\cos\delta\cos\eta\Omega_{sgn}R\sin\theta_{1s}a_1\overline{r}\theta_{bl1} \\
&- 3\cos\delta\cos\theta_{1s}\Omega_{sgn}R\sin\eta a_1\overline{r}\theta_{bl1} \\
&+ 3\cos\delta\Omega_{sgn}R\sin\eta\sin\theta_{1s}a_1\overline{p}\theta_{bl1})
\end{aligned}
$$

B.5. Equation C_H

Simplified equation (further reductions lead to inaccuracies)

$$
\begin{aligned}
C_H = \frac{\sigma}{24}(&4C_{l_{\alpha bl}}a_1\theta_0 \\
&- 9C_{l_{\alpha bl}}a_1(\lambda_i - \lambda_c) \\
&+ 6C_{l_{\alpha bl}}\mu_c\theta_0(\lambda_i - \lambda_c) \\
&+ 3C_{l_{\alpha bl}}Ra_1\theta_{bl1} \\
&+ 3C_{l_{\alpha bl}}R\mu_c\theta_{bl1}(\lambda_i - \lambda_c) \\
&+ c_{d_0}6\mu_c \\
&+ c_{d_1}(-2a_1 \\
&- 6\mu_c(\lambda_i - \lambda_c)) \\
&+ c_{d_2}(-4a_1\theta_0 \\
&+ 6a_1(\lambda_i - \lambda_c) \\
&+ 6\mu_c({\theta_0}^2 + \theta_0) \\
&+ 3a_1\mu_c^2\theta_0 \\
&- 12\mu_c\theta_0(\lambda_i - \lambda_c) \\
&- 3Ra_1\theta_{bl1} \\
&+ 4R\mu_c\theta_{bl1} \\
&+ 3/2Ra_1\mu_c^2\theta_{bl1} \\
&+ 3R^2\mu_c\theta_{bl_1}^2 \\
&+ 8R\mu_c\theta_0\theta_{bl1} \\
&- 6R\mu_c\theta_{bl1}(\lambda_i - \lambda_c)))
\end{aligned}
$$

Full equation (next page)

$$
\begin{aligned}
C_H = \frac{1}{C_{l_\alpha bl} R^5 \rho} 0.0033 I_{bl} N \gamma_{bl} (
& 24 c_{d_0} \hat{\mu}_c \\
& - 12 C_{l_\alpha bl} a_1 \lambda_i \\
& + 12 C_{l_\alpha bl} a_1 \hat{\lambda}_c \\
& + 8 C_{l_\alpha bl} a_1 \theta_{bl0} \\
& - 24 c_{d_1} \lambda_i \hat{\mu}_c \\
& + 24 c_{d_1} \hat{\lambda}_c \hat{\mu}_c \\
& + 24 c_{d_2} \hat{\mu}_c \theta_{bl0} \\
& + 24 c_{d_2} \hat{\mu}_c \theta_{bl_0}^2 \\
& + 12 a_1 c_{d_2} \hat{\mu}_c^2 \theta_{bl0} \\
& - 48 c_{d_2} \lambda_i \hat{\mu}_c \theta_{bl0} \\
& + 48 c_{d_2} \hat{\lambda}_c \hat{\mu}_c \theta_{bl0} \\
& - 8 \cos\delta C_{l_\alpha bl} a_0 \overline{q} \\
& - 8 \Omega_{sgn} \bar{\Omega}_{RZR} a_1 c_{d_1} \\
& + 6 C_{l_\alpha bl} R a_1 \theta_{bl1} \\
& + 24 C_{l_\alpha bl} \lambda_i \hat{\mu}_c \theta_{bl0} \\
& - 24 C_{l_\alpha bl} \hat{\lambda}_c \hat{\mu}_c \theta_{bl0} \\
& + 16 R c_{d_2} \hat{\mu}_c \theta_{bl1} \\
& + 12 R^2 c_{d_2} \hat{\mu}_c \theta_{bl_1}^2 \\
& - 24 C_{l_\alpha bl} \Omega_{sgn} \bar{\Omega}_{RZR} a_1 \lambda_i \\
& + 24 C_{l_\alpha bl} \Omega_{sgn} \bar{\Omega}_{RZR} a_1 \hat{\lambda}_c \\
& + 8 C_{l_\alpha bl} \Omega_{sgn} \bar{\Omega}_{RZR} a_1 \theta_{bl0} \\
& + 24 C_{l_\alpha bl} \Omega_{sgn} \sin\delta \dot{\overline{\eta}} \lambda_i \\
& - 24 C_{l_\alpha bl} \Omega_{sgn} \sin\delta \dot{\overline{\eta}} \hat{\lambda}_c \\
& - 8 C_{l_\alpha bl} \Omega_{sgn} \sin\delta \dot{\overline{\eta}} \theta_{bl0} \\
& + 24 C_{l_\alpha bl} \Omega_{sgn} \sin\delta \lambda_i \overline{q} \\
& - 24 C_{l_\alpha bl} \Omega_{sgn} \sin\delta \hat{\lambda}_c \overline{q} \\
& - 8 C_{l_\alpha bl} \Omega_{sgn} \sin\delta \overline{q} \theta_{bl0} \\
& + 24 \Omega_{sgn} \bar{\Omega}_{RZR} a_1 c_{d_2} \lambda_i \\
& - 24 \Omega_{sgn} \bar{\Omega}_{RZR} a_1 c_{d_2} \hat{\lambda}_c \\
& - 16 \Omega_{sgn} \bar{\Omega}_{RZR} a_1 c_{d_2} \theta_{bl0} \\
& + 24 \Omega_{sgn} \sin\delta c_{d_2} \dot{\overline{\eta}} \hat{\lambda}_c \\
& + 16 \Omega_{sgn} \sin\delta c_{d_2} \dot{\overline{\eta}} \theta_{bl0} \\
& + 12 C_{l_\alpha bl} R \lambda_i \hat{\mu}_c \theta_{bl1} \\
& - 12 C_{l_\alpha bl} R \hat{\lambda}_c \hat{\mu}_c \theta_{bl1} \\
& - 24 \Omega_{sgn} \sin\delta c_{d_2} \lambda_i \overline{q} \\
& + 24 \Omega_{sgn} \sin\delta c_{d_2} \hat{\lambda}_c \overline{q} \\
& + 16 \Omega_{sgn} \sin\delta c_{d_2} \overline{q} \theta_{bl0} \\
& + 6 R a_1 c_{d_2} \hat{\mu}_c^2 \theta_{bl1} \\
& - 24 R c_{d_2} \lambda_i \hat{\mu}_c \theta_{bl1} \\
& + 24 R c_{d_2} \hat{\lambda}_c \hat{\mu}_c \theta_{bl1} \\
& + 32 R c_{d_2} \hat{\mu}_c \theta_{bl0} \theta_{bl1}
\end{aligned}
$$

$$
\begin{aligned}
&+ 8\cos\delta\cos\eta\cos\theta_{1s}\Omega_{sgn}c_{d_1}\overline{p}\\
&+ 8\cos\eta C_{l_\alpha bl}\cos\theta_{1s}\sin\delta a_0\overline{p}\\
&- 8C_{l_\alpha bl}\cos\theta_{1s}\sin\delta\sin\eta a_0\overline{r}\\
&+ 6C_{l_\alpha bl}\Omega_{sgn}\bar{\Omega}_{RZR}Ra_1\theta_{bl1}\\
&- 6C_{l_\alpha bl}\Omega_{sgn}R\sin\delta\dot{\overline{\eta}}\theta_{bl1}\\
&- 6C_{l_\alpha bl}\Omega_{sgn}R\sin\delta\overline{q}\theta_{bl1}\\
&+ 8C_{l_\alpha bl}\cos{\theta_{1s}}^2\sin\eta^2 a_1\overline{p}^2\theta_{bl0}\\
&- 3C_{l_\alpha bl}\Omega_{sgn}\sin\delta a_1\hat{\mu}_c\overline{q}\\
&- 12\Omega_{sgn}\bar{\Omega}_{RZR}Ra_1c_{d_2}\theta_{bl1}\\
&+ 12\Omega_{sgn}R\sin\delta c_{d_2}\dot{\overline{\eta}}\theta_{bl1}\\
&+ 12\cos\delta C_{l_\alpha bl}a_0\hat{\lambda}_c\overline{q}\theta_{bl0}\\
&+ 12\Omega_{sgn}R\sin\delta c_{d_2}\overline{q}\theta_{bl1}\\
&- 16\cos\theta_{1s}\sin\delta\sin\eta c_{d_2}\overline{pq}\theta_{bl0}\\
&- 24\Omega_{sgn}\sin\eta\sin\theta_{1s}c_{d_2}\hat{\mu}_c\overline{r}\theta_{bl0}\\
&- 24\Omega_{sgn}\sin\eta\sin\theta_{1s}c_{d_2}\hat{\mu}_c\overline{r}\theta_{bl_0}^2\\
&- 24\cos\delta Ra_0c_{d_2}\overline{q}\theta_{bl0}\theta_{bl1}\\
&+ 24\cos\delta\cos\eta C_{l_\alpha bl}\cos\theta_{1s}\Omega_{sgn}\lambda_i\overline{p}\\
&- 24\cos\delta\cos\eta C_{l_\alpha bl}\cos\theta_{1s}\Omega_{sgn}\hat{\lambda}_c\overline{p}\\
&- 8\cos\delta\cos\eta C_{l_\alpha bl}\cos\theta_{1s}\Omega_{sgn}\overline{p}\theta_{bl0}\\
&+ 8\cos\delta\cos\eta C_{l_\alpha bl}\cos{\theta_{1s}}^2\sin\eta\overline{p}^2\theta_{bl0}\\
&- 8\cos\delta\cos\eta^2 C_{l_\alpha bl}\cos\theta_{1s}\sin\theta_{1s}\overline{p}^2\theta_{bl0}\\
&- 8\cos\delta\cos\eta C_{l_\alpha bl}\cos{\theta_{1s}}^2\sin\eta\overline{r}^2\theta_{bl0}\\
&+ 24\cos\delta\cos\eta C_{l_\alpha bl}\Omega_{sgn}\sin\theta_{1s}\lambda_i\overline{r}\\
&- 24\cos\delta C_{l_\alpha bl}\cos\theta_{1s}\Omega_{sgn}\sin\eta\lambda_i\overline{r}\\
&- 24\cos\delta\cos\eta C_{l_\alpha bl}\Omega_{sgn}\sin\theta_{1s}\hat{\lambda}_c\overline{r}\\
&+ 24\cos\delta C_{l_\alpha bl}\cos\theta_{1s}\Omega_{sgn}\sin\eta\hat{\lambda}_c\overline{r}\\
&- 8\cos\delta\cos\eta C_{l_\alpha bl}\Omega_{sgn}\sin\theta_{1s}\overline{r}\theta_{bl0}\\
&+ 8\cos\delta C_{l_\alpha bl}\cos\theta_{1s}\Omega_{sgn}\sin\eta\overline{r}\theta_{bl0}\\
&+ 8\cos\delta C_{l_\alpha bl}\cos\theta_{1s}\sin\eta^2\sin\theta_{1s}\overline{p}^2\theta_{bl0}\\
&+ 12\cos\eta C_{l_\alpha bl}\cos\theta_{1s}\Omega_{sgn}a_1\lambda_i\overline{r}\\
&- 12\cos\eta C_{l_\alpha bl}\cos\theta_{1s}\Omega_{sgn}a_1\hat{\lambda}_c\overline{r}\\
&- 24\cos\delta\cos\eta\cos\theta_{1s}\Omega_{sgn}c_{d_2}\lambda_i\overline{p}\\
&+ 24\cos\delta\cos\eta\cos\theta_{1s}\Omega_{sgn}c_{d_2}\hat{\lambda}_c\overline{p}\\
&+ 24\cos\delta C_{l_\alpha bl}\Omega_{sgn}\sin\eta\sin\theta_{1s}\lambda_i\overline{p}\\
&- 24\cos\delta C_{l_\alpha bl}\Omega_{sgn}\sin\eta\sin\theta_{1s}\hat{\lambda}_c\overline{p}\\
&- 16\cos\eta C_{l_\alpha bl}\cos\theta_{1s}\Omega_{sgn}a_1\overline{r}\theta_{bl0}\\
&- 8\cos\eta C_{l_\alpha bl}\cos\theta_{1s}\bar{\Omega}_{RZR}a_1\overline{r}\theta_{bl0}\\
&+ 16\cos\delta\cos\eta\cos\theta_{1s}\Omega_{sgn}c_{d_2}\overline{p}\theta_{bl0}\\
&- 8\cos\delta C_{l_\alpha bl}\Omega_{sgn}\sin\eta\sin\theta_{1s}\overline{p}\theta_{bl0}\\
&+ 8\cos\delta\cos\eta^2 C_{l_\alpha bl}\cos{\theta_{1s}}^2\overline{pr}\theta_{bl0}\\
&- 16\cos\delta\cos\eta\cos{\theta_{1s}}^2\sin\eta c_{d_2}\overline{p}^2\theta_{bl0}\\
&+ 12C_{l_\alpha bl}\cos\theta_{1s}\Omega_{sgn}\sin\eta a_1\lambda_i\overline{p}\\
&+ 12\cos\eta C_{l_\alpha bl}\Omega_{sgn}\sin\theta_{1s}a_1\hat{\lambda}_c\overline{p}
\end{aligned}
$$

$$
\begin{aligned}
&- 12C_{l_{\alpha bl}} \cos\theta_{1s}\Omega_{sgn} \sin\eta a_1 \hat{\lambda}_c \overline{p} \\
&+ 24 \cos\delta \cos\theta_{1s}\Omega_{sgn} \sin\eta c_{d_2} \lambda_i \overline{r} \\
&+ 24 \cos\delta \cos\eta\Omega_{sgn} \sin\theta_{1s} c_{d_2} \hat{\lambda}_c \overline{r} \\
&- 24 \cos\delta \cos\theta_{1s}\Omega_{sgn} \sin\eta c_{d_2} \hat{\lambda}_c \overline{r} \\
&+ 16 \cos\eta C_{l_{\alpha bl}} \Omega_{sgn} \sin\theta_{1s} a_1 \overline{p} \theta_{bl0} \\
&- 16 C_{l_{\alpha bl}} \cos\theta_{1s}\Omega_{sgn} \sin\eta a_1 \overline{p} \theta_{bl0} \\
&+ 8 \cos\eta C_{l_{\alpha bl}} \bar{\Omega}_{RZR} \sin\theta_{1s} a_1 \overline{p} \theta_{bl0} \\
&- 8 C_{l_{\alpha bl}} \cos\theta_{1s} \bar{\Omega}_{RZR} \sin\eta a_1 \overline{p} \theta_{bl0} \\
&+ 16 \cos\delta \cos\eta\Omega_{sgn} \sin\theta_{1s} c_{d_2} \overline{r} \theta_{bl0} \\
&- 16 \cos\delta \cos\theta_{1s}\Omega_{sgn} \sin\eta c_{d_2} \overline{r} \theta_{bl0} \\
&- 8 \cos\delta C_{l_{\alpha bl}} \cos{\theta_{1s}}^2 \sin\eta^2 \overline{pr} \theta_{bl0} \\
&+ 8 \cos\eta C_{l_{\alpha bl}} \cos\theta_{1s} \sin\delta \overline{qr} \theta_{bl0} \\
&- 12 C_{l_{\alpha bl}} \Omega_{sgn} \sin\eta \sin\theta_{1s} a_1 \hat{\lambda}_c \overline{r} \\
&- 24 \Omega_{sgn} \sin\eta \sin\theta_{1s} c_{d_2} \hat{\mu}_c \overline{r} \theta_{bl0} \\
&- 24 \Omega_{sgn} \sin\eta \sin\theta_{1s} c_{d_2} \hat{\mu}_c \overline{r} \theta_{bl_0}^2 \\
&- 24 \cos\delta R a_0 c_{d_2} \overline{q} \theta_{bl0} \theta_{bl1} \\
&+ 24 \cos\delta \cos\eta C_{l_{\alpha bl}} \cos\theta_{1s} \Omega_{sgn} \lambda_i \overline{p} \\
&- 24 \cos\delta \cos\eta C_{l_{\alpha bl}} \cos\theta_{1s} \Omega_{sgn} \hat{\lambda}_c \overline{p} \\
&- 8 \cos\delta \cos\eta C_{l_{\alpha bl}} \cos\theta_{1s} \Omega_{sgn} \overline{p} \theta_{bl0} \\
&+ 8 \cos\delta \cos\eta C_{l_{\alpha bl}} \cos{\theta_{1s}}^2 \sin\eta \overline{p}^2 \theta_{bl0} \\
&- 8 \cos\delta \cos\eta^2 C_{l_{\alpha bl}} \cos\theta_{1s} \sin\theta_{1s} \overline{p}^2 \theta_{bl0} \\
&- 8 \cos\delta \cos\eta C_{l_{\alpha bl}} \cos{\theta_{1s}}^2 \sin\eta \overline{r}^2 \theta_{bl0} \\
&+ 24 \cos\delta \cos\eta C_{l_{\alpha bl}} \Omega_{sgn} \sin\theta_{1s} \lambda_i \overline{r} \\
&- 24 \cos\delta C_{l_{\alpha bl}} \cos\theta_{1s} \Omega_{sgn} \sin\eta \lambda_i \overline{r} \\
&- 24 \cos\delta \cos\eta C_{l_{\alpha bl}} \Omega_{sgn} \sin\theta_{1s} \hat{\lambda}_c \overline{r} \\
&+ 24 \cos\delta C_{l_{\alpha bl}} \cos\theta_{1s} \Omega_{sgn} \sin\eta \hat{\lambda}_c \overline{r} \\
&- 8 \cos\delta \cos\eta C_{l_{\alpha bl}} \Omega_{sgn} \sin\theta_{1s} \overline{r} \theta_{bl0} \\
&+ 8 \cos\delta C_{l_{\alpha bl}} \cos\theta_{1s} \Omega_{sgn} \sin\eta \overline{r} \theta_{bl0} \\
&+ 8 \cos\delta C_{l_{\alpha bl}} \cos\theta_{1s} \sin\eta^2 \sin\theta_{1s} \overline{p}^2 \theta_{bl0} \\
&+ 12 \cos\eta C_{l_{\alpha bl}} \cos\theta_{1s} \Omega_{sgn} a_1 \lambda_i \overline{r} \\
&- 12 \cos\eta C_{l_{\alpha bl}} \cos\theta_{1s} \Omega_{sgn} a_1 \hat{\lambda}_c \overline{r} \\
&- 24 \cos\delta \cos\eta \cos\theta_{1s} \Omega_{sgn} c_{d_2} \lambda_i \overline{p} \\
&+ 24 \cos\delta \cos\eta \cos\theta_{1s} \Omega_{sgn} c_{d_2} \hat{\lambda}_c \overline{p} \\
&+ 24 \cos\delta C_{l_{\alpha bl}} \Omega_{sgn} \sin\eta \sin\theta_{1s} \lambda_i \overline{p} \\
&- 24 \cos\delta C_{l_{\alpha bl}} \Omega_{sgn} \sin\eta \sin\theta_{1s} \hat{\lambda}_c \overline{p} \\
&- 16 \cos\eta C_{l_{\alpha bl}} \cos\theta_{1s} \Omega_{sgn} a_1 \overline{r} \theta_{bl0} \\
&- 8 \cos\eta C_{l_{\alpha bl}} \cos\theta_{1s} \bar{\Omega}_{RZR} a_1 \overline{r} \theta_{bl0} \\
&+ 16 \cos\delta \cos\eta \cos\theta_{1s} \Omega_{sgn} c_{d_2} \overline{p} \theta_{bl0} \\
&- 8 \cos\delta C_{l_{\alpha bl}} \Omega_{sgn} \sin\eta \sin\theta_{1s} \overline{p} \theta_{bl0} \\
&+ 8 \cos\delta \cos\eta^2 C_{l_{\alpha bl}} \cos{\theta_{1s}}^2 \overline{pr} \theta_{bl0} \\
&- 16 \cos\delta \cos\eta \cos{\theta_{1s}}^2 \sin\eta c_{d_2} \overline{p}^2 \theta_{bl0} \\
&+ 12 C_{l_{\alpha bl}} \cos\theta_{1s} \Omega_{sgn} \sin\eta a_1 \lambda_i \overline{p} \\
&+ 12 \cos\eta C_{l_{\alpha bl}} \Omega_{sgn} \sin\theta_{1s} a_1 \hat{\lambda}_c \overline{p}
\end{aligned}
$$

$$
\begin{aligned}
&- 12C_{l_\alpha bl}\cos\theta_{1s}\Omega_{sgn}\sin\eta a_1\hat{\lambda}_c\overline{p}\\
&+ 24\cos\delta\cos\theta_{1s}\Omega_{sgn}\sin\eta c_{d_2}\lambda_i\overline{r}\\
&+ 24\cos\delta\cos\eta\Omega_{sgn}\sin\theta_{1s}c_{d_2}\hat{\lambda}_c\overline{r}\\
&- 24\cos\delta\cos\theta_{1s}\Omega_{sgn}\sin\eta c_{d_2}\hat{\lambda}_c\overline{r}\\
&+ 16\cos\eta C_{l_\alpha bl}\Omega_{sgn}\sin\theta_{1s}a_1\overline{p}\theta_{bl0}\\
&- 16C_{l_\alpha bl}\cos\theta_{1s}\Omega_{sgn}\sin\eta a_1\overline{p}\theta_{bl0}\\
&+ 8\cos\eta C_{l_\alpha bl}\bar{\Omega}_{RZR}\sin\theta_{1s}a_1\overline{p}\theta_{bl0}\\
&- 8C_{l_\alpha bl}\cos\theta_{1s}\bar{\Omega}_{RZR}\sin\eta a_1\overline{p}\theta_{bl0}\\
&+ 16\cos\delta\cos\eta\Omega_{sgn}\sin\theta_{1s}c_{d_2}\overline{r}\theta_{bl0}\\
&- 16\cos\delta\cos\theta_{1s}\Omega_{sgn}\sin\eta c_{d_2}\overline{r}\theta_{bl0}\\
&- 8\cos\delta C_{l_\alpha bl}\cos{\theta_{1s}}^2\sin\eta^2\overline{pr}\theta_{bl0}\\
&+ 8\cos\eta C_{l_\alpha bl}\cos\theta_{1s}\sin\delta\overline{qr}\theta_{bl0}\\
&- 12C_{l_\alpha bl}\Omega_{sgn}\sin\eta\sin\theta_{1s}a_1\hat{\lambda}_c\overline{r}\\
&+ 24\cos\delta\Omega_{sgn}\sin\eta\sin\theta_{1s}c_{d_2}\hat{\lambda}_c\overline{p}\\
&+ 16\cos\eta\cos\theta_{1s}\bar{\Omega}_{RZR}a_1c_{d_2}\overline{r}\theta_{bl0}\\
&- 16C_{l_\alpha bl}\Omega_{sgn}\sin\eta\sin\theta_{1s}a_1\overline{r}\theta_{bl0}\\
&- 8C_{l_\alpha bl}\bar{\Omega}_{RZR}\sin\eta\sin\theta_{1s}a_1\overline{r}\theta_{bl0}\\
&+ 16\cos\delta\Omega_{sgn}\sin\eta\sin\theta_{1s}c_{d_2}\overline{p}\theta_{bl0}\\
&+ 16\cos\eta\cos\theta_{1s}\sin\delta a_0c_{d_2}\overline{p}\theta_{bl_0}^2\\
&+ 8C_{l_\alpha bl}\cos\theta_{1s}\sin\delta\sin\eta\overline{pq}\theta_{bl0}\\
&- 16\cos\delta\cos\eta^2\cos{\theta_{1s}}^2c_{d_2}\overline{pr}\theta_{bl0}\\
&+ 8\cos\delta C_{l_\alpha bl}Ra_0\hat{\lambda}_c\overline{q}\theta_{bl1}\\
&- 24\cos\eta\cos\theta_{1s}\Omega_{sgn}c_{d_2}\hat{\mu}_c\overline{r}\theta_{bl0}\\
&- 24\cos\eta\cos\theta_{1s}\Omega_{sgn}c_{d_2}\hat{\mu}_c\overline{r}\theta_{bl_0}^2\\
&- 16\cos\eta\bar{\Omega}_{RZR}\sin\theta_{1s}a_1c_{d_2}\overline{p}\theta_{bl0}\\
&+ 16\cos\theta_{1s}\bar{\Omega}_{RZR}\sin\eta a_1c_{d_2}\overline{p}\theta_{bl0}\\
&+ 16\cos\delta\cos{\theta_{1s}}^2\sin\eta^2c_{d_2}\overline{pr}\theta_{bl0}\\
&+ 24\cos\eta\Omega_{sgn}\sin\theta_{1s}c_{d_2}\hat{\mu}_c\overline{p}\theta_{bl0}\\
&- 24\cos\theta_{1s}\Omega_{sgn}\sin\eta c_{d_2}\hat{\mu}_c\overline{p}\theta_{bl0}\\
&+ 24\cos\eta\Omega_{sgn}\sin\theta_{1s}c_{d_2}\hat{\mu}_c\overline{p}\theta_{bl_0}^2\\
&- 24\cos\theta_{1s}\Omega_{sgn}\sin\eta c_{d_2}\hat{\mu}_c\overline{p}\theta_{bl_0}^2\\
&- 6\cos\delta\cos\eta C_{l_\alpha bl}\Omega_{sgn}R\sin\theta_{1s}\overline{r}\theta_{bl1}\\
&+ 6\cos\delta C_{l_\alpha bl}\cos\theta_{1s}\Omega_{sgn}R\sin\eta\overline{r}\theta_{bl1}\\
&+ 3\cos\delta C_{l_\alpha bl}\cos\theta_{1s}\Omega_{sgn}\sin\eta a_1\hat{\mu}_c\overline{r}\\
&- 12\cos\eta C_{l_\alpha bl}\cos\theta_{1s}\Omega_{sgn}Ra_1\overline{r}\theta_{bl1}\\
&- 6\cos\eta C_{l_\alpha bl}\cos\theta_{1s}\bar{\Omega}_{RZR}Ra_1\overline{r}\theta_{bl1}\\
&+ 12\cos\delta\cos\eta\cos\theta_{1s}\Omega_{sgn}Rc_{d_2}\overline{p}\theta_{bl1}\\
&- 6\cos\delta C_{l_\alpha bl}\Omega_{sgn}R\sin\eta\sin\theta_{1s}\overline{p}\theta_{bl1}\\
&+ 6\cos\delta\cos\eta^2C_{l_\alpha bl}\cos{\theta_{1s}}^2R\overline{pr}\theta_{bl1}\\
&- 12\cos\delta\cos\eta\cos{\theta_{1s}}^2R\sin\eta c_{d_2}\overline{p}^2\theta_{bl1}
\end{aligned}
$$

$$
\begin{aligned}
&+ 12\cos\eta C_{l_\alpha bl}\Omega_{sgn}R\sin\theta_{1s}a_1\overline{p}\theta_{bl1}\\
&- 12C_{l_\alpha bl}\cos\theta_{1s}\Omega_{sgn}R\sin\eta a_1\overline{p}\theta_{bl1}\\
&+ 6\cos\eta C_{l_\alpha bl}\bar{\Omega}_{RZR}R\sin\theta_{1s}a_1\overline{p}\theta_{bl1}\\
&- 6C_{l_\alpha bl}\cos\theta_{1s}\bar{\Omega}_{RZR}R\sin\eta a_1\overline{p}\theta_{bl1}\\
&+ 12\cos\delta\cos\eta\Omega_{sgn}R\sin\theta_{1s}c_{d_2}\overline{r}\theta_{bl1}\\
&- 12\cos\delta\cos\theta_{1s}\Omega_{sgn}R\sin\eta c_{d_2}\overline{r}\theta_{bl1}\\
&- 6\cos\delta C_{l_\alpha bl}\cos{\theta_{1s}}^2R\sin\eta^2\overline{pr}\theta_{bl1}\\
&+ 6\cos\eta C_{l_\alpha bl}\cos\theta_{1s}R\sin\delta\overline{qr}\theta_{bl1}\\
&- 12\cos\eta C_{l_\alpha bl}\cos\theta_{1s}\sin\delta a_0\hat{\lambda}_c\overline{p}\theta_{bl0}\\
&+ 12\cos\eta\cos\theta_{1s}\bar{\Omega}_{RZR}Ra_1c_{d_2}\overline{r}\theta_{bl1}\\
&- 12C_{l_\alpha bl}\Omega_{sgn}R\sin\eta\sin\theta_{1s}a_1\overline{r}\theta_{bl1}\\
&- 6C_{l_\alpha bl}\bar{\Omega}_{RZR}R\sin\eta\sin\theta_{1s}a_1\overline{r}\theta_{bl1}\\
&+ 12\cos\delta\Omega_{sgn}R\sin\eta\sin\theta_{1s}c_{d_2}\overline{p}\theta_{bl1}\\
&+ 6C_{l_\alpha bl}\cos\theta_{1s}R\sin\delta\sin\eta\overline{pq}\theta_{bl1}\\
&+ 16\cos\eta C_{l_\alpha bl}\cos{\theta_{1s}}^2\sin\eta a_1\overline{pr}\theta_{bl0}\\
&- 16\cos\eta\cos\theta_{1s}\Omega_{sgn}Rc_{d_2}\hat{\mu}_c\overline{r}\theta_{bl1}\\
&- 12\cos\eta\cos\theta_{1s}\Omega_{sgn}R^2c_{d_2}\hat{\mu}_c\overline{r}\theta_{bl_1}^2\\
&+ 12\cos\theta_{1s}\bar{\Omega}_{RZR}R\sin\eta a_1c_{d_2}\overline{p}\theta_{bl1}\\
&+ 12C_{l_\alpha bl}\cos\theta_{1s}\sin\delta\sin\eta a_0\hat{\lambda}_c\overline{r}\theta_{bl0}\\
&+ 16\cos\eta\Omega_{sgn}R\sin\theta_{1s}c_{d_2}\hat{\mu}_c\overline{p}\theta_{bl1}\\
&- 16\cos\theta_{1s}\Omega_{sgn}R\sin\eta c_{d_2}\hat{\mu}_c\overline{p}\theta_{bl1}\\
&+ 12\cos\eta\Omega_{sgn}R^2\sin\theta_{1s}c_{d_2}\hat{\mu}_c\overline{p}\theta_{bl_1}^2\\
&- 12\cos\theta_{1s}\Omega_{sgn}R^2\sin\eta c_{d_2}\hat{\mu}_c\overline{p}\theta_{bl_1}^2\\
&- 16\Omega_{sgn}R\sin\eta\sin\theta_{1s}c_{d_2}\hat{\mu}_c\overline{r}\theta_{bl1}\\
&- 12\Omega_{sgn}R^2\sin\eta\sin\theta_{1s}c_{d_2}\hat{\mu}_c\overline{r}\theta_{bl_1}^2\\
&- 6\cos\delta\cos\eta C_{l_\alpha bl}\cos\theta_{1s}\Omega_{sgn}R\overline{p}\theta_{bl1}\\
&+ 6\cos\delta\cos\eta C_{l_\alpha bl}\cos{\theta_{1s}}^2R\sin\eta\overline{p}^2\theta_{bl1}\\
&- 6\cos\delta\cos\eta C_{l_\alpha bl}\cos{\theta_{1s}}^2R\sin\eta\overline{r}^2\theta_{bl1}\\
&- 3\cos\delta\cos\eta C_{l_\alpha bl}\cos\theta_{1s}\Omega_{sgn}a_1\hat{\mu}_c\overline{p}\\
&+ 32\cos\delta\cos\eta C_{l_\alpha bl}\cos\theta_{1s}\sin\eta\sin\theta_{1s}\overline{pr}\theta_{bl0}\\
&- 8\cos\eta C_{l_\alpha bl}\cos\theta_{1s}R\sin\delta a_0\hat{\lambda}_c\overline{p}\theta_{bl1}\\
&+ 12\cos\eta C_{l_\alpha bl}\cos{\theta_{1s}}^2R\sin\eta a_1\overline{pr}\theta_{bl1}\\
&+ 8C_{l_\alpha bl}\cos\theta_{1s}R\sin\delta\sin\eta a_0\hat{\lambda}_c\overline{r}\theta_{bl1}\\
&+ 24\cos\eta\cos\theta_{1s}R\sin\delta a_0c_{d_2}\overline{p}\theta_{bl0}\theta_{bl1}\\
&- 32\cos\eta\cos\theta_{1s}\Omega_{sgn}Rc_{d_2}\hat{\mu}_c\overline{r}\theta_{bl0}\theta_{bl1}\\
&- 24\cos\theta_{1s}R\sin\delta\sin\eta a_0c_{d_2}\overline{r}\theta_{bl0}\theta_{bl1}\\
&+ 32\cos\eta\Omega_{sgn}R\sin\theta_{1s}c_{d_2}\hat{\mu}_c\overline{p}\theta_{bl0}\theta_{bl1}\\
&- 32\cos\theta_{1s}\Omega_{sgn}R\sin\eta c_{d_2}\hat{\mu}_c\overline{p}\theta_{bl0}\theta_{bl1}\\
&- 32\Omega_{sgn}R\sin\eta\sin\theta_{1s}c_{d_2}\hat{\mu}_c\overline{r}\theta_{bl0}\theta_{bl1}\\
&+ 24\cos\delta\cos\eta C_{l_\alpha bl}\cos\theta_{1s}R\sin\eta\sin\theta_{1s}\overline{pr}\theta_{bl1}\\
&- 8\cos\delta\cos\eta\cos\theta_{1s}\Omega_{sgn}Ra_1c_{d_2}\hat{\mu}_c\overline{p}\theta_{bl0}\theta_{bl1})
\end{aligned}
$$

B.6. Equation C_S

Simplified equation (Extra assumption: $c_{d_2} = 0$)

$$
\begin{aligned}
C_s = -\frac{C_{l_\alpha}\sigma}{2}(\mu_c^2(&\frac{Rb_1\theta_{bl1}}{4} \\
&+ \frac{b_1\theta_0}{2}) \\
&+ \frac{b_1\theta_0}{3} \\
&- \frac{3b_1(\lambda_i - \lambda_c)}{4} \\
&+ \frac{Rb_1\theta_{bl1}}{4} \\
&+ \frac{3\Omega_{sgn}a_0\mu_c(\lambda_i - \lambda_c)}{2} \\
&- \frac{3\Omega_{sgn}a_0\mu_c\theta_0}{4} \\
&- \frac{\Omega_{sgn}Ra_0\mu_c\theta_{bl1}}{2} \\
&+ \frac{\Omega_{sgn}a_0c_{d_1}\mu_c}{4C_{l_\alpha bl}})
\end{aligned}
$$

Full equation (next page)

$$
\begin{aligned}
C_S = \frac{6.6315e-04 I_{bl} N \gamma_{bl}}{C_{l_{\alpha bl}} R^5 \rho} (
& 60 C_{l_{\alpha bl}} b_1 \lambda_i \\
& - 60 C_{l_{\alpha bl}} b_1 \hat{\lambda}_c \\
& - 40 C_{l_{\alpha bl}} b_1 \theta_{bl0} \\
& + 60 b_1 c_{d_2} \hat{\mu}_c^2 \theta_{bl0} \\
& + 40 \cos\delta \Omega_{sgn} c_{d_1} \overline{q} \\
& + 40 C_{l_{\alpha bl}} \sin\delta a_0 \overline{q} \\
& - 30 C_{l_{\alpha bl}} R b_1 \theta_{bl1} \\
& - 60 \Omega_{sgn} a_0 c_{d_1} \hat{\mu}_c \\
& - 120 C_{l_{\alpha bl}} b_1 \hat{\mu}_c^2 \theta_{bl0} \\
& + 120 \cos\delta C_{l_{\alpha bl}} \Omega_{sgn} \dot{\overline{\eta}} \lambda_i \\
& - 120 \cos\delta C_{l_{\alpha bl}} \Omega_{sgn} \dot{\overline{\eta}} \hat{\lambda}_c \\
& - 40 \cos\delta C_{l_{\alpha bl}} \Omega_{sgn} \dot{\overline{\eta}} \theta_{bl0} \\
& + 120 C_{l_{\alpha bl}} \Omega_{sgn} \bar{\Omega}_{RZR} b_1 \lambda_i \\
& - 120 C_{l_{\alpha bl}} \Omega_{sgn} \bar{\Omega}_{RZR} b_1 \hat{\lambda}_c \\
& + 120 \cos\delta C_{l_{\alpha bl}} \Omega_{sgn} \lambda_i \overline{q} \\
& - 120 \cos\delta C_{l_{\alpha bl}} \Omega_{sgn} \hat{\lambda}_c \overline{q} \\
& - 40 C_{l_{\alpha bl}} \Omega_{sgn} \bar{\Omega}_{RZR} b_1 \theta_{bl0} \\
& - 40 \cos\delta C_{l_{\alpha bl}} \Omega_{sgn} \overline{q} \theta_{bl0} \\
& + 120 \cos\delta \Omega_{sgn} c_{d_2} \dot{\overline{\eta}} \hat{\lambda}_c \\
& - 360 C_{l_{\alpha bl}} \Omega_{sgn} a_0 \lambda_i \hat{\mu}_c \\
& + 360 C_{l_{\alpha bl}} \Omega_{sgn} a_0 \hat{\lambda}_c \hat{\mu}_c \\
& + 80 \cos\delta \Omega_{sgn} c_{d_2} \dot{\overline{\eta}} \theta_{bl0} \\
& - 120 \Omega_{sgn} \bar{\Omega}_{RZR} b_1 c_{d_2} \lambda_i \\
& + 120 \Omega_{sgn} \bar{\Omega}_{RZR} b_1 c_{d_2} \hat{\lambda}_c \\
& - 120 \cos\delta \Omega_{sgn} c_{d_2} \lambda_i \overline{q} \\
& + 120 \cos\delta \Omega_{sgn} c_{d_2} \hat{\lambda}_c \overline{q} \\
& + 180 C_{l_{\alpha bl}} \Omega_{sgn} a_0 \hat{\mu}_c \theta_{bl0} \\
& + 80 \Omega_{sgn} \bar{\Omega}_{RZR} b_1 c_{d_2} \theta_{bl0} \\
& - 60 C_{l_{\alpha bl}} R b_1 \hat{\mu}_c^2 \theta_{bl1} \\
& + 80 \cos\delta \Omega_{sgn} c_{d_2} \overline{q} \theta_{bl0} \\
& + 240 \Omega_{sgn} a_0 c_{d_2} \lambda_i \hat{\mu}_c \\
& - 240 \Omega_{sgn} a_0 c_{d_2} \hat{\lambda}_c \hat{\mu}_c \\
& - 120 \Omega_{sgn} a_0 c_{d_2} \hat{\mu}_c \theta_{bl0} \\
& + 80 \sin\delta a_0 c_{d_2} \overline{q} \theta_{bl0} \\
& + 80 \sin\delta a_0 c_{d_2} \overline{q} \theta_{bl_0}^2 \\
& + 40 \cos\delta \cos\eta C_{l_{\alpha bl}} \cos\theta_{1s} a_0 \overline{p} \\
& + 40 \cos\delta \cos\eta C_{l_{\alpha bl}} \sin\theta_{1s} a_0 \overline{r} \\
& - 40 \cos\delta C_{l_{\alpha bl}} \cos\theta_{1s} \sin\eta a_0 \overline{r} \\
& - 40 \cos\eta \cos\theta_{1s} \Omega_{sgn} \sin\delta c_{d_1} \overline{p} \\
& + 40 \cos\delta C_{l_{\alpha bl}} \sin\eta \sin\theta_{1s} a_0 \overline{p} \\
& - 30 \cos\delta C_{l_{\alpha bl}} \Omega_{sgn} R \dot{\overline{\eta}} \theta_{bl1}
\end{aligned}
$$

$$
\begin{aligned}
&- 105 \cos\delta C_{l_\alpha bl}\Omega_{sgn}a_1\dot{\overline{\eta}}\hat{\mu}_c \\
&- 30 C_{l_\alpha bl}\Omega_{sgn}\bar{\Omega}_{RZR}Rb_1\theta_{bl1} \\
&- 30 \cos\delta C_{l_\alpha bl}\Omega_{sgn}R\overline{q}\theta_{bl1} \\
&+ 40 \cos\theta_{1s}\Omega_{sgn}\sin\delta\sin\eta c_{d_1}\overline{r} \\
&- 105 \cos\delta C_{l_\alpha bl}\Omega_{sgn}a_1\hat{\mu}_c\overline{q} \\
&+ 60 \cos\delta\Omega_{sgn}Rc_{d_2}\dot{\overline{\eta}}\theta_{bl1} \\
&- 75 C_{l_\alpha bl}\Omega_{sgn}\sin\delta b_1\hat{\mu}_c\overline{q} \\
&+ 120 C_{l_\alpha bl}\Omega_{sgn}Ra_0\hat{\mu}_c\theta_{bl1} \\
&+ 60\Omega_{sgn}\bar{\Omega}_{RZR}Rb_1c_{d_2}\theta_{bl1} \\
&+ 60 \cos\delta\Omega_{sgn}Rc_{d_2}\overline{q}\theta_{bl1} \\
&+ 90 \cos\delta\Omega_{sgn}a_1c_{d_2}\hat{\mu}_c\overline{q} \\
&- 80\Omega_{sgn}Ra_0c_{d_2}\hat{\mu}_c\theta_{bl1} \\
&+ 60 C_{l_\alpha bl}\sin\delta a_0\lambda_i\overline{q}\theta_{bl0} \\
&- 60 C_{l_\alpha bl}\sin\delta a_0\hat{\lambda}_c\overline{q}\theta_{bl0} \\
&+ 60R\sin\delta a_0c_{d_2}\overline{q}\theta_{bl1} \\
&+ 48R^2\sin\delta a_0c_{d_2}\overline{q}\theta_{bl_1}^2 \\
&+ 120\sin\delta a_0c_{d_2}\hat{\lambda}_c\overline{q}\theta_{bl0} \\
&+ 20 \cos\delta C_{l_\alpha bl}\sin\delta a_1\overline{q}^2\theta_{bl0} \\
&- 80 \cos\theta_{1s}{}^2\sin\delta\sin\eta^2c_{d_2}\overline{pr}\theta_{bl0} \\
&+ 30 \cos\delta\Omega_{sgn}a_1c_{d_2}\hat{\mu}_c\overline{q}\theta_{bl0} \\
&+ 30 \cos\delta\Omega_{sgn}a_1c_{d_2}\hat{\mu}_c\overline{q}\theta_{bl_0}^2 \\
&+ 120 \cos\theta_{1s}\sin\eta a_0c_{d_2}\hat{\mu}_c\overline{p}\theta_{bl0} \\
&+ 80R\sin\delta a_0c_{d_2}\hat{\lambda}_c\overline{q}\theta_{bl1} \\
&+ 120R\sin\delta a_0c_{d_2}\overline{q}\theta_{bl0}\theta_{bl1} \\
&- 120 \cos\eta C_{l_\alpha bl}\cos\theta_{1s}\Omega_{sgn}\sin\delta\lambda_i\overline{p} \\
&+ 120 \cos\eta C_{l_\alpha bl}\cos\theta_{1s}\Omega_{sgn}\sin\delta\hat{\lambda}_c\overline{p} \\
&+ 40 \cos\eta C_{l_\alpha bl}\cos\theta_{1s}\Omega_{sgn}\sin\delta\overline{p}\theta_{bl0} \\
&- 40 \cos\eta C_{l_\alpha bl}\cos\theta_{1s}{}^2\sin\delta\sin\eta\overline{p}^2\theta_{bl0} \\
&+ 40 \cos\eta^2 C_{l_\alpha bl}\cos\theta_{1s}\sin\delta\sin\theta_{1s}\overline{p}^2\theta_{bl0} \\
&+ 40 \cos\eta C_{l_\alpha bl}\cos\theta_{1s}{}^2\sin\delta\sin\eta\overline{r}^2\theta_{bl0} \\
&- 40 \cos\eta^2 C_{l_\alpha bl}\cos\theta_{1s}\sin\delta\sin\theta_{1s}\overline{r}^2\theta_{bl0} \\
&+ 60 \cos\eta C_{l_\alpha bl}\cos\theta_{1s}\Omega_{sgn}b_1\hat{\lambda}_c\overline{r} \\
&- 120 \cos\eta C_{l_\alpha bl}\Omega_{sgn}\sin\delta\sin\theta_{1s}\lambda_i\overline{r} \\
&+ 120 C_{l_\alpha bl}\cos\theta_{1s}\Omega_{sgn}\sin\delta\sin\eta\lambda_i\overline{r} \\
&+ 120 \cos\eta C_{l_\alpha bl}\Omega_{sgn}\sin\delta\sin\theta_{1s}\hat{\lambda}_c\overline{r} \\
&- 120 C_{l_\alpha bl}\cos\theta_{1s}\Omega_{sgn}\sin\delta\sin\eta\hat{\lambda}_c\overline{r} \\
&+ 80 \cos\eta C_{l_\alpha bl}\cos\theta_{1s}\Omega_{sgn}b_1\overline{r}\theta_{bl0} \\
&+ 40 \cos\eta C_{l_\alpha bl}\cos\theta_{1s}\bar{\Omega}_{RZR}b_1\overline{r}\theta_{bl0} \\
&+ 40 \cos\eta C_{l_\alpha bl}\Omega_{sgn}\sin\delta\sin\theta_{1s}\overline{r}\theta_{bl0} \\
&- 40 C_{l_\alpha bl}\cos\theta_{1s}\Omega_{sgn}\sin\delta\sin\eta\overline{r}\theta_{bl0} \\
&+ 40 \cos\delta\cos\eta C_{l_\alpha bl}\cos\theta_{1s}\overline{qr}\theta_{bl0} \\
&- 40 C_{l_\alpha bl}\cos\theta_{1s}\sin\delta\sin\eta^2\sin\theta_{1s}\overline{p}^2\theta_{bl0} \\
&+ 40 \cos\delta C_{l_\alpha bl}\cos\theta_{1s}\sin\eta\dot{\overline{\eta}}\overline{p}\theta_{bl0}
\end{aligned}
$$

$$
\begin{aligned}
&+ 40C_{l_\alpha bl} \cos\theta_{1s} \sin\delta \sin\eta^2 \sin\theta_{1s} \overline{r}^2 \theta_{bl0} \\
&+ 60C_{l_\alpha bl} \cos\theta_{1s} \Omega_{sgn} \sin\eta b_1 \hat{\lambda}_c \overline{p} \\
&+ 120 \cos\eta \cos\theta_{1s} \Omega_{sgn} \sin\delta c_{d_2} \lambda_i \overline{p} \\
&- 120 \cos\eta \cos\theta_{1s} \Omega_{sgn} \sin\delta c_{d_2} \hat{\lambda}_c \overline{p} \\
&- 120C_{l_\alpha bl} \Omega_{sgn} \sin\delta \sin\eta \sin\theta_{1s} \lambda_i \overline{p} \\
&+ 120C_{l_\alpha bl} \Omega_{sgn} \sin\delta \sin\eta \sin\theta_{1s} \hat{\lambda}_c \overline{p} \\
&- 80 \cos\eta C_{l_\alpha bl} \Omega_{sgn} \sin\theta_{1s} b_1 \overline{p} \theta_{bl0} \\
&+ 80C_{l_\alpha bl} \cos\theta_{1s} \Omega_{sgn} \sin\eta b_1 \overline{p} \theta_{bl0} \\
&+ 40C_{l_\alpha bl} \cos\theta_{1s} \bar{\Omega}_{RZR} \sin\eta b_1 \overline{p} \theta_{bl0} \\
&- 80 \cos\eta \cos\theta_{1s} \Omega_{sgn} \sin\delta c_{d_2} \overline{p} \theta_{bl0} \\
&+ 40C_{l_\alpha bl} \Omega_{sgn} \sin\delta \sin\eta \sin\theta_{1s} \overline{p} \theta_{bl0} \\
&+ 80 \cos\delta \cos\eta \cos\theta_{1s} a_0 c_{d_2} \overline{p} \theta_{bl0} \\
&+ 80 \cos\delta \cos\eta \cos\theta_{1s} a_0 c_{d_2} \overline{p} \theta_{bl_0}^2 \\
&- 40 \cos\delta \cos\eta C_{l_\alpha bl} \sin\theta_{1s} \overline{pq} \theta_{bl0} \\
&+ 40 \cos\delta C_{l_\alpha bl} \cos\theta_{1s} \sin\eta \overline{pq} \theta_{bl0} \\
&- 40 \cos\eta^2 C_{l_\alpha bl} \cos{\theta_{1s}}^2 \sin\delta \overline{pr} \theta_{bl0} \\
&+ 80 \cos\eta \cos{\theta_{1s}}^2 \sin\delta \sin\eta c_{d_2} \overline{p}^2 \theta_{bl0} \\
&- 80 \cos\eta^2 \cos\theta_{1s} \sin\delta \sin\theta_{1s} c_{d_2} \overline{p}^2 \theta_{bl0} \\
&- 80 \cos\eta \cos{\theta_{1s}}^2 \sin\delta \sin\eta c_{d_2} \overline{r}^2 \theta_{bl0} \\
&+ 120 \cos\eta \Omega_{sgn} \sin\delta \sin\theta_{1s} c_{d_2} \lambda_i \overline{r} \\
&- 120 \cos\theta_{1s} \Omega_{sgn} \sin\delta \sin\eta c_{d_2} \lambda_i \overline{r} \\
&- 120 \cos\eta \Omega_{sgn} \sin\delta \sin\theta_{1s} c_{d_2} \hat{\lambda}_c \overline{r} \\
&+ 120 \cos\theta_{1s} \Omega_{sgn} \sin\delta \sin\eta c_{d_2} \hat{\lambda}_c \overline{r} \\
&- 180 \cos\eta C_{l_\alpha bl} \cos\theta_{1s} a_0 \hat{\mu}_c \overline{r} \theta_{bl0} \\
&+ 80C_{l_\alpha bl} \Omega_{sgn} \sin\eta \sin\theta_{1s} b_1 \overline{r} \theta_{bl0} \\
&- 80 \cos\eta \Omega_{sgn} \sin\delta \sin\theta_{1s} c_{d_2} \overline{r} \theta_{bl0} \\
&+ 80 \cos\theta_{1s} \Omega_{sgn} \sin\delta \sin\eta c_{d_2} \overline{r} \theta_{bl0} \\
&+ 40C_{l_\alpha bl} \cos{\theta_{1s}}^2 \sin\delta \sin\eta^2 \overline{pr} \theta_{bl0} \\
&- 80 \cos\delta \cos\theta_{1s} \sin\eta a_0 c_{d_2} \overline{r} \theta_{bl0} \\
&- 80 \cos\delta \cos\theta_{1s} \sin\eta a_0 c_{d_2} \overline{r} \theta_{bl_0}^2 \\
&- 80 \cos\delta \cos\eta \cos\theta_{1s} c_{d_2} \overline{qr} \theta_{bl0} \\
&+ 40 \cos\delta C_{l_\alpha bl} \sin\eta \sin\theta_{1s} \overline{qr} \theta_{bl0} \\
&+ 80 \cos\theta_{1s} \sin\delta \sin\eta^2 \sin\theta_{1s} c_{d_2} \overline{p}^2 \theta_{bl0} \\
&+ 120 \Omega_{sgn} \sin\delta \sin\eta \sin\theta_{1s} c_{d_2} \lambda_i \overline{p} \\
&- 120 \Omega_{sgn} \sin\delta \sin\eta \sin\theta_{1s} c_{d_2} \hat{\lambda}_c \overline{p} \\
&+ 180 \cos\eta C_{l_\alpha bl} \sin\theta_{1s} a_0 \hat{\mu}_c \overline{p} \theta_{bl0} \\
&- 180C_{l_\alpha bl} \cos\theta_{1s} \sin\eta a_0 \hat{\mu}_c \overline{p} \theta_{bl0} \\
&- 80 \cos\theta_{1s} \bar{\Omega}_{RZR} \sin\eta b_1 c_{d_2} \overline{p} \theta_{bl0} \\
&- 80 \Omega_{sgn} \sin\delta \sin\eta \sin\theta_{1s} c_{d_2} \overline{p} \theta_{bl0} \\
&- 80 \cos\delta \cos\theta_{1s} \sin\eta c_{d_2} \overline{pq} \theta_{bl0} \\
&+ 80 \cos\eta^2 \cos{\theta_{1s}}^2 \sin\delta c_{d_2} \overline{pr} \theta_{bl0} \\
&- 40C_{l_\alpha bl} R \sin\delta a_0 \hat{\lambda}_c \overline{q} \theta_{bl1} \\
&+ 120 \cos\eta \cos\theta_{1s} a_0 c_{d_2} \hat{\mu}_c \overline{r} \theta_{bl0} \\
&- 180C_{l_\alpha bl} \sin\eta \sin\theta_{1s} a_0 \hat{\mu}_c \overline{r} \theta_{bl0}
\end{aligned}
$$

$$
\begin{aligned}
&+ 30\cos\eta C_{l_\alpha bl}\cos\theta_{1s}\Omega_{sgn}R\sin\delta\overline{p}\theta_{bl1}\\
&- 20\cos\delta\cos\eta^2 C_{l_\alpha bl}\cos{\theta_{1s}}^2\sin\delta a_1\overline{p}^2\theta_{bl0}\\
&- 30\cos\eta C_{l_\alpha bl}\cos{\theta_{1s}}^2 R\sin\delta\sin\eta\overline{p}^2\theta_{bl1}\\
&+ 30\cos\eta^2 C_{l_\alpha bl}\cos\theta_{1s}R\sin\delta\sin\theta_{1s}\overline{p}^2\theta_{bl1}\\
&+ 30\cos\eta C_{l_\alpha bl}\cos{\theta_{1s}}^2 R\sin\delta\sin\eta\overline{r}^2\theta_{bl1}\\
&- 30\cos\eta^2 C_{l_\alpha bl}\cos\theta_{1s}R\sin\delta\sin\theta_{1s}\overline{r}^2\theta_{bl1}\\
&+ 105\cos\eta C_{l_\alpha bl}\cos\theta_{1s}\Omega_{sgn}\sin\delta a_1\hat{\mu}_c\overline{p}\\
&+ 75\cos\delta C_{l_\alpha bl}\cos\theta_{1s}\Omega_{sgn}\sin\eta b_1\hat{\mu}_c\overline{r}\\
&+ 60\cos\eta C_{l_\alpha bl}\cos\theta_{1s}\Omega_{sgn}Rb_1\overline{r}\theta_{bl1}\\
&+ 30\cos\eta C_{l_\alpha bl}\cos\theta_{1s}\bar{\Omega}_{RZR}Rb_1\overline{r}\theta_{bl1}\\
&+ 30\cos\eta C_{l_\alpha bl}\Omega_{sgn}R\sin\delta\sin\theta_{1s}\overline{r}\theta_{bl1}\\
&- 30C_{l_\alpha bl}\cos\theta_{1s}\Omega_{sgn}R\sin\delta\sin\eta\overline{r}\theta_{bl1}\\
&+ 30\cos\delta\cos\eta C_{l_\alpha bl}\cos\theta_{1s}R\overline{qr}\theta_{bl1}\\
&- 30C_{l_\alpha bl}\cos\theta_{1s}R\sin\delta\sin\eta^2\sin\theta_{1s}\overline{p}^2\theta_{bl1}\\
&- 20\cos\delta C_{l_\alpha bl}\cos{\theta_{1s}}^2\sin\delta\sin\eta^2 a_1\overline{r}^2\theta_{bl0}\\
&+ 30C_{l_\alpha bl}\cos\theta_{1s}R\sin\delta\sin\eta^2\sin\theta_{1s}\overline{r}^2\theta_{bl1}\\
&+ 105\cos\eta C_{l_\alpha bl}\Omega_{sgn}\sin\delta\sin\theta_{1s}a_1\hat{\mu}_c\overline{r}\\
&- 105C_{l_\alpha bl}\cos\theta_{1s}\Omega_{sgn}\sin\delta\sin\eta a_1\hat{\mu}_c\overline{r}\\
&+ 60\cos\delta\cos\eta C_{l_\alpha bl}\cos\theta_{1s}a_0\lambda_i\overline{p}\theta_{bl0}\\
&- 60\cos\delta\cos\eta C_{l_\alpha bl}\cos\theta_{1s}a_0\hat{\lambda}_c\overline{p}\theta_{bl0}\\
&- 60\cos\eta C_{l_\alpha bl}\Omega_{sgn}R\sin\theta_{1s}b_1\overline{p}\theta_{bl1}\\
&+ 60C_{l_\alpha bl}\cos\theta_{1s}\Omega_{sgn}R\sin\eta b_1\overline{p}\theta_{bl1}\\
&+ 30C_{l_\alpha bl}\cos\theta_{1s}\bar{\Omega}_{RZR}R\sin\eta b_1\overline{p}\theta_{bl1}\\
&- 60\cos\eta\cos\theta_{1s}\Omega_{sgn}R\sin\delta c_{d_2}\overline{p}\theta_{bl1}\\
&+ 30C_{l_\alpha bl}\Omega_{sgn}R\sin\delta\sin\eta\sin\theta_{1s}\overline{p}\theta_{bl1}\\
&+ 20\cos\delta^2\cos\eta C_{l_\alpha bl}\cos\theta_{1s}a_1\overline{pq}\theta_{bl0}\\
&+ 60\cos\delta\cos\eta\cos\theta_{1s}Ra_0c_{d_2}\overline{p}\theta_{bl1}\\
&- 30\cos\delta\cos\eta C_{l_\alpha bl}R\sin\theta_{1s}\overline{pq}\theta_{bl1}\\
&+ 30\cos\delta C_{l_\alpha bl}\cos\theta_{1s}R\sin\eta\overline{pq}\theta_{bl1}\\
&+ 48\cos\delta\cos\eta\cos\theta_{1s}R^2a_0c_{d_2}\overline{p}\theta_{bl_1}^2\\
&- 30\cos\eta^2 C_{l_\alpha bl}\cos{\theta_{1s}}^2 R\sin\delta\overline{pr}\theta_{bl1}\\
&+ 60\cos\eta\cos{\theta_{1s}}^2 R\sin\delta\sin\eta c_{d_2}\overline{p}^2\theta_{bl1}\\
&- 60\cos\eta\cos{\theta_{1s}}^2 R\sin\delta\sin\eta c_{d_2}\overline{r}^2\theta_{bl1}\\
&- 90\cos\eta\cos\theta_{1s}\Omega_{sgn}\sin\delta a_1c_{d_2}\hat{\mu}_c\overline{p}\\
&+ 105C_{l_\alpha bl}\Omega_{sgn}\sin\delta\sin\eta\sin\theta_{1s}a_1\hat{\mu}_c\overline{p}\\
&- 120\cos\eta C_{l_\alpha bl}\cos\theta_{1s}Ra_0\hat{\mu}_c\overline{r}\theta_{bl1}\\
&- 60\cos\delta C_{l_\alpha bl}\cos\theta_{1s}\sin\eta a_0\lambda_i\overline{r}\theta_{bl0}\\
&- 60\cos\delta\cos\eta C_{l_\alpha bl}\sin\theta_{1s}a_0\hat{\lambda}_c\overline{r}\theta_{bl0}\\
&+ 60\cos\delta C_{l_\alpha bl}\cos\theta_{1s}\sin\eta a_0\hat{\lambda}_c\overline{r}\theta_{bl0}\\
&+ 60C_{l_\alpha bl}\Omega_{sgn}R\sin\eta\sin\theta_{1s}b_1\overline{r}\theta_{bl1}\\
&- 20\cos\eta C_{l_\alpha bl}\cos\theta_{1s}\sin\delta^2 a_1\overline{pq}\theta_{bl0}\\
&- 60\cos\eta\Omega_{sgn}R\sin\delta\sin\theta_{1s}c_{d_2}\overline{r}\theta_{bl1}\\
&+ 60\cos\theta_{1s}\Omega_{sgn}R\sin\delta\sin\eta c_{d_2}\overline{r}\theta_{bl1}\\
&- 20\cos\delta^2 C_{l_\alpha bl}\cos\theta_{1s}\sin\eta a_1\overline{qr}\theta_{bl0}
\end{aligned}
$$

$$
\begin{aligned}
&+ 30C_{l_\alpha bl} \cos {\theta_{1s}}^2 R \sin\delta \sin\eta^2 \overline{pr}\theta_{bl1} \\
&- 60 \cos\delta \cos\theta_{1s} R \sin\eta a_0 c_{d_2} \overline{r}\theta_{bl1} \\
&- 60 \cos\delta \cos\eta \cos\theta_{1s} R c_{d_2} \overline{qr}\theta_{bl1} \\
&+ 30 \cos\delta C_{l_\alpha bl} R \sin\eta \sin\theta_{1s} \overline{qr}\theta_{bl1} \\
&- 48 \cos\delta \cos\theta_{1s} R^2 \sin\eta a_0 c_{d_2} \overline{r}\theta_{bl_1}^2 \\
&+ 90 \cos\theta_{1s} \Omega_{sgn} \sin\delta \sin\eta a_1 c_{d_2} \hat{\mu}_c \overline{r} \\
&+ 120 \cos\eta C_{l_\alpha bl} R \sin\theta_{1s} a_0 \hat{\mu}_c \overline{p}\theta_{bl1} \\
&- 120 C_{l_\alpha bl} \cos\theta_{1s} R \sin\eta a_0 \hat{\mu}_c \overline{p}\theta_{bl1} \\
&+ 120 \cos\delta \cos\eta \cos\theta_{1s} a_0 c_{d_2} \hat{\lambda}_c \overline{p}\theta_{bl0} \\
&- 60 \cos\delta C_{l_\alpha bl} \sin\eta \sin\theta_{1s} a_0 \hat{\lambda}_c \overline{p}\theta_{bl0} \\
&- 60 \cos\theta_{1s} \bar{\Omega}_{RZR} R \sin\eta b_1 c_{d_2} \overline{p}\theta_{bl1} \\
&- 60 \Omega_{sgn} R \sin\delta \sin\eta \sin\theta_{1s} c_{d_2} \overline{p}\theta_{bl1} \\
&- 60 \cos\delta \cos\theta_{1s} R \sin\eta c_{d_2} \overline{pq}\theta_{bl1} \\
&+ 60 \cos\eta^2 \cos {\theta_{1s}}^2 R \sin\delta c_{d_2} \overline{pr}\theta_{bl1} \\
&+ 20 C_{l_\alpha bl} \cos\theta_{1s} \sin\delta^2 \sin\eta a_1 \overline{qr}\theta_{bl0} \\
&- 90 \Omega_{sgn} \sin\delta \sin\eta \sin\theta_{1s} a_1 c_{d_2} \hat{\mu}_c \overline{p} \\
&- 120 C_{l_\alpha bl} R \sin\eta \sin\theta_{1s} a_0 \hat{\mu}_c \overline{r}\theta_{bl1} \\
&- 120 \cos\delta \cos\theta_{1s} \sin\eta a_0 c_{d_2} \hat{\lambda}_c \overline{r}\theta_{bl0} \\
&- 60 \cos {\theta_{1s}}^2 R \sin\delta \sin\eta^2 c_{d_2} \overline{pr}\theta_{bl1} \\
&+ 20 \cos\delta \Omega_{sgn} R a_1 c_{d_2} \hat{\mu}_c \overline{q}\theta_{bl1} \\
&+ 15 \cos\delta \Omega_{sgn} R^2 a_1 c_{d_2} \hat{\mu}_c \overline{q}\theta_{bl_1}^2 \\
&+ 80 \cos\theta_{1s} R \sin\eta a_0 c_{d_2} \hat{\mu}_c \overline{p}\theta_{bl1} \\
&- 75 \cos\delta \cos\eta C_{l_\alpha bl} \cos\theta_{1s} \Omega_{sgn} b_1 \hat{\mu}_c \overline{p} \\
&- 15 \cos\delta \cos\eta^2 C_{l_\alpha bl} \cos {\theta_{1s}}^2 R \sin\delta a_1 \overline{p}^2 \theta_{bl1} \\
&- 15 \cos\delta C_{l_\alpha bl} \cos {\theta_{1s}}^2 R \sin\delta \sin\eta^2 a_1 \overline{r}^2 \theta_{bl1} \\
&+ 40 \cos\delta \cos\eta C_{l_\alpha bl} \cos\theta_{1s} R a_0 \lambda_i \overline{p}\theta_{bl1} \\
&- 40 \cos\delta \cos\eta C_{l_\alpha bl} \cos\theta_{1s} R a_0 \hat{\lambda}_c \overline{p}\theta_{bl1} \\
&+ 15 \cos\delta^2 \cos\eta C_{l_\alpha bl} \cos\theta_{1s} R a_1 \overline{pq}\theta_{bl1} \\
&- 160 \cos\eta C_{l_\alpha bl} \cos\theta_{1s} \sin\delta \sin\eta \sin\theta_{1s} \overline{pr}\theta_{bl0} \\
&- 40 \cos\delta \cos\eta C_{l_\alpha bl} R \sin\theta_{1s} a_0 \hat{\lambda}_c \overline{r}\theta_{bl1} \\
&+ 40 \cos\delta C_{l_\alpha bl} \cos\theta_{1s} R \sin\eta a_0 \hat{\lambda}_c \overline{r}\theta_{bl1} \\
&- 15 \cos\eta C_{l_\alpha bl} \cos\theta_{1s} R \sin\delta^2 a_1 \overline{pq}\theta_{bl1} \\
&+ 80 \cos\delta \cos\eta \cos\theta_{1s} R a_0 c_{d_2} \hat{\lambda}_c \overline{p}\theta_{bl1} \\
&- 40 \cos\delta C_{l_\alpha bl} R \sin\eta \sin\theta_{1s} a_0 \hat{\lambda}_c \overline{p}\theta_{bl1} \\
&+ 120 \cos\delta \cos\eta \cos\theta_{1s} R a_0 c_{d_2} \overline{p}\theta_{bl0}\theta_{bl1} \\
&+ 320 \cos\eta \cos\theta_{1s} \sin\delta \sin\eta \sin\theta_{1s} c_{d_2} \overline{pr}\theta_{bl0} \\
&- 30 \cos\eta \cos\theta_{1s} \Omega_{sgn} \sin\delta a_1 c_{d_2} \hat{\mu}_c \overline{p}\theta_{bl0} \\
&- 30 \cos\eta \cos\theta_{1s} \Omega_{sgn} \sin\delta a_1 c_{d_2} \hat{\mu}_c \overline{p}\theta_{bl_0}^2 \\
&- 80 \cos\delta \cos\theta_{1s} R \sin\eta a_0 c_{d_2} \hat{\lambda}_c \overline{r}\theta_{bl1} \\
&- 120 \cos\delta \cos\theta_{1s} R \sin\eta a_0 c_{d_2} \overline{r}\theta_{bl0}\theta_{bl1} \\
&+ 30 \cos\theta_{1s} \Omega_{sgn} \sin\delta \sin\eta a_1 c_{d_2} \hat{\mu}_c \overline{r}\theta_{bl0} \\
&+ 30 \cos\theta_{1s} \Omega_{sgn} \sin\delta \sin\eta a_1 c_{d_2} \hat{\mu}_c \overline{r}\theta_{bl_0}^2 \\
&+ 120 \cos\delta R \sin\eta \sin\theta_{1s} a_0 c_{d_2} \overline{p}\theta_{bl0}\theta_{bl1}
\end{aligned}
$$

$$
\begin{aligned}
&+ 40\cos\delta\Omega_{sgn}Ra_1c_{d_2}\hat{\mu}_c\overline{q}\theta_{bl0}\theta_{bl1}\\
&+ 20\cos\theta_{1s}\Omega_{sgn}R\sin\delta\sin\eta a_1c_{d_2}\hat{\mu}_c\overline{r}\theta_{bl1}\\
&+ 15\cos\theta_{1s}\Omega_{sgn}R^2\sin\delta\sin\eta a_1c_{d_2}\hat{\mu}_c\overline{r}\theta_{bl_1}^2\\
&+ 40\cos\delta\cos\eta C_{l_{\alpha bl}}\cos{\theta_{1s}}^2\sin\delta\sin\eta a_1\overline{pr}\theta_{bl0}\\
&- 120\cos\eta C_{l_{\alpha bl}}\cos\theta_{1s}R\sin\delta\sin\eta\sin\theta_{1s}\overline{pr}\theta_{bl1}\\
&+ 240\cos\eta\cos\theta_{1s}R\sin\delta\sin\eta\sin\theta_{1s}c_{d_2}\overline{pr}\theta_{bl1}\\
&- 20\cos\eta\cos\theta_{1s}\Omega_{sgn}R\sin\delta a_1c_{d_2}\hat{\mu}_c\overline{p}\theta_{bl1}\\
&- 15\cos\eta\cos\theta_{1s}\Omega_{sgn}R^2\sin\delta a_1c_{d_2}\hat{\mu}_c\overline{p}\theta_{bl_1}^2\\
&+ 30\cos\delta\cos\eta C_{l_{\alpha bl}}\cos{\theta_{1s}}^2R\sin\delta\sin\eta a_1\overline{pr}\theta_{bl1}\\
&- 40\cos\eta\cos\theta_{1s}\Omega_{sgn}R\sin\delta a_1c_{d_2}\hat{\mu}_c\overline{p}\theta_{bl0}\theta_{bl1}\\
&+ 40\cos\theta_{1s}\Omega_{sgn}R\sin\delta\sin\eta a_1c_{d_2}\hat{\mu}_c\overline{r}\theta_{bl0}\theta_{bl1})
\end{aligned}
$$

B.7. Equation C_Q

Simplified equation

$$C_Q = \frac{-\sigma\Omega_{sgn}}{8}(4\lambda_i\lambda_c - 2(\square_c^2 + \square_i^2) + \frac{4(\lambda_i - \lambda_c)\theta_{bl0}}{3} + \frac{c_{d_0}}{C_{l_\alpha bl}} + R(\lambda_i - \lambda_c)\theta_{bl1} + 2a_1(\lambda_i - \lambda_c)\mu_c - \frac{4c_{d_1}(\lambda_i - \lambda_c)}{3C_{l_\alpha bl}} + \frac{c_{d_1}\theta_{bl0}}{C_{l_\alpha bl}} + \frac{4Rc_{d_1}\theta_{bl1}}{5C_{l_\alpha bl}})$$

Full equation

$$\begin{aligned} C_Q = -\frac{0.0013 I_{bl} N \gamma_{bl}}{C_{l_\alpha bl} R^5 \rho}(&30\Omega_{sgn}c_{d_0} \\ &- 60C_{l_\alpha bl}\Omega_{sgn}\lambda_i^2 \\ &- 60C_{l_\alpha bl}\Omega_{sgn}\hat{\lambda}_c^2 \\ &- 40\Omega_{sgn}c_{d_1}\lambda_i \\ &+ 40\Omega_{sgn}c_{d_1}\hat{\lambda}_c \\ &+ 60\Omega_{sgn}c_{d_2}\lambda_i^2 \\ &+ 60\Omega_{sgn}c_{d_2}\hat{\lambda}_c^2 \\ &+ 30\Omega_{sgn}c_{d_1}\theta_{bl0} \\ &+ 30\Omega_{sgn}c_{d_2}\theta_{bl_0}^2 \\ &+ 120C_{l_\alpha bl}\Omega_{sgn}\lambda_i\hat{\lambda}_c \\ &+ 40C_{l_\alpha bl}\Omega_{sgn}\lambda_i\theta_{bl0} \\ &- 40C_{l_\alpha bl}\Omega_{sgn}\hat{\lambda}_c\theta_{bl0} \\ &+ 24\Omega_{sgn}Rc_{d_1}\theta_{bl1} \\ &+ 20\Omega_{sgn}R^2c_{d_2}\theta_{bl_1}^2 \\ &- 120\Omega_{sgn}c_{d_2}\lambda_i\hat{\lambda}_c \\ &- 80\Omega_{sgn}c_{d_2}\lambda_i\theta_{bl0} \\ &+ 80\Omega_{sgn}c_{d_2}\hat{\lambda}_c\theta_{bl0} \\ &+ 30\Omega_{sgn}c_{d_1}\hat{\mu}_c^2\theta_{bl0} \\ &+ 30\Omega_{sgn}c_{d_2}\hat{\mu}_c^2\theta_{bl_0}^2 \\ &+ 30C_{l_\alpha bl}\Omega_{sgn}R\lambda_i\theta_{bl1} \\ &- 30C_{l_\alpha bl}\Omega_{sgn}R\hat{\lambda}_c\theta_{bl1} \\ &+ 60C_{l_\alpha bl}\Omega_{sgn}a_1\lambda_i\hat{\mu}_c \\ &- 60C_{l_\alpha bl}\Omega_{sgn}a_1\hat{\lambda}_c\hat{\mu}_c \\ &- 60\cos\eta\cos\theta_{1s}c_{d_1}\overline{r}\theta_{bl0} \\ &- 60\cos\eta\cos\theta_{1s}c_{d_2}\overline{r}\theta_{bl_0}^2 \\ &- 20C_{l_\alpha bl}\Omega_{sgn}a_1\hat{\mu}_c\theta_{bl0} \\ &+ 20C_{l_\alpha bl}\bar{\Omega}_{RZR}a_1\hat{\mu}_c\theta_{bl0} \\ &- 60\cos\theta_{1s}\sin\eta c_{d_1}\overline{p}\theta_{bl0} \\ &+ 60\cos\eta\sin\theta_{1s}c_{d_2}\overline{p}\theta_{bl_0}^2 \\ &- 60\cos\theta_{1s}\sin\eta c_{d_2}\overline{p}\theta_{bl_0}^2 \\ &- 60\Omega_{sgn}Rc_{d_2}\lambda_i\theta_{bl1} \end{aligned}$$

$$
\begin{aligned}
&+ 60\Omega_{sgn} R c_{d_2} \hat{\lambda}_c \theta_{bl1} \\
&+ 20\Omega_{sgn} R c_{d_1} \hat{\mu}_c^2 \theta_{bl1} \\
&+ 15\Omega_{sgn} R^2 c_{d_2} \hat{\mu}_c^2 \theta_{bl_1}^2 \\
&- 20 C_{l_\alpha bl} \sin\delta \hat{\mu}_c \overline{q} \theta_{bl0} \\
&+ 48\Omega_{sgn} R c_{d_2} \theta_{bl0} \theta_{bl1} \\
&- 60\Omega_{sgn} a_1 c_{d_2} \lambda_i \hat{\mu}_c \\
&+ 60\Omega_{sgn} a_1 c_{d_2} \hat{\lambda}_c \hat{\mu}_c \\
&- 60 \sin\eta \sin\theta_{1s} c_{d_2} \overline{r} \theta_{bl_0}^2 \\
&+ 40\Omega_{sgn} a_1 c_{d_2} \hat{\mu}_c \theta_{bl0} \\
&- 40\bar{\Omega}_{RZR} a_1 c_{d_2} \hat{\mu}_c \theta_{bl0} \\
&- 30 \sin\delta a_1 c_{d_2} \overline{q} \theta_{bl_0}^2 \\
&+ 40 \sin\delta c_{d_2} \hat{\mu}_c \overline{q} \theta_{bl0} \\
&- 15 \cos\delta^2 \cos\eta^2 C_{l_\alpha bl} \cos{\theta_{1s}}^2 \Omega_{sgn} \overline{p}^2 \\
&- 15 \cos\eta^2 C_{l_\alpha bl} \cos{\theta_{1s}}^2 \Omega_{sgn} \sin\delta^2 \overline{p}^2 \\
&- 15 \cos\delta^2 C_{l_\alpha bl} \cos{\theta_{1s}}^2 \Omega_{sgn} \sin\eta^2 \overline{r}^2 \\
&- 15 C_{l_\alpha bl} \cos{\theta_{1s}}^2 \Omega_{sgn} \sin\delta^2 \sin\eta^2 \overline{r}^2 \\
&+ 30 C_{l_\alpha bl} \Omega_{sgn} \bar{\Omega}_{RZR} \sin\delta a_1 \overline{q} \\
&- 40 \cos\eta C_{l_\alpha bl} \cos\theta_{1s} \lambda_i \overline{r} \theta_{bl0} \\
&+ 40 \cos\eta C_{l_\alpha bl} \cos\theta_{1s} \hat{\lambda}_c \overline{r} \theta_{bl0} \\
&- 48 \cos\eta \cos\theta_{1s} R c_{d_1} \overline{r} \theta_{bl1} \\
&- 40 \cos\eta \cos\theta_{1s} R^2 c_{d_2} \overline{r} \theta_{bl_1}^2 \\
&- 15 C_{l_\alpha bl} \Omega_{sgn} R a_1 \hat{\mu}_c \theta_{bl1} \\
&+ 15 C_{l_\alpha bl} \bar{\Omega}_{RZR} R a_1 \hat{\mu}_c \theta_{bl1} \\
&- 30\Omega_{sgn} \bar{\Omega}_{RZR} \sin\delta a_1 c_{d_2} \overline{q} \\
&+ 40 \cos\eta C_{l_\alpha bl} \sin\theta_{1s} \lambda_i \overline{p} \theta_{bl0} \\
&- 40 C_{l_\alpha bl} \cos\theta_{1s} \sin\eta \lambda_i \overline{p} \theta_{bl0} \\
&- 40 \cos\eta C_{l_\alpha bl} \sin\theta_{1s} \hat{\lambda}_c \overline{p} \theta_{bl0} \\
&+ 40 C_{l_\alpha bl} \cos\theta_{1s} \sin\eta \hat{\lambda}_c \overline{p} \theta_{bl0} \\
&- 48 \cos\theta_{1s} R \sin\eta c_{d_1} \overline{p} \theta_{bl1} \\
&+ 40 \cos\eta R^2 \sin\theta_{1s} c_{d_2} \overline{p} \theta_{bl_1}^2 \\
&- 40 \cos\theta_{1s} R^2 \sin\eta c_{d_2} \overline{p} \theta_{bl_1}^2 \\
&- 15 C_{l_\alpha bl} R \sin\delta \hat{\mu}_c \overline{q} \theta_{bl1} \\
&+ 80 \cos\eta \cos\theta_{1s} c_{d_2} \lambda_i \overline{r} \theta_{bl0} \\
&- 80 \cos\eta \cos\theta_{1s} c_{d_2} \hat{\lambda}_c \overline{r} \theta_{bl0} \\
&- 40 C_{l_\alpha bl} \sin\eta \sin\theta_{1s} \lambda_i \overline{r} \theta_{bl0} \\
&+ 40 C_{l_\alpha bl} \sin\eta \sin\theta_{1s} \hat{\lambda}_c \overline{r} \theta_{bl0} \\
&- 40 R^2 \sin\eta \sin\theta_{1s} c_{d_2} \overline{r} \theta_{bl_1}^2 \\
&+ 30\Omega_{sgn} R a_1 c_{d_2} \hat{\mu}_c \theta_{bl1} \\
&- 30\bar{\Omega}_{RZR} R a_1 c_{d_2} \hat{\mu}_c \theta_{bl1} \\
&+ 20 C_{l_\alpha bl} \sin\delta a_1 \hat{\lambda}_c \overline{q} \theta_{bl0}
\end{aligned}
$$

$$
\begin{aligned}
&+ 80 \cos\theta_{1s} \sin\eta c_{d_2} \lambda_i \overline{p} \theta_{bl0} \\
&+ 80 \cos\eta \sin\theta_{1s} c_{d_2} \hat{\lambda}_c \overline{p} \theta_{bl0} \\
&- 80 \cos\theta_{1s} \sin\eta c_{d_2} \hat{\lambda}_c \overline{p} \theta_{bl0} \\
&- 20 R^2 \sin\delta a_1 c_{d_2} \overline{q} \theta_{bl_1}^2 \\
&+ 40 \Omega_{sgn} R c_{d_2} \hat{\mu}_c^2 \theta_{bl0} \theta_{bl1} \\
&+ 30 R \sin\delta c_{d_2} \hat{\mu}_c \overline{q} \theta_{bl1} \\
&- 80 \sin\eta \sin\theta_{1s} c_{d_2} \hat{\lambda}_c \overline{r} \theta_{bl0} \\
&- 40 \sin\delta a_1 c_{d_2} \hat{\lambda}_c \overline{q} \theta_{bl0} \\
&+ 96 \cos\eta R \sin\theta_{1s} c_{d_2} \overline{p} \theta_{bl0} \theta_{bl1} \\
&- 96 \cos\theta_{1s} R \sin\eta c_{d_2} \overline{p} \theta_{bl0} \theta_{bl1} \\
&- 60 R \sin\eta \sin\theta_{1s} c_{d_2} \hat{\lambda}_c \overline{r} \theta_{bl1} \\
&- 96 R \sin\eta \sin\theta_{1s} c_{d_2} \overline{r} \theta_{bl0} \theta_{bl1} \\
&- 30 R \sin\delta a_1 c_{d_2} \hat{\lambda}_c \overline{q} \theta_{bl1} \\
&- 48 R \sin\delta a_1 c_{d_2} \overline{q} \theta_{bl0} \theta_{bl1} \\
&- 20 \cos\delta \cos\eta C_{l_\alpha bl} \cos\theta_{1s} \hat{\mu}_c \overline{p} \theta_{bl0} \\
&- 30 \cos\eta C_{l_\alpha bl} \cos\theta_{1s} R \lambda_i \overline{r} \theta_{bl1} \\
&+ 30 \cos\eta C_{l_\alpha bl} \cos\theta_{1s} R \hat{\lambda}_c \overline{r} \theta_{bl1} \\
&- 20 \cos\delta \cos\eta C_{l_\alpha bl} \sin\theta_{1s} \hat{\mu}_c \overline{r} \theta_{bl0} \\
&+ 20 \cos\delta C_{l_\alpha bl} \cos\theta_{1s} \sin\eta \hat{\mu}_c \overline{r} \theta_{bl0} \\
&- 30 \cos\delta \cos\eta \cos\theta_{1s} a_1 c_{d_2} \overline{p} \theta_{bl_0}^2 \\
&+ 30 \cos\eta C_{l_\alpha bl} R \sin\theta_{1s} \lambda_i \overline{p} \theta_{bl1} \\
&- 30 C_{l_\alpha bl} \cos\theta_{1s} R \sin\eta \lambda_i \overline{p} \theta_{bl1} \\
&- 30 \cos\eta C_{l_\alpha bl} R \sin\theta_{1s} \hat{\lambda}_c \overline{p} \theta_{bl1} \\
&+ 30 C_{l_\alpha bl} \cos\theta_{1s} R \sin\eta \hat{\lambda}_c \overline{p} \theta_{bl1} \\
&+ 20 \cos\eta C_{l_\alpha bl} \cos\theta_{1s} a_1 \hat{\mu}_c \overline{r} \theta_{bl0} \\
&+ 40 \cos\delta \cos\eta \cos\theta_{1s} c_{d_2} \hat{\mu}_c \overline{p} \theta_{bl0} \\
&- 20 \cos\delta C_{l_\alpha bl} \sin\eta \sin\theta_{1s} \hat{\mu}_c \overline{p} \theta_{bl0} \\
&+ 30 \cos\delta \cos\theta_{1s} \sin\eta a_1 c_{d_2} \overline{r} \theta_{bl_0}^2 \\
&+ 20 C_{l_\alpha bl} \cos\theta_{1s} \sin\eta a_1 \hat{\mu}_c \overline{p} \theta_{bl0} \\
&+ 60 \cos\eta \cos\theta_{1s} R c_{d_2} \lambda_i \overline{r} \theta_{bl1} \\
&- 60 \cos\eta \cos\theta_{1s} R c_{d_2} \hat{\lambda}_c \overline{r} \theta_{bl1} \\
&- 30 C_{l_\alpha bl} R \sin\eta \sin\theta_{1s} \lambda_i \overline{r} \theta_{bl1} \\
&+ 30 C_{l_\alpha bl} R \sin\eta \sin\theta_{1s} \hat{\lambda}_c \overline{r} \theta_{bl1} \\
&- 40 \cos\delta \cos\theta_{1s} \sin\eta c_{d_2} \hat{\mu}_c \overline{r} \theta_{bl0} \\
&- 96 \cos\eta \cos\theta_{1s} R c_{d_2} \overline{r} \theta_{bl0} \theta_{bl1} \\
&+ 15 C_{l_\alpha bl} R \sin\delta a_1 \hat{\lambda}_c \overline{q} \theta_{bl1} \\
&+ 60 \cos\theta_{1s} R \sin\eta c_{d_2} \lambda_i \overline{p} \theta_{bl1} \\
&+ 60 \cos\eta R \sin\theta_{1s} c_{d_2} \hat{\lambda}_c \overline{p} \theta_{bl1} \\
&- 60 \cos\theta_{1s} R \sin\eta c_{d_2} \hat{\lambda}_c \overline{p} \theta_{bl1} \\
&+ 30 \cos\eta C_{l_\alpha bl} \cos {\theta_{1s}}^2 \Omega_{sgn} \sin\delta^2 \sin\eta \overline{pr} \\
&+ 30 \cos\delta \cos\theta_{1s} \Omega_{sgn} \bar{\Omega}_{RZR} \sin\eta a_1 c_{d_2} \overline{r}
\end{aligned}
$$

$$
\begin{aligned}
&- 15\cos\delta\cos\eta C_{l_{\alpha bl}}\cos\theta_{1s}R\hat{\mu}_c\overline{p}\theta_{bl1}\\
&- 20\cos\delta\cos\eta C_{l_{\alpha bl}}\cos\theta_{1s}a_1\lambda_i\overline{p}\theta_{bl0}\\
&+ 20\cos\delta\cos\eta C_{l_{\alpha bl}}\cos\theta_{1s}a_1\hat{\lambda}_c\overline{p}\theta_{bl0}\\
&- 15\cos\delta\cos\eta C_{l_{\alpha bl}}R\sin\theta_{1s}\hat{\mu}_c\overline{r}\theta_{bl1}\\
&+ 15\cos\delta C_{l_{\alpha bl}}\cos\theta_{1s}R\sin\eta\hat{\mu}_c\overline{r}\theta_{bl1}\\
&- 20\cos\delta\cos\eta\cos\theta_{1s}R^2a_1c_{d_2}\overline{p}\theta_{bl_1}^2\\
&+ 15\cos\eta C_{l_{\alpha bl}}\cos\theta_{1s}Ra_1\hat{\mu}_c\overline{r}\theta_{bl1}\\
&+ 20\cos\delta\cos\eta C_{l_{\alpha bl}}\sin\theta_{1s}a_1\hat{\lambda}_c\overline{r}\theta_{bl0}\\
&- 20\cos\delta C_{l_{\alpha bl}}\cos\theta_{1s}\sin\eta a_1\hat{\lambda}_c\overline{r}\theta_{bl0}\\
&+ 30\cos\delta\cos\eta\cos\theta_{1s}Rc_{d_2}\hat{\mu}_c\overline{p}\theta_{bl1}\\
&- 15\cos\delta C_{l_{\alpha bl}}R\sin\eta\sin\theta_{1s}\hat{\mu}_c\overline{p}\theta_{bl1}\\
&+ 20\cos\delta\cos\theta_{1s}R^2\sin\eta a_1c_{d_2}\overline{r}\theta_{bl_1}^2\\
&+ 15C_{l_{\alpha bl}}\cos\theta_{1s}R\sin\eta a_1\hat{\mu}_c\overline{p}\theta_{bl1}\\
&- 40\cos\delta\cos\eta\cos\theta_{1s}a_1c_{d_2}\hat{\lambda}_c\overline{p}\theta_{bl0}\\
&+ 20\cos\delta C_{l_{\alpha bl}}\sin\eta\sin\theta_{1s}a_1\hat{\lambda}_c\overline{p}\theta_{bl0}\\
&- 30\cos\delta\cos\theta_{1s}R\sin\eta c_{d_2}\hat{\mu}_c\overline{r}\theta_{bl1}\\
&+ 60\cos\eta\cos{\theta_{1s}}^2\Omega_{sgn}\sin\eta c_{d_2}\overline{pr}\theta_{bl_0}^2\\
&+ 40\cos\delta\cos\theta_{1s}\sin\eta a_1c_{d_2}\hat{\lambda}_c\overline{r}\theta_{bl0}\\
&+ 48\cos{\theta_{1s}}^2\Omega_{sgn}R\sin\eta^2c_{d_2}\overline{p}^2\theta_{bl0}\theta_{bl1}\\
&+ 30\cos\delta\cos\eta C_{l_{\alpha bl}}\cos\theta_{1s}\Omega_{sgn}\bar{\Omega}_{RZR}a_1\overline{p}\\
&+ 30\cos\delta\cos\eta C_{l_{\alpha bl}}\Omega_{sgn}\bar{\Omega}_{RZR}\sin\theta_{1s}a_1\overline{r}\\
&- 30\cos\delta C_{l_{\alpha bl}}\cos\theta_{1s}\Omega_{sgn}\bar{\Omega}_{RZR}\sin\eta a_1\overline{r}\\
&+ 30\cos\delta^2\cos\eta C_{l_{\alpha bl}}\cos{\theta_{1s}}^2\Omega_{sgn}\sin\eta\overline{pr}\\
&- 30\cos\delta\cos\eta\cos\theta_{1s}\Omega_{sgn}\bar{\Omega}_{RZR}a_1c_{d_2}\overline{p}\\
&+ 30\cos\delta C_{l_{\alpha bl}}\Omega_{sgn}\bar{\Omega}_{RZR}\sin\eta\sin\theta_{1s}a_1\overline{p}\\
&+ 15\cos\delta\cos\eta C_{l_{\alpha bl}}\cos\theta_{1s}Ra_1\hat{\lambda}_c\overline{p}\theta_{bl1}\\
&- 15\cos\delta C_{l_{\alpha bl}}\cos\theta_{1s}R\sin\eta a_1\hat{\lambda}_c\overline{r}\theta_{bl1}\\
&- 30\cos\delta\cos\eta\cos\theta_{1s}Ra_1c_{d_2}\hat{\lambda}_c\overline{p}\theta_{bl1}\\
&+ 15\cos\delta C_{l_{\alpha bl}}R\sin\eta\sin\theta_{1s}a_1\hat{\lambda}_c\overline{p}\theta_{bl1}\\
&- 48\cos\delta\cos\eta\cos\theta_{1s}Ra_1c_{d_2}\overline{p}\theta_{bl0}\theta_{bl1}\\
&+ 30\cos\delta\cos\theta_{1s}R\sin\eta a_1c_{d_2}\hat{\lambda}_c\overline{r}\theta_{bl1}\\
&+ 48\cos\delta\cos\theta_{1s}R\sin\eta a_1c_{d_2}\overline{r}\theta_{bl0}\theta_{bl1}\\
&+ 96\cos\eta\cos{\theta_{1s}}^2\Omega_{sgn}R\sin\eta c_{d_2}\overline{pr}\theta_{bl0}\theta_{bl1})
\end{aligned}
$$

C

GTRS look-up tables

C.1. Horizontal stabilizers downwash angle

α(deg)	$\eta = 90$ deg	$\eta = 60$ deg	$\eta = 30$ deg	$\eta = 15$ deg	$\eta = 0$ deg
-90	0	0	0	0	0
-16	0	0	0	0	0
-12	0	0	0	0	0
-8	0.06	0	0	0	0.09
-4	1.32	1.2	1.8	1.26	1.62
0	2.58	2.6	2.7	2.8	3.15
4	3.84	4	4.22	4.34	4.68
8	5.1	5.2	5.74	5.88	6.21
12	5.9	6.4	7	7.1	7.1
16	6.3	6.8	7.3	7.3	7.5
20	6	6.3	6.7	6.7	7
24	4	4.1	4.1	4.1	4.8
28	0	0	0	0	0
90	0	0	0	0	0

Table C.1: Horizontal stabilizers downwash angle due to wake of the wing, XFL = 1 [8]

α(deg)	$\eta = 90$ deg	$\eta = 60$ deg	$\eta = 30$ deg	$\eta = 15$ deg	$\eta = 0$ deg
-90	0	0	0	0	0
-16	0	0	0	0	0
-12	0.45	0	0	0.4	0.8
-8	1.25	0.9	0.7	1.2	1.6
-4	2.6	2.25	2.1	2.7	3.1
0	4.08	3.8	3.6	4.3	4.7
4	5.35	5.3	5.2	6	6.2
8	6.6	6.8	6.7	7.1	7.8
12	7.4	7.8	7.9	8.7	8.5
16	7.55	8.2	8.2	8.9	8.6
20	6.7	7.4	7.4	8.2	7.5
24	4.4	4.8	4.8	5.3	4.9
28	0	0	0	0	0
90	0	0	0	0	0

Table C.2: Horizontal stabilizers downwash angle due to wake of the wing, XFL = 2 [8]

α(deg)	$\eta = 90$ deg	$\eta = 60$ deg	$\eta = 30$ deg	$\eta = 15$ deg	$\eta = 0$ deg
-90	0	0	0	0	0
-16	0	0	0	0	0
-12	0.95	0	0	0.7	1.47
-8	2.54	1.78	1.3	2.4	3.03
-4	3.92	3.38	2.9	4.1	4.59
0	5.4	4.98	4.5	5.8	6.15
4	6.88	6.58	6.1	7.5	7.71
8	8.26	8.18	7.7	9.2	9.27
12	8.9	9.2	8.9	10.4	9.8
16	8.8	9.5	9.1	10.8	9.7
20	7.3	8.4	8.1	9.8	8
24	4.8	5.5	5.5	6.4	5
28	0	0	0	0	0
90	0	0	0	0	0

Table C.3: Horizontal stabilizers downwash angle due to wake of the wing, XFL = 3 [8]

α(deg)	$\eta = 90$ deg	$\eta = 60$ deg	$\eta = 30$ deg	$\eta = 15$ deg	$\eta = 0$ deg
-90	0	0	0	0	0
-16	0	0	0	0	0
-12	0.95	0	0	0.7	1.47
-8	2.54	1.78	1.3	2.4	3.03
-4	3.92	3.38	2.9	4.1	4.59
0	5.4	4.98	4.5	5.8	6.15
4	6.88	6.58	6.1	7.5	7.71
8	8.26	8.18	7.7	9.2	9.27
12	8.9	9.2	8.9	10.4	9.8
16	8.8	9.5	9.1	10.8	9.7
20	7.3	8.4	8.1	9.8	8
24	4.8	5.5	5.5	6.4	5
28	0	0	0	0	0
90	0	0	0	0	0

Table C.4: Horizontal stabilizers downwash angle due to wake of the wing, XFL = 4 [8]

C.2. Fuselage aerodynamic coefficients

α_f	$C_{L,f}$	$C_{D,f}$	$C_{M,f}$
-28	-1.5794	2.3226	-12.4594
-24	-1.3935	1.8581	-12.1762
-20	-1.0099	1.4298	-10.7604
-16	-0.6735	1.0015	-10.4772
-12	-0.3372	0.5732	-8.3535
-8	-0.0009	0.2787	-6.2014
-4	0.3354	0.1672	-4.0352
0	0.6717	0.1449	-1.8831
4	1.008	0.1672	0.269
8	1.3443	0.2137	2.4211
12	1.6806	0.341	3.4971
16	2.0169	0.537	4.0352
20	2.3532	0.733	3.7661
24	2.6013	0.929	2.6901
28	2.9729	1.3935	2.6901

Table C.5: Fuselage aerodynamic coefficients [8]

D

Sensitivity Analysis Stability Derivatives

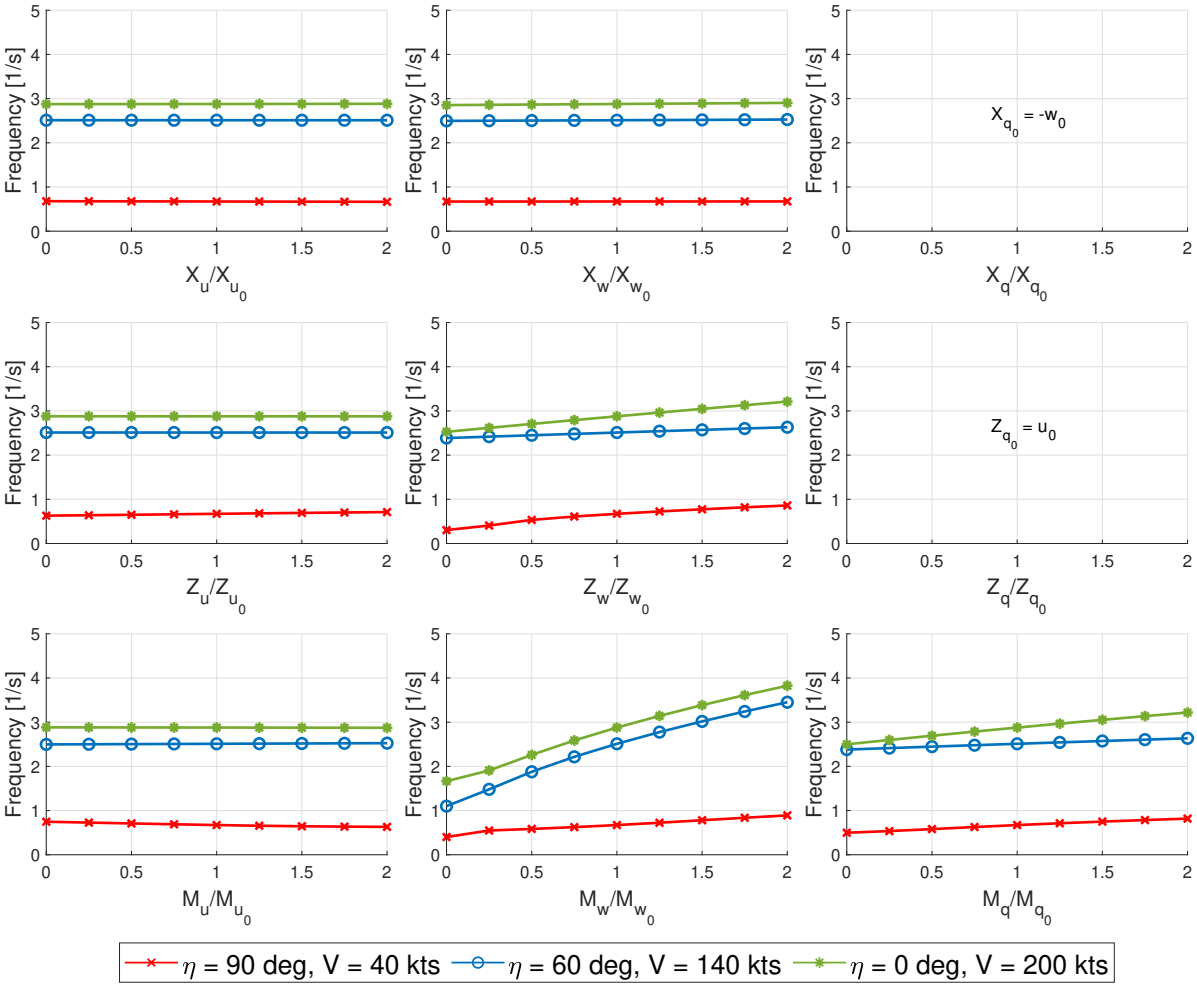

Figure D.1: Sensitivity Analysis of the Stability Derivatives on the Frequency of the Short Period

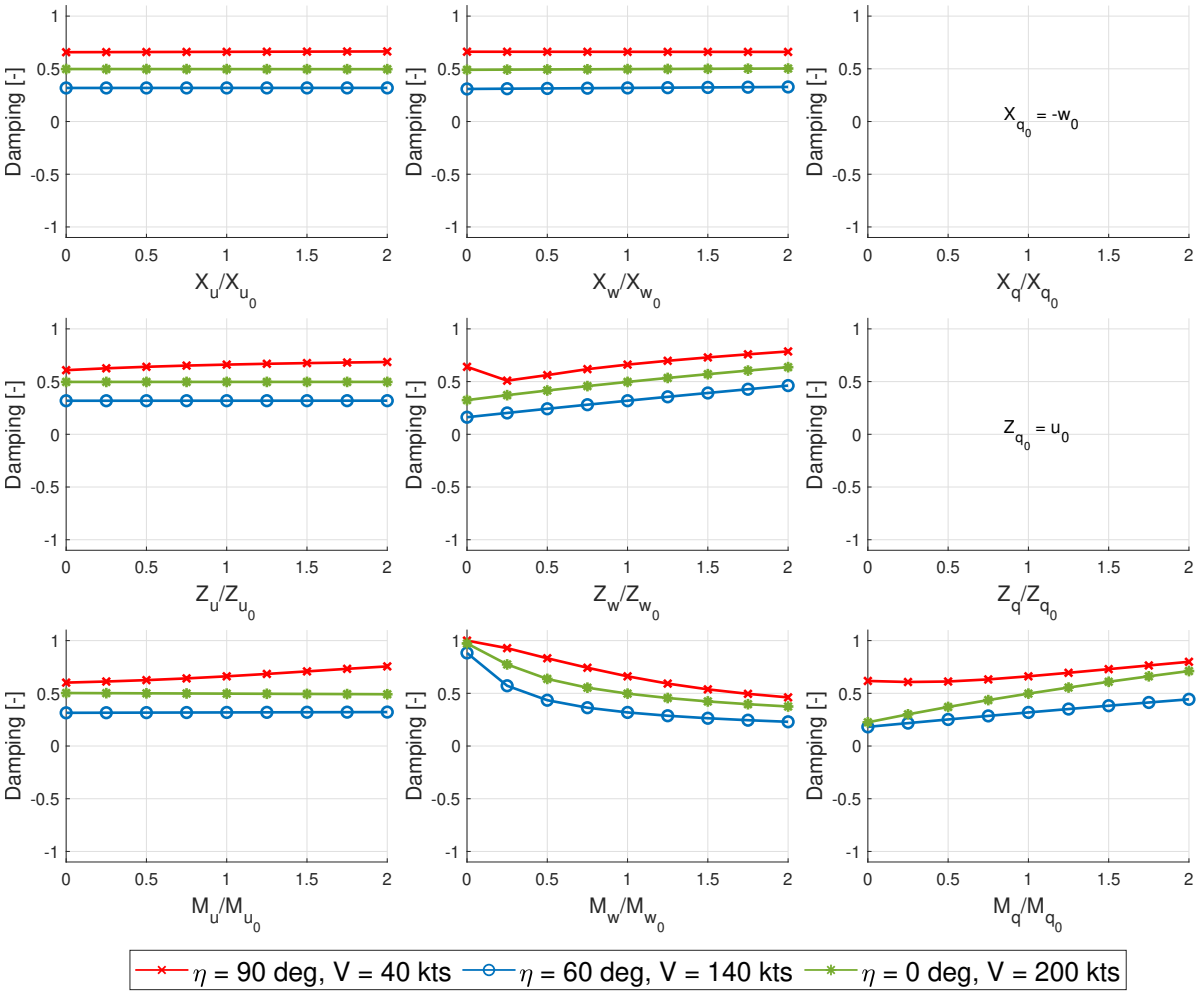

Figure D.2: Sensitivity Analysis of the Stability Derivatives on the Damping of the Short Period

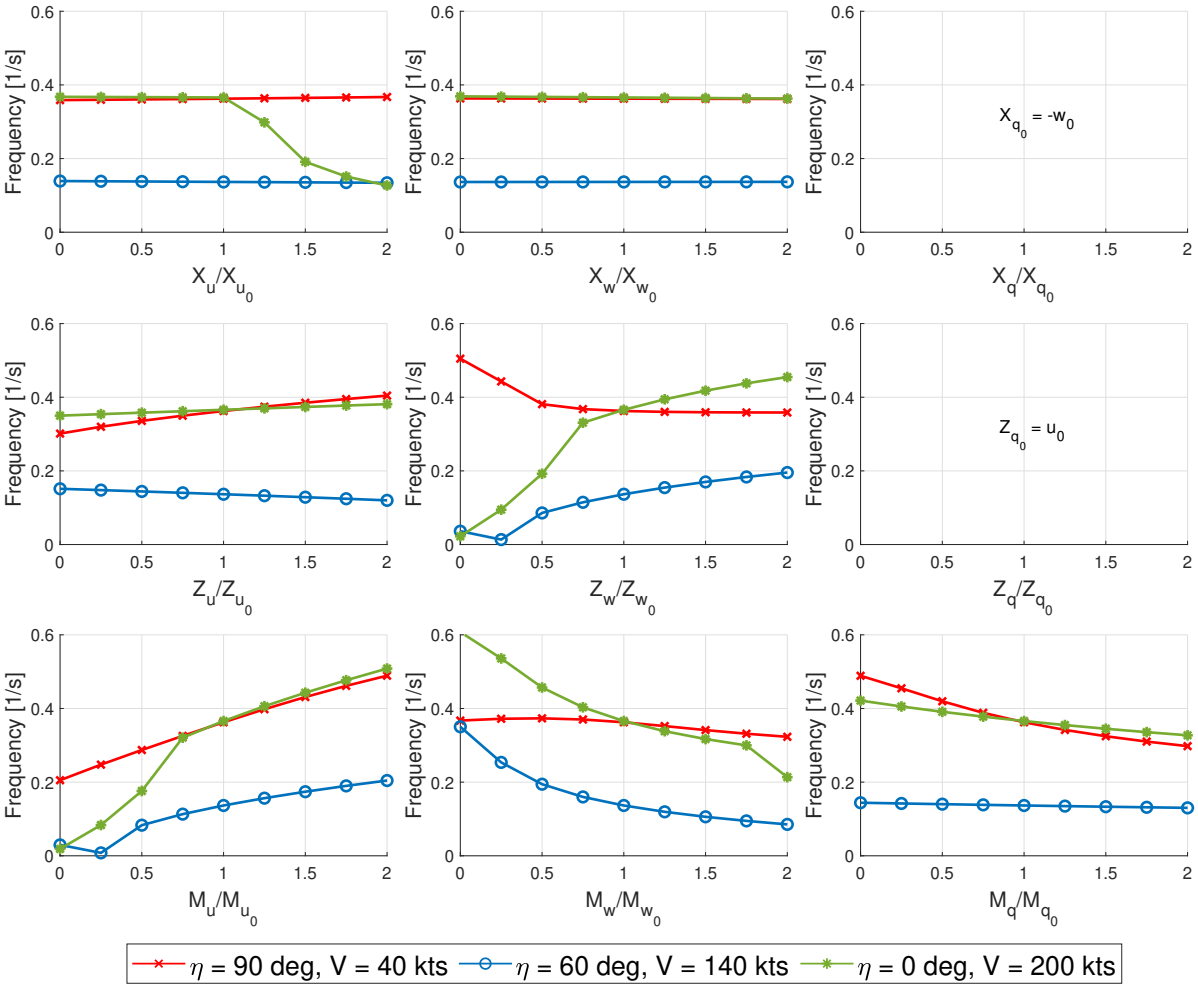

Figure D.3: Sensitivity Analysis of the Stability Derivatives on the Frequency of the Phugoid

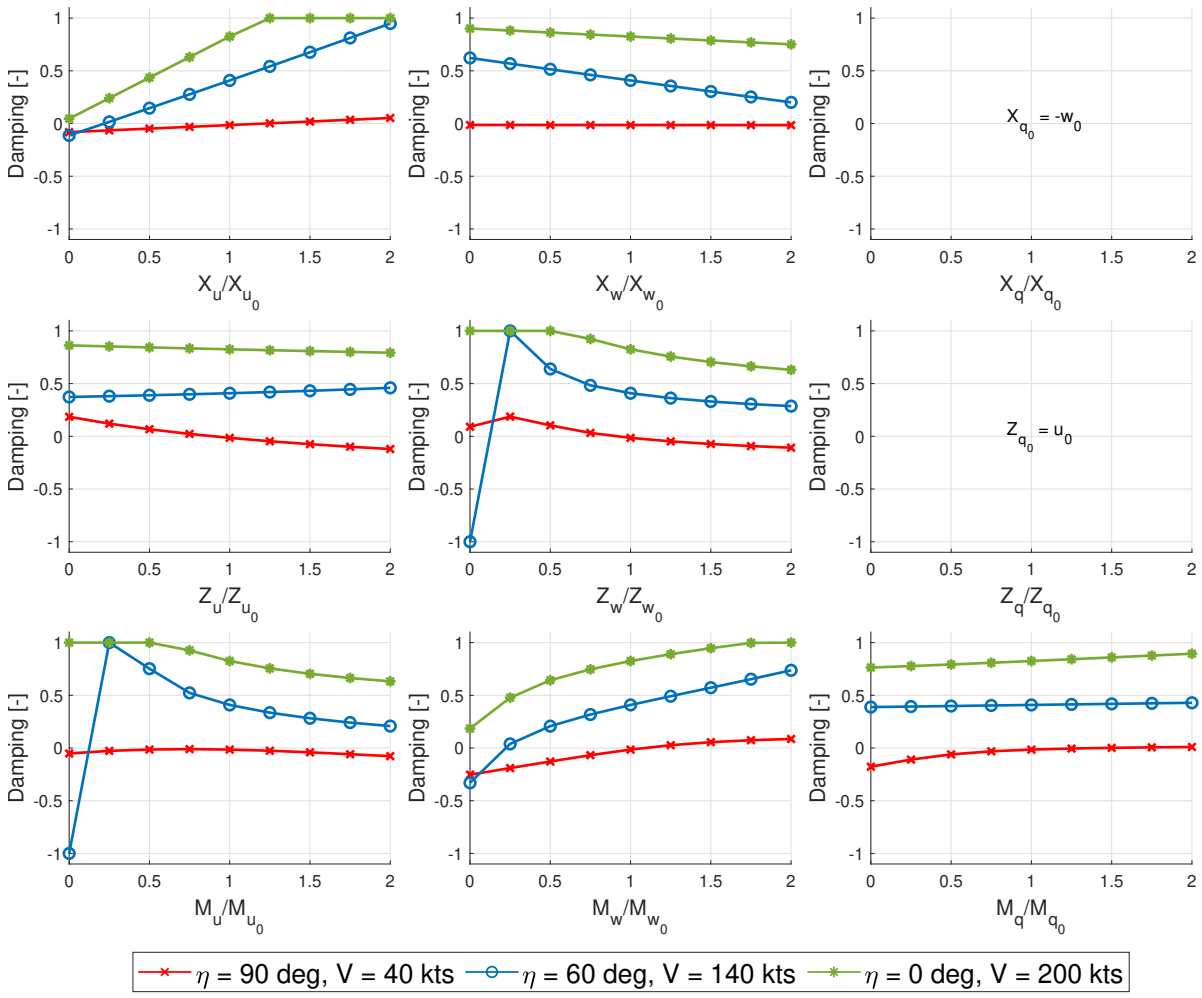

Figure D.4: Sensitivity Analysis of the Stability Derivatives on the Damping of the Phugoid

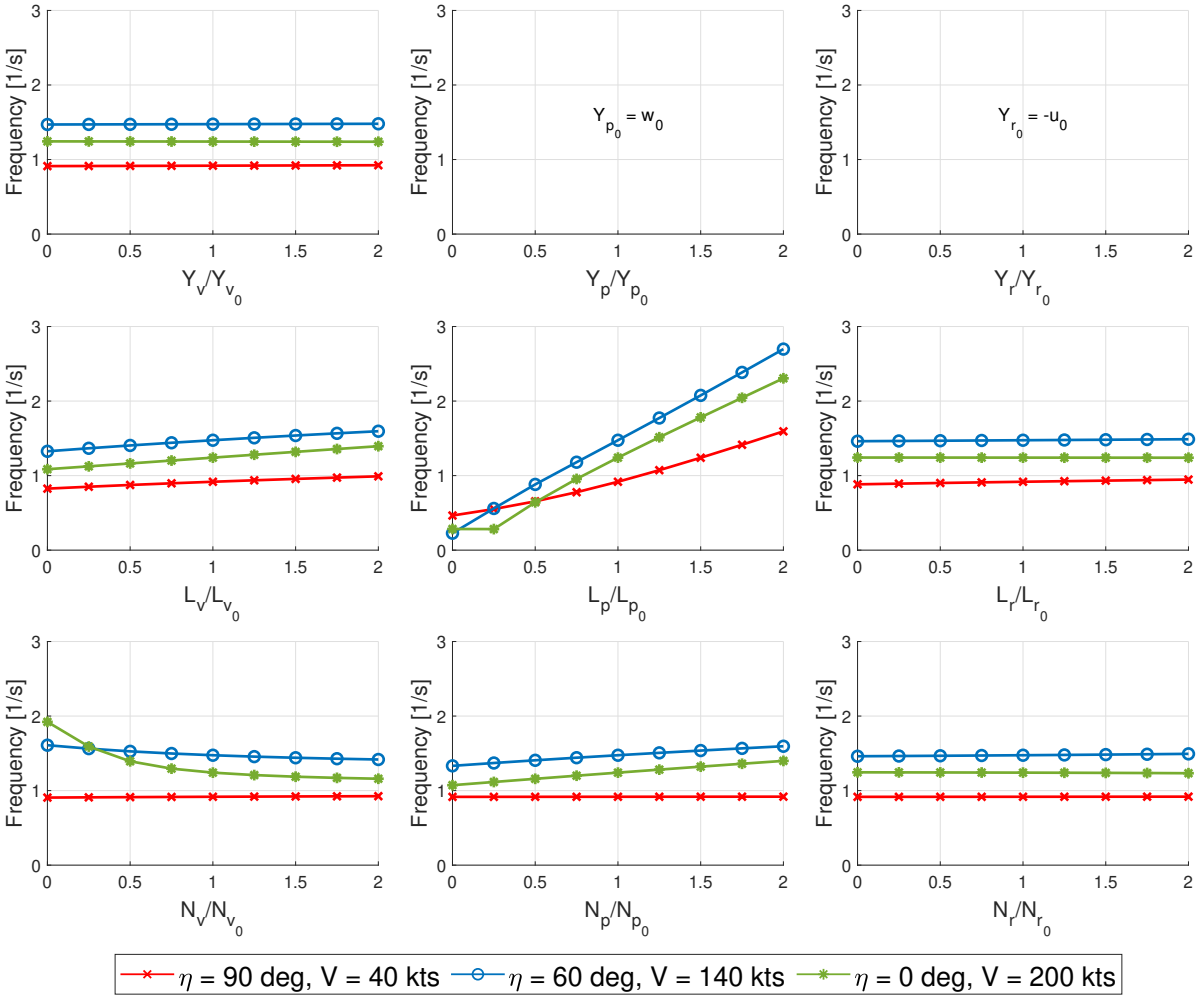

Figure D.5: Sensitivity Analysis of the Stability Derivatives on the Frequency of the Roll Mode

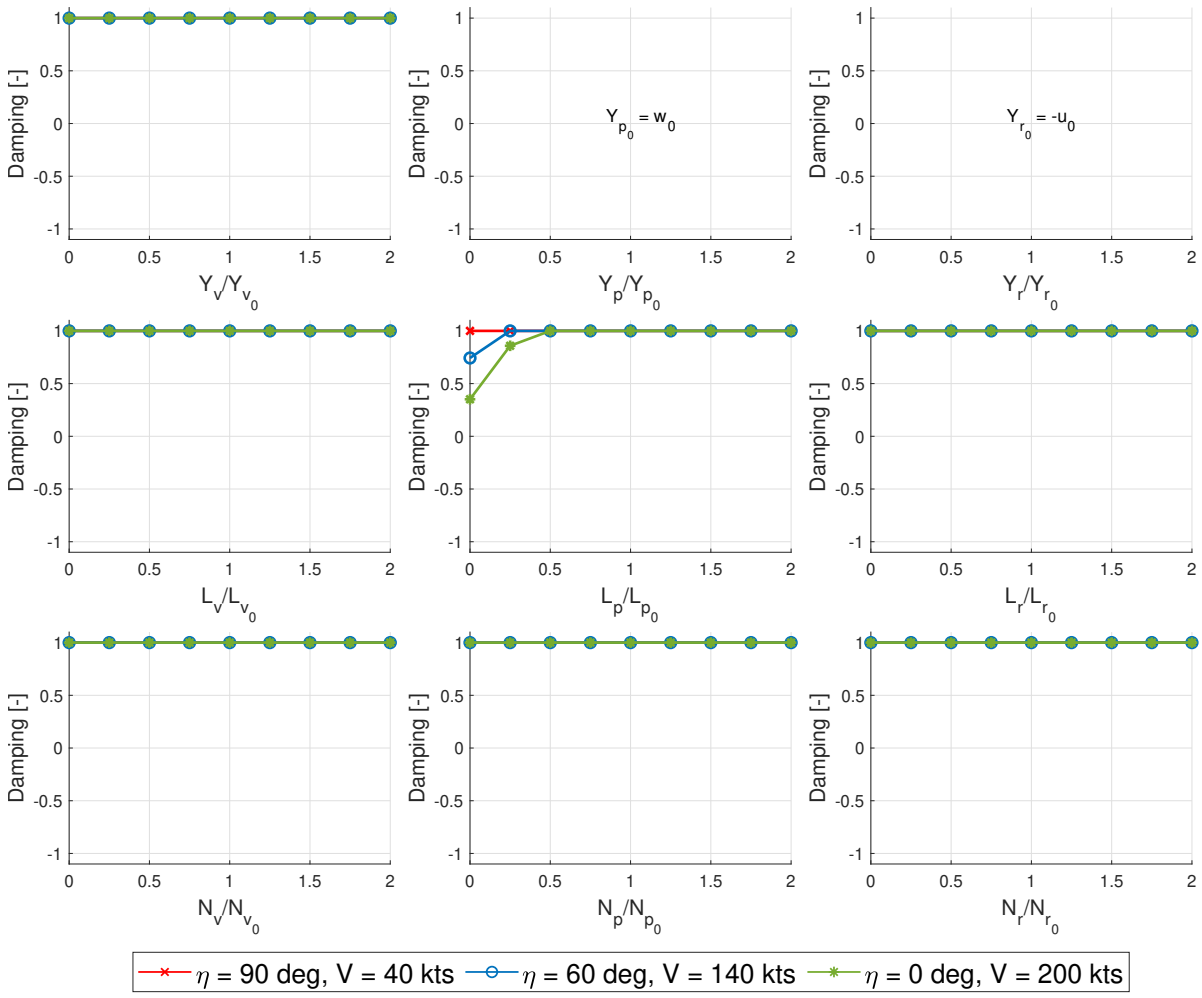

Figure D.6: Sensitivity Analysis of the Stability Derivatives on the Damping of the Roll Mode

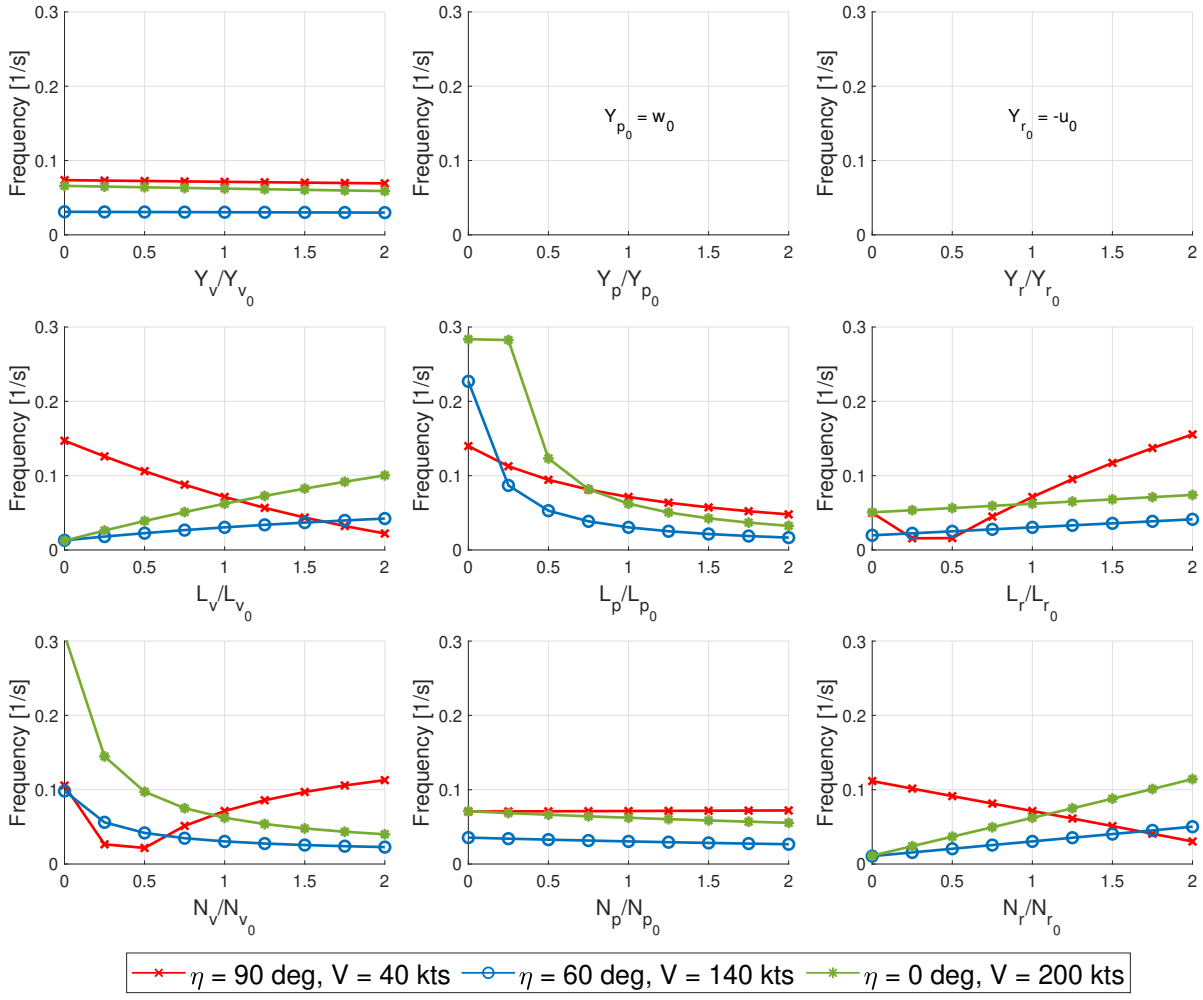

Figure D.7: Sensitivity Analysis of the Stability Derivatives on the Frequency of the Spiral Mode

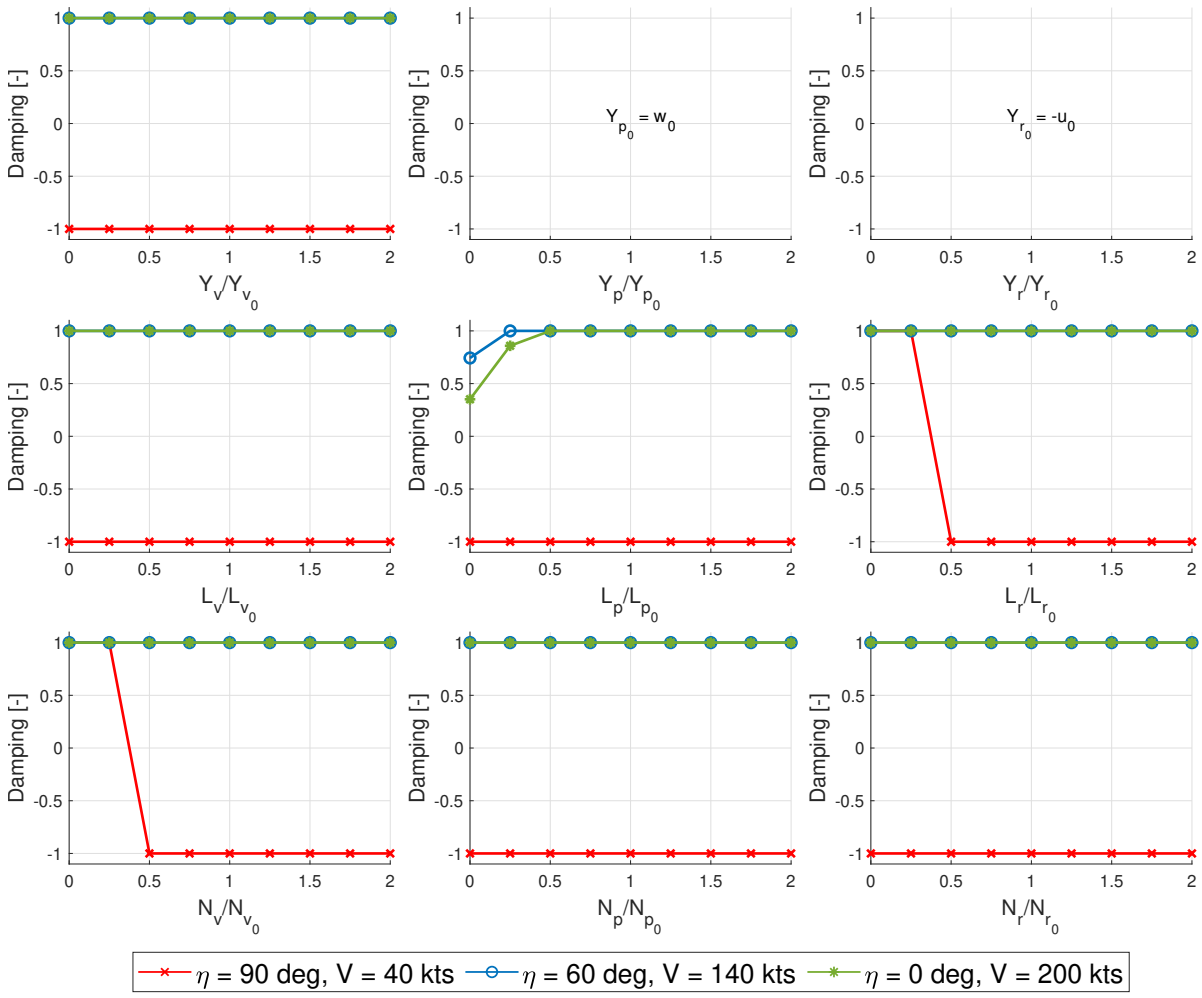

Figure D.8: Sensitivity Analysis of the Stability Derivatives on the Damping of the Spiral Mode

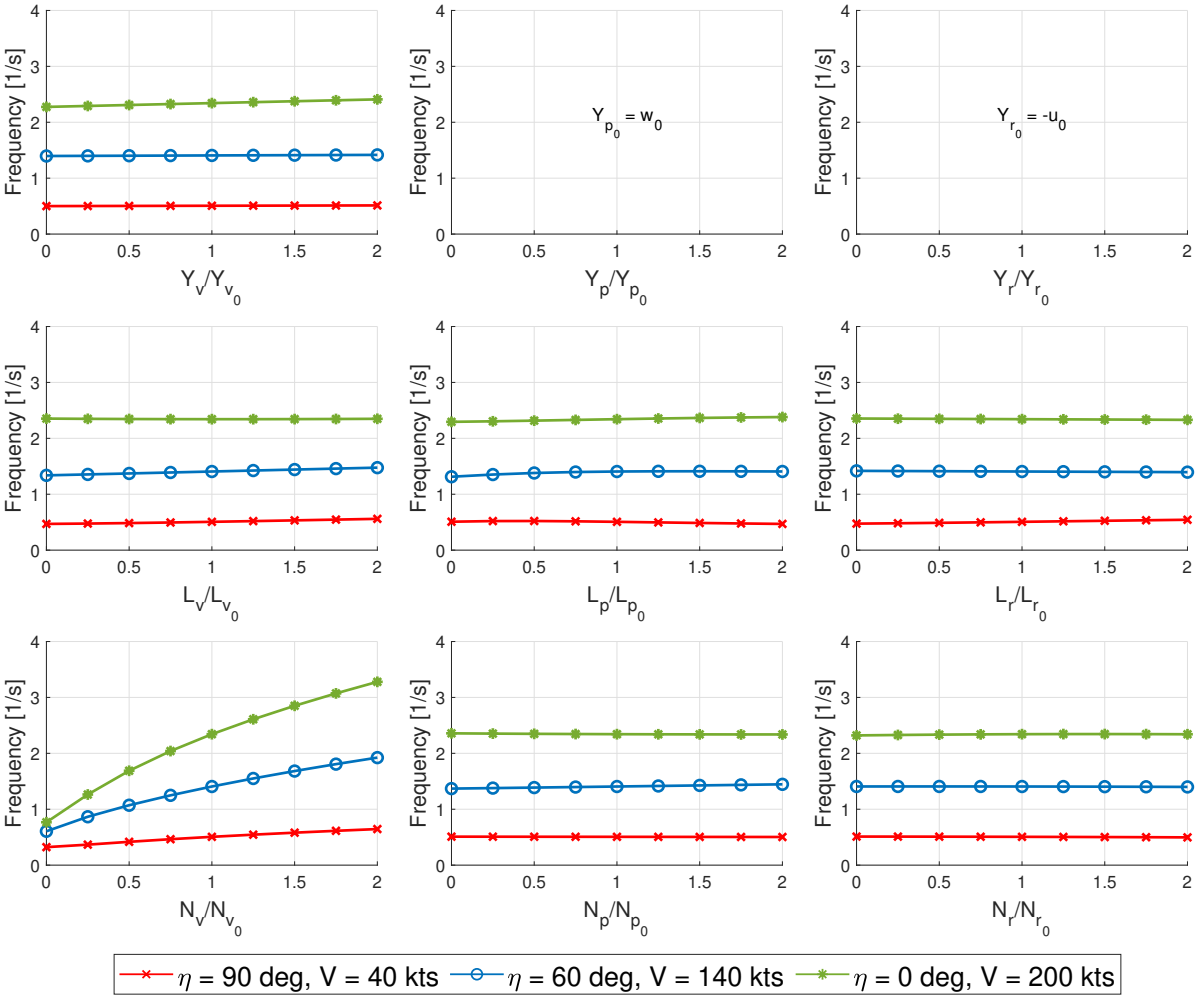

Figure D.9: Sensitivity Analysis of the Stability Derivatives on the Frequency of the Dutch Roll

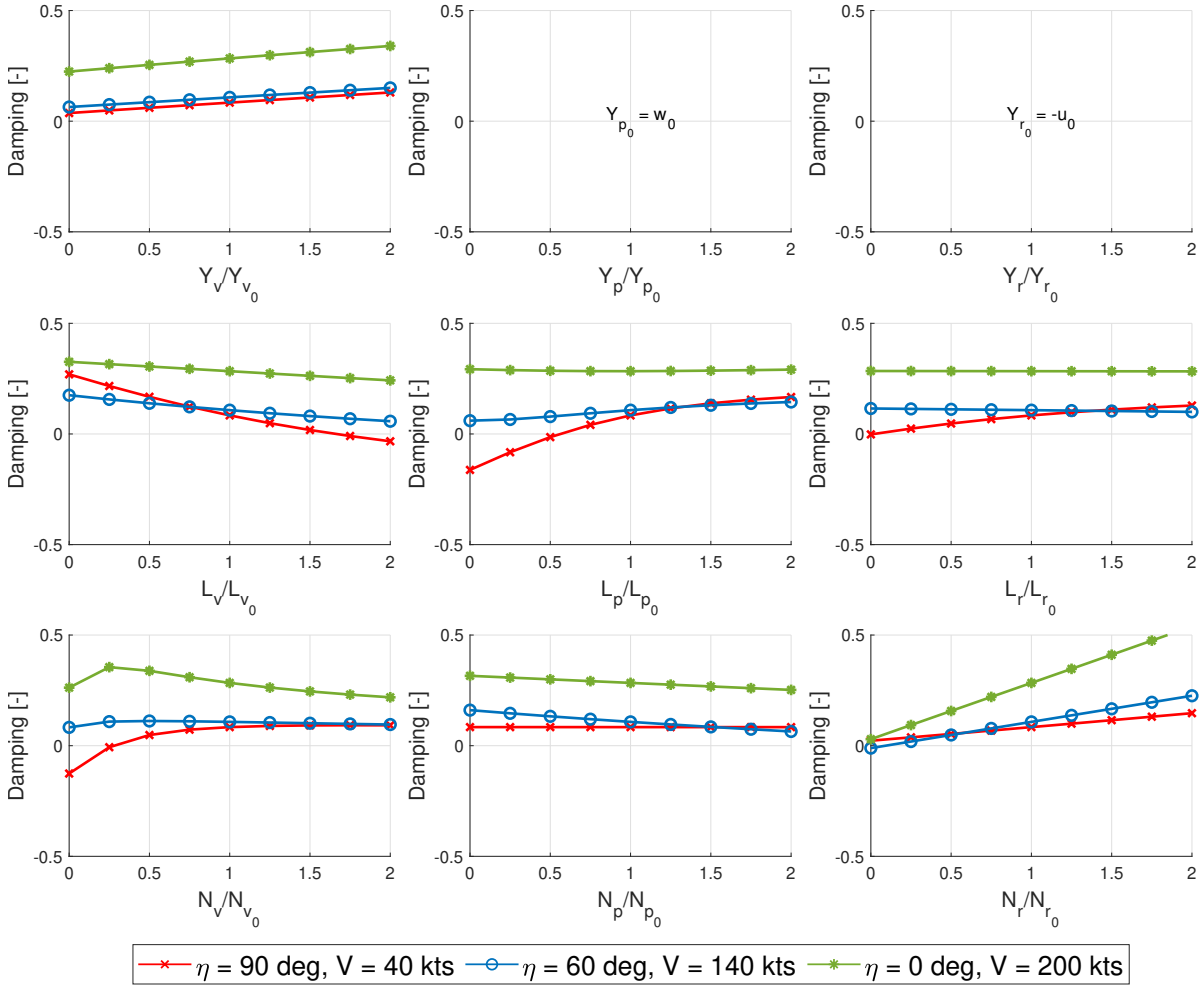

Figure D.10: Sensitivity Analysis of the Stability Derivatives on the Damping of the Dutch Roll